INVESTIGATING TURBULENT MIXING PROCESSES USING HIGH-RESOLUTION TEMPERATURE SENSORS ON AUTONOMOUS OCEAN GLIDERS

A thesis submitted to the School of Environmental Science
of the University of East Anglia in partial fulfilment
of the requirements for the degree of Doctor of Philosophy

PHILIP JAMES LEADBITTER

SEPTEMBER 2022

ABSTRACT

Turbulent processes play a key role in ocean mixing. However, lack of spatial and temporal data collection limits our understanding of these processes, especially in the deep ocean away from boundaries. In this thesis we investigate the suitability of using the Thorpe scale method on high resolution temperature data from buoyancy driven gliders and vertical microstructure profilers to improve provision of estimates of turbulent kinetic dissipation rates.

Using three datasets a robust methodology was developed to estimate dissipation rates from Thorpe length scales using both a vertical microstructure profiler and Seagliders.

Three distinct regions were investigated; open ocean over the Mid-Atlantic Ridge using a vertical microstructure profiler, open ocean in the Subtropical North Atlantic away from boundaries using a Seaglider, and the flank of a submarine ridge in the Faroe-Shetland channel using a Seaglider. All regions showed dissipations ($(O)10^{-11}$ to $(O)10^{-6}$ W kg^{-1}) and diffusivities ($(O)10^{-6}$ to $(O)10^{-4}$ m^{-2} s^{-1}) within expected global ranges, although the latter two showed up to an order of magnitude difference to other studies from the same region.

Over the Mid-Atlantic Ridge, Thorpe scale matched the structure and tidal cycle provided by shear data from the same platform. In contrast, in the Faroe-Shetland channel the method performed poorer, not showing the elevated values of dissipation expected in an internal tide generating region. Additionally, Thorpe scaling showed elevated levels of diapycnal mixing in the Subtropical North Atlantic associated with Thermohaline staircases even though this is non-mechanical process.

The benefits, drawbacks and relevance of Thorpe scaling high resolution temperature are discussed and compared with other finescale parametrisations, leading to suggestions as to where the method is most applicable within the oceans for further study.

Access Condition and Agreement

Each deposit in UEA Digital Repository is protected by copyright and other intellectual property rights, and duplication or sale of all or part of any of the Data Collections is not permitted, except that material may be duplicated by you for your research use or for educational purposes in electronic or print form. You must obtain permission from the copyright holder, usually the author, for any other use. Exceptions only apply where a deposit may be explicitly provided under a stated licence, such as a Creative Commons licence or Open Government licence.

Electronic or print copies may not be offered, whether for sale or otherwise to anyone, unless explicitly stated under a Creative Commons or Open Government license. Unauthorised reproduction, editing or reformatting for resale purposes is explicitly prohibited (except where approved by the copyright holder themselves) and UEA reserves the right to take immediate ‘take down’ action on behalf of the copyright and/or rights holder if this Access condition of the UEA Digital Repository is breached. Any material in this database has been supplied on the understanding that it is copyright material and that no quotation from the material may be published without proper acknowledgement.

CONTENTS

LIST OF FIGURES

LIST OF TABLES

LISTS OF SYMBOLS AND ACRONYMS

Common symbols used in this thesis (alphabetical; lower case, upper case, Greek). Dashes in the units column indicate either changeable units or a dimensionless variable.

Symbol	Name	units
g	Gravitational acceleration	$\mathrm{m\,s^{-2}}$
z	Depth	m
C_p	Ocean Specific heat capacity	$\mathrm{J\,kg^{-1}\,K^{-1}}$
F_{net}	Net energy flux	$\mathrm{kW\,m^{-1}}$
L_O	Ozmidov scale, dissipation length scale	-
N	Buoyancy frequency	$\mathrm{s^{-2}}$
(O)	Order of	-
P	Pressure	$\mathrm{kg\,m^{-1}\,s^{-2}}$
R_ρ	Density stability ratio	-
S_a	Absolute salinity	$\mathrm{g\,kg^{-1}}$
S_z	Vertical gradient of Absolute salinity	$\mathrm{kg\,g^{-1}\,m^{-1}}$
T_d	Thorpe Displacement	m
T_f	Thorpe fluctuation	°C or $\mathrm{kg\,m^{-3}}$
T_L	Thorpe Length Scale	m
Tu	Turner angle	°
Q	Vertical Heat flux	$\mathrm{W\,m^{-2}}$
ε	TKE dissipation rate	$\mathrm{W\,kg^{-1}}$
ε_{ms}	TKE dissipation rate from temperature variance	$\mathrm{W\,kg^{-1}}$
ε_{Shear}	TKE dissipation rate from shear	$\mathrm{W\,kg^{-1}}$
ε_{Thorpe}	TKE dissipation rate from Thorpe scales	$\mathrm{W\,kg^{-1}}$
κ_ρ	vertical diapycnal eddy diffusivity	- $\mathrm{m^{-2}\,s^{-1}}$
θ	Potential temperature	°C
Θ	Conservative temperature	°C
Θ_z	Vertical gradient of Conservative temperature	° $\mathrm{m^{-1}}$
ξ	Vertical Isopycnal Displacement	m
ρ	Density	$\mathrm{kg\,m^{-3}}$
σ_1	Potential density 1000 m reference	$\mathrm{kg\,m^{-3}}$
σ_θ	Potential density 0 m reference	$\mathrm{kg\,m^{-3}}$
ϕ	Glide angle	°
χ	Temperature variance	-

Acronyms used in this thesis (alphabetical order).

ADCP	Acoustic Doppler Current Profiler
AIW	Arctic Intermediate Water
AUV	Autonomous Underwater Vehicles
BBTRE	Brazil Basin Tracer Release Experiment
C-SALT	Caribbean-Sheets and Layers Transect
CTD	Conductivity temperature depth
CT	Conductivity Temperature
D	Deep Station
DAC	Dive Averaged Current
EM	Electromagnetic
EUREC^{4}A	Elucidating the Role of Cloud-Circulation Coupling in the Climate
FBC	Faroe Bank Channel
FP07	Fast response thermistor
FSC	Faroe Shetland Channel
GPS	Global Positioning System
GSR	Scotland-Greenland Ridge
HOME	Hawaii Ocean Mixing Experiment
IWISE	Internal Waves in Straights Experiment
LADCP	Lowered Acoustic Doppler Current Profiler
MAR	Mid Atlantic Ridge
MASSMO4	4th Marine Autonomous Systems in Support of Marine Observations
MNAW	Modified North Atlantic Water
MEIW	Modified East Icelandic Water
MSP	Microstructure profiler
NATRE	North Atlantic Tracer Release Experiment
NAW	North Atlantic Water
NOC	National Oceanography Centre
NSAIW	Norwegian Sea Arctic Intermediate Water
NSDW	Norwegian Sea Deep Water
ODAS	Oceanographic Data Acquisition System
OMG	Ocean Microstructure Glider
RMS	Root Mean Square
RN	Ridge Station Neap (combined)
RoD	Rate of Descent
RS	Ridge Station Spring
RSI	Rockland Scientific
SG	Seaglider
SSE	Sea Surface Elevation
SSH	Sea Surface Height
SST	Sea Surface Temperature
T/S or T-S	Temperature Salinity
TMD	Tide Model Driver
TKE	Turbulent Kinetic Energy
VMP	Vertical Microstructure Profiler
WTB	Wyville Thomson Basin
WTR	Wyville Thomson Ridge

ACKNOWLEDGEMENTS

Firstly I must thank all my supervisors. At the University of East Anglia; Rob Hall for the continued support throughout this project and letting me go down rabbit holes of investigation. Karen Heywood for pulling me out of those rabbit holes when I dug too deep and reminding me I didn't need to do everything. Alex Brearley from the British Antarctic Survey for scientific input during our catch ups and Elizabeth Creed from Seaglider for pushing me to think differently and always being happy to chat about her experiences. You have all been invaluable to me completing this project.

Thanks to all in the University of East Anglia Glider group. I thoroughly enjoyed being part of the team, providing me with experiences that I would have not had if I had done my studies at a different institution. I will miss being involved in future deployments. Individual thanks also goes to Gillian Damerell and Peter Sheehan for providing me with the initial quality controlled data from glider deployments; as well as the glider pilots and ship crews that made the data collection possible.

To all the friends and lasting friendships I made along the way whilst living in Norwich, especially Sophie for the dancing, Tom for the drinks at the bar and Chris for all the games of tiny planes. Also to all the members of office ENV 3.16 over the three years I had a desk there before it was all abruptly cut short by a global pandemic.

For my parents Neil and Thalia who had to deal with me moving the furthest from home I have ever been and supporting me from start to finish with this. Finally a huge thanks needs to be given to my partner Nikki, for sticking with me when I moved away from Southampton, becoming my new office mate when we had to suddenly start working from home, being there through the highs and lows, listening to me ramble through my work when I need to think out loud and providing tech support when my laptop wasn't working. I wouldn't have finished this without your continued support.

This work was supported by the Natural Environmental Research Council [grant number NE/N012070/1]

For the one that opened my eyes to the oceanographic world,
Clive Cussler
(1931 - 2020)

"There's a little bit of Pitt in everybody"

1

INTRODUCTION AND BACKGROUND

Ocean mixing is a vast subject that encompasses a wide range of processes and is vital to closing the Meridional Overturning Circulation. Without upward mixing of cold waters the ocean would eventually form a single water mass of cold salty water (Munk and Wunsch, 1998a). Ocean mixing is split into two main regimes; geostrophic turbulence that is mediated by mesoscale eddies $\geq (O)100$ m and small scale three dimensional isotropic turbulence $(O)0.1-100$ m (Melet et al., 2022), which can be estimated at both microscale and finescale. Observations at these smaller scales have been traditionally time intensive, based on ship supported surveys giving a localised snapshot of mixing in the ocean and turbulent conditions (Frajka-Williams et al., 2022). Since the 1960s the core platform for measuring turbulent dissipation at microscales has been the vertical profiler (Lueck et al., 2002). In the 1990s microstructure instruments (fast response thermistors and shear probes) had been fitted to all manner of autonomous underwater vehicles (AUV) and even manned submersibles (Lueck et al., 2002). AUVs provided the opportunity for longer surveys, in more remote regions, to be conducted than would be possible using ship dependent vertical profiler deployments. In 2001 the US Office of Naval Research provided funding for the development of three underwater buoyancy driven gliders; the Spray from Scripps Institution of Oceanography and Wood Hole Oceanographic Institution (Sherman et al., 2001), the Seaglider from the University of Washington (Eriksen et al., 2001) and the Slocum from Webb Research (Webb et al., 2001). These platforms have a range in the 1000s of kilometres, are depth capable to 1000 m on average and have a duration of up to 12 months (Rudnick, 2016; Frajka-Williams et al., 2022). In 2009 a microstructure instrument package was mounted successfully to the Slocum glider (a MicroRider from Rockland Scientific [RSI]) collecting usable data for estimating turbulent kinetic energy (TKE) dissipation rates of the same quality as a vertical profiler (Wolk et al., 2009). Although considerably reducing the duration of the glider's flight, a new tool for measuring the microscale had been made available to the oceanographic mixing community that was capable of recording data over a number of weeks for a fraction of the cost a ship survey. Of the sensors available to provide data to estimate TKE dissipation rates from the shear probe is the more readily used; however, faster response thermistors are also capable of providing estimates of TKE dissipation (Frajka-Williams et al., 2022). In this thesis we use fast response thermistor (FP07) measurements from both vertical profilers and Seagliders to develop a methodology for estimating TKE dissipation rates based on the Thorpe scale method proposed by Thorpe (1977).

1.1 OCEAN TURBULENT MIXING

Ocean turbulent mixing is a broad title that encompasses the three dimensional turbulent mixing of oceanic waters (Naveira Garabato and Meredith, 2022). Turbulence is widely accepted as being an energetic motion that disperses material and transfers energy (for example kinetic energy to heat) at a higher rate than molecular processes by themselves (Thorpe, 2007).

Mixing (in any fluid) is made up of two main components; stirring, a process that increases property gradients in a fluid and diffusion which acts to reduce the gradients of a property. Through stirring, parcels that are initially close together are separated, but stirring does not itself change the properties of a parcel, rather it increases the surface area between parcels of different properties allowing for these properties to diffuse across the boundaries (stirring in a fluid occurs in three dimensions not two). Diffusion occurs either through molecular diffusion or thermal conduction depending on the property in question (Thorpe, 2007).

Many different physical processes contribute to ocean turbulent mixing such as, but not limited to breaking waves (surface and internal), wind passing over the oceans' surface and ocean currents passing over rough bottom topography (Knauss, 2005). The intensity of ocean mixing is dominated by large scale processes creating gradients (via stirring) in properties such as salinity, temperature, density etc. However, it is at the smallest scales where molecular viscosity and diffusion work to reduce the gradients and homogenise the properties (Frajka-Williams et al., 2022). These small scale turbulent processes across property gradients are considered key to closing this circulation by vertically mixing water properties resulting in water mass transformations (Munk, 1966; Osborn, 1980). Although it is these small-scale variations in properties at the microscale that form the focus of the work presented in this thesis, a broad scale synopsis is first given to place these small scale variations into a global context.

MIXING AND GLOBAL OCEAN CIRCULATION

At the largest scale ocean mixing redistributes heat gained by the oceans from solar radiation at low latitudes, transferring this heat to higher latitudes where it can be lost to the atmosphere (de Lavergne et al., 2022). This transfer of heat results in a meridional overturning circulation (MOC), with deep water formation at the poles through surface densification (Melet et al., 2022) feeding the return flow at depth, although the exact actual process and paths of this flow are more complex.

This redistribution of heat via the MOC is vital to maintain the global climate in some form of equilibrium that we see on the planet today. Changes to the overturning circulation from decadal to millennial length scales can have a large impact on the global climate. These changes range from changes in precipitation and the North Atlantic storm tract (Jackson et al., 2015) to abrupt climate changes (Kageyama et al., 2010), with most being caused by a level of weakening of the Atlantic section of the MOC. During a water mass's southward flow from the poles, mixing at overflows determines its density in North Atlantic Deep Water (NADW), setting its depth for the remainder of its journey (Melet et al., 2022). This occurs through a number of processes including bottom drag induced mixing and shear induced mixing leading to entrainment of water into water masses above it (Legg et al., 2009).

The return of NADW to the surface involves adiabatic, wind-driven up-welling along isopycnals, where it forms Antarctic Bottom Water (AABW) and Antarctic Intermediate Water (AAIW). Through a mixture of internal wave driven mixing, geothermal heating and diapycnal mixing with overlying water masses, both the AAIW and AABW begin to make the journey northward again. Diapycnal mixing helps set the heat content of the water masses and the strength of the MOC and model studies have shown that increasing the background diapycnal mixing increases the strength of both the upper and lower branches of the MOC (St. Laurent et al., 2002; Hieronymus et al., 2019). In addition, it has been shown that it is not only the magnitude of this background mixing that is important but also its spatial (horizontally and vertically) distribution that influences the MOC (Melet et al., 2013).

It is then vital to improve our understanding of where such mixing is occurring in the oceans, a task proved more difficult by the sporadic nature of mixing. In contrast to the open ocean the coastal oceans cover less than 10% of the worlds water masses (Woods Hole Oceanographic Insitution), yet these coastal areas contribute both to distinct water mass input into the open oceans and have a large impact on the human populace. Water that leaves these zones is distinct from those water masses formed in the open ocean and has a significant impact on modifying water masses in the oceans interior (Melet et al., 2022).

The world's largest rivers introduce fresh water to the ocean basins as near-surface fresh water plumes, which in turn are influenced by shear, wind and tidal driven mixing. Basins such as the Mediterranean, where there is net evaporation, or at the poles, where there is net ice formation both contribute more saline water masses to the global ocean (Melet et al., 2022). Dense overflows at ridges and sills around coastal waters (Legg et al., 2009), such as the Wyville Thompson Ridge (see Chapter 4) see significant entrainment and diapycnal mixing through various processes until the water overflow density matches that of the water surrounding it and detaches from the slope.

MIXING AND BIOGEOCHEMICAL CYCLING

Ocean mixing is a physical process that as well as impacting and being impacted by other physical processes also acts upon and influences biogeochemical processes within the ocean. The oceans are not dead expanses of water but filled with life from some of the largest creatures on the planet to micro-organisms (phytoplankton) that form the base of marine ecosystems, produce oxygen and sequester carbon to the deep oceans (Luyten et al., 1982). It is these smallest organisms that ocean mixing impacts directly, an impact that can be felt all the way up the ocean food chain and on the climate.

Phytoplankton growth is largely regulated by the availability of nutrients in the well-lit near surface euphotic zones. Phytoplankton require nutrients and micronutrients such as phosphate, nitrate and iron to grow in addition to sunlight. During growth periods, phytoplankton will strip out these nutrients in the stratified surface waters of the ocean. These nutrients are then removed from the euphotic zone through phytoplankton faecal pellets being grazed by zooplankton or other sinking particulates formed on the death of phytoplankton, broadly referred to as marine snow. Some of this marine snow can re-mineralise at depths and can then be mixed back up to the euphotic zone via vertical mixing. Where these nutrients are returned to the euphotic zone is then influenced by spatially varying turbulent mixing processes at the base of the mixed layer, the seasonal cycle of the mixed layer depth and regions of net up-welling (Melet et al., 2022). Nutrients can also be transported laterally via mesoscale eddies (Abernathey et al., 2021), in some instances even supplying nutrient limited regions with vital nutrient sources (Lee et al., 2007).

The stratification of the mixed later inhibits the vertical mixing of nutrients into it. One of the impacts of climate change that has been shown is that the stratification of the mixed layer will strengthen. This increase in strength will decrease the effectiveness of vertical turbulent mixing supplying needed nutrients to the upper oceans, with net primary productivity expected to fall between 4% and 11% in the next 80 years (Bindoff et al., 2019).

MIXING AND OCEAN MODELLING

Ocean modelling, although directly impacted by ocean mixing, is influenced by the ocean mixing studies which feed back into the modelling community to give values to processes that are usually themselves not modelled. Most of the ocean mixing processes occur at too small a scale compared to the grid size used for the oceanic systems of large global climate models (GMC). For example internal waves generate events over spatial scales of 1-100 m with a time frame of minutes to hours, which is much smaller than the minimum $O(100)$km of a grid cell ($\sim 1^\circ$). However, as it is these small-scale events combined play a large role in potential climatic changes, their correct implementation into GMCs is vital. One method of implementing turbulent mixing into a GMC is to use a single number value representing dissipation or diffusivity for a given grid or layer. Although computationally faster this route may lead to more long-term errors as it does not take into consideration any variation seen in turbulent mixing. More commonly implemented in a GMC (or other model) is a series of parametrisations of mixing, a number of different parametrisations are required to effectively represent the many sub cell processes that go into ocean mixing. Some of these include parametrisations for shear driven mixing, internal tide dissipation and boundary layer turbulence. Other considerations need also be included such as the mixing efficiency (originally thought to be around 0.2 but is now understood to depend on flow properties) and time-evolving mixing to take into account the non-steady nature of turbulent mixing.

Above we have shown a variety of ways in which ocean turbulent mixing can impact the climate system and the scientific community. As such it is important to continue to work at providing better estimates of turbulent mixing in the world's oceans using field work to constrain and better understand some of these large scale processes.

As this is only a brief synopsis of the role of ocean turbulent mixing at a global scale, readers are directed to Thorpe (2007) and Meredith and Naveira Garabato (2021) if a more in depth break down is required.

1.1.1 DISSIPATION AND DIFFUSIVITY

TURBULENT KINETIC ENERGY DISSIPATION

Dissipation (ε) represents an irreversible loss of kinetic energy from the ocean (Thorpe, 2007), transferring kinetic energy into heat and typically expressed as a rate of dissipation of turbulent kinetic energy per unit mass ($\mathrm{W\,kg^{-1}}$). This loss of energy to heat is due to the viscosity of the water. Any fluid will have a molecular viscosity that slowly reduces the gradients of a property within it. The oceans, however, dissipate energy much more quickly than is suggested by the molecular viscosity of sea water (Talley et al., 2011). In a fluid where there are large scale mixing and stirring events occur (such as the oceans) it is these processes that allow for the surface area over which molecular processes can take effect to be increased (Knauss, 2005). In an isotropic fluid, a fluid where there is no preferential direction of flow such as where there is fully developed turbulence, ε can be defined as

$$\varepsilon = \left(\frac{15}{2}\right) \nu \left\langle \left(\frac{\partial u}{\partial z}\right)^2 \right\rangle \tag{1.1}$$

Where ν is kinematic viscosity of water and $\partial u / \partial z$ is the gradient of velocity (here the horizontal direction is shown, the most common used for free fall profilers).

Values of TKE in the worlds oceans span a range of over nine orders of magnitude (Thorpe, 2007). Values in the open ocean typically range between 10^{-11} W kg^{-1} to 10^{-6} W kg^{-1}. The highest values are found in shallow coastal waters or near the bottom boundary, with regions away from the surface and bottom boundary at the lower end of this range (Smyth and Moum, 2019; Tanaka et al., 2021). It has been possible to measure values down to 10^{-12} W kg^{-1} using temperature (Scheifele et al., 2018), which is below the noise floor of traditional shear based measurements, although this requires specific conditions to be able to do so.

EDDY DIFFUSIVITY

Eddy diffusion (κ_ρ) is the process by which turbulent ‘eddies‘ at small scale accomplish diffusion of properties within a fluid, in this case the oceans, (Talley et al., 2011) and it has been argued that the motion of eddies is analogous to molecular motion (Knauss, 2005). Diffusion via eddy diffusion is, however, much higher than that of molecular diffusion as turbulent eddies can penetrate and carry the fluid further into other regions of fluid with different initial properties than by molecular diffusion alone. Eddy diffusivity can be related to ε by:

$$\kappa_\rho = \Gamma \varepsilon / N^2 \tag{1.2}$$

where Γ is the mixing efficiency (discussed in more detail in Section 2.2.6) and N the mean buoyancy frequency (Osborn, 1980). This assumes that the region of study is in steady state and that other contributions to TKE are negligible (Thorpe, 2007). In the context of this thesis the vertical component (diapycnal) of eddy diffusivity is used to calculate vertical heat fluxes as a result of turbulent mixing.

To account for the vertical density structure of the ocean Munk (1966) proposed a value of vertical eddy diffusivity of 1×10^{-4} m^2 s^{-1}. However observed values of vertical eddy diffusivity on the open oceans are an order of magnitude lower at 1×10^{-5} m^2 s^{-1} (Talley et al., 2011). To counter these lower values seen in the open ocean, regions of higher diffusivity must exist to make up this shortfall. Close to bottom topography values of κ_ρ have been found up to and between 9×10^{-5} m^2 s^{-1} and 12×10^{-5} m^2 s^{-1} from basin wide estimates (Ganachaud and Wunsch, 2001). A collation of potential eddy diffusivities by Wunsch and Ferrari (2004) show values possible up to 500×10^{-5} m^2 s^{-1} in restricted ocean channels. Diapycnal eddy diffusivity also varies according to latitude. At low latitudes it is small ($(O)10^{-6}$ m^2 s^{-1}), increasing to a maximum between 20° and 30° and then declining again in the higher latitudes to an average of $\sim 0.5 \times 10^{-5}$ m^2 s^{-1} (Talley et al., 2011). All the values presented above are for vertical eddy diffusivities. Horizontal eddy diffusivities are typically of $(O)10^{-3}$ m^2 s^{-1}, due to the increased length and velocity scales that are possible horizontally compared to vertically in the oceans.

1.1.2 MEASUREMENT OF TURBULENT DISSIPATION AT MICROSCALE

Ocean mixing and turbulence at the fine or microscale can be estimated with measurements at those scales. Microscale or 'microstructure' variations are $(O)0.1$ - 1 cm with finestructure being larger at $(O)10$ - 100 m (Frajka-Williams et al., 2022).

The current standard method for measuring turbulence at the fine and microscale is using air-foil shear probes, mounted to a free fall vertical microstructure profiler (VMP) or towed body. The probe measures variations in flow normal to the platform's direction of travel through the water. The time series of these velocity fluctuations is then converted to a velocity gradient spectrum and fitted to the theoretical Nasmyth curve (Nasmyth, 1973). The spectrum is then integrated to estimate TKE dissipation rate, ε. The noise floor for estimates of TKE dissipation rates from shear data from free fall microstructure profilers are typically $(O)10^{-10}$ W kg^{-1}.

A second method for estimating TKE dissipation rates is by using the temperature variance, χ. High resolution temperature is measured in a similar fashion to shear but uses instead a fast response thermistor. Again the measurements are converted to a spectrum in wave number scale and compared with the theoretical Batchelor spectrum (Batchelor, 1959). In the correct regime the noise floor for TKE dissipation estimates from this method can be as low as $(O)10^{-12}$ W kg^{-1}.

Although estimates of TKE dissipation rate are themselves of interest, a major advantage is the ability to utilise these estimates to further understand the consequences of mixing such as vertical fluxes of heat or salt. One benefit to measuring turbulence and then estimating ε is that direct measurement of fluxes, although possible, is very difficult (Frajka-Williams et al., 2022). Direct measurements can be achieved using tracer release experiments (Mater et al., 2015). An intentional tracer (such as the red dye rhodamine-B or sulfur hexafluoride, SF_6) can be released in small concentrations in an area of interest. Samples of water in all directions from the release site are analysed (chemically or by fluorescence) over a period of time to determine the spread of the tracer away from its release location in three dimensions (Talley et al., 2011). Instead of conducting a tracer release experiment it is possible to estimate diffusivity (κ) from both ε and χ from easier sampling methods and use it to estimate fluxes of the property of interest (Talley et al., 2011; Lique et al., 2014).

1.1.3 THE THORPE SCALE METHOD

In addition to the above methods, Thorpe (1977) put forward a method for estimating TKE dissipation, which was later supported by Dillon (1982), referred to as Thorpe Scaling using,

$$\langle \varepsilon \rangle = C L_T^2 N^3 \tag{1.3}$$

where ε is the kinetic energy dissipation rate, N is the buoyancy frequency and C is a pseudo constant. The method is possible due to a correlation between the vertical scale of a density overturn, the Thorpe Length Scale (L_T) and the Ozmidov scale (L_O), the dissipation length-scale (Ozmidov, 1965). The Thorpe Scale method allows for a TKE dissipation rate to be estimated from vertical profile of density (Thorpe, 2007). Due to the relative ease of being able to collect density profiles using conductivity-temperature-depth (CTD) instruments it presents an accessible method of obtaining estimates of TKE dissipation rates without requiring access to microstructure capable free fall profilers (Mater et al., 2015).

A common density overturn (where dense water overlies less dense water) that is seen in geophysical flows is the Kelvin-Helmholtz (K-H) billow (Smyth et al., 2002), accounting for some of the largest overturns in the ocean (Mater et al., 2015).

As a K-H billow builds denser water overlays over lighter water and increases the available potential energy (APE) of the immediate system. As the K-H breaks this APE is converted to TKE. “Young“ turbulence has a more easily defined, and more likely composed of a single overturn. “Old“ turbulence is less defined, typically comprising of a series of a complex selection of smaller overturns in a region of reduced stratification due to the mixing processes (Smyth et al., 2002). It is structures such as these that the Thorpe scale method uses to estimate TKE dissipation rates.

THE THORPE LENGTH SCALE AND THE OZMIDOV SCALE

As previously stated above, the ability to estimate ε for an overturning length scale comes from the relationship between the Thorpe Length scale and the Ozmidov Length scale,

$$L_O = \langle\varepsilon\rangle^{1/2} N^{3/2} \tag{1.4}$$

where ε is the TKE rate of dissipation and N the bouyancy frequency. When L_O is found to be proportional to L_T and this relationship is used to estimate dissipation rate as and is represented by C in Equation 1.3 as a pseudo constant equal to $(L_T/L_O)^2$ (Thorpe, 1977). The mean values of this constant have been empirically found to be in the range of 0.64 to 0.91 (Thorpe, 2007). Thorpe (1977) put forward that there was a linear relationship between L_O and L_T, which was supported by Dillon (1982), and subsequently by others (Crawford, 1986; Wijesekera et al., 1993; Mourn, 1996). However, a level of uncertainty in this linear relationship exists due to the scatter that is seen between L_O and L_T (Ferron et al., 1998; Thorpe, 2007). Observations by Seim and Gregg (1994) put forward the notion that the relationship between L_O and L_T evolves over the collapse of a K-H billow with the average being $L_T/L_O \sim 1$. More recently it has been shown that the linear relationship is also dependent on both the size of K-H billow turbulence and the physical parameters that instigate such billows. Mater et al. (2015) showed that L_T increased with respect to L_O with respect to the size of K-H billows, either shear or convectively driven, leading to biases in Thorpe Scaling where larger-scale instabilities exist. This bias is not found where the value of L_T/L_O is generated from a geometrically averaged sample across all depths and overturn scales, apart from in regions where double-diffusive structures may exist and be interpreted as overturns again causing a positive bias in values of ε. However, it was found that in regions where turbulence is convectively driven that a bias may exist, as the physical conditions do not support the relationship that $L_O \sim L_T$.

CALCULATING THE THORPE LENGTH SCALE

To calculate L_T a profile of density is first reordered so that it is monotonically increasing with depth, giving a profile that is statically stable with no inversions. In a profile with n samples of density (ρ_n) where each sample has an associated depth (Z_n), when the profile is re-ordered ρ_n will become ρ_m with a new associated depth (Z_m). From this both vertical displacement, the Thorpe displacement (T_d) and associated difference in density, the Thorpe fluctuation (T_f), can be calculated.

$$T_d = Z_m - Z_n \tag{1.5}$$

$$T_f = \rho_m - \rho_n \tag{1.6}$$

The Thorpe length scale (L_T) is defined as the root mean square (r.m.s) of T_d,

$$L_T = \langle T_d^2 \rangle^{1/2} \tag{1.7}$$

over an identified overturn. In this thesis we follow the methods of Mater et al. (2015) and Ijichi and Hibiya (2018) to identify an overturn. A top down cumulative sum of T_d, ΣT_d is carried out (it is also possible to use T_f). Where ΣT_d remains non-zero and is bounded by depths where $\Sigma T_d = 0$ it is identified as an overturn (see Figure 1.1 c for an example).

If the shear data collected is of poor quality then any remaining data streams need to be exploited. Oceanographic data collection is both complex and expensive, and additional methods that exploit any data collected are vital, especially in situations where the primary data stream of interest fails. This is so that insight can still be made into mixing processes. The Thorpe scale method was chosen to be developed as it can be applied to both high resolution and low resolution data.

In this thesis we look at the suitability of this method when applied to temperature data as the Thorpe scale method is more conventionally applied to density data (Galbrath and Kelley, 1995; Gargett and Garner, 2008; Hall et al., 2011; Mater et al., 2015; Ijichi and Hibiya, 2018). A number of considerations need to be taken into account when attempting to Thorpe scale temperature (irrespective of temperature

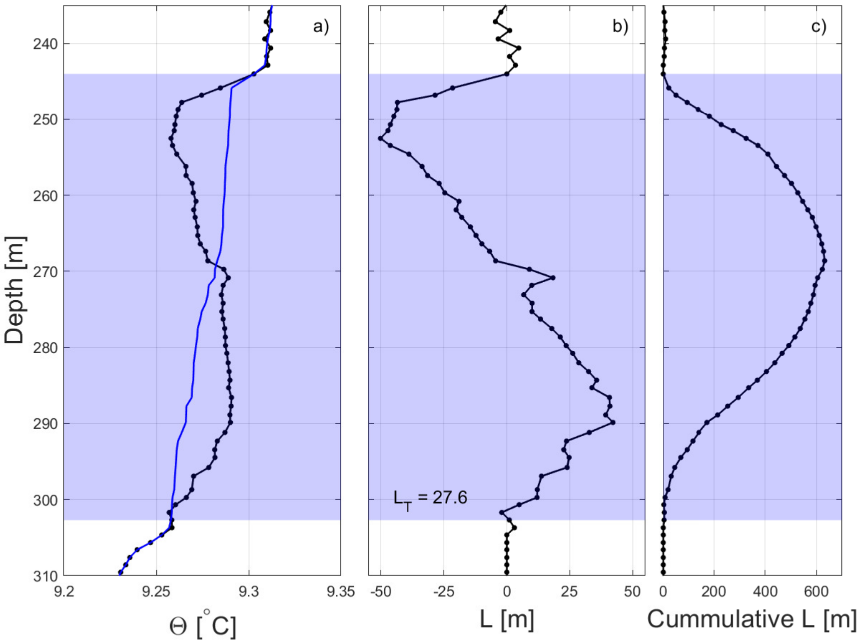

Figure 1.1: Figure showing a) Measured (black) and reordered (blue) conservative temperatures profiles. b) Associated Thorpe displacements c) Cumulative Thorpe displacements. Shaded blue areas mark the vertical extent of the complete overturn. Data presented in this image was collected during MASSMO4 (Chapter 4)

data resolution) including; providing a value for the buoyancy frequency required in Equation 1.3 and which regions of the water column are salinity compensated. These are investigated in detail in Chapters 2 and 3 in this thesis.

1.2 BUOYANCY DRIVEN GLIDERS

1.2.1 BACKGROUND TO BUOYANCY DRIVEN GLIDERS

In 1989 Stommel put forward a vision of a centralised command for over 400 gliders run from a command centre on Nonamesset Island (one of the Elizabeth Islands), with 200 of these machines being permanently deployed at sea and the other 200 used as and when needed for global research projects (Stommel, 1989). This piece of work brought to the attention a new and visionary method for observing the oceans (Rudnick, 2016).

Traditional methods for taking oceanographic measurements have been limited both temporally and spatially. Data collection from vessels is limited temporally (typical expeditions lasting weeks to months) and rarely repeated to show the space-time variability associated with the oceans (Eriksen et al., 2001). Mooring deployments that cover longer time spans are fixed in space (mooring arrays have been used to monitor ocean basins (Cunningham et al., 2007)) so lack spatial variability. Both typically have high costs associated with them (Schofield et al., 2007). To provide better temporal and spatial understanding profiling floats were developed. The earliest of these was the swallow float (Gould, 2005) used in the 1950s. The modern (since the year 2000) ARGO float reached 3000 active instruments world wide in 2007 (Roemmich et al., 2009). Profiling floats change their volume and hence buoyancy (Rudnick, 2016) through a buoyancy engine, where oil is pumped in or out of an external bladder at the base of the the float (Roemmich et al., 2004). This allows them to vertically profile by being less or more dense than the surrounding water masses and to stay at depth by becoming neutrally buoyant. As a Lagrangian (Batchelor, 1973) method of ocean observation a profiling float will follow the ocean currents giving current movements by GPS location every time an instrument surfaces on an ~10 day cycle. Floats are capable of collecting core hydrographic data (temperature and salinity) as well as being fitted with a range of biogeochemical sensor packages(Roemmich et al., 2009).

Following the successes of the ARGO float network (Roemmich et al., 2004, 2009), the underwater glider was the next step in the evolutionary train. Adding wings to profiling floats gave the ability to somewhat control their horizontal position (Rudnick, 2016; Davis et al., 2002). In 2001 a strategic funding boost from the United States Office of Naval Research led to the development of three buoyancy driven gliders (Davis et al., 2002). Each glider was designed with the following in mind. To be small devices that didn't need a major vessel for deployment, and could be handled by a few individuals. To be comparably cheap compared to research vessels both in construction and per mission costs. To be able to resolve ocean phenomena such as internal waves, or biological patchiness and if possible have a mission duration of up to 1 year (Davis et al., 2002). The three gliders were; the Spray (Sherman et al., 2001), the Seaglider (Eriksen et al., 2001) and the Slocum (Webb et al., 2001). Other buoyancy driven gliders now exist, such as the SeaExplorer (ALSEAMAR-ALCEN, 2019); however, the original three still constitute most of the platforms operated by the scientific community. (Rudnick, 2016)

As with a profiling float, gliders change their buoyancy providing vertical movement that is then converted to horizontal motion by the lift from the wings. Pitch is controlled by buoyancy changes and internal mass redistribution by moving the battery pack forward and aft within the device. Similarly, roll is controlled by rotating the battery (or in the case of the Slocum a rear mounted rudder). This pattern control leads to the formation of the gliders' sawtooth pattern (descent and ascent) of flying and gives a glide angle (ϕ) which typically lies between 16° and 25° with potential angles up to 45° (Eriksen, 2009). Glide angle is typically steeper than most (although not all) oceanic changes leading to each profile (descent or ascent) being considered equivalent to a vertical ocean profile (Davis et al., 2002; Rudnick et al., 2004).

1.2.2 BUOYANCY DRIVEN GLIDERS AND MICROSTRUCTURE MEASUREMENTS

TRADITIONAL MICROSTRUCTURE MEASUREMENTS

Ocean turbulence research as we know it today originated from two sources, one Russian and one British, and was motivated by attempts to detect submarine wakes during the cold war Lueck et al. (2002). Many platforms have been used successfully to conduct ocean turbulence research from the earliest towed vehicles to density driven ocean gliders (Lueck et al., 2002; Rudnick, 2016). There are three main requirements for a platform to successfully take turbulence measurements Lueck et al. (2002). A probe capable of detecting the parameter; the electronics to amplify the signal; and a platform that moves smoothly through the ocean. Traditional examples of such devices are towed bodies (Johnston et al., 2011), propeller driven AUVs (Boyd et al., 2010; McPhail et al., 2019) as well as a range of tethered free-fall profilers such as the TurboMAP (Wolk et al., 2002), the FLY Simpson et al. (1996) and Vertical Microstructure Profilers (VMP) produced by Rockland Scientific (Palmer et al., 2013). Each platform has limitations. Towed bodies need their vertical motion decoupled from the vessel towing them (Lueck et al., 2002). AUVs produce mechanical vibrations from their propulsion source that contaminate shear measurements (Lueck et al., 2002; Boyd et al., 2010). Towed bodies, AUVs and Free fall profilers are all limited by the location and operational capabilities of the vessels that carry them. In addition to these individual drawbacks, turbulence measurements should be taken over a period of time in the same area to resolve tidal cycles, a financially expensive prospect (Palmer et al., 2015). Since 2009 (Wolk et al., 2009) it has been possible to get microstructure data from buoyancy driven gliders, a platform that has endurance but also a mechanically smooth ride Rudnick (2016).

1.2.3 MICROSTRUCTURE MEASUREMENTS FROM GLIDERS

Gliders have great potential for measuring ocean turbulence due to having near-neutral buoyancy and a mechanically quiet ride (Wolk et al., 2002; Fer et al., 2014; Rudnick, 2016). All three main scientific gliders mentioned earlier in the chapter have had microstructure packages installed. Microstructure instruments have been tested on a Spray glider (Park et al., 2012) but no peer reviewed literature exists from any Spray deployments and so won't be discussed here. Today the two main packages being used are the the *MicroRider-1000-6* (from here on referred to as MicroRider) developed by RSI (Wolk et al., 2009) found on Slocums (Figure 1.2) and SeaExplorers (as well as AUVs) and the MicroPod system, developed by RSI and designed to be mounted on the Seaglider system. Two different systems are required due to a geometry mismatch between the shape of the seaglider and MicroRider (Creed et al. (2015)).

MICRORIDER EQUIPPED GLIDERS

The MicroRider package is a self contained package (Fer et al., 2014) with two airfoil velocity shear probes, two fast-response thermistors (FP07) and two piezo-accelerometers mounted in the same orientations as the shear probes that record at 512Hz (fast channels). Also included are a pressure transducer and inclinometer for pitch and roll measurements that record at 64Hz (labelled as slow channels) (Wolk et al., 2009; Fer et al., 2014). The MicroRider is mounted to brackets on top of the Slocum with the probes protruding just ahead of the glider nose, see Figure 1.2.

The first test of a Slocum glider for microstructure was conducted by Wolk et al. (2009). This was done in a small lake of 20 m depth, with 5 sets of dives performed each comprised of either 2 or 4 ascent-descent cycles. During testing Wolk et al. (2009) saw vibration signals in the shear data at the top and bottom of a dive associated with the glider pumps and motors. Smaller vibration signals were also seen at 6 second intervals, linked to the rudder movement correcting the glider's path through

Figure 1.2: Ocean Microstructure glider being deployed in the Antarctic from a small boat. Image courtesy of Brearley (2018)

the water. Both regions of vibrations were removed in post processing. Fixing the rudder in place to remove associated vibrations was put forward by Fer et al. (2014). Using both shear and temperature data Wolk et al. (2009) clearly showed an active surface mixed layer and much less active layer below the thermocline. Shear spectra were computed both above and below the thermocline. Dissipation rates were estimated from the spectra giving values of $\sim 7 \times 10^{-7}$ W kg^{-1} in the surface layer and $\sim 5 \times 10^{-11}$ W kg^{-1} below the thermocline, comparable estimates to vertical microstructure profilers (Wolk et al., 2009). Since 2009 Slocums with MicroRiders have been succesfully deployed in a number of ocean regions with publications first appearing in 2014.

The first of these was Fer et al. (2014) deploying an ocean microstructure glider (OMG) in the Faroe Bank Channel collecting 154 profiles, alongside 90 profiles from a free fall profiler over the period of a week. This study showed that gliders could provide comparable estimates of dissipation equalling the best quality VMP data with a noise floor of 5×10^{-11} W kg^{-1}. When comparing the dissipation estimates between VMP and OMG outputs Fer et al. (2014) shows an over estimation (three to nine times greater) in the OMG shear in the interfacial layer of the Faroe Bank Channel overflow plume. This was attributed to three factors; the difference between the vertical profiling of a VMP and the slanted transects of the glider, the fact that turbulence is not constant (location of VMP casts vs location of glider profiles), and finally the interaction with the overflow plume boundaries. Fer et al. (2014) concluded that microstructure profilers on gliders are a suitable platform for collecting ocean microstructure data, but will give differing values to VMPs in areas that challenge glider flight behaviour. As TKE dissipation rates scale with velocity (U^2 or U^4 for temperature and shear respectively) a well tuned flight model is vital to good microstructure results (Merckelbach et al., 2019). A follow up study by Peterson and Fer (2014) was conducted using the same study data as Fer et al. (2014) and showed that estimates of TKE dissipation rates are also possible from microstructure temperature, but tend to underestimate compared to shear in regions of higher dissipation.

Palmer et al. (2015) deployed am OMG in the Celtic Sea to look at turbulence and mixing related to internal tides. Over a 9 day deployment 766 profiles were collected in a highly energetic internal wave-field. In this instance the glider was able to sample in the surface mixed layer, a section of the bottom mixed layer and the pycnocline that makes up the space in between (water depth ~100m) and was able to resolve ε at all three depths. The data showed a difference in the variability at the three depths, with a large difference between the wind driven surface mixing and the pycnocline being of particular interest showcasing the impact of the internal tide field on the mixing that takes place in the pycnocline. This is a perfect example of a glider showing the benefit of increased sampling rate compared to ship based measurements.

St. Laurent and Merrifield (2017) investigated the ability of gliders to provide microstructure measurements in near surface regions that are more difficult to observe as they are typically disturbed by the presence of a vessel attempting sampling. This study draws attention to surface stable layers in the North Atlantic that showed elevated turbulent mixing during peak warming and densely sampled a strongly stratified layer in the Bay of Bengal separating a turbulent surface layer and a quiescent ocean interior by 20 m.

Schultze et al. (2017) identified highly intermittent mixing in the stratified thermocline in the North Sea. The study showed the importance of long term measurements to adequately assess dissipation of kinetic energy, showing that 50% of bottom mixed layer temperature increases were generated by four distinct events. They point to gliders as being a useful platform in providing these longer term measurements.

Scheifele et al. (2018) used both shear and temperature data to estimate TKE dissipation rates in the low energy Beaufort Gyre in the Arctic. Using 10 days worth of data they find that both temperature and shear provide estimates of TKE dissipation rates within a factor of 2 from each other, with values as low as 3×10^{-11} W kg^{-1}. However, they argue that due to the noise floor of the shear probe TKE dissipation rates below $(O)10^{-10}$ W kg^{-1} are skewed, but that temperature derived estimates are reliable to 2×10^{-12} W kg $^{-1}$.

Molodtsov et al. (2020) investigated an anticyclonic loop eddy in the Gulf of Mexico using an OMG. They show elevated mixing at the flank and below the core of the eddy (up to $(O)10^{-7}$ W kg^{-1}) and a quiescent core ($(\sim O)10^{-7}$ W kg^{-1}). They also see double diffusive thermohaline intrusions at the sides of the eddy, with the region below the eddy core being more prone to a salt fingering regime and suggest that due to these processes the life span of such an eddy may be ~ 1.5 years.

Most recently Howatt et al. (2021) used data from a 10 day OMG deployment in the Roseway Basin (south of Nova Scotia) and compared estimates of TKE dissipation rates from finescale parametrization, Thorpe scaling and fitting spectra to both temperature and shear data. They show that finescale parametrization captures the magnitude and distribution of dissipation but not the spatial or temporal features and the opposite is true of the Thorpe scaled estimates, where estimates are overestimated due to the resolution of the glider's CTD sampling frequency of 0.5 Hz. The study supports the idea that CTD data collected by gliders can be used to improve the spatial and temporal gaps in our understanding of ocean mixing.

MICROPOD EQUIPPED SEAGLIDERS

In 2015 a microstructure package from RSI (MicroPods) was successfully integrated with a Kongsberg Seaglider (Creed et al. (2015), Figure 1.3). Due to the design of the Seaglider (physical shape and software integration) an "all-in-one" set up such as the MicroRider (Wolk et al., 2009) or mASTP (Boyd et al., 2010) was not possible. The microstructure package installed on the Seaglider consists of a pressure casing with a data logger mounted in the aft fairing (Figure 1.4) and a pair of MicroPods located either side of the CT sail (Figures 1.5). The standard MicroPod can be configured to take either a FP07 'fast' thermistor or a shear probe. A separate MicroPod is also

Figure 1.3: A pair of Seagliders equipped with MicroPods on the rear deck of the RV *Seòl Mara* during glider trials in Oban, 2018

available so that an Electromagnetic (EM) current meter can be mounted in place of one of the other pods. In June 2015 a scientific sea trial was conducted in Oban, Scotland where four deployments were carried out. From the four deployments it was was shown that the FP07 matched well with the temperature from the CT sail. The shear probe provided spectra that matched well with the naysmyth spectra when oriented laterally to the glider path. When oriented vertically along the glider path low wave numbers were suppressed by the glider's hull.

There are considerably fewer studies using results from MicroPod equipped Seagliders compared with MicroRider systems on Slocums. The initial development and testing of the platform are presented in Creed et al. (2015). Rainville et al. (2017) report on a successful 6 month long mission. Within this study they developed a method for providing near real time dissipation rates from temperature variance and kinetic energy by returning the averaged dive spectra to the glider's base station. However, the recovery of the glider is still required to fully process the data. The prior development to the work in this thesis is presented in Leadbitter et al. (2019) where it is shown that it is possible to get comparable results of TKE dissipation rates from Thorpe scaling high resolution temperature to those from traditional CTD based Thorpe scale estimates. The most recent published work using MicroPods on Seagliders is from Damerell et al. (2021) looking at dissipation in the Bay of Bengal carried out using data from both shear and high resolution temperature. This study

Figure 1.4: Figure showing the microstructure logger mounted in the aft fairing of a Kongsberg Seaglider. The rear of the MicroPods from Figure 1.5 can be seen at the bottom of this figure.

shows high dissipation rates in the near surface ((O)10^{-5} W kg^{-1}) that drops rapidly over the uppermost 50 m to (O)10^{-7} W kg^{-1}, following a more gradual decrease to $\sim 5 \times 10^{-10}$ W kg^{-1}. Work is currently being done using high resolution temperature from the EUREC^{4}A project (for further details see Chapter 5) using both temperature variance and Thorpe scaling (Sheehan et al., 2021).

MICROSTRUCTURE PLATFORMS COMPARED

The main source of microstructure data presented in this thesis was collected by a microstrucure package mounted on a Seaglider. Further data examined also used was collected by an RSI tethered VMP-2000. As a summary of the differences between the two platforms used in this work and how they compare to other microstructure capable gliders (the Teledyne-Webb Slocum with MicroRider (Wolk et al., 2009) and the Alseamar SeaExplorer with MicroRider SE (ALSEAMAR-ALCEN, 2019)) Table 1.1 lays out the key technical specifications of each platform. All the systems across the range of platforms are equipped with the same core instrumentation of shear probes and fast response thermistors. However, the set up of each system varies across the

	Seaglider	Slocum	Sea Explorer	VMP
Instrument name and Manufacturer	MicroPods - RSI	MicroRider 1000-6 - RSI	MicroRider SE - RSI	VMP-2000 - RSI
Mounting	2 MicroPods one either side of the CT sail, Logger in rear fairing	Neutrally buoyant package mounted on top at front, end further forward than glider nose	Neutrally buoyant package mounted instead of nose cone	All in one package with sensors mounted at the base
Instruments	2 from; shear probe, FP07 fast thermistor or EM current meter (typically only one FP07 or EM current meter)	2x shear probe, 2x FP07 fast thermistor, 1x SBE micro conductivity, optional EM current meter	2x Shear Probe, 1x FP07 fast thermistor, 1x combination CT sensor, EM current meter	2x Shear Probe, 2x FP07 fast thermistor, SBE3 temperature and conductivity, optional micro-conductivity.
Motion	Buoyancy controlled diving, internal mass movement pitch and roll	Buoyancy controlled diving, internal mass movement for pitch, external rudder for turning	Buoyancy controlled diving, internal mass movement pitch and roll	Tethered to vessel, free fall deployment, winch up recovery
Endurance	220 days, 4500km, only CT sail	2300km only CT sail	64 -160 days, 1300-3200km, rechargeable	N/A

Table 1.1: Table comparing the two platforms that provided data for this thesis and two other commercially available glider platforms

Figure 1.5: Figure showing the MicroPod mounted either side of the CT sail on a Kongsberg Seaglider. Note the metal dummy probes that are inserted when the Seaglider is in storage or transit.

platforms.

1.3 THESIS OVERVIEW

The aims of this thesis are twofold. First, to determine the suitability of applying the Thorpe scale method to high resolution temperature data. Thorpe scaling is useful in providing another method for determining TKE dissipation rates, but has a number of caveats, especially when using temperature. We aim to provide a complementary set of tools to the ocean mixing community with the potential to improve spatial and temporal estimates of TKE dissipation rates available for study. We wish to show what considerations are required for using the Thorpe scale method. Second, to estimate vertical turbulent kinetic dissipation rates from both a VMP and a Seaglider. We aim to show that the method is platform agnostic and can be applied to datasets collected in varied ocean regions. To achieve these aims the following questions and sub questions are posed:

1. How can the Thorpe Scale algorithm be applied to high resolution temperature datasets from microstructure systems? Considering that:
    (a) Only temperature is being used, where traditionally density is used for Thorpe Scaling and the physical issues that come from this
    (b) The resolution of data is an order of magnitude greater than the traditional CTD data this method is applied to.
2. What challenges arise from Thorpe Scaling high resolution temperature data from gliders? Considering that:
    (a) Gliders both do not move vertically through the water and don't measure their exact path through the water
    (b) A glider is a less stable platform for collecting microstructure data that a free fall profiler
3. Do values of turbulent kinetic energy dissipation and associated products from Thorpe Scaling high resolution temperature fit with estimates of the same products from other methods across different oceanic regions? Considering that:
    (a) Temperature based Thorpe Scaling is heavily dependant on the temperature and salinity, which is considerably varied across oceanic regions.
    (b) Thorpe Scaling may under- or over- estimate turbulent kinetic energy dissipation given the local conditions.

The rest of this thesis is presented in 4 main chapters. In Chapter 2 we provide a complete methodology for Thorpe scaling high resolution temperature from both vertical profilers and gliders. We also lay out how averaging was conducted, as the method used can have an impact on final estimates of TKE dissipation rates. Chapter 3 describes the further development of the methodology presented in Chapter 2 using VMP-2000 data from above the Mid-Atlantic Ridge. Outputs from Thorpe scaling are also compared to the results from shear probes on the platform as well as other studies. Chapter 4 uses the methodology described in Chapter 2 and applies it to data collected from a Seaglider and glider specific considerations are investigated. Spatial and temporal differences in mixing on the flank of the Wyville-Thomson Ridge in the Faroe Shetland channel are also presented. Chapter 5 uses the developments from the previous chapters and applies it to a dataset from the Subtropical North Atlantic, to the east of Barbados. The impact of thermohaline staircases on the Thorpe scaling methodology are investigated alongside the comparison of estimates of TKE dissipation rates from Thorpe scaling to those from temperature variance. The key results from the four main chapters are brought together in Chapter 6 to provide answers to the questions posed above.

2

METHODS

2.1 INTRODUCTION

In the previous chapter an overview of the thesis was presented including an introduction to the Thorpe Scale method and microstructure sensor equipped ocean gliders. In this chapter the Thorpe scale method presented in Chapter 1 is expanded and the following highlighted:

- The methodological process applied to high resolution temperature data from Seagliders and VMP-2000s.
- Several high resolution temperature specific considerations.
- Some broader considerations for reading this thesis.

First, sampling frequency and associated nomenclature for the thesis is laid out. An overview of the idealised work flow for taking raw data from the Seaglider to a usable science product is then described followed by each of the steps in this flow being described in detail. Finally a short section on where this flow differs when processing VMP-2000 data and laying out how temporal and spatial averages are calculated in this thesis.

2.1.1 RECORDING FREQUENCY

Unlike the MicroRider setup on a Slocum glider or powered AUV, the MicroPod system does not measure pressure so relies on the Seaglider pressure sensor to determine depth and vertical speed through the water column. The Seaglider flight model is required to estimate along-path speed (Frajka-Williams et al., 2011) and convert the raw engineering units to physical units Creed et al. (2015). The lack of direct measurement of along-path speed is a problem common to all glider microstructure systems. The logger saves data from individual profiles in a file with a .p extension which is converted to a .mat file using a tool box (ODAS, Lueck et al. (2018)) developed by RSI for this process. During conversion the tool box imports all the necessary glider flight parameters from the associated glider dive. The clocks on the logger and glider are synchronised at the beginning of each microstructure profile providing a means to co-locate the microstructure and Seaglider data (Lueck et al., 2018). Not all microstructure channels are recorded at 512 Hz. The shear probe, the associated accelerometer and FP07 thermistor are recorded at 512 Hz. The logger battery voltage, roll and pitch are recorded at 64 Hz. The glider records pressure, conductivity, temperature and engineering data at 0.2 Hz.

During conversion the slower 64 Hz and 0.2 Hz channels, are up-sampled to 512 Hz, the same speed as the ‘fast’ channels. To reduce confusion where different channel speeds are being used three different naming conventions will be used in this thesis. These are **CT Sail**, **intermediate resolution** and **high resolution** (see Table 2.1 for usage) and refer to data sampled at 0.2 Hz (or glider speeds), 64 Hz and equal to or greater than 100 Hz respectively. Due to the three differing sampling frequencies, up-sampling applied to measured variables, and the fact that the sensors are in different physical locations, extra consideration is needed during processing. This includes dealing with physical separation between the pressure sensor on the glider’s pressure case and the microstructure probes (addressed in Section 2.2.2) and a lack of conductivity (and thus salinity) measurements at 512 Hz (addressed in Section 2.2.5).

2.1.2 PROCESSING OVERVIEW AND IDEALISED DATA FLOW

The following section of this chapter describes the idealised work flow for taking raw data from the Seaglider to a usable science product. Figure 2.1 shows the idealised

Sampling frequency	Naming convention	Example
0.2 Hz	CT sail	"CT sail temperature"
64 Hz	intermediate resolution	"intermediate resolution pitch"
≥100 Hz	high resolution	"high resolution temperature"

Table 2.1: Table showing different naming conventions used to define different channel sampling frequencies.

flow. The process starts with downloading the raw data files from the microstructure logger. The data files from the logger are then combined with flight model data from the Seaglider (in the form of a 'hotel' file) using the ODAS MatLab library (version 4.3 at the time of writing) converting the data within the files to physical units (for more information see Lueck et al. (2018)). Following on from this, the high resolution temperature data is calibrated (Section 2.2.1). After the temperature calibration two additional steps are taken with the physical data. The first of these is applying a depth offset based on the Seaglider's pitch and distance between the Seaglider's pressure sensor and the microstructure sensors to the depth outputted from ODAS (Section 2.2.2). The second is to convert the high resolution data from in situ temperature to conservative temperature and apply filtering and binning to take into account the response time of the FP07 fast thermistor and the Seaglider's vertical speed through the water (Section 2.2.3). Once these first three steps, and any mission specific quality control, have been carried out the Thorpe scaling algorithms are applied (Section 2.2.4) and an overturn associated density variable determined (Section 2.2.5). TKE dissipation estimates (ε_{Thorpe}) and diapycnal eddy diffusivity (κ_ρ) are then calculated (Section 2.2.6). The final step that yields a usable scientific product is to bin ε_{Thorpe} and κ_ρ into 25 m bins and apply a final set of quality control to remove bins where the background hydrographic properties may be unsuitable for application of this method (Section 2.2.7).

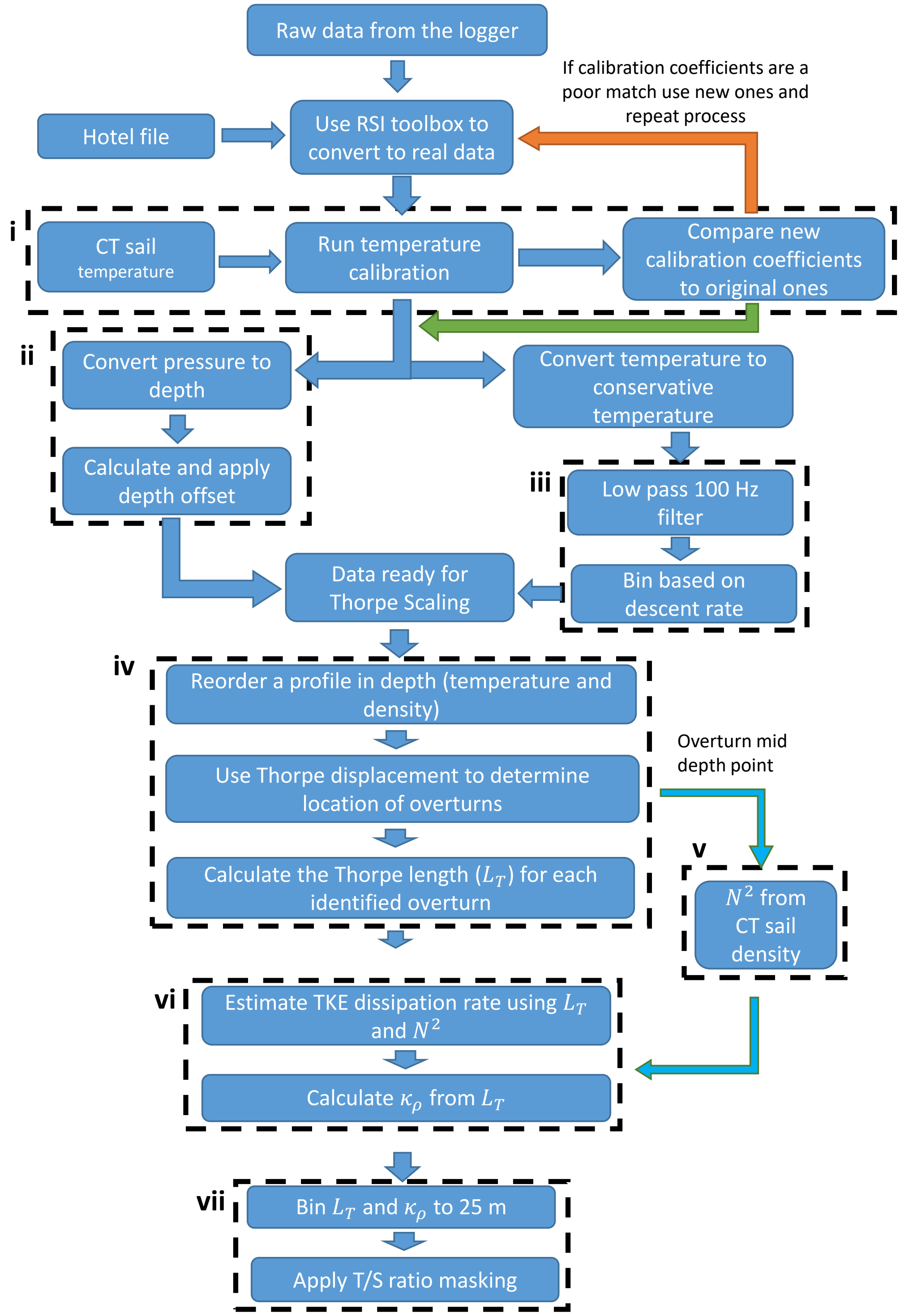

Figure 2.1: Flow diagram showing the steps needed to take raw data from the microstructure logger to usable scientific product. Roman numerals and the associated dashed boxes group sets of processes and link them with subsections of Chapter 2.

2.2 RAW DATA TO SCIENTIFIC OUTPUT

2.2.1 CALIBRATION OF HIGH RESOLUTION TEMPERATURE [I]

To conduct Thorpe scale analysis on temperature the absolute temperature recorded by the FP07 thermistor is not critical as it focuses on temperature variation. However, it is useful to obtain the absolute values of high resolution temperature for other applications e.g. study of thermohaline staircases (Rollo et al., 2021). To get the absolute values of temperature the FP07 thermistors must be calibrated, or re-calibrated post deployment (if previously calibrated by RSI), by comparing the fast thermistor measured temperature to the calibrated in-situ temperature from the Seaglider's CT sail. For a given profile, high resolution temperature is regressed against CT sail temperature data using the function *cal_FP07_in_situ* from the ODAS MatLab library (see Rockland Scientific technical note TN039 for a full description) to provide calibration coefficients T_0, β_1 and β_2. The calibration coefficients are then used in the Steinhart-Hart equation

$$T^{-1} = T_0 + \beta_1 lnR + \beta_2 (lnR)^3 \tag{2.1}$$

where T is the temperature in kelvin, R the resistance at T, and T_0, β_1 and β_2 the Steinhart-Hart coefficients (which vary based on model and type of thermistor) (Steinhart and Hart, 1968). The Steinhart-Hart equation is used to derive the precise temperature of the thermistor. The calculation of the Steinhart-Hart coefficients and the application of them in Equation 2.1 are all included in the function *cal_FP07_in_situ*.

The newly calculated coefficients are added to the configuration file that contains the relevant coefficients to convert raw data to physical units. The raw data is then reprocessed with the updated configuration file.

The temperature calibration is then re-run and the new calibration coefficients are compared to those in the configuration file. If the two sets of calibration coefficients compare well the high resolution temperature data is considered calibrated. In this thesis calibration coefficients were plotted (Figure 2.2.1.1) but a scatter plot with linear regression would also work. If there is a discrepancy between the two sets of coefficients the process is re-run. This can be done as many times as required to get a good match between coefficients and hence provide a good calibration for the high resolution temperature.

The number of profiles that are run through this process to provide acceptable coefficients is related to mission length. On a short deployment (hours to days) profile by profile calibration is possible (this was done for MASSMO4, Chapter 4, to confirm that on a profile by profile basis the coefficients stay the same. For longer deployments (days to weeks) profile by profile calibration would be unnecessarily time consuming. In a situation where a very long deployment is carried out calibration process can be carried out on a sample of profiles over the deployment to check that the calibration coefficients stay within an acceptable tolerance. If it is believed that there is little or no drift in the fast thermistor a single profile calibration will suffice (as with RidgeMix and EUREC^{4}A, Chapters 3 and 5).

PROFILE BY PROFILE CALIBRATION EXAMPLE

During MASSMO4 only 25 usable microstructure profiles were recorded (see Section 4.2.3 for more detail). Each profile was run through *cal_FP07_in_situ* twice to make sure that the applied calibrations were acceptable and compared well to on the bench calibrations provided by RSI on purchase[1]. Figure 2.2 shows the first pass and second pass calibration coefficients on a profile by profile basis from MASSMO4. The first two calibration coefficients, T_0 and β_1, show a very good fit between the first and second passes. The mean values of these also compare well to the original calibrations from RSI (Table 2.2). The coefficient β_2 shows a poorer fit. There is large variation in the first 6 profiles which is likely due to these profiles not being long enough for a good regression. Due to this variation, these profiles were excluded from the calculation of average coefficient for the first and second pass presented in Table 2.2. The β_2 component averages still show a larger variation than the other two components between the two passes and the bench test values, so a mid point of the three was used as the final calibration coefficient. The final values used for the MASSMO4 processing were, T_0 =290.608, β_1 =3040.20 and β_2 =252303.76.

---

[1] Early fast thermistors from RSI were shipped calibrated. Later fast thermistors were shipped uncalibrated. For uncalibrated fast thermistors the in-situ calibration is essential.

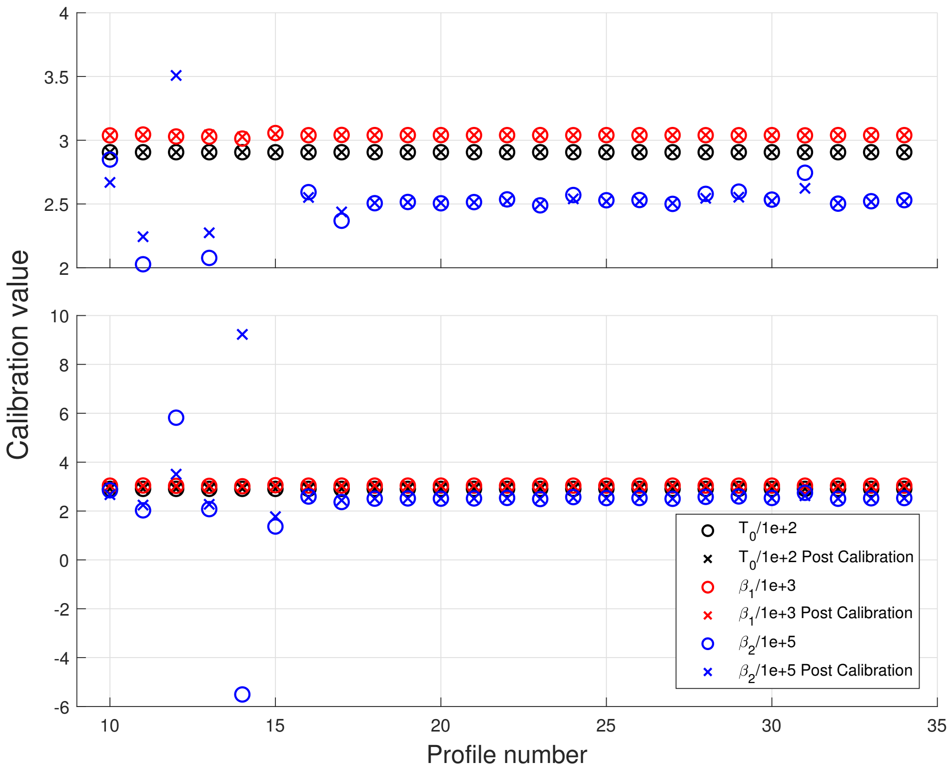

Figure 2.2: Comparison between the first (O's) and second (X's) pass of temperature calibration coefficients through the Rockland Scientific Inc toolbox. The upper panel shows a zoomed in version of the lower panel to provide a better idea of the small scale variation seen on a dive by dive basis.

Calibration	Bench test	First Pass	Second Pass
T_0	290.608	290.608	290.608
β_1	3040.31	3040.10	3040.20
β_2	251108.14	253533.77	252269.39

Table 2.2: Mean calibration coefficients (T_0, β_1 and β_2) from profiles 16-34 following two passes through the calibration scripts.

2.2.2 CALCULATING AND APPLYING A DEPTH OFFSET [II]

After converting the raw microstructure data to physical units the ODAS output provides a pressure value for each microstructure data point. However, pressure is not measured at the same location of the microstructure sensors due to the difference between the locations of the Seaglider pressure sensor and the microstructure sensors. The method below is derived from Giddings (2019) to adjust the pressure to be representative of the actual location of the microstructure instrument. The

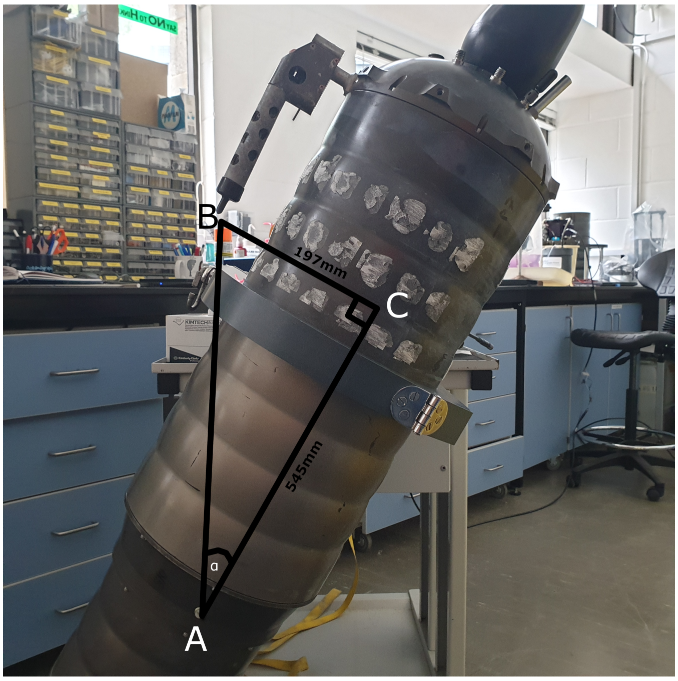

Figure 2.3: Figure showing the pressure sensor (A) the location of the tip of the CT sail (B). AB is 579mm. α is 19°

Seaglider pressure sensor is mounted near the front of the pressure pupa (Figure 2.3, location A). The two microstructure sensors on a Seaglider are mounted either side of the CT sail (Figure 1.5). This results in an offset (BC) along the normal axis of the glider, and a longitudinal offset (AC).

When the glider is in operation, pitched at an angle (ϕ) to the horizontal, the vertical offset (a) between the pressure sensor and the CT sail will vary according to ϕ. If the glider is descending (ascending) [Figure 2.4] through the water ϕ will be negative (positive). Variation in the value of ϕ will result in a change to the vertical offset (Figure 2.4, a) between the pressure sensor and the CT sail.

The parameters required to calculate the vertical offset are:

- Longitudinal offset (AC), d = 545 mm.
- Normal offset (BC), c = 197 mm.
- The pitch of the glider from the vertical, ϕ.
- The distance from the pressure sensor to the CT sail (AB), h = 579 mm

$$h = \sqrt{AC^2 + BC^2} \tag{2.2}$$

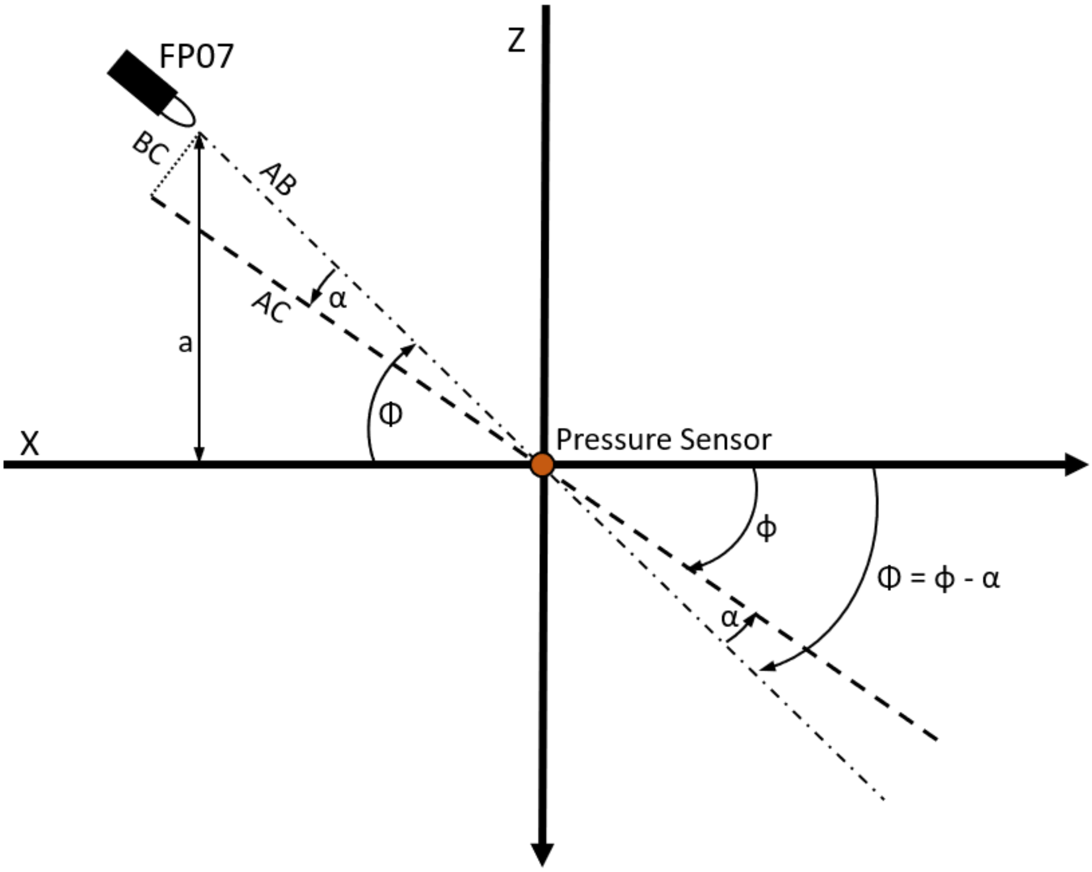

Figure 2.4: Schematic showing the various angles and distances required to calculate the depth offset for the FP07 fast thermistor for both descending and ascending scenarios. The calculated vertical distance (a) between the depth of the pressure sensor and the FP07 is based on the angle $\Phi = \phi - \alpha$ and the distance between the microstructure and pressure sensors (AB).

- The angle between the glider's longitudinal axis (AC) and the line AB, $\alpha = 19°$

$$\alpha = \arctan(\frac{BC}{AC}) \tag{2.3}$$

The angle between the line AB and the horizontal is calculated as $\Phi = \phi - \alpha$ which is then used to calculate the vertical offset $a = -hsin(\Phi)$ and hence $z_{\text{corrected}} = z + a$. where z is the depth of the glider calculated from the glider's pressure sensor. This can be simplified to:

$$z_{\text{corrected}=-hsin(\phi-\alpha)} \tag{2.4}$$

2.2.3 RESOLUTION ADJUSTMENT [III]

An important consideration of using high resolution temperature to estimate TKE dissipation using a Thorpe scale methodology is to minimise the chance of instrument noise in the data manifesting itself as ‘fake’ small overturns. Filtering and binning the high resolution data before applying the Thorpe scaling methodology removes the need to use a run length filter to identify ‘fake’ small overturns. Galbrath and Kelley (1995) proposed using run lengths as a method to determine overturns that arise due to instrument noise. More recent studies using Thorpe scaling (Mater et al. (2015), Ijichi and Hibiya (2018) and Carter (2020)) use pre processing binning to mitigate spurious overturns due to instrument noise. However, run-length tests were investigated as part of the work to develop the methods in this thesis but were rejected and can be found in Appendix A. In an attempt to minimise the problem the following steps are applied to all high resolution temperature data.

Although a FP07 fast thermistor has a sampling frequency of 512 Hz this does not equate to the sensors response time. Sommer et al. (2013) conclude that the response time is 10 ms, a value that equates to a sampling frequency of 100 Hz, five times lower than the sampling frequency of the FP07 fast thermistor. To counter this the high resolution data has a low pass filter of 100 Hz applied to it to remove any higher resolution variability. The filter used is a 12th order butterworth filter using a cut off frequency of 100 Hz and a sampling frequency of 512 Hz. An example of the filter applied is seen in Figure 2.5.

In addition to the filtering process the high resolution temperature data was also binned to a lower resolution based on along-path rate of descent of the platform and the sensor response time. This is done to further reduce noise from spurious overturns by confirming each temperature measurement is independent. Simple trigonometry is used to determine along-path rate of descent (RoD) based on the pitch of the glider and the rate of descent ($RoD = \frac{dz}{dt} / tan\phi$). The minimum resolution along-path is then calculated as:

$$\delta z_{min} = (RoD_{median} \times \delta t) \tag{2.5}$$

where RoD_{median} is the median RoD across the mission and δt is 512/100, the sensor response time.

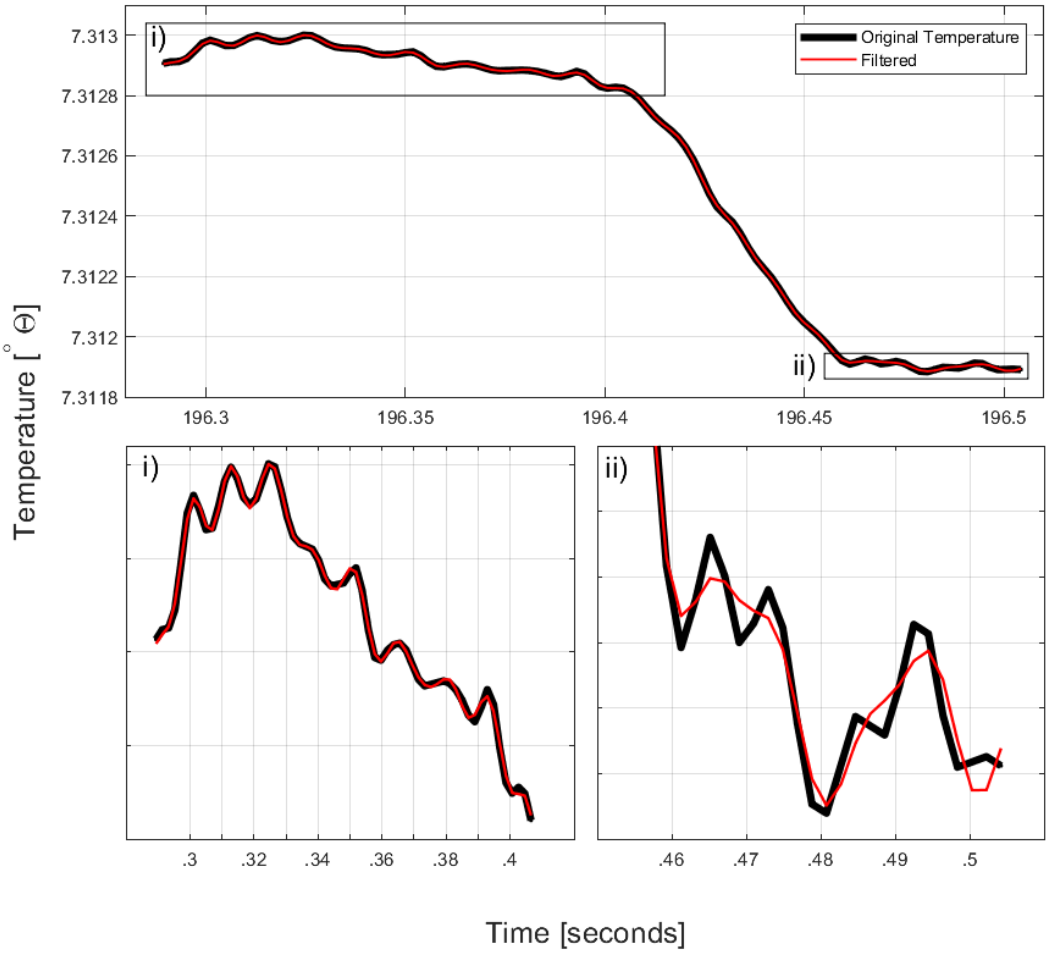

Figure 2.5: Schematic plot from the development of the 100 Hz filter. Panels i) and ii) show zoomed in sections, making the function of the filter clear. Note the differing time frames for each panel.

Using this minimum along-path resolution a new vertical depth resolution is calculated. The new depth resolution varies with how the glider was flown during the mission. In this thesis the new depth resolution is 0.003 ± 0.0005 m. Following this temperature and year day are binned to the new depth resolution. Once all required high resolution variables have been binned, the high resolution temperature data is ready to be passed through the Thorpe scaling algorithms.

2.2.4 THORPE SCALING HIGH RESOLUTION TEMPERATURE DATA [IV]

The processed high resolution temperature data is run through a set of Thorpe scaling algorithms based on the equations in Section 1.1.3. The first step is to reorder the high resolution temperature profile. Thorpe displacement (T_d) and Thorpe fluctuation (T_f) are calculated using Equations 1.5 and 1.6. The L_T is then calculated using T_d and Equation 1.7. Following Ijichi and Hibiya (2018) and Carter (2020), all overturning regions that are vertically smaller than 2 m and within 1 m of a neighbouring overturning region are combined until the region is vertically larger than 2 m. During this process a mid point year day and depth are calculated for each of the overturning regions in each profile. Each profile is then visually examined to confirm that the processing has completed correctly (using the diagnostic plot, e.g. Figure 3.3). In some instances a temperature spike will cause an unrealistically large overturning region. The temperature spike can then be removed manually and reprocessed to prevent such large spikes. An example of manual spike removal is shown in Section 4.2.3.

To prevent instrument noise from contributing spurious overturns to the final results a number of steps were taken. Two of these (filtering and binning the raw temperature data) were discussed in greater detail in Section 2.2.3. In addition, whilst calculating the Thorpe displacement if a run of displacements with fewer than 3 points was identified, and this was within a single data point (of zero displacement) to a region with a run of 3 or more points of displacement they were combined together. A run containing 3 or less data points wouldn't physically be able to represent an overturn and is likely to be noise. This was done instead of applying a run length test (see Appendix), which was discounted as a method of reducing noise, due to the large number of smaller overturns that existed pushing the cut-off length to a very small value.

2.2.5 BUOYANCY FREQUENCY [V]

Buoyancy frequency (N) is required for the calculation of ε (Equation 1.3). When Thorpe scaling density, the density gradient across an overturning region is used. However, in the case of high resolution temperature for Thorpe scaling this is not possible as there is no high resolution conductivity, and hence salinity, that can be used to calculate density at high resolution. A number of different methods to provide a density value have been investigated. These methods include the 'bulk' and 'mean' methods presented in Ijichi and Hibiya (2018) (expanded in Section 3.2.3), creating a high resolution density profile by up sampling salinity (not carried forward) and using the CT sail temperature and salinity to calculate N. The latter method is used in this thesis. Specifically, a profile of buoyancy frequency is calculated using Equation 2.6 with density calculated from CT sail variables.

$$N = \sqrt{\frac{-g/}{\rho}\frac{\partial \rho}{\partial z}} \tag{2.6}$$

where g is the gravitational acceleration, ρ the potential density and $\partial\rho/\partial z$ is the gradient of potential density. Using the mid point depth of an overturning region the closest value of buoyancy frequency is selected. This is then used to estimate TKE dissipation (Section 2.2.6).

2.2.6 ESTIMATING ε AND CALCULATING κ_ρ [VI]

At this stage in the processing a value of L_T and N^3 has been calculated for each overturning region identified by the Thorpe scaling process across a whole deployment. Using Equation 2.7 a value for TKE dissipation rate is estimated.

$$\varepsilon_{Thorpe} = CL_T^2 N^3 \tag{2.7}$$

where C is a constant of 0.64 is used in this equation throughout this thesis. Throughout the rest of the thesis any TKE dissipation estimates from this method will be referred to as ε_{Thorpe}. Using the values of L_T and N diapycnal eddy diffusivity can also be estimated. Diapycnal eddy diffusivity (κ_ρ) is related to TKE dissipation rate by Equation 1.2 and so can be estimated from L_T using the relationship:

$$\kappa_\rho \simeq 0.1 L_T^2 N \tag{2.8}$$

assuming a mixing efficiency of 0.2 (Oakey, 1982; Gregg et al., 2018). Newer studies of the mixing coefficient from laboratory experiments (Barry et al., 2001; Strang and Fernando, 2001; Jackson and Rehmann, 2003), numerical simulations (Mashayek et al., 2013; de Bruyn Kops, 2015; Salehipour et al., 2016), and direct measurements (Laurent and Schmitt, 1999a; Gregg and Horne, 2009; Pujiana et al., 2015) do not converge with those gathered at sea from tracer release experiments (Ledwell et al., 2004, 2011), with Gregg et al. (2018) suggesting the continued use of 0.2 as a value until a better understanding is put forward.

Estimates of ε_{Thorpe} and κ_ρ from Thorpe scaling are not in uniform bins unlike the output from processing shear microstructure data. Consequently, to make profile by profile comparisons easier, each profile of ε_{Thorpe} and κ_ρ is then binned to 25 m bins. This bin size was picked as a balance between maintaining high vertical resolution and a sufficient bin size to reduce noise when averaging (bin sizes of 0.5, 1, 20 25 and 50 m were investigated). The bin that a specific ε_{Thorpe} or κ_ρ is placed in is determined by the depth of the centre point of the overturn. Thus, a specific value cannot influence more than one bin.

2.2.7 FINAL QUALITY CONTROL [VII]

The final steps in the idealised work flow are to apply any manual quality control (if required) and apply a temperature/salinity ratio filter to the binned ε_{Thorpe} and κ_ρ data. The first of these two steps involves visual inspection of ε_{Thorpe} and κ_ρ to identify any areas with potential issues. For example, regions that exhibit very clear distinctions compared to the surrounding water column, typically characterised by highly elevated values of either ε_{Thorpe} or κ_ρ. The second of these steps is to filter based on the ratio of temperature variability to salinity variability across each 25 m depth bin. Where this ratio is higher than 0.5, ε_{Thorpe} and κ_ρ values are excluded. This is expanded on in Chapter 3, where this method is development is presented.

Using this work flow the FP07 data has been taken from a raw state, after being download from the logger aboard the Seaglider, through to a scientifically useful product that can be used to investigate local mixing processes.

2.3 MODIFICATIONS TO WORK FLOW FOR VMPS

The work flow above, including Figure 2.1, lays out how raw microstructure data is processed to provide a scientifically useful product when taking data from a Seaglider. In this thesis data from a VMP-2000 (Chapter 3) is also used. There are two small amendments that are needed to this work flow to accommodate for the difference in platform.

The first difference is found before the main work flow. There is no need for an

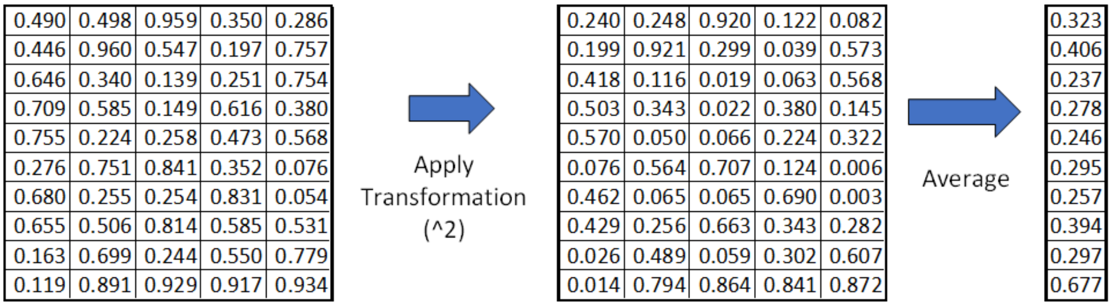

0.490	0.498	0.959	0.350	0.286
0.446	0.960	0.547	0.197	0.757
0.646	0.340	0.139	0.251	0.754
0.709	0.585	0.149	0.616	0.380
0.755	0.224	0.258	0.473	0.568
0.276	0.751	0.841	0.352	0.076
0.680	0.255	0.254	0.831	0.054
0.655	0.506	0.814	0.585	0.531
0.163	0.699	0.244	0.550	0.779
0.119	0.891	0.929	0.917	0.934

0.240	0.248	0.920	0.122	0.082
0.199	0.921	0.299	0.039	0.573
0.418	0.116	0.019	0.063	0.568
0.503	0.343	0.022	0.380	0.145
0.570	0.050	0.066	0.224	0.322
0.076	0.564	0.707	0.124	0.006
0.462	0.065	0.065	0.690	0.003
0.429	0.256	0.663	0.343	0.282
0.026	0.489	0.059	0.302	0.607
0.014	0.794	0.864	0.841	0.872

0.323
0.406
0.237
0.278
0.246
0.295
0.257
0.394
0.297
0.677

Figure 2.6: Schematic flow showing the two methods of averaging in this thesis. The x axis in the table is representative of time. This examples uses random values between 0 and 1. The transformation is applied and then averaged over time.

additional file to provide pressure data as this is already included in the raw data from the VMP. When converting raw data to real values via ODAS there is no hotel file to draw in from the glider as the data that would be provided via this file is already included in the raw data file from the VMP.

The second of the differences is found during the resolution adjustment step (Section 2.2.3). A VMP falls vertically through the water column rather than along a slope as a Seaglider does. When calculating the new depth resolution, the RoD for a VMP is simply dz/dt there is no need to take into account the angle the platform takes through the water as it is assumed to be vertical.

2.4 AVERAGING METHODS

In this thesis data was averaged by profile over time. In addition, averaging data with non-normal distributions also required extra consideration. This section aims to explain these variations.

2.4.1 AVERAGING ALONG THE X AXIS

In this thesis there are many situations where a data was averaged over time (typically the x axis). To do this the initial data was taken, required transformations are applied to the data and then an average of the data taken (Figure 2.6). The transformation could be as simple as squaring the data or a more complex equation being applied. The averaging step is then either a mean or median over time. In future chapters this will be referred to as a **time mean/median** as it represents a final product mean.

It is important to make this distinction as there are other methods of getting to a x axis mean that have the potential to give different final mean values, especially if the transformation is non-linear.

2.4.2 AVERAGING NON-NORMAL DISTRIBUTIONS

One of challenges that arose during the work was the influence of the averaging method applied to values of ε_{Thorpe} where differences greater than an order of magnitude arose. During initial investigations taking an arithmetic mean, defined as,

$$mean_x = \frac{1}{n}\sum_{i=1}^{n} x_i \tag{2.9}$$

where n is the number of values and x_i are the dataset values (Lambourne and Tinker, 2000), the final value was heavily weighted towards the largest value. This was especially true in situations where the largest value was 3 or more orders of magnitude higher than median of the data. To mitigate the weighting from large values it was decided to use an approximation of the geometric mean. The geometric mean is defined as,

$$\left(\prod_{i=1}^{n} x_i\right)^{\frac{1}{n}} = \sqrt[n]{x_1 x_2 \cdots x_n} \tag{2.10}$$

where n is the number of values and x_i are the dataset values (Holmes et al., 2017). The approximation of the geometric mean used in this thesis is to take the arithmetic mean of the $\log_{10}$ of the data values. It is this approximation that has been used throughout this thesis where the mean of either ε_{Thorpe} or κ_ρ is taken. The reason that the mean was taken over the median of the given dataset was to allow easier comparison of ε_{Thorpe} and κ_ρ to other studies, which tend to cite time means or equivalent. In situations where data had a non-normal distribution including both positive and negative values (Chapter 5) the median was taken because the log of a negative value yields a complex number.

2.5 HOW DOES THE THORPE SCALE METHOD COMPARE WITH OTHER INDIRECT METHODS OF ESTIMATING DISSIPATION

Over the course of this thesis the main focus of the study and exploration was focused on the Thorpe scale method and how to use it to utilise high resolution temperature data. As covered in Chapter 1 the Thorpe scale uses a length scale based on a perceived mechanical mixing process to estimate a value of TKE dissipation. However, the Thorpe scale method is not the only indirect method of estimating dissipation in the oceans. A few of these methods will now be discussed and put in context with the Thorpe scale method. Broadly these other methods fit under the banner of finescale parametrisation. This broad term doesn't cover one specific method but a variety of methods that use larger physical mixing features to infer a value of dissipation at scales smaller than can be measured using instrumentation that is not specifically designed for measuring at the microscale. These parametrisations are based on the assumptions that:

- the production of turbulent energy at small scales is related to a steady turbulent energy cascade from larger scales, where energy at larger scales passes energy to smaller and smaller scales until it can be dissipated (also assuming no leakage of energy by other means) (Beaird et al., 2012; Polzin et al., 2014).
- there is a stationary energy balance in which turbulent energy production is matched by dissipation and a buoyancy flux (Polzin et al., 2014).

Methods that fit within the reach of finescale parametrisation include the Large-Eddy method (LEM) (Beaird et al., 2012; Evans et al., 2018) and internal wave shear and strain parametrisation (Kunze, 2003; Frants et al., 2013). These two methods will be outlined below. The benefits and drawbacks of these methods will be compared with the benefits and drawbacks of the Thorpe scale method in a short discussion.

2.5.1 THE LARGE-EDDY METHOD

The first of the methods we will look at is the Large-eddy method (LEM). As this method has been applied to Seagliders (Beaird et al., 2012; Evans et al., 2018) comparing it to the Thorpe scale methods seems pertinent.

ESTIMATING DISSIPATION USING THE LARGE EDDY METHOD

Utilising the first assumption above, the dissipation at viscous scales can be determined from the kinetic energy velocity scale (q') in the largest turbulent eddies O(1-10 m) and the associated with a time scale, leading to $\varepsilon \sim (q')^3/l$ (Gargett, 1999). The scales of these larger turbulent eddies can be resolved by platforms such as CTD rosettes and gliders. For this estimate of dissipation a length scale (l) is required. This can be the Thorpe length scale (Equation 1.3) (Thorpe, 1977), but alternatives such as the Ozmidov length scale (Equation 1.4) have been suggested as well. Beaird et al. (2012) used the relationship between the Thorpe and Ozmidov lengths scales to estimate dissipation using the velocity scale and buoyancy frequency using $\varepsilon = C_\varepsilon N(q')^2$, where C_ε is a constant of proportionality allowing the scaling of ε. This specific variation allows for l to be removed from the equation. The velocity scale (q') can be calculated as the rms of the vertical velocity, which is determined using instruments such as specialised narrow band acoustic Doppler current profilers (Gargett, 1999) or comparing the vertical profiling speed of a glider to an idealised model of glider flight (Frajka-Williams et al., 2011). Internal wave variability is then removed using a high pass filter. Fixed value filters (Beaird et al., 2012) and adaptive filters based on the buoyancy frequency (Evans et al., 2018) have both been used to do so. TKE dissipation estimates are then calculated in 20 m bins (Evans et al., 2018).

COMPARISON TO THORPE SCALING

The LEM is a useful method for utilising long glider deployments to generate estimates of TKE dissipation, especially as microstructure equipped gliders typically have a shorter deployment time than those without, due to battery constraints. This helps aid in providing good resolution TKE dissipation estimates without requiring ship based observations. By following the methods presented by Beaird et al. (2012) the removal of the requirement for a length scale also benefits glider deployments as the glider's vertical and horizontal path through the water (see Section 4.2.2) does not need to be taken into account for the estimation of a length scale, although it is still involved in the calculation of the vertical velocity. This allows the estimation of dissipation to be impacted less by the lower resolution of a glider's CT sail, compared with Thorpe scaling low resolution data which will be biased towards higher dissipation estimates (Evans et al., 2018; Leadbitter et al., 2019). This method also removes one of the drawbacks of the Thorpe scaling method in that it doesn't rely on the detection of overturns to provide an estimate.

However, specifically when using the LEM on glider data, a number of limitations need to be taken into account. First, the reliance on the glider flight model to provide the vertical velocity values. A poorly tuned flight model will provide poor values of vertical velocity (Frajka-Williams et al., 2011). This is due to a glider flight model assuming a steady flight and not taking into account changes made by the glider at guidance and control intervals. These changes include changes to roll and pitch (especially at apogee), and as such data may be compromised at these times and needs to be removed.

Another consideration when using long glider deployments is the sampling frequency of the CT sail. On longer deployments to conserve battery the sampling frequency, especially at depth, will be reduced to save battery. When calculating the buoyancy, densities and filters required for the LEM, the change in sampling frequency must be taken into consideration. A final disadvantage to the method is for the constant C_ε, comparison to an existing estimate of dissipation is required (Evans et al., 2018), such as from an ADCP or vertical microstructure profiler, making the method both dependent on such equipment being present and any errors that come from those determinations of dissipation rate.

2.5.2 INTERNAL WAVE SHEAR AND STRAIN PARAMETRISATION

The second of the methods explored is the internal wave shear and strain parametrisation. This method is based on rate of transfer of energy through the internal wave spectrum to small scales and in turn turbulence production (Kunze, 2003).

ESTIMATING DISSIPATION FROM SHEAR AND STRAIN

The method described here is based on work presented and built on by Polzin et al. (1994, 2002); Damerell et al. (2012) and Frants et al. (2013). It is important to note that this method relies on the premise that it is internal waves breaking locally that initiate an energy cascade to smaller scales and finally turbulent mixing. This means that this method is only suitable at estimating TKE dissipation due to internal wave breaking and not other non-internal wave processes (such as the double diffusion examined in Chapter 5). The core of the method involves comparing the spectrum of the internal wave field strain with a model Garrett and Munk (GM) spectrum proposed by (Garrett and Munk, 1975).

To explain the process of estimating ε from strain and shear the methodology provided by Damerell et al. (2012) and Frants et al. (2013) are summarised. Firstly, the variance of vertical shear $\langle V_z^2 \rangle$ from lowered acoustic Doppler current profiler (LADCP). The LADCP shear profile is split into overlapping segments (Damerell et al. (2012) uses 320 m bins, Frants et al. (2013) uses 100 m bins) and they are normalised by the average buoyancy frequency. Each bin then has a Fourier transform applied to give a vertical wave number power spectral density. After a number of quality control processes (for details the reader is directed to Polzin et al. (2002)) $\langle V_z^2 \rangle$ is calculated by integrating the power spectral density between a minimum and maximum vertical wave length. The minimum and maximum wave lengths are picked to minimise noise contamination from the instrument and background stratification. A similar variable $\langle V_z^2 \rangle_{GM}$ is calculated using the GM model, integrated over the same wave length range as $\langle V_z^2 \rangle$. The strain variance level $\langle \xi_z^2 \rangle$ is calculated in a similar fashion to $\langle V_z^2 \rangle$ but uses buoyancy frequency instead of shear profiles. The calculation of $\langle \xi_z^2 \rangle_{GM}$ is slightly more complex and the reader is directed to Frants et al. (2013) for a full description. Shear derived dissipation can then be calculated as,

$$\varepsilon = \varepsilon_0 \frac{\langle V_z^2 \rangle^2}{\langle V_z^2 \rangle_{GM}^2} H(R_\omega) J(f, N) \tag{2.11}$$

and strain derived diffusivity as,

$$\kappa = \kappa_0 \frac{\langle x1_z^2 \rangle^2}{\langle \xi_z^2 \rangle_{GM}^2} H(R_\omega) J(f, N) \tag{2.12}$$

where ε_0 and κ_0 are background values for dissipation and diffusivity, R_ω the shear/strain variance ratio, with H and J being empirical functions that account for the effects of latitude on the internal wave field. Again the reader is directed to Frants et al. (2013) for a full breakdown of R_ω,H amd J.

COMPARISON TO THORPE SCALING

Shear-strain parametrisation provides good estimates of dissipation and diffusivity in regions where the assumptions associated with it hold true (Polzin et al., 2014), which is not always the case. The works referenced in the previous section are a small selection of those that have successfully used the shear-strain parametrisation. Unlike the LEM a profile of shear is still required for the shear section, although the strain section can be applied to any suitable buoyancy profile. This does, however, make the method less useful over longer time scales using autonomous platforms and requires either ship based LADCPs or ADCPs attached to moorings (Damerell et al. (2012) computed an 18 month time series using moorings). In contrast to the Thorpe scale method the shear-strain method is only computed over large bins, typically of the $O(100)$m. This is due to requiring enough data points to construct a robust wave number power spectral density. This then links back to the assumption that it is internal waves breaking and starting an energy cascade locally to provide the dissipation estimates. Although Thorpe scale estimates of dissipation are also binned due to the sporadic nature of individual overturns this binning can be of the $O(10)$m, with the correct data cleaning. Neither of these methods can provide an estimation of dissipation that is not related to a mechanical process within the ocean, although for different reasons. Both also require good data processing techniques to be applied to remove instrument noise.

These are just two of a number of finescale parametrisations that exist for estimating dissipation in the oceans. A further brief discussion relating these to the Thorpe scale method will be provided in Chapter 6.

2.6 SUMMARY

In this chapter the methodology that is used in later chapters for calculating

ε_{Thorpe} has been comprehensively described. A step-by-step breakdown shows each processing step carried out to produce a robust and usable scientific data product. Within this a number of process specific considerations are expanded on as well as how averaging is done to aid the readers understanding of the results. A brief description of finescale methods of estimating TKE dissipation have been presented and compared with the Thorpe scale method. The next chapter explores in more detail how this methodology was developed. ε_{Thorpe} is also compared to TKE dissipation rate estimates from microstructure shear probes to determine the robustness of the developed methods.

3

RIDGEMIX: DEVELOPMENT OF METHODS

3.1 INTRODUCTION

In the previous chapter the method work flow developed for the work presented in this thesis is laid out in full. This chapter expands on the development of the work flow, setting out to investigate the following questions:

- What considerations are required when developing a methodology for Thorpe Scaling high resolution temperature data?
- When using a dataset with both high resolution shear and temperature, does Thorpe scaling high resolution temperature give comparable values of TKE dissipation rate estimates to those estimated with shear data?

To investigate these questions, data published in Vic et al. (2018) from the RidgeMix project is used to provide high resolution temperature and shear data from the same platform for study.

In studies including Peterson and Fer (2014) and Mater et al. (2015) TKE dissipation rates calculated from temperature are compared to the same rates estimated with shear data. Both of these studies involve estimating TKE dissipation rates from

Thorpe scaling, fitting temperature variance spectra to theoretical curves and comparing the estimates. Peterson and Fer (2014) applied this to glider data and Mater et al. (2015) to VMP data. In both studies the shear estimates are considered the standard to be matched by the Thorpe scale estimates. Similarly to those studies and to provide validity of the methods developed in this thesis, estimates of TKE dissipation rates from Thorpe scaling are compared to those from shear.

In the following subsections the data being used is described, followed by temperature specific considerations of Thorpe scaling, Thorpe scale quality control and then mission specific quality control. Finally estimates of TKE dissipation rates from Thorpe scaling are compared with those from shear, based on the work presented by Vic et al. (2018).

3.1.1 RIDGEMIX DATA

The RidgeMix project set out to provide a better understanding of the upward nutrient supply in the North Atlantic Subtropical Gyre (Vic et al., 2018). Part of this project was a cruise undertaken between the 25 may 2015 and 10 July 2015 aboard the RRS *James Clark Ross*. A complete overview can be found in cruise report JR15-007 (Sharples, 2016); VMP specific information is presented between pages 30 and 35. During the cruise vertical profiles of microstructure data were collected using an RSI tethered VMP-2000. Vic et al. (2018) presents data from 2 occupations of a station over the Mid Atlantic Ridge (MAR), one at the spring of the tidal cycle and one at the neap. The two occupations show a clear difference in TKE dissipation estimates. The clear distinction between spring and neap makes them good candidates for testing the viability of the Thorpe scaled TKE dissipation rate estimates. Also included in this work are VMP-2000 deployments from a station away from the MAR, providing a different regime to compare to the MAR stations. Table 3.1 provides the station names, the station and CTD number and the abbreviation used in this chapter to refer to them. The station locations and deployments can be seen in Figure 3.1.

As well as providing microstructure data the VMP also measured low resolution temperature and conductivity. Hydrographic data from this instrument is used to aid in the estimation of TKE dissipation rates from Thorpe scales. A time mean of conservative temperature, absolute salinity, density and buoyancy frequency are

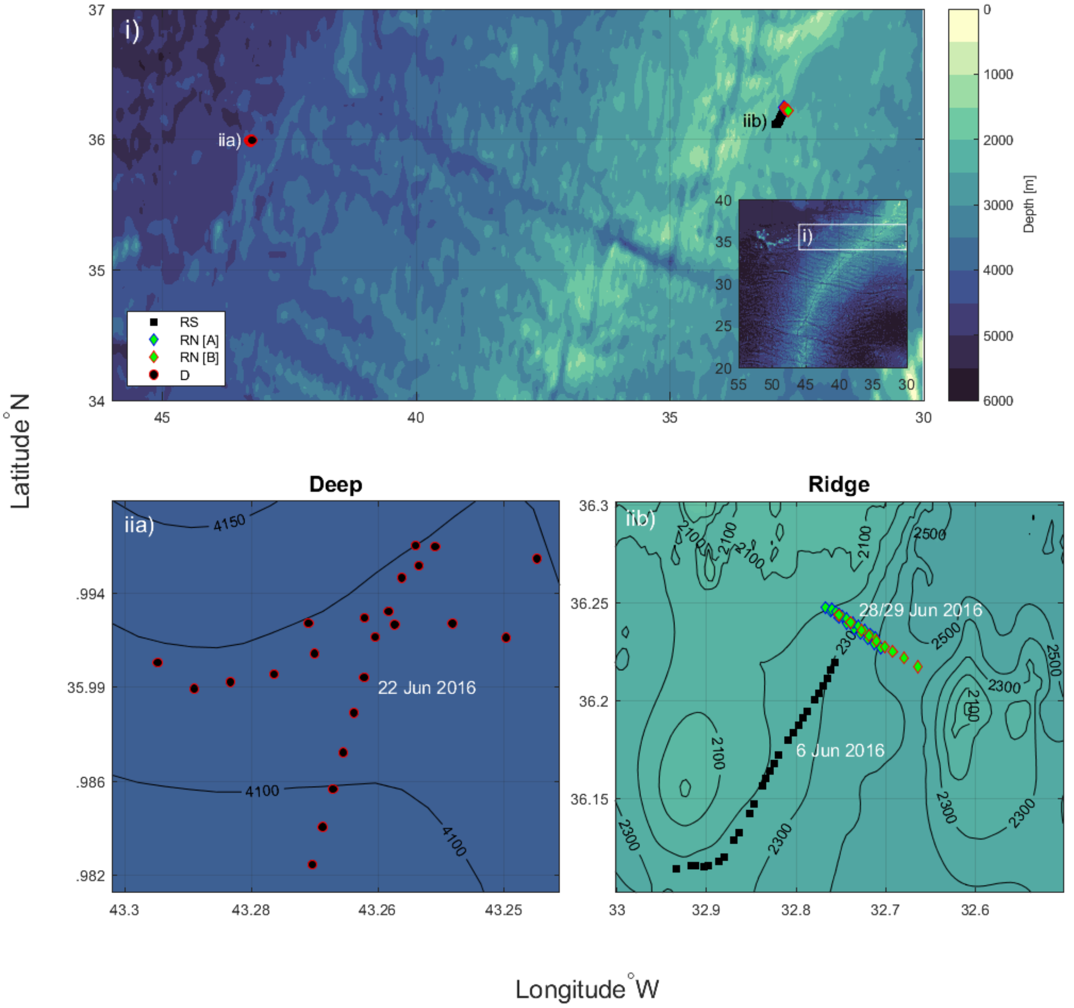

Figure 3.1: Locations of stations used in this chapter with background shading representing the region's bathymetry. i) shows both stations together with the inset showing the overall RidgeMix experiment location. Four VMP stations are marked. One deep station [D] and three close to the ridge [RS, RN[A] and RN[B]]. (iia) Bathymetry and launch locations of VMP station D. (iib) Bathymetry and launch locations of VMP stations RS, RN[A] and RN[B]. Note: All plots share the same depth map and colour scale.

VMP Station Name	Abbreviation	Station CTD
Deep Station	D	D3(055)
Ridge Station Spring	RS	R1(009)
Ridge Station Neap	RN[A]	R1a(064)
Ridge Station Neap	RN[B]	R1b(065)
Ridge Station Neap combined	RN	-

Table 3.1: VMP station names, abbreviations found in this thesis and station identifiers from (Sharples, 2016) which are included for completeness but are not used elsewhere in this thesis. RN[A] and RN[B] are only used in Figure 3.1 (ii). RN will be used to refer to a combined dataset comprised of RN[A] and [B].

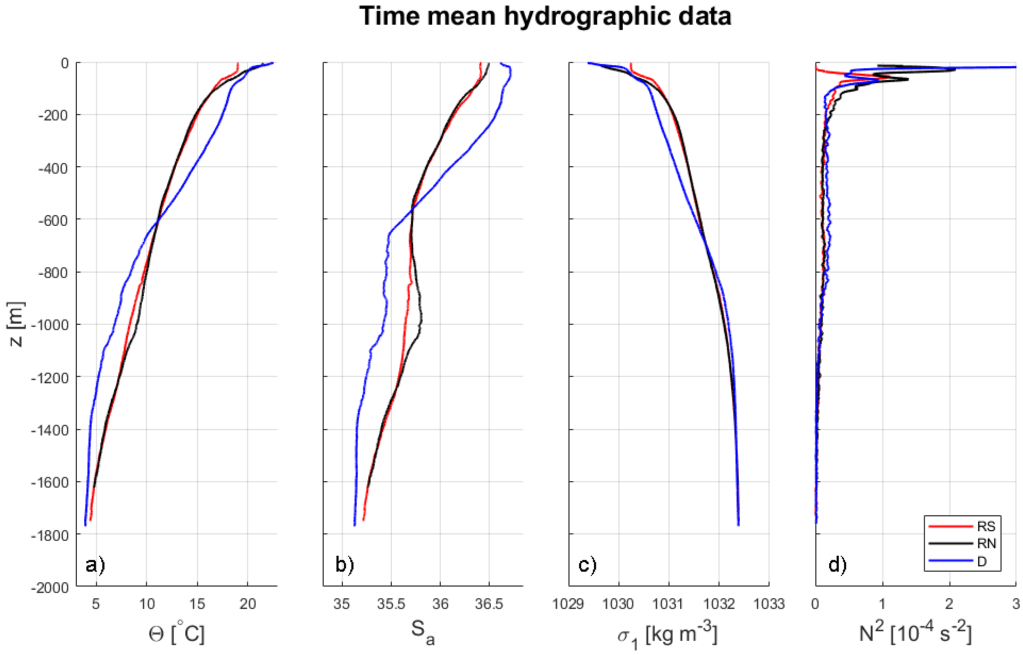

Figure 3.2: Time mean hydrographic data from each of the VMP stations RS, RN and D. a) conservative temperature Θ, b) absolute salinity S_A, c) potential density with 1000m reference and d) panel shows the buoyancy frequency.

provided in Figure 3.2.

For each station and occupation a tethered VMP-2000 was deployed continuously for a 25-h period (sampling 2 semi-diurnal cycles). Station D was conducted in deep water to the west of the MAR on the 22 June 2015. Stations RS, RN[A] and RN[B] were conducted in the vicinity of the project's mooring on the eastern flank of the MAR with RS at spring tide (6 June 2015) and RN (A and B) at the neap tide (28/29 June 2015). The locations of these stations can be seen in Figure 3.1, with panels iia and iib providing clearer details on exact deployment locations.

RIDGE SPRING (RS)

This subset of the data consists of 28 individual VMP profiles collected on 6 June 2015. 18 profiles are shallow (up to 950 m) with 10 being deep profiles (ranging between 1500 m and 1700 m). The first collected profile was aborted at 80 m and has been removed from the analysis of the spring dataset. The numbering of the profiles has been adjusted accordingly (all profile values decreased by one) leaving a total of 27 profiles.

RIDGE NEAP (RN)

This subset of the data was collected in two groups (RN[A] and RN[B]). On 28 June 2015 19 shallow profiles (down to 950 m) were taken (RN[A]). On the 29 June 2015 9 deep profiles (ranging between 1500 m and 1650 m) were taken (RN[B]). The break in collection was due to adverse weather conditions on the evening of the 28th. Due to the proximity to each other and the short time frame these two groups of data will be treated as a single dataset (RN) processed and analysed as one. Within the data collected on profiles 8 and 9 there were some issues with all the instruments on the VMP-2000. A section between 70 m and 220 m on these two profiles was therefore removed. These data were removed from the microstructure data after the initial stages of processing but before any Thorpe scaling work was started.

DEEP (D)

This subset of the data was collected on 22 June 2015 and contains a total of 24 profiles. There are 18 shallow profiles (ranging between 700 m and 1000 m) and 6 deep profiles (ranging between 1550 m and 1800 m). One of the profiles was aborted early (profile 21) and has been removed from the analysis and all profiles above this have had their number decreased by one. This leaves a total of 23 profiles for the deep subset.

3.2 ESTIMATING TURBULENT KINETIC ENERGY DISSIPATION RATES FROM THORPE LENGTH SCALES

3.2.1 PROBE BIAS

After the conversion from raw microstructure data to physical units (but before any further processing, step i from the work flow in Chapter 2) temperature from FP07 1 and 2 were compared to each other to determine if either probe exhibited a bias. The comparison was done for each station. Neither FP07 showed positive or negative bias at any of the stations. Due to the lack of any bias it was decided to use only the temperature data from FP07 1 for the rest of the processing. The same check for bias was carried out on estimates of TKE dissipation rates from shear probe 1 and 2. Neither shear probe exhibited any positive or negative bias. Shear probe 1 was therefore chosen as the probe to be used for all shear comparisons. The data used to determine if there was bias can be found in Appendix B. Once bias had been checked the high resolution temperature data was passed through steps ii and iii of the work flow.

3.2.2 THORPE SCALING OF THE DATA

The first part of the data processing was to run each of the data subsets through the calculation of the Thorpe Length scale and the associated parameters (step iv of the work flow). The process for this can be seen in the diagnostic plot, Figure 3.3 (profile 24, RS), which shows the original and reordered FP07 thermistor data for FP07 1 plus the associated Thorpe fluctuations, Thorpe displacements and Thorpe Length scales. A diagnostic plot is generated for each profile, allowing for visual inspection of the calculation process. If there are any errors at this stage, required fixes can be applied and the process re-run.

3.2.3 CALCULATING BUOYANCY FREQUENCY

To estimate TKE dissipation rates using the Thorpe scale method a buoyancy frequency (N^2) is required (see Equation 1.3). The buoyancy frequency used here should be representative of the stratification that a given overturn (or overturning

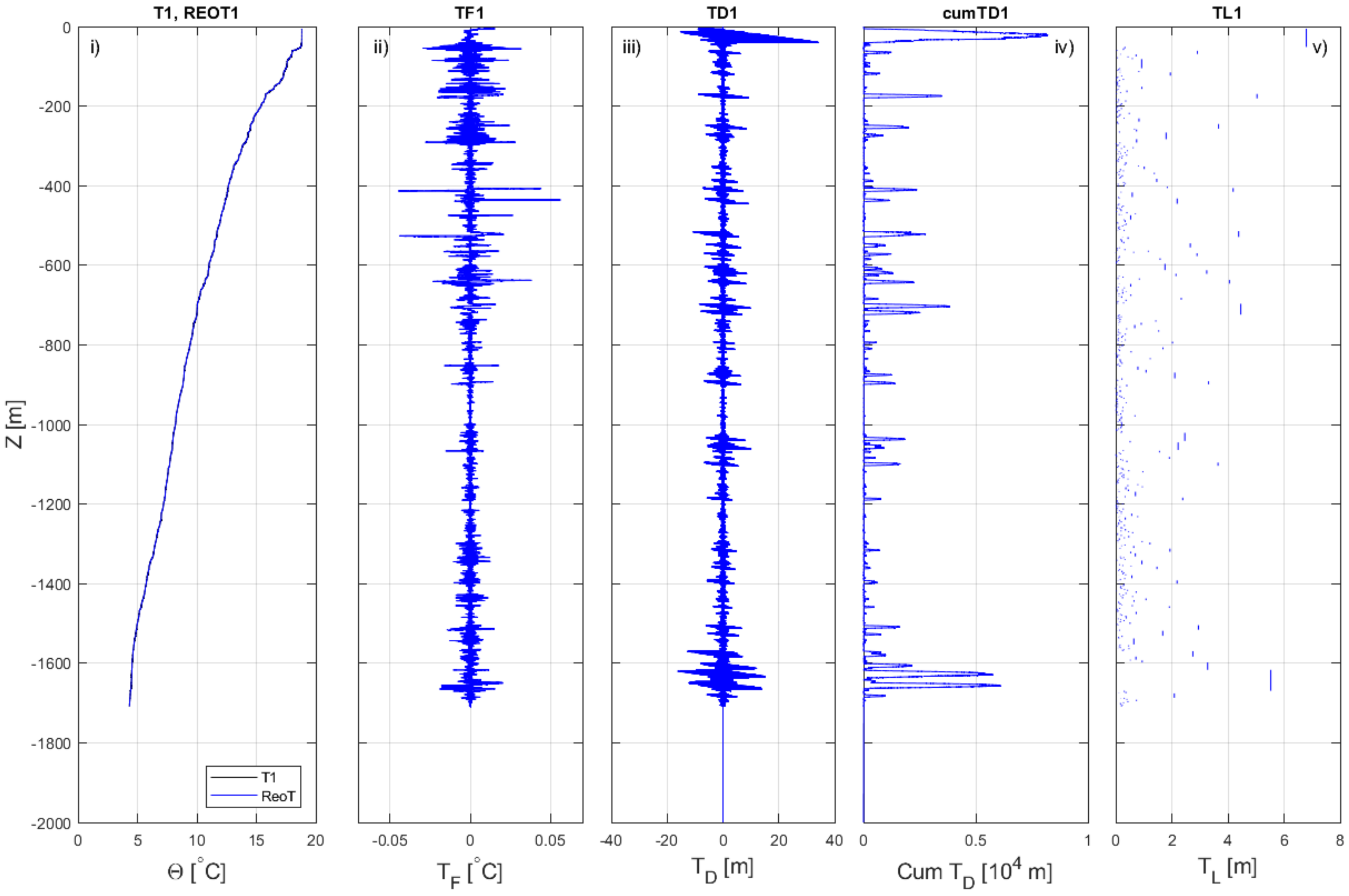

Figure 3.3: Diagnostic figure showing profile 24 from the Ridge Spring dataset. These plots are generated for each profile to act as a visual preliminary check that the processing has worked successfully. (i) shows the temperature and reordered temperature for FP07 1. (ii) shows the Thorpe fluctuations, (iii) shows the Thorpe displacement, (iv) shows the cumulative Thorpe displacement and (v) shows the Thorpe length for each overturning region identified using iv.

Platform	Instrument	Buoyancy Frequency	TKE dissipation
VMP/Seaglider	CTD	N^2_{CTD}	-
VMP/Seaglider	CTD	$N^2_{closest}$	ε_{Thorpe}
VMP/Seaglider	FP07 Thermistor	N^2_{bulk}	-
VMP/Seaglider	FP07 Thermistor	N^2_{mean}	-
VMP/Seaglider	Shear Probe	-	ε_{shear}

Table 3.2: Table showing different naming conventions for buoyancy frequencies calculated in this thesis with the TKE dissipation estimates associated with them

region) is working to break down (Mater et al., 2015). This should be a density gradient that characterises the background potential energy. When Thorpe scaling density profiles this gradient is calculated from the Thorpe sorted density for a given overturn, or overturning region (Thorpe, 1977). One of the primary difficulties in using temperature as a proxy for density in the Thorpe scaling process is the necessity to have an associated buoyancy frequency to use in the estimate of TKE dissipation rate. This cannot be done directly with temperature profiles so another method must be sought to provide the needed value. A number of possible methods exist of defining a suitable N^2 value; these are presented in detail below. A list of variations on N^2, associated values of ε and abbreviations used is provided in Table 3.2.

THE BULK AND MEAN GRADIENT METHODS

(Ijichi and Hibiya, 2018) provide two methods for calculating N^2 using the gradients calculated from high resolution temperature over any given overturning region, as well as using the lower resolution associated conductivity-temperature data. N^2 is calculated as,

$$\langle N^2 \rangle = g\alpha \langle \Theta_z \rangle (1 - 1/R_\rho) \tag{3.1}$$

where g is the acceleration due to gravity, α the coefficient of thermal expansion, R_ρ the density stability ratio and $\langle \Theta_z \rangle$ the vertical gradient of temperature in a given overturning region, R_ρ is defined as,

$$R_\rho = \frac{\alpha \Theta_z}{\Theta_z / \beta S_z} \tag{3.2}$$

where β is the coefficient for saline contraction and S_z is the vertical gradient of

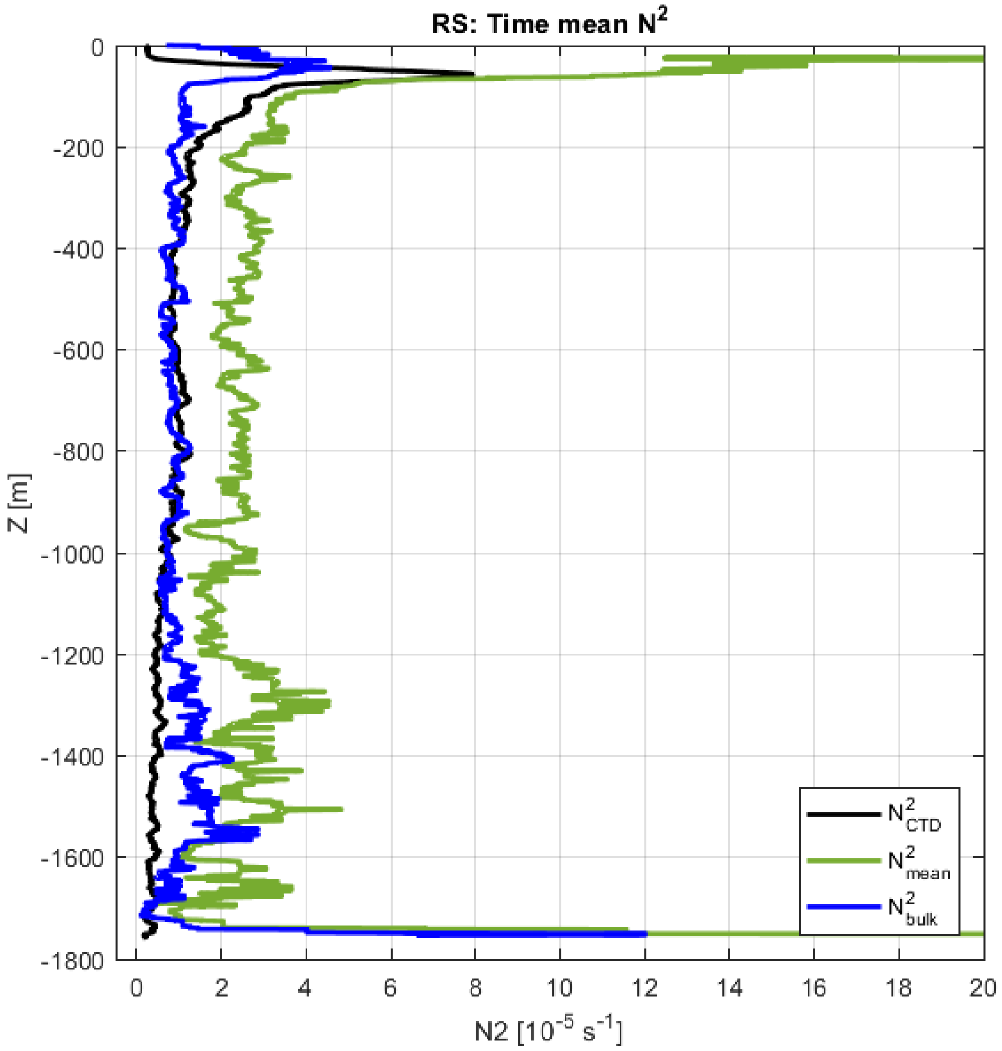

Figure 3.4: Time averaged bulk and mean estimations of N^2 against time averaged N^2 from CTD data. This dataset is from the Ridge Spring.

salinity in a given overturning region. Example profiles of both N^2_{bulk} and N^2_{mean} can be seen in Figure 3.4.

The value of $\langle\Theta_z\rangle$ can be provided from one of two methods of assigning a gradient to an overturning region. The first of these is the mean gradient, $\langle\Theta_z\rangle_{mean}$, which is calculated by simply fitting a linear gradient through a sorted profile Θ within an overturning region. The second is using a bulk gradient, $\langle\Theta_z\rangle_{bulk}$, which is calculated as,

$$\langle\Theta_z\rangle_{bulk} = \langle T_f^2\rangle^{1/2}/L_T \tag{3.3}$$

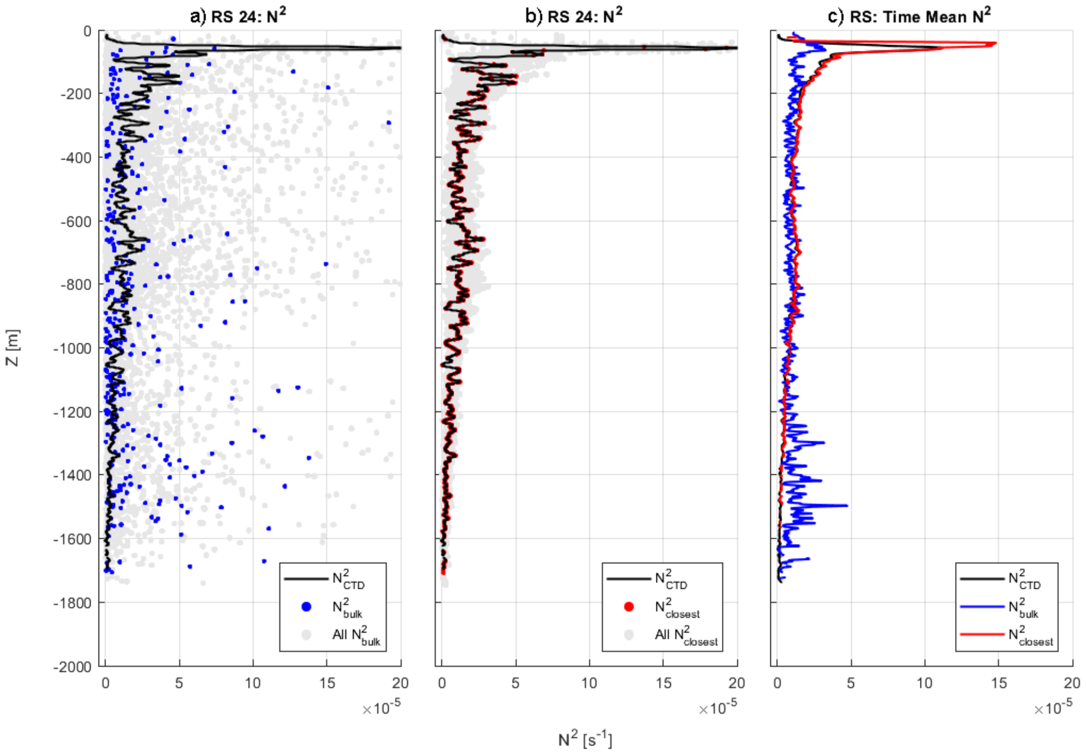

Figure 3.5: Different N^2 values from the RS subset a) N^2_{bulk} from profile 24 (blue), N^2_{bulk} from all profiles (grey), and time mean N^2_{CTD} (black) b) $N^2_{closest}$ from profile 24 (blue), $N^2_{closest}$ from all profiles (grey), and time mean N^2_{CTD} (black) c) time mean N^2_{bulk}, $N^2_{closest}$ and N^2_{CTD} binned to 1 m.

where T_f is the Thorpe fluctuation for any given overturning region and L_T is the Thorpe length scale.

CTD temperature and salinity were used for the calculation of R_ρ which is then interpolated onto the same resolution as the FP07 data. FP07 high resolution temperature was used to calculate the gradients $\langle \Theta_z \rangle_{mean}$ and $\langle \Theta_z \rangle_{bulk}$ for use in Equation 3.1. Of these two methods Ijichi and Hibiya (2018) found that both methods provided nearly equal values of N^2 when an overturning region was dominated by a single overturn, whereas the mean method would overestimate N^2 when compared with the bulk method if multiple smaller overturns dominated the overturning region. The bulk method is also the method used by Mater et al. (2015), which forms the foundations of some of the work in this thesis.

THE CLOSEST METHOD

In addition to the two methods described above, a third method was also investigated in this thesis, a method termed the closest method. Here the value of N^2_{CTD} closest in depth to the mid point depth of an overturn region for a given Thorpe Scale value is used, giving $N^2_{closest}$. An example of such a profile can be seen in Figure 3.5 b. A smooth time mean over time is not used. This is due to the fact that although it gives a potential background value for N^2 it is not taking into account what is occurring with the local stratification around any given overturning region (Ijichi and Hibiya, 2018).

COMPARING THE CLOSEST, BULK AND MEAN METHODS

Three methods for determining N^2 for an overturn have been defined. The three methods were then compared to determine the most suitable one to use in step v of the work flow. Initial analysis compared N^2_{bulk} and N^2_{mean} with N^2_{CTD} (Figure 3.4) using the RS subset. N^2_{CTD} is calculated using temperature and conductivity from the VMP and is used as the standard. The N^2_{bulk} and N^2_{mean} were compared first as they are related to overturning regions, with $N^2_{closest}$ being overturn independent. Figure 3.4 shows that N^2_{mean} gave a poor estimation of N^2 when compared with N^2_{CTD}, overestimating by $\sim 1.5 \times 10^{-5}$ s^{-2} across the whole depth. Values from N^2_{mean} show a similar profile shape below 200 m to that of the N^2_{bulk} and match the surface values of N^2_{CTD}. In comparison N^2_{bulk} does a good job of matching the time mean N^2_{CTD} between 200 m and 1200 m with slight under estimations in the upper parts of the water column and slightly over estimating at depth. This was supported by repeating the comparison on the RN and D subsets. The elevated values of N^2 from N^2_{mean} are consistent across all three datasets. The vertical structure of N^2_{mean} is also considerably more varied than when compared with the other two methods. Because of these reasons and evidence provided by other studies it was decided not use N^2_{mean} for any further analysis.

N^2_{bulk} and $N^2_{closest}$ were then compared in more depth to decide which should be used as the N^2 for estimating TKE dissipation from Thorpe scaling (step v of the work flow). The two were compared on a profile by profile basis, for all three stations. Figure 3.5 shows profile 24 of the RS dataset and the time mean of both N^2_{bulk} and $N^2_{closest}$. Large variation in N^2_{bulk} can be seen when compared with that of N^2_{CTD}

(values up to 20 times greater, Figure 3.3, certain regions) this comparison was also conducted on the RN and D subsets and provided patterns consistent with those seen in RS. In addition to these variations future work based on this method would be pulling R_ρ from a low resolution CT sail on a glider. This would require either up sampling salinity values to be used in Equation 3.2 or for multiple smaller overturns (vertically smaller than the resolution of a glider CT sail) to use the same value of R_ρ. Due to the impact that N^2 can have on Equation 1.3, minimising the steps required to provide a value for buoyancy is vital. With this in mind and to reduce complexity and provide a guaranteed realistic value of N^2 for a given overturning region the decision to use $N^2_{closest}$ for the value of N^2 used in the estimation of ε_{Thorpe} was taken.

3.2.4 BINNING DATA FOR ANALYSIS

Overturning regions are not uniformly spread with depth meaning that TKE dissipation estimates from Thorpe scaling are also not uniformly spread with depth. Estimates need to be binned to regular intervals to be compared with shear derived estimates (and other profiles). During the development stage two methods were used for storing the outputs.

Pillar method: data is stored as a 'pillar'. Each depth point within an overturning region is assigned the same value. For example if a 0.5 m overturning region contains 10 samples with a Thorpe Length scale of 0.3 m all 10 samples would be assigned the Thorpe Length scale 0.3 m. This was done for every overturning region.

Point method: data is stored is as a 'point'. This is where a single value is assigned to an overturning region. For example if a 0.5 m overturning region contained 10 samples with a Thorpe Length scale of 0.3 m there would only be a single value of the Thorpe length scale assigned at the mid point (in depth) of the overturning region rather than 10.

Both methods have merit, with the pillar method good for showing an overturning region as a continuous block of a set value (Figure 3.3 panel v) and the point method for showing the distribution of data. For binning the data into larger depth bins one of the two methods needed to be selected. Figure 3.6 shows the RS subset of data binned to 25 m increments, with the two methods plotted against each other and a line of best fit calculated. The pillar method for storing data is useful but shows a bias towards

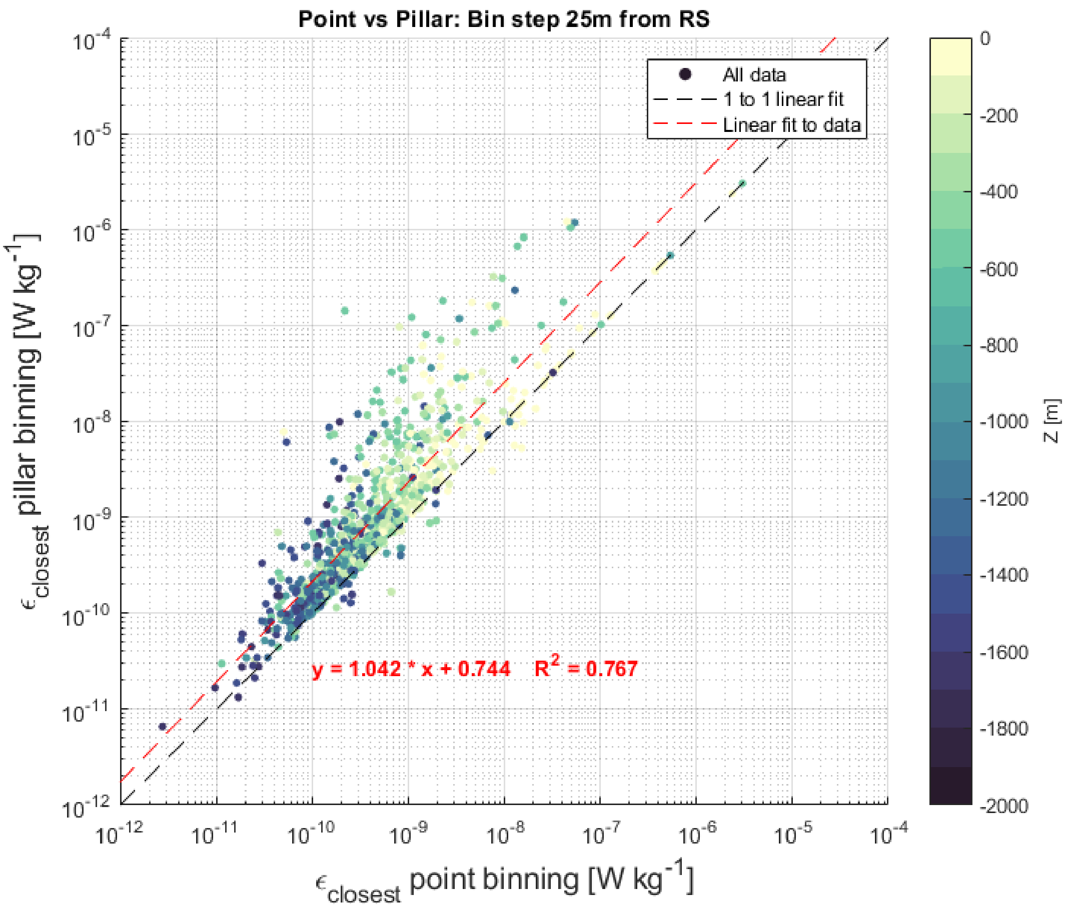

Figure 3.6: The point binning method plotted against the pillar binning method for 25m binned data from RS. A fit between the methods is close to one to one but shows an over estimation bias in the pillar method. Data is coloured by depth.

higher values of TKE dissipation values than the point method. This is unsurprising as larger overturning regions, which typically show higher Thorpe Length scales, have a greater weighting during averaging in the binning process. The pillar method also allows for overturning regions to appear in multiple bins, biasing values with very tall overturns (taller in height than the bin width). To prevent bias in Thorpe Lengths and overturning regions appearing in multiple bins all vertical binned values of both ε_{Thorpe} and ε_{shear} for the rest of this work use the point method. All vertical averaging was done as,

$$\overline{\varepsilon_z} = \frac{1}{n} \sum_{z_l \leq z < z_u} log_{10}(\varepsilon_i) \tag{3.4}$$

where z_l and z_u are the lower and upper limits of the bin, ε_i the values of ε within the bin, n the number of values of ε in the bin and $\overline{\varepsilon_z}$ the average of ε from the bin.

3.2.5 INITIAL COMPARISON OF THORPE SCALE ESTIMATED TKE DISSIPATION RATES TO SHEAR

At this stage high resolution temperature data for each subset has been taken through stages i to vi of the work flow in Chapter 2. The high resolution data has also been binned to 25 m, the first part of step vii. At this point in the development no further QC had been applied so that ε_{Thorpe} could be compared with ε_{shear} to determine if the methods were functioning as intended and if there were specific regions of the water column where the ε_{Thorpe} methodology was showing a distinct difference to the values of ε_{shear}. Figures 3.7, 3.8 and 3.9 show the time mean and profile values of ε_{shear} and ε_{Thorpe} for RS, RN and D respectively. The broad structure of all is first shown followed by a more in depth break down of each dataset.

Across all three subsets the following broad structures can be seen:

- In the time mean ε_{Thorpe} shows a smaller overestimation when compared with ε_{shear} in the upper 1400 m of the water column.
- On a profile by profile basis ε_{Thorpe} shows a larger variability in bin value when compared to ε_{shear}. Values both greater and smaller than ε_{shear} are seen, typically within half an order of magnitude of ε_{shear}.
- In all three subsets ε_{Thorpe} captures enhanced mixing in the upper 25 to 150 m (depth dependant on subset) that is seen in all ε_{shear} subsets.
- Between 600 m and the 1800 m all three subsets of ε_{Thorpe} exhibit a region of elevated values (of varying sizes) that is not present with ε_{shear}.

With the broad structure of the ε_{Thorpe} values showing a reasonable match when compared with values of ε_{shear}, the differences were then examined in more detail to aid in the development of quality control steps to remove poor data.

RS SUBSET

The region in the RS subset (Figure 3.7) that shows the greatest variation of ε_{Thorpe} compared with ε_{shear} can be seen in the time mean centred at 800 m. When the

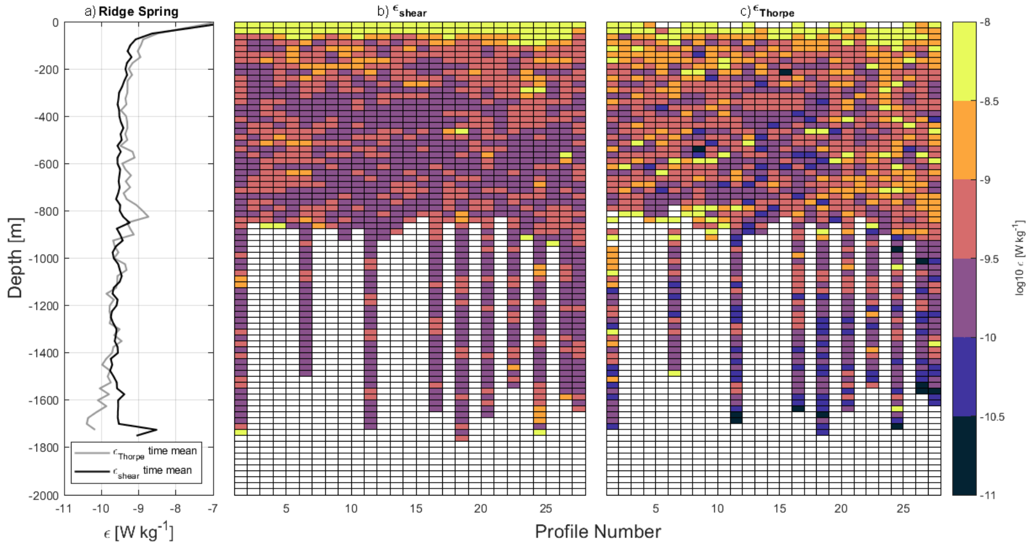

Figure 3.7: Comparison of ε_{shear} and ε_{Thorpe} in 25 m bins for the Ridge Spring dataset. a) Time mean ε_{shear} and ε_{Thorpe}. b) and c) individual profiles of ε_{shear} and ε_{Thorpe} respectively.

profiles were examined, profiles between 1 and 10 show a marked increased of ε_{Thorpe} compared with those in the rest of the ε_{Thorpe} subset or the ε_{shear} data values. Here the values of ε_{Thorpe} are $(O)10^{-9}$ W kg^{-1} compared with $(O)10^{-10}$ W kg^{-1} of ε_{shear}. An important distinction can be made between bins of $(O)10^{-9}$ W kg^{-1} in the first 10 profiles and those seen elsewhere in the subset. The distinction is that a number of the bins are bounded on one or both sides by an empty bin. This is important as an empty bin can be caused by two different reasons. The first of these, which is the cause of elevated values in bin profiles 2,3 5 and 7 and the elevated bin at the end of profile 6, is that the bin encompasses the end of the temperature profile. During the reordering process to calculate T_L the final overturning region has not closed as the VMP-2000 stopped recording before the overturn finished. If the overturning region was substantial in size this would give rise to a large L_T value, and from that a large ε_{Thorpe} value. The second reason for empty bins, which is the cause of empty bins in profile 1 and 6 is the presence of a tall overturn. The centre of the overturning region sits in a single bin, with the physical structure encompassing the 37.5 m above and below the overturning region mid point. Both of these situations are unlikely to be true indications of mixing processes occurring; especially as these features are not seen else where in the RS data subset, or in ε_{Thorpe} at the same depths.

The other noticeable difference between ε_{Thorpe} and ε_{shear} in the RS subset is

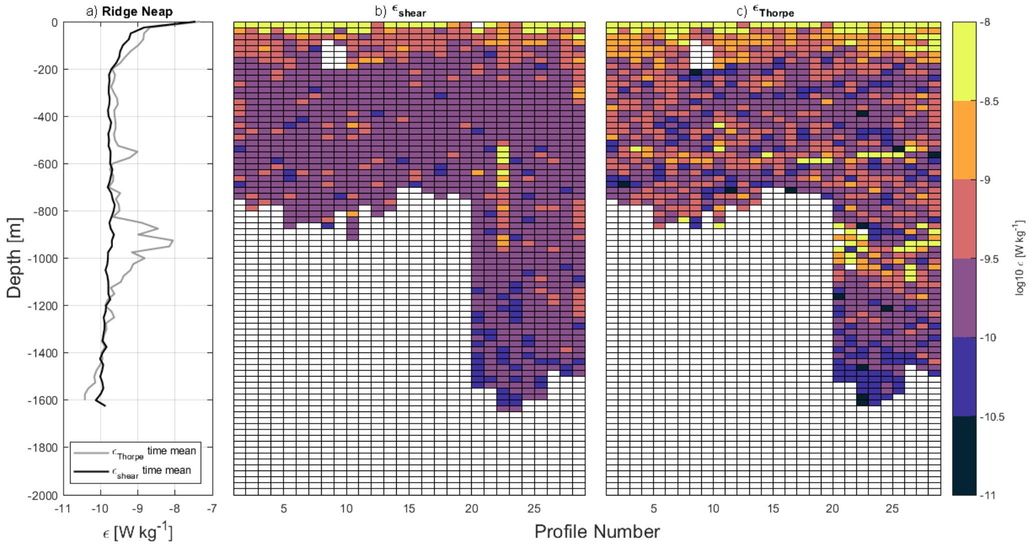

Figure 3.8: Comparison of ε_{shear} and ε_{Thorpe} in 25 m bins for the Ridge Neap dataset. a) Time mean ε_{shear} and ε_{Thorpe}. b) and c) individual profiles of ε_{shear} and ε_{Thorpe} respectively.

below 1400 m where ε_{Thorpe} tends to values of $(O)10^{-11}$ W kg^{-1} and ε_{shear} stays steady at $(O)10^{-10}$ W kg^{-1}.

RN SUBSET

The RN subset (Figure 3.8) shows two separate regions of ε_{Thorpe} that are a poor match when compared with ε_{shear}. The first is between 525 m and 575 m appearing as a peak in the time mean of $(O)10^{-9}$ W kg^{-1} in ε_{Thorpe} compared with $(O)10^{-10}$ W kg^{-1} in ε_{shear}. This is associated with bins in profiles 18 and 26 at these depths. The second region is between 900 m and 1100 m in profiles 20 to 27. In this region ε_{Thorpe} deviates substantially from ε_{shear} with ε_{Thorpe} reaching $(O)10^{-8}$ W kg^{-1} at 900 m. Bins in profiles 20, 21 and 22 have empty bins either side as seen in the RS subset. Profiles 23 to 28 have a number of bins with elevated TKE dissipation estimates but with no empty bins to either side. Values below 1400 m of ε_{Thorpe} are lower than those in ε_{shear} with a smaller magnitude difference than that seen in RS. There was also a location in ε_{shear} that compared poorly with ε_{Thorpe} (the only subset to do so). This is seen an elevated strip in ε_{shear} on profile 22 between 500 m and 1000 m. This strip does not seem to influence the time mean across these depths. No cause for this has been determined and was left in during further analysis. It is also clear in Figure 3.8 where there is removal of data in profiles 8 and 9 due to instrument sampling issues.

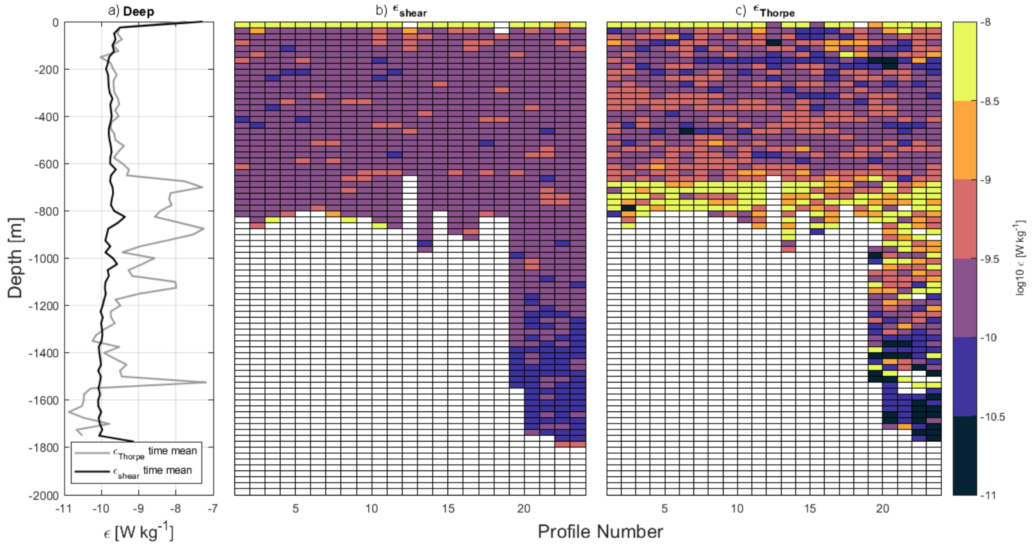

Figure 3.9: Comparison of ε_{shear} and ε_{Thorpe} in 25 m bins for the Deep dataset. a) Time mean ε_{shear} and ε_{Thorpe}. b) and c) individual profiles of ε_{shear} and ε_{Thorpe} respectively.

D SUBSET

The D subset (Figure 3.9) shows the greatest deviations when comparing ε_{Thorpe} with ε_{shear}. This is clearest in both the time mean and profiles between 650 m and 1200 m, although below 1200 m is still a poor fit. The region of over estimated ε_{Thorpe} (up to $(O)10^{-8}$ W kg^{-1} compared with $(O)10^{-10}$ W kg^{-1} of ε_{shear}) can be seen across every profile. In comparison to RS and RN the elevated region of ε_{Thorpe} is not limited to smaller sections but affects the entire subset, suggesting a different reason for over estimation to those in RS and RN. Specific work was carried out to determine the cause of these discrepancies and can be found in Section 3.4.3.

At 1500 m there is one region of elevated ε_{Thorpe}, that matches the features seen in the RS subset, between profiles 20 and 24. This region was unlikely to be a true representation of local mixing as it was not seen in the ε_{shear} data. Below 1000 m a greater variation in values of ε_{Thorpe} was seen (range of $(O)10^{-11}$ W kg^{-1} to $(O)10^{-9}$ W kg^{-1}) both in the profiles and the time mean. Higher variation in the time mean is attributed to the small number of bins included in the averaging process leading to substantial bias in the time mean (both positive and negative).

3.3 QUALITY CONTROL DEVELOPMENT

From the results presented in the previous section it was clear that when ε_{Thorpe} was compared with ε_{shear} there are large regions of the water column where values are comparable but also several regions that were not. With the aim of reducing the differences between the two methods of estimating TKE dissipation rates, additional quality control steps were investigated and a final, post TKE dissipation rate estimation quality control methodology was developed. The process of that development is discussed below, starting with methods presented by other studies before looking at the development of a new method. This also includes how manual quality control was conducted.

3.3.1 TUNER ANGLE AND THE STABILITY RATIO

There are regions of the water column, such as where it is salinity stratified, where Thorpe scaling temperature will be a poor proxy for Thorpe scaling density. There are several methods in the previous studies that have been used to exclude data from the Thorpe Scaling process. These include visual inspection of the T/S relationship and spiciness (Gargett and Garner (2008), Mater et al. (2015)), examining the tightness of the T/S relationship overturn by overturn (Gargett and Garner, 2008) or using the Stability ratio (Ijichi and Hibiya, 2018) to remove overturns within a given range. All of the methods above require some level of manual investigation of overturning regions. The aim of the work in this section was to determine a simple method to minimise individual inspection of overturning regions and instead use an algorithm to find regions of the water column, once the data has been binned, that do not fit a set of criteria. A method is required for removing bins where the temperature salinity relationship would lead to a temperature overturn being detected where no overturn exists in density.

The initial concept was to use the effects of thermal expansion and haline contraction to determine unsuitable bins of ε_{Thorpe}. The two methods examined were based on the Stability ratio (R_ρ, Equation 3.2) and the Turner angle (Tu, Equation 3.5) as potential methods for excluding data. R_ρ is used by Ijichi and Hibiya (2018) to exclude overturning regions where $-1/2 \leq R_\rho \leq 2$ to avoid contamination

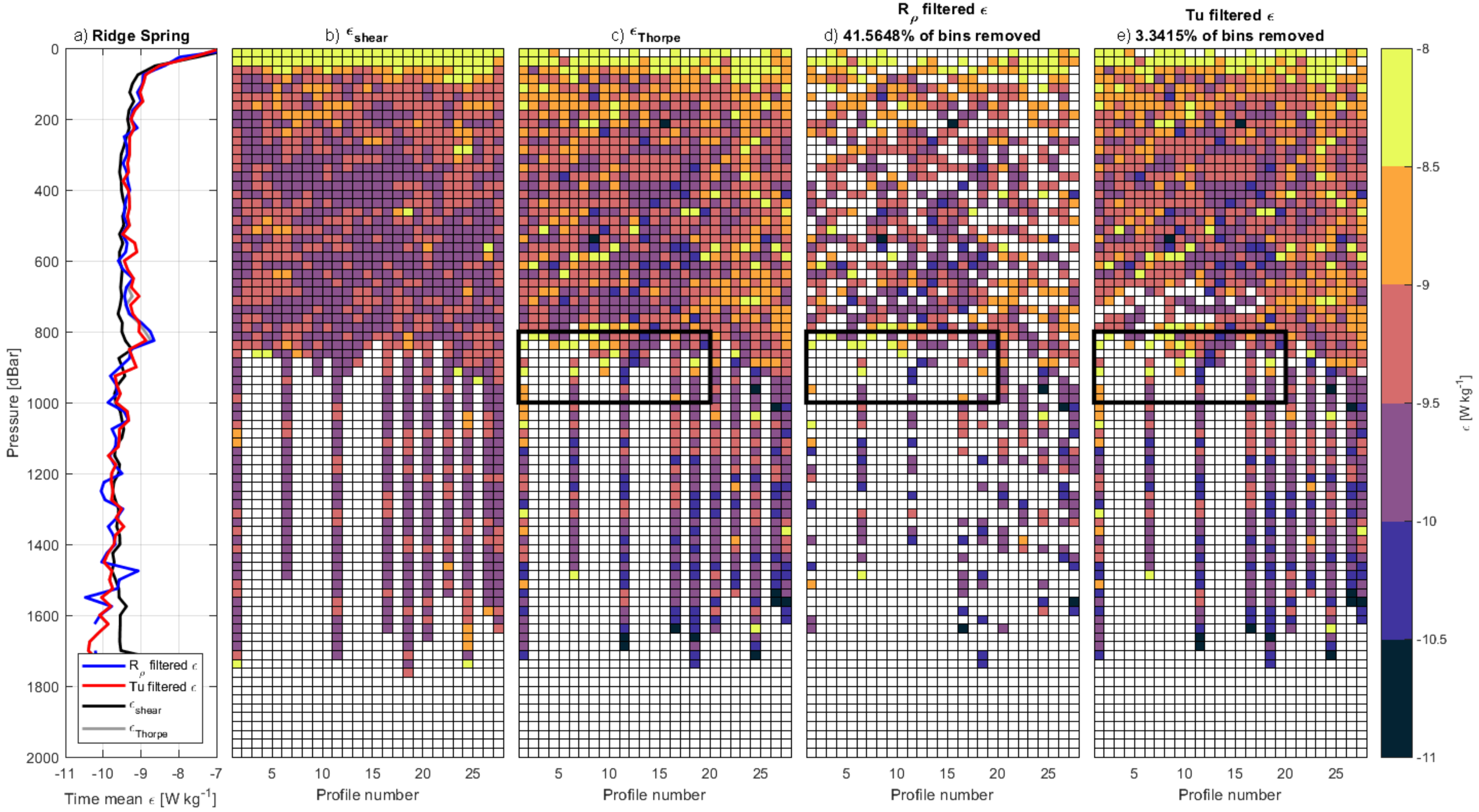

Figure 3.10: A comparison of using the Turner Angle and the Stability Ratio as filtering parameters for the Ridge Spring dataset. a) Time mean averages of b - e. b) 25 m binned TKE dissipation estimates from shear data. c) 25 m binned TKE dissipation estimates from Thorpe Scaling. d) 25 m binned TKE dissipation estimates from Thorpe Scaling after removal where $-0.5 \geq R_\rho \geq 2$. e) 25 m binned TKE dissipation estimates from Thorpe Scaling after removal where $-45 \geq Tu \geq 45$. Data encased in a black rectangle is later removed manually.

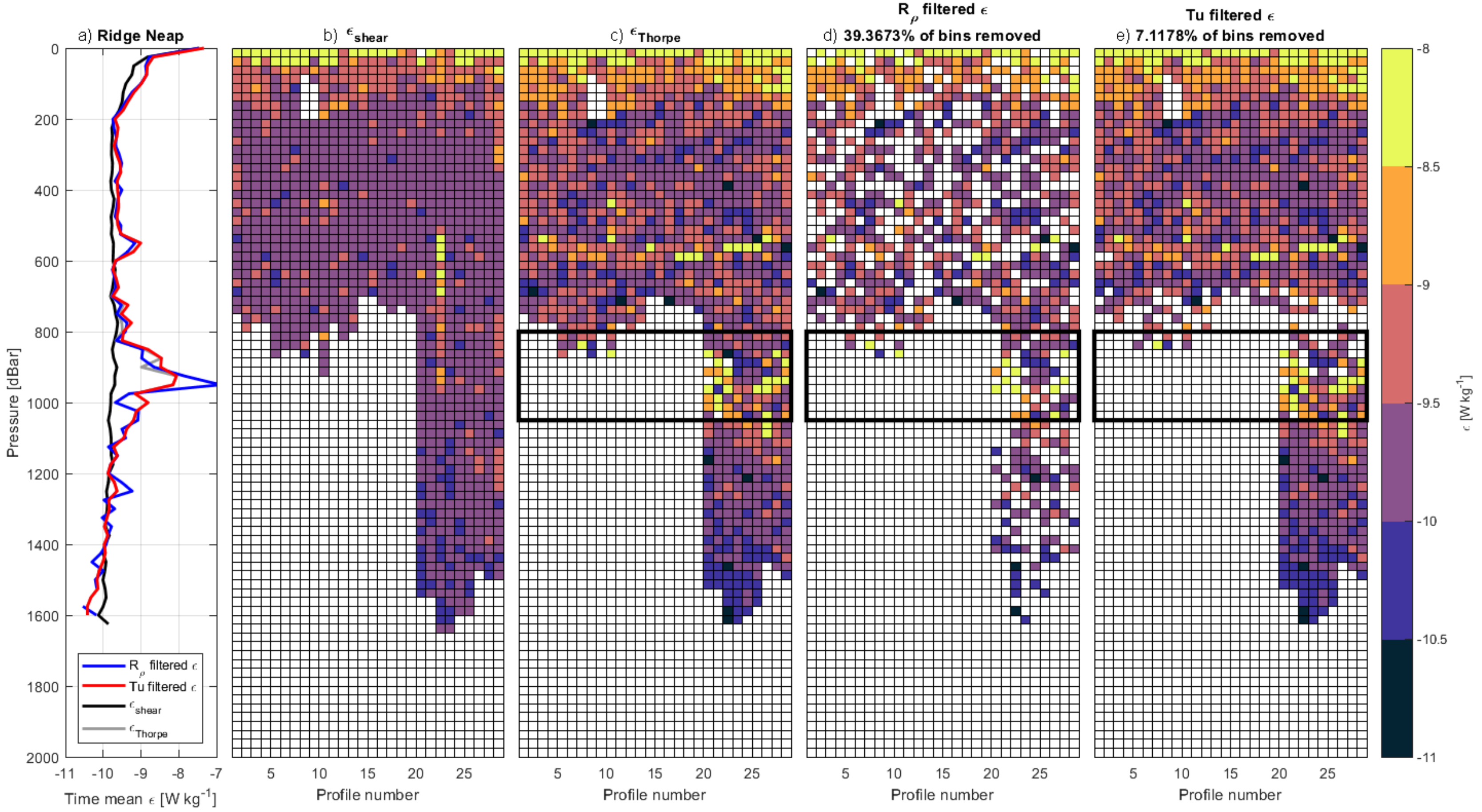

Figure 3.11: A comparison of using the Turner Angle and the Stability Ratio as filtering parameters for the Ridge Neap dataset. a) Time mean averages of b - e. b) 25 m binned TKE dissipation estimates from shear data. c) 25 m binned TKE dissipation estimates from Thorpe Scaling. d) 25 m binned TKE dissipation estimates from Thorpe Scaling after removal where $-0.5 \geq R_\rho \geq 2$. e) 25 m binned TKE dissipation estimates from Thorpe Scaling after removal where $-45 \geq Tu \geq 45$. Data encased in a black rectangle is later removed manually.

from strongly salinity stratified layers and density intrusions (Laurent and Schmitt, 1999b). In this work this step was originally used to exclude identified overturns. This led to the removal of over 90% of overturning regions across all three subsets and was dropped as a quality control method during calculation, as it was decided that 90% data removal made further work unviable. Instead it was calculated on a 25 m bin basis for each dataset and used to mask any bins where R_ρ fitted the criteria set out by Ijichi and Hibiya (2018).

The second method was to calculate Tu, defined as a four-quadrant arctangent (Ruddick (1983),McDougall et al. (1988)),

$$Tu = tan^{-1}(\alpha\Theta_z - \beta S_z, \alpha\Theta_z + \beta S_z) \tag{3.5}$$

where α is the coefficient of thermal expansion, β the coefficient for saline contraction, Θ_z and S_z the vertical gradients for conservative temperature and absolute salinity (IOC et al., 2010). The turner angle is used to categorise the water column into regions presented as a degree of rotation between $-180°$ and $180°$. The regions are doubly stable ($-45° \leq Tu \leq 45°$), prone to salt fingers ($45° \leq Tu \leq 90°$), prone to diffusion-convection ($-90° \leq Tu \leq -45°$) or statically unstable ($-90° \leq Tu \leq 90°$) (Ruddick, 1983). A value for Tu was calculated for each 25 m bin. Where $-45° \leq Tu \leq 45°$ the bin was excluded. R_ρ and Tu were calculated using the GSW Oceanographic ToolBox (IOC et al., 2010). The results of excluding bins based on R_ρ and Tu can be found in Figure 3.10, 3.11 and 3.12 for RS, RN and D respectively.

Applying both of these methods to the RS, RN and D subsets shared clear similarities in the outcomes:

- Using R_ρ removed $\sim$ 40% of possible data bins from each subset but had minimal impact on the time mean
- Using Tu removed between 0.3% and 7% of possible data bins from each subset and had minimal impact on the time mean
- Neither method targeted the areas of concern presented in Section 3.2.5

RS SUBSET

Tu and R_ρ perform best on the RS subset (Figure 3.10). Between the surface and 600 m R_ρ, although removing more data, performs better than Tu reducing the ε_{Thorpe}

values towards the ε_{shear} values. Both Tu and R_ρ perform poorly at removing the region of elevated TKE dissipation seen in ε_{Thorpe} at 800 m. Below 900 m filtering based on R_ρ adds a greater amount of variation to the time mean of ε_{Thorpe} than by filtering with Tu or not applying any quality control filtering to ε_{Thorpe}. Below 1400 m both do a poor job of reducing the difference between ε_{Thorpe} and ε_{shear}.

RN SUBSET

In the RN subset (Figure 3.11) Tu and R_ρ perform equally well as exclusion metrics (down to 500 m) with minimal difference between the time mean of the filtered ε_{Thorpe}. R_ρ excludes 32% more bins than Tu to provide a very similar value of time mean in the top 500 m. Neither metric removes the peak at 550 m.

Between 800 m and 1000 m there is a region of increased ε_{Thorpe}. In this region Tu does not reduce the magnitude of the peak and ε_{Thorpe} filtered by R_ρ increases the peak from $(O)10^{-8}$ W kg^{-1} to $(O)10^{-7}$ W kg^{-1}, making the filtered values a worse fit to ε_{shear} than without a filter. Below 1000 m a similar pattern to the surface depths (< 500 m) can be seen with both Tu and R_ρ providing a reduced difference in time mean between ε_{Thorpe} and ε_{shear}. It should be noted that in RS and RN datasets filtering by Tu provides a smoother time mean compared with filtering by R_ρ.

D SUBSET

The D subset (Figure 3.12) has the poorest match between the ε_{Thorpe} and the ε_{shear} results, both before and after the Tu and R_ρ filtering is applied. Above 650 m there is little change between the pre and post filtered time mean of ε_{Thorpe}. As with the RS and RN subsets R_ρ removes more bins to provide a similar time mean to that of Tu or unfiltered ε_{Thorpe}. Between 650 m and 1000 m there is the raised region of ε_{Thorpe}. In this region filtering by R_ρ removes over 50% of the bins compared with filtering by Tu which removes none of the bins. However, neither filtering metric makes a large difference to the time mean. Below 1000 m the subset only has 5 profiles and due to the patchy nature of Thorpe Scaled TKE dissipation estimates the time mean in this region is impacted by a lack of values (at some depth bins only a single point is available). It is unsurprising that the data in this region is noisier than the upper water column. Filtering by R_ρ removes 75% of the bins in this region with Tu again removing none. Due to the lack of total bins in this region of the water column it will not be subject to heavy scrutiny during the rest of the chapter as it is believed that the

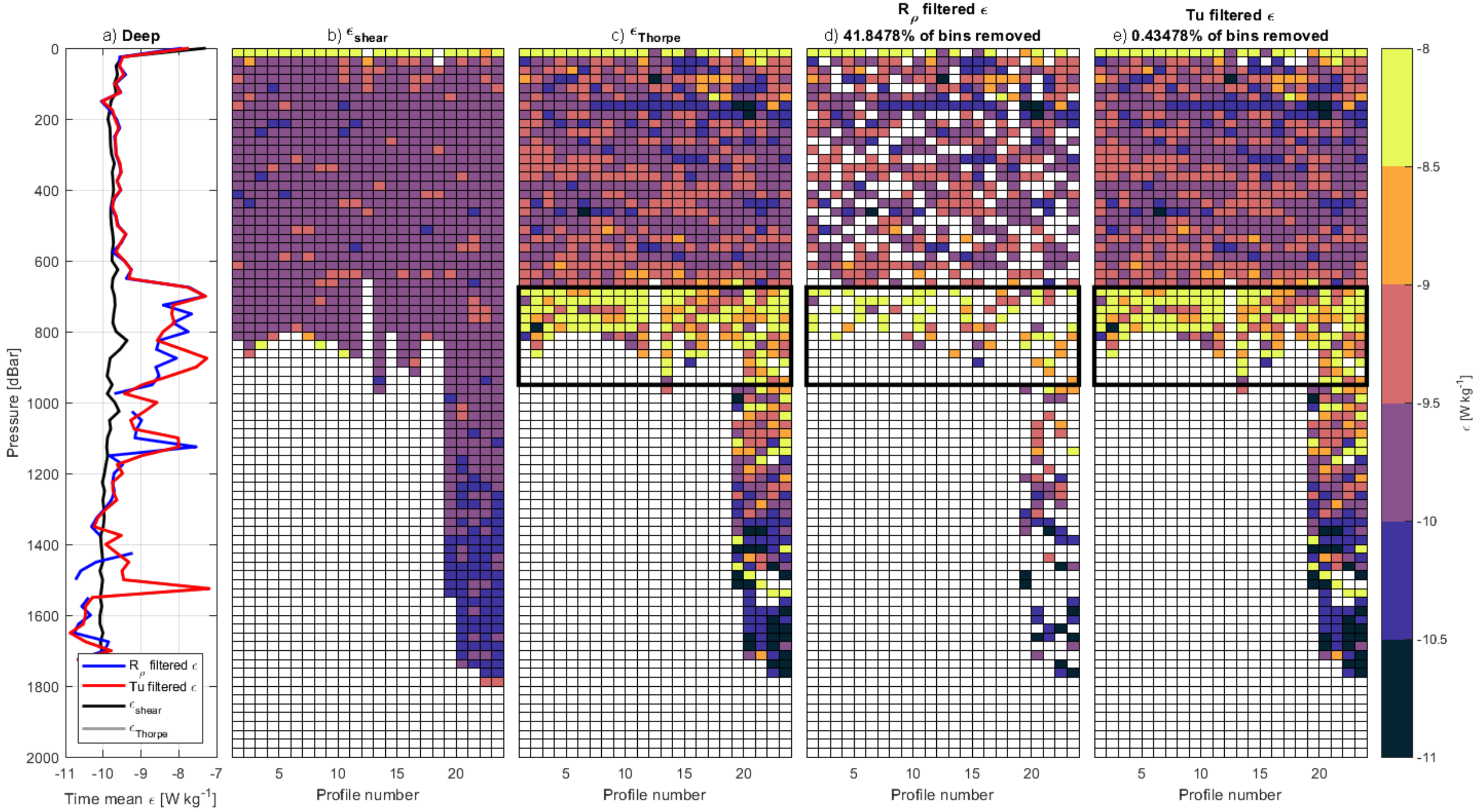

Figure 3.12: A comparison of using the Turner Angle and the Stability Ratio as filtering parameters for the Deep dataset. a) Time mean averages of b - e. b) 25 m binned TKE dissipation estimates from shear data. c) 25 m binned TKE dissipation estimates from Thorpe Scaling. d) 25 m binned TKE dissipation estimates from Thorpe Scaling after removal where $-0.5 \geq R_\rho \geq 2$. e) 25 m binned TKE dissipation estimates from Thorpe Scaling after removal where $-45 \geq Tu \geq 45$. Data encased in a black rectangle is later removed manually.

results given from these averages are poor both before and after any sort of filtering.

Both exclusion metrics (R_ρ and Tu) improve the time mean values of ε_{Thorpe} when compared with ε_{shear}. R_ρ does however, remove up to 40% more bins than Tu, and in some regions of the water column provided no improvement to time means. Neither metric seems to performs well at points of enhanced TKE dissipation estimates seen in ε_{Thorpe}. Tu seems to be a poor metric to exclude bins of ε_{Thorpe} due to the lack of bins removed, with R_ρ giving more potential but removing significantly more bins in the process. Before deciding if either of these metrics were suitable to be used as additional quality control a third method was investigated.

3.4 VARIANCE ALGORITHMS

In the previous section two methods for quality control where presented. In this section a third method that is related to the variability of T-S in the ocean interior, away from both heat and salt sources is presented. The T-S relationships in such areas of the ocean are maintained by advection, stirring and mixing with the latter two of these having differing effects on the T-S structure witnessed (Ferrari and Polzin, 2005). Before discussing the methods developed in this thesis the importance of temperature variance and the impacts of stiring and mixing on the T-S structure of the region will be outlined.

3.4.1 TEMPERATURE VARIANCE BUDGET

Two processes have been highlighted that have differing impacts on the T-S relationship seen in the ocean interior. The first of these is turbulent mixing. Turbulent mixing is typically of $O(10^{-2}$-$10)$m. Turbulent mixing drives fluxes both along and across isopycnals and leads to less variability in T-S space, mixing water masses along straight lines. In contrast, stirring typically occurs at $O(10$-$100)$km and is dominated by mesoscale eddies. Stirring drives fluxes along isopycnals, but not across them. Finally stirring tends to increase the variability seen in T-S space (Ferrari and Polzin, 2005).

The increased T-S space variability caused by stirring presents itself as being near perfectly compensated in density with large temperature anomalies being offset by large anomalies in salinity space with an equal and opposite effect on the density (examples of such structures can be seen in figures in Section 3.4.3). This temperature and salinity structure although varied is not visible in the density structure (panel c) Figure 3.2). Klein et al. (1998) put forward a theory for why such a structure appears. This is due to the transfer of kinetic energy to large vertical and horizontal scales via inverse energy cascade. T-S variability along density surfaces is instead transferred to smaller scales as it is not affected by the inverse energy cascade which leads to large compensated T-S structure but smooth density profiles.

The mean T-S relationship in the ocean is created by flows acting on different ranges of spatial and temporal scales (Garabato et al., 2016). This can be expressed as the conservation equation for the mean potential temperature based on (Ferrari and Polzin, 2005),

$$\underbrace{\frac{\partial \theta'^2}{\partial t}}_{\text{tendency}} + \underbrace{\nabla \cdot (\bar{\mathbf{u}}\overline{\theta'^2} + \overline{\mathbf{u}'\theta'^2} - \kappa_\theta \nabla \overline{\theta'^2})}_{\text{advective and diffusive fluxes}} + \underbrace{2\overline{\mathbf{u}'\theta'^2} \cdot \nabla \bar{\theta}}_{\text{production}} = \underbrace{-\chi}_{\text{dissipation}} \tag{3.6}$$

where θ is the potential temperature, t time, χ the rate of dissipation of temperature variance, κ_θ the molecular diffusivity of temperature, $\mathbf{u}$ the full three-dimensional velocity and ∇ a full three-dimensional gradient operator. The over bars represent the time average and the primes are the deviation from this average (Spingys et al., 2021). Equation 3.6 shows that there is a balance between the production of temperature variance, the divergence of the advective and diffusive fluxes, the tendency of temperature variance and the dissipation of temperature variance. This balance is useful in determining what forces are impacting the local T-S regime. Based on work by Spingys et al. (2021) using the same dataset as this chapter the tendency and divergence terms of 3.6 can be neglected. This leaves a balance between the production and dissipation of temperature variance,

$$\overline{\mathbf{u}'\theta'} \cdot \nabla \bar{\theta} = -\chi/2 \tag{3.7}$$

Following Garabato et al. (2016), Spingys et al. (2021) decomposes the production of temperature variance into microscale turbulence, that provides the diapycnal transfer (the element of interest in this thesis), and the mesoscale eddy stirring, that provides isopycnal transfer, giving,

$$\overline{\mathbf{u}'_t\theta'_t}\cdot\frac{\partial\overline{\theta}}{\partial z}+\overline{\mathbf{u}'_e\theta'_e}\cdot\nabla_\sigma\overline{\theta}=-\chi/2 \tag{3.8}$$

where subscript e and t represent the contributions of the mesoscale and micro scale respectively.

It is clear then that the local regime is influenced by both diapycnal and isopycnal transfer of energy. As we are only interested in the diapycnal element of this (the Thorpe scale method can only estimate from the diapycnal element) the isopycnal aspect needed to be removed. This is explored in the following two Sections (3.4.2 and 3.4.3).

3.4.2 DEVELOPING A VARIANCE ALGORITHM

To remove regions dominated by isopycnal processes a ratio of the variance in temperature and salinity within a 25 m depth bin was explored. Bins where the variance ratio exceeded a threshold (see below) were excluded. The aim was to provide an algorithmic method of removing the isopycnal influences both in the RidgeMix dataset as well as in future datasets. The temperature and salinity data was taken from the VMP-2000 CTD and binned to 0.5 m. The ratio of the variance of salinity with temperature is calculated as,

$$r=\frac{std.dev(salinty_{bin})}{std.dev(temperature_{bin})} \tag{3.9}$$

over a 25 m bin. We can infer from the value of r whether there is greater variance in temperature or salinity. A larger value of r suggests a greater variation in salinity than temperature. So that this method could be used on other datasets or oceanic regions the ratio (r) was normalised using the z score method (Holmes et al., 2017),

$$r_{normalised}=\frac{r-mean(r)}{std.dev(r)} \tag{3.10}$$

giving r a mean of 0 and a standard deviation of 1.

The mean and standard deviation in these equations are calculated on the $log_{10}(r)$ bins to minimise the impact of bias of very positive or negative bins. To confirm that $r_{normalised}$ of RS, RN and D datasets have a mean of 0 and a standard

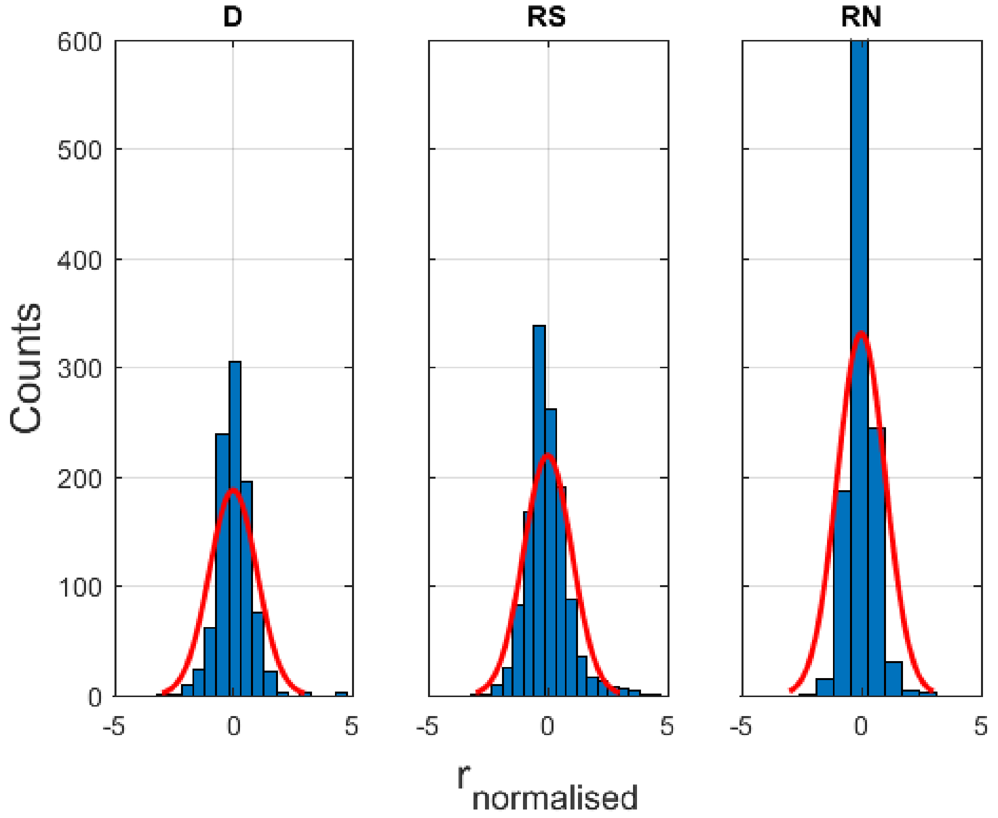

Figure 3.13: Data range of the ratio for each of our datasets (Deep, Ridge Spring, Ridge Neap) once the normalisation process has been applied to them. This image is produced to check that this process has been carried out correctly during processing.

deviation of 1 the distribution of $r_{normalised}$ is plotted (Figure 3.13).

Once a value of $r_{normalised}$ had been calculated for each bin a threshold value was required to exclude bins. The following was applied to RS, RN and D subsets. A range of potential threshold values were decided upon, with values between -3 to 3 in increments of 0.125 being used as a majority of $r_{normalised}$ fell in this range. ε_{Thorpe} was filtered by excluding bins where the $r_{normalised}$ value for a given bin equalled or exceeded the threshold. The number of data bins remaining was calculated and taken from the unfiltered number of bins to determine the number of bins removed. To directly compare ε_{Thorpe} with ε_{shear} the difference $(log_{10}(\varepsilon_{Thorpe}) - log_{10}(\varepsilon_{shear}))$ was calculated on a bin by bin basis. The root-mean-square (rms) difference for the whole dataset was then calculated. This was done for each threshold and the outputs from this can be seen in Figure 3.14 (where threshold values are referred to as cut off values). This allowed for a comparison of the amount of data removed from a given subset as well as showing if excluding the bins improved or worsened the difference

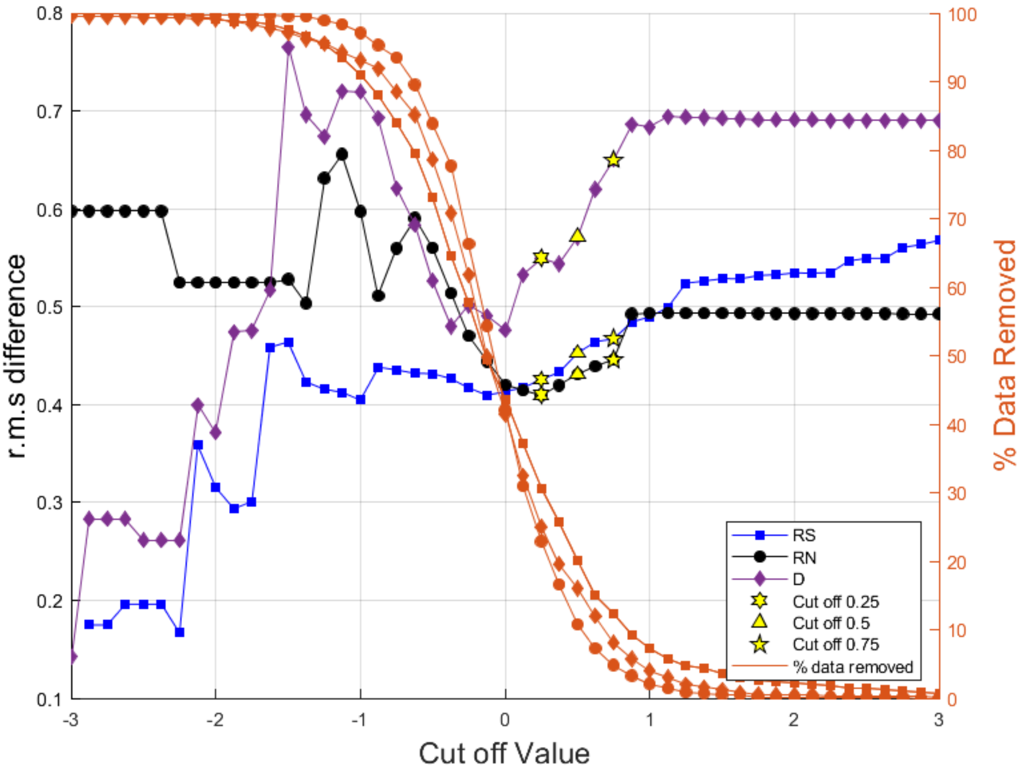

Figure 3.14: Range of possible cut off values plotted against the difference in datasets when a cut off is applied. Also plotted are the data percentage data removed for each of these values. In yellow are three cut off values used later in the chapter.

between ε_{Thorpe} and ε_{shear}. Between threshold values of 3 and 1 a minimal change in the rms difference (RN, D) or a steady decline (RS) is seen, indicating no or limited improvement. Between 1 and 0 there is a marked decrease in the rms difference before increasing again below a threshold value of 0. The point of 50% bins excluded occurs just below a threshold value of 0. As the number of bins removed and the rms difference between ε_{Thorpe} and ε_{shear} both increase below a threshold value of 0 the exclusion threshold was set between 0 and 1. Figures 3.15, 3.16 and 3.17 show examples using a threshold (cut off) of 0.25, 0.5 and 0.75 for RS, RN and D respectively.

RS SUBSET

In the RS subset (Figure 3.15) we see that across the whole dataset all three threshold values improve the time mean ε_{Thorpe} estimates, including around the 800 m region where a peak existed that neither Tu or R_ρ removed. Below 1400 m where the ε_{Thorpe} data begins to deviate more from the ε_{shear} data only the 0.75 cut off managed to

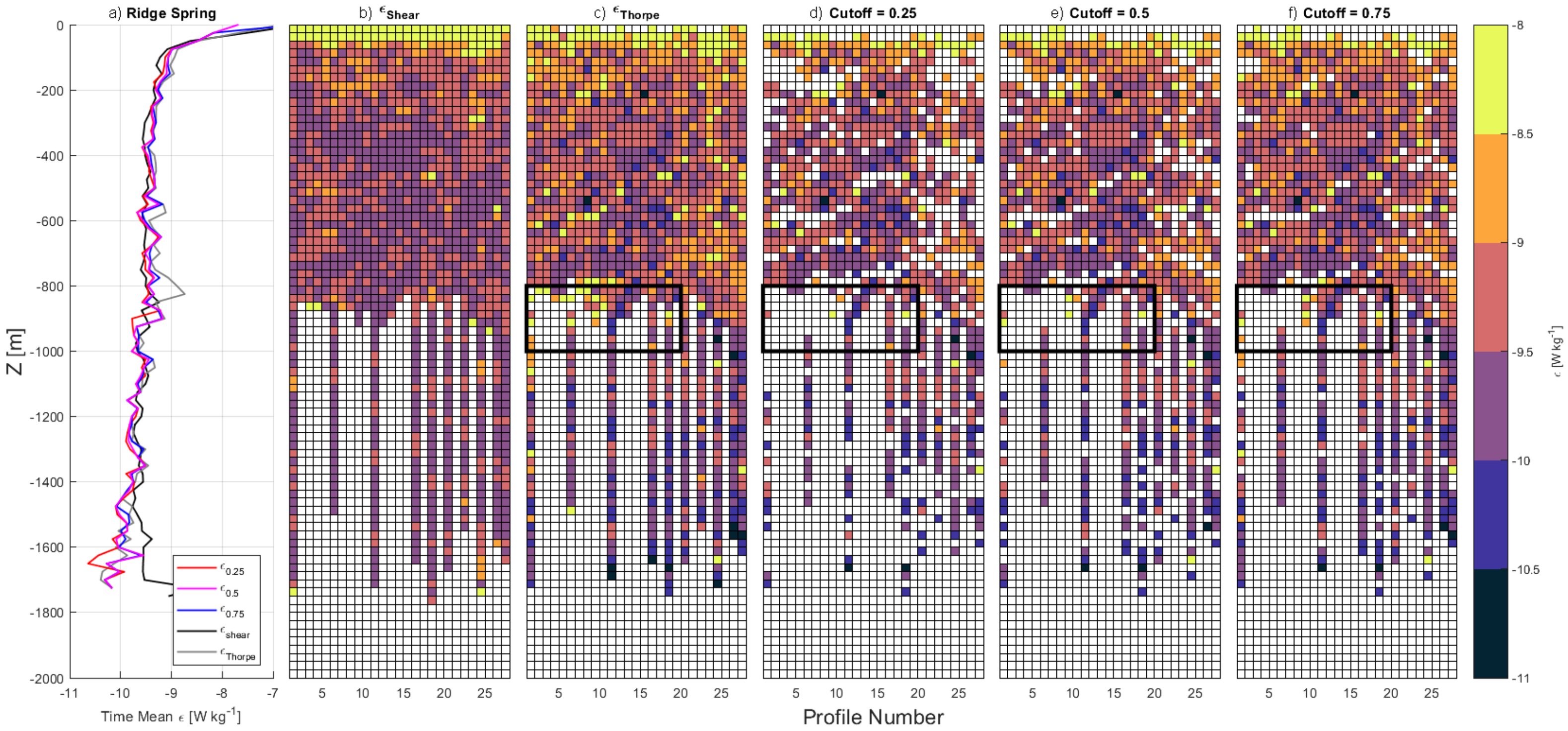

Figure 3.15: A comparison of using variance cut offs as filtering parameters on Ridge Spring data. a) Time mean averages of b - f. b) 25 m binned TKE dissipation estimates from shear data. c) 25 m binned TKE dissipation estimates from Thorpe Scaling. d,e,f) 25 m binned TKE dissipation estimates from Thorpe Scaling after being filtered by 0.25, 0.5 or 0.75 respectively. Data encased in a black rectangle is later removed manually.

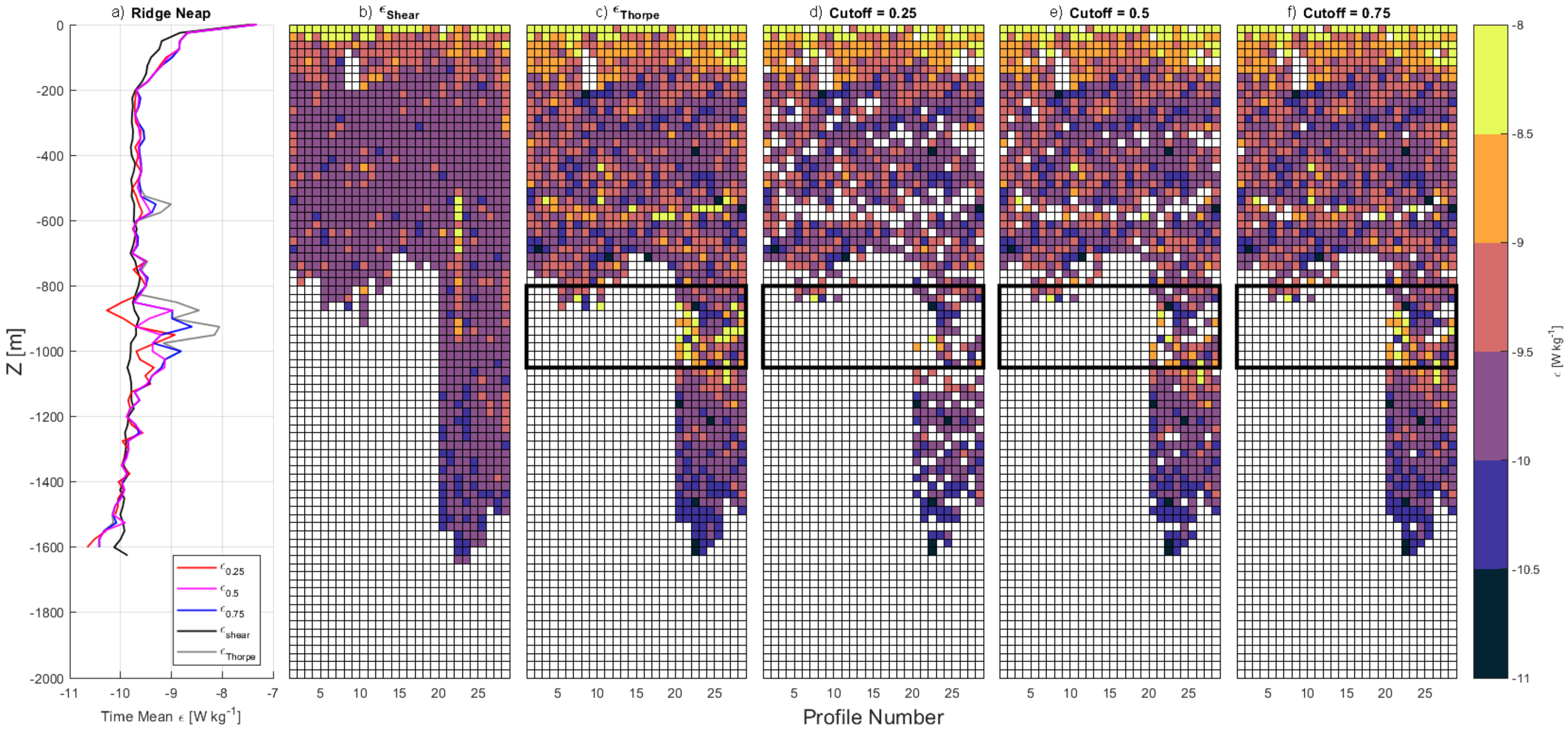

Figure 3.16: A comparison of using variance cut offs as filtering parameters on Ridge Neap data. a) Time mean averages of b - f. b) 25 m binned TKE dissipation estimates from shear data. c) 25 m binned TKE dissipation estimates from Thorpe Scaling. d,e,f) 25 m binned TKE dissipation estimates from Thorpe Scaling after being filtered by 0.25, 0.5 or 0.75 respectively. Data encased in a black rectangle is later removed manually.

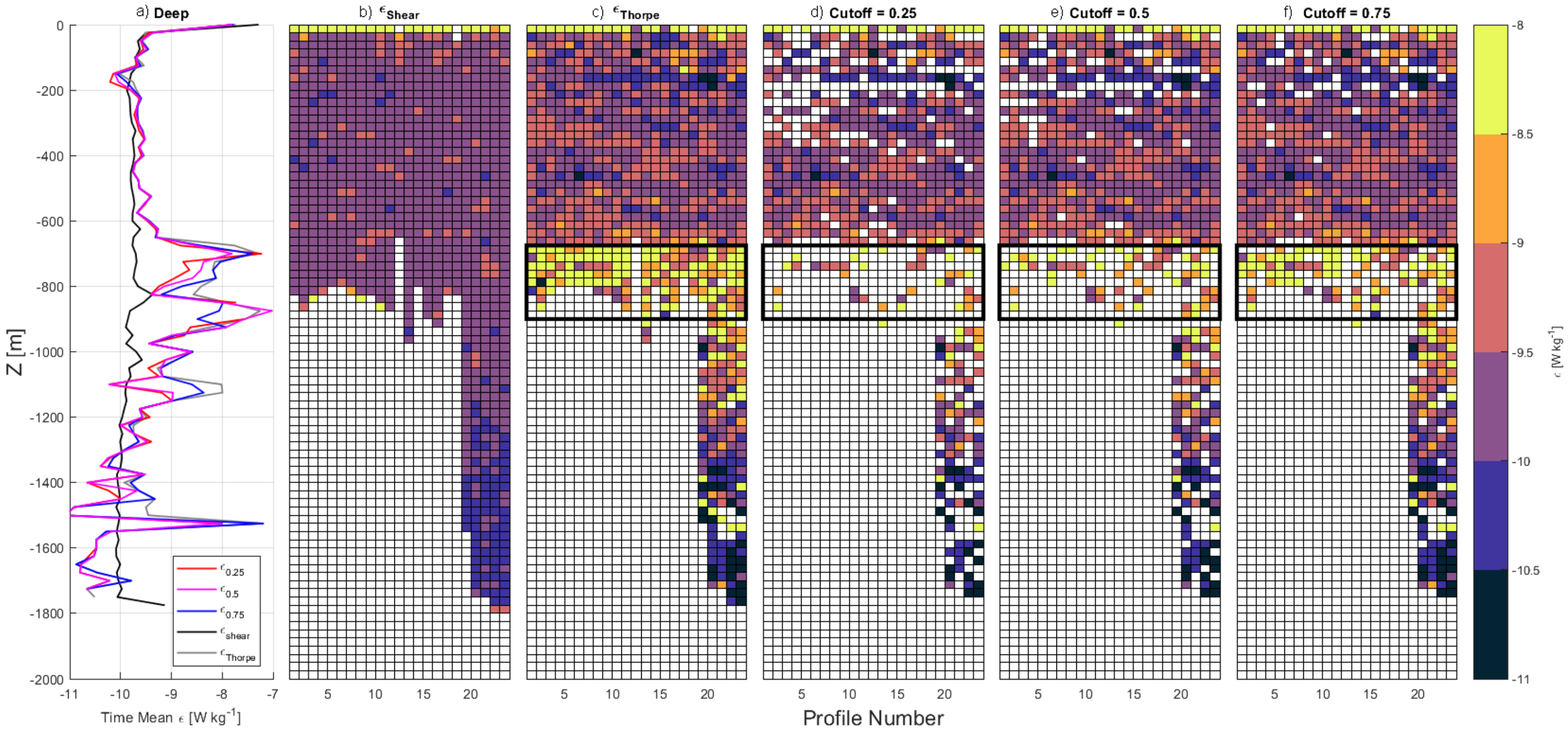

Figure 3.17: A comparison of using variance cut offs as filtering parameters on Deep data. a) Time mean averages of b - f. b) 25 m binned TKE dissipation estimates from shear data. c) 25 m binned TKE dissipation estimates from Thorpe Scaling. d,e,f) 25 m binned TKE dissipation estimates from Thorpe Scaling after being filtered by 0.25, 0.5 or 0.75 respectively. Data encased in a black rectangle is later removed manually.

make the two datasets more comparable but the data removal here actually removes lower values leaving the larger ones. At these threshold values between 12% and 32% of the bins were removed. The RS dataset is the most impacted by the amount of data removed at higher threshold values. A threshold value higher than 0.75 would have been a reasonable exclusion metric but would not work for either the RN or D datasets (see below).

RN SUBSET

In the upper water column of the RN subset (Figure 3.16) the 0.25 threshold performed the best until a depth of 800 m. Both the 0.5 and 0.75 threshold values also perform well in this region. Between 800 m and 1100 m all three threshold values show a narrowing of the difference between the ε_{Thorpe} and ε_{shear} time means. The 0.25 threshold excludes bins around 850 m which neither the 0.5 and 0.75 threshold values do. All three of these threshold values do an improved job of filtering compared to Tu and R_ρ. Below 1200 m all three threshold values provide very similar outputs with no threshold value out performing the others. At these threshold values between 5% and 24% of the bins were removed.

D SUBSET

As with using Tu and R_ρ as cut off values, the impact of using threshold values is poorest with the D subset (Figure 3.17). Above 650 m all three cut off values provide a minimal amount of exclusion with only a small negative peak in the time mean above 200 m being a region where the three vary the most. Unlike in the exclusion metrics Tu and R_ρ we do see some success here of the different thresholds excluding bins between 650 m and 1000 m. Here the 0.25 threshold performed the best with the 0.5 matching it just 800 m. None of the threshold values, however, provide an adequate exclusion solution at this depth. Again below 1000 m we still see a poor match between the ε_{Thorpe} and ε_{shear} data. At these threshold values between 8% and 25% of the bins had been removed.

Of the three threshold values presented here 0.5 shows the best compromise between amount of data removed (between 10% and 15% across the three subsets) and improvement over ε_{Thorpe} with no exclusion metrics applied. A cut off value of 0.5 is taken forward into the rest of this analysis as the preferred variance exclusion threshold value.

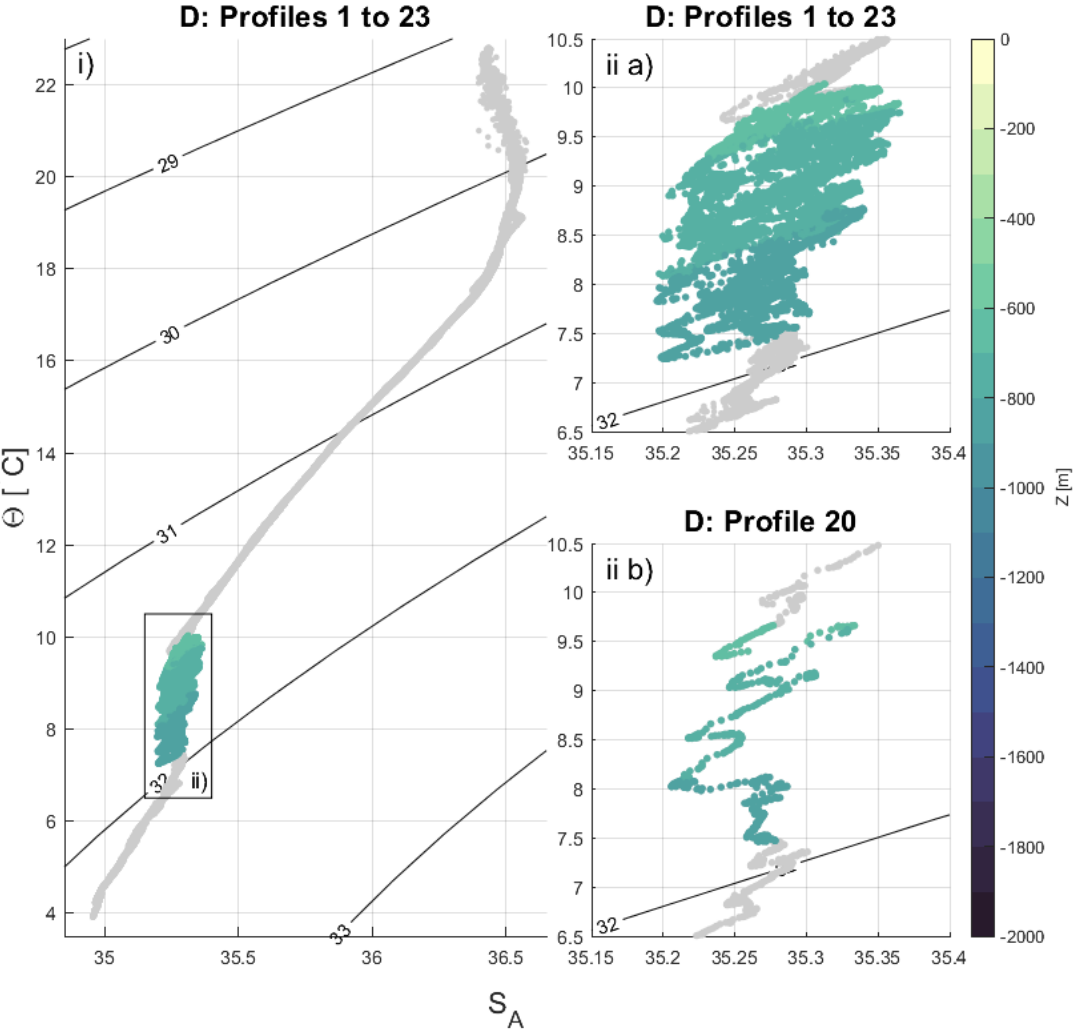

Figure 3.18: T/S diagram showing regions of data removed for the D subset. In each panel light grey indicates data that is kept and the data coloured by depth indicates the data removed i) every profile in full. iia) close up of the region marked ii in panel i. iib) a single profile as an example of the interleaving that is not visible when all profiles are plotted.

3.4.3 MANUAL DATA REMOVAL

Neither excluding bins using Tu, R_ρ or one of the variance threshold values removes all of the regions of high TKE dissipation estimates related to the mid depth, high salinity regions of ε_{Thorpe}. Especially the higher value regions seen in the D subset. Instead of trying to remove this region algorithmically, it was decided to use manual data removal. In the D subset the region of the water column between 650 m and 1000 m shows a consistent over estimation of ε_{Thorpe} when compared with ε_{shear}. This suggests that this is a subset feature and not just an event occurring in a

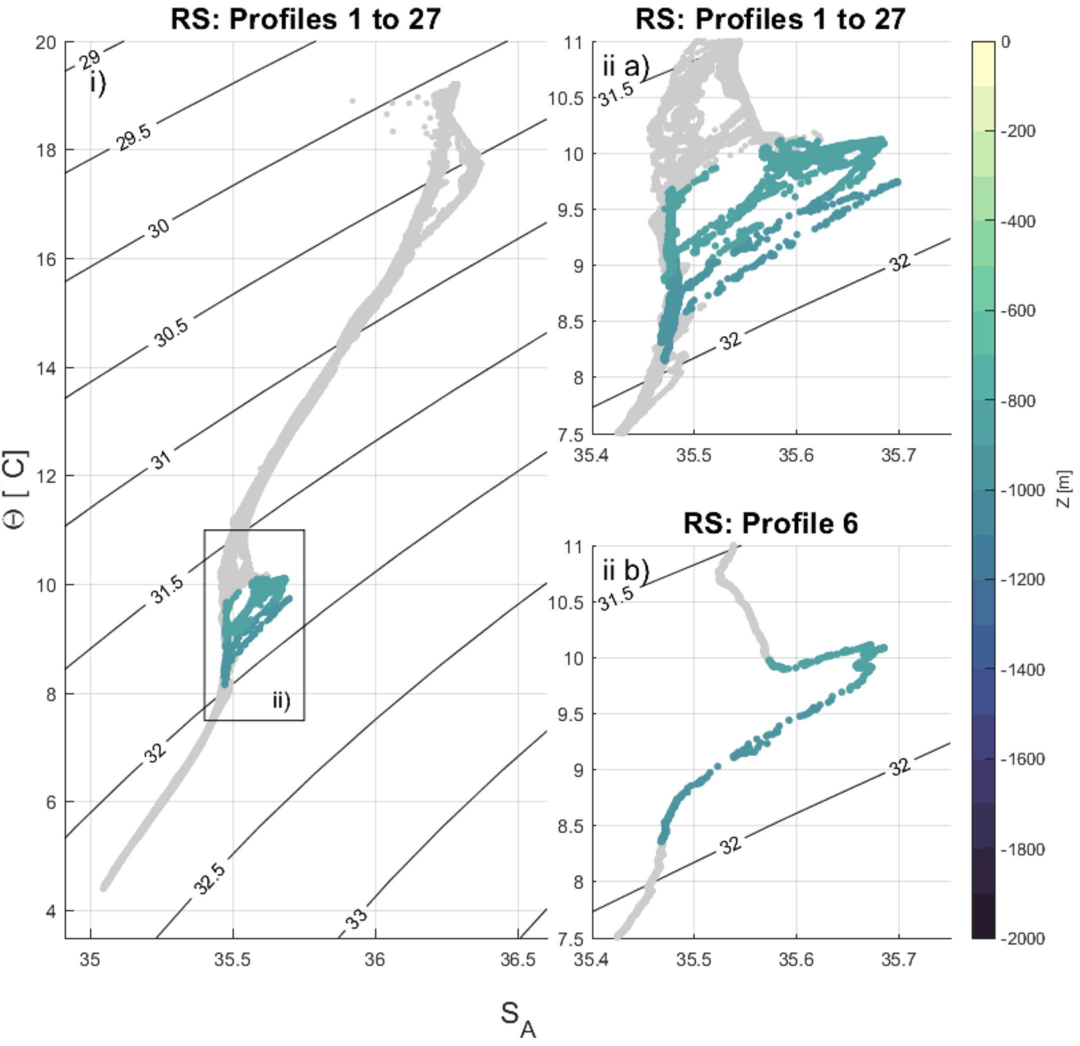

Figure 3.19: T/S diagram showing regions of data removed for the RS subset. In each panel light grey indicates data that is kept and the data coloured by depth indicates the data removed i) every profile in full. iia) close up of the region marked ii in panel i. iib) a single profile as an example of the interleaving that is not visible when all profiles are plotted.

given profile. The temperature salinity relationship in this region was more closely investigated. Figure 3.18 shows the T/S relationship for the D subset, highlighting the region of interest for quality control. It is clear that there is a large amount of interleaving of temperature and salinity present in this subset (Figure 3.18 ii b) with most of the variability seen in salinity. This interleaving is indicative of isopycnal processes, with very similar examples of such structures given in Figure 3 by Ferrari and Polzin (2005). To remove these regions each profile from the D subset was manually inspected for this patterning and any profiles that exhibited this

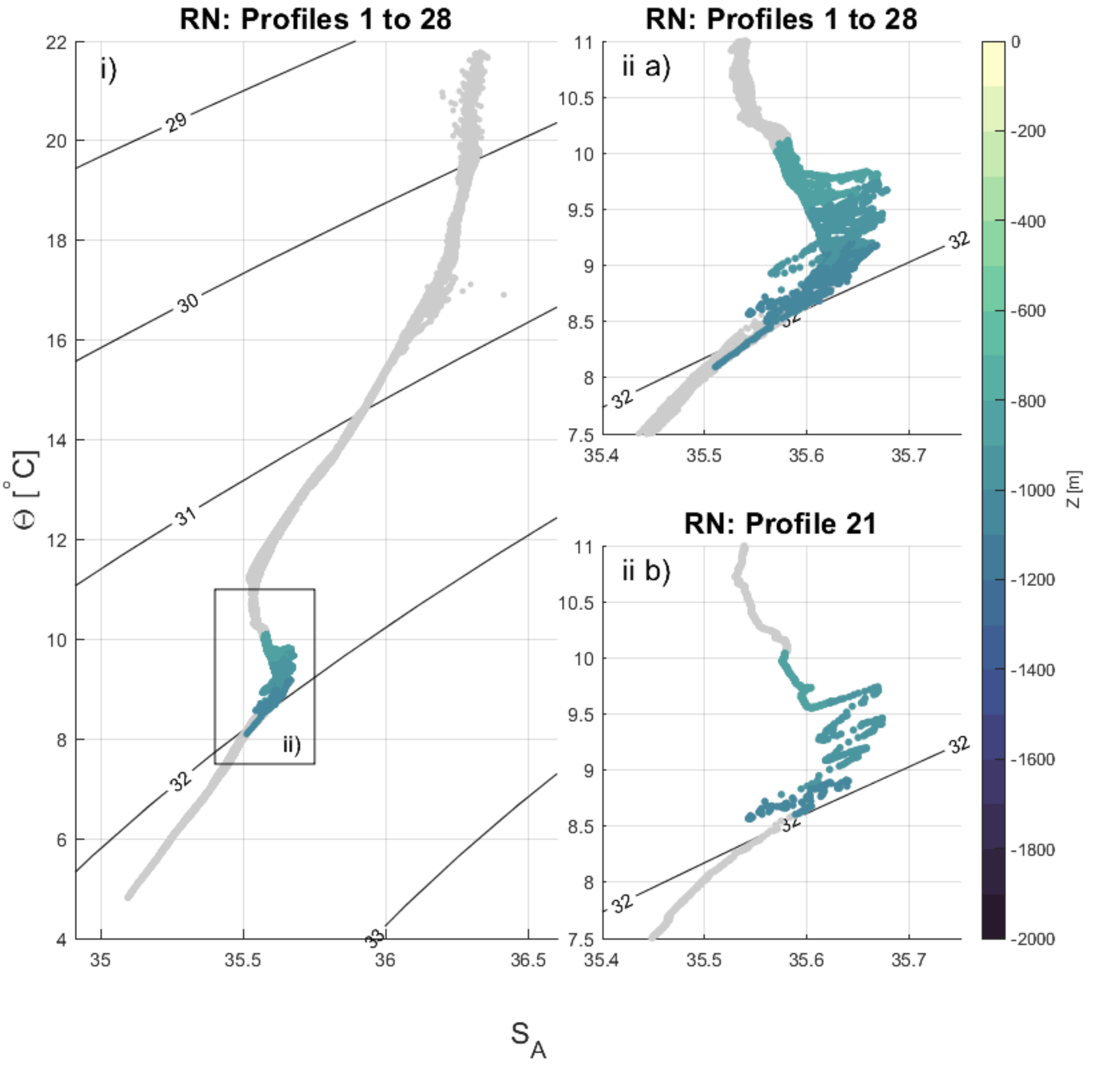

Figure 3.20: T/S diagram showing regions of data removed for the RN subset. In each panel light grey indicates data that is kept and the data coloured by depth indicates the data removed i) every profile in full. iia) a close up of the region marked ii in panel i. iib) a single profile as an example of the interleaving that is not visible when all profiles are plotted.

interleaving was marked for manual data removal. One depth range was picked to apply across the whole of each subset to make profiles comparable. For D the depth range removed was between 675 m and 900 m, a compromise to remove the poor bins but leaving as many good bins as possible. The process of manual cleaning was additionally applied to both RS and RN as both exhibit anomalous regions. Depth ranges of 800 m to 1000 m, profiles 1 to 19 (as these were the only profiles affected) were removed for RS (Figure 3.19) and 800 m to 1050 m removed for all profiles in RN (Figure 3.20). Visual inspection of data that is not suitable has been implemented elsewhere before (Mater et al., 2015). This process however, is normally done before processing temperature or density data through the Thorpe Scaling steps. Here it has been implemented post estimation of TKE dissipation rates but will be done before processing with future datasets.

The outcome of combining manual data removal and exclusion of bins through filtering can be seen as time means presented in Figure 3.21 for the Tu and R_ρ threshold values and Figure 3.22 for the variance threshold values. This processing step has a minimal impact on the RS subset, but does improve the closeness of the ε_{Thorpe} to the ε_{shear} below 800 m, which was largely impacted by a small number of points in the first 10 profiles. In the RN and D subsets the change is more marked as a band of bins is removed that covers all profiles. In the D subset it is clear that very few low value points are removed during this process and the manual removal processing on the D subset does not improve the deeper values which are still very noisy. In the RN subset more data bins were removed from the excluded region than were likely to contaminated by salinity intrusions, especially in the upper portion of profiles 20 to 28. Manual data removal does not impact the slightly high region seen in profile 26 which skews the time mean at around 1100 m.

3.5 DISCUSSION

With a variety of quality control methods investigated, including algorithmic and manual, a final decision was required on the most appropriate method to use in the idealised work flow presented in Chapter 2. Discussed below are the similarities, differences and benefits of the different quality control methods which were used to determine the best to use. The outcomes of ε_{Thorpe} from high resolution temperature data were also compared to 0.5 m binned ε_{shear} presented by Vic et al. (2018) to determine the viability of Thorpe scaling high resolution temperature data to provide solid estimates of TKE dissipation rates.

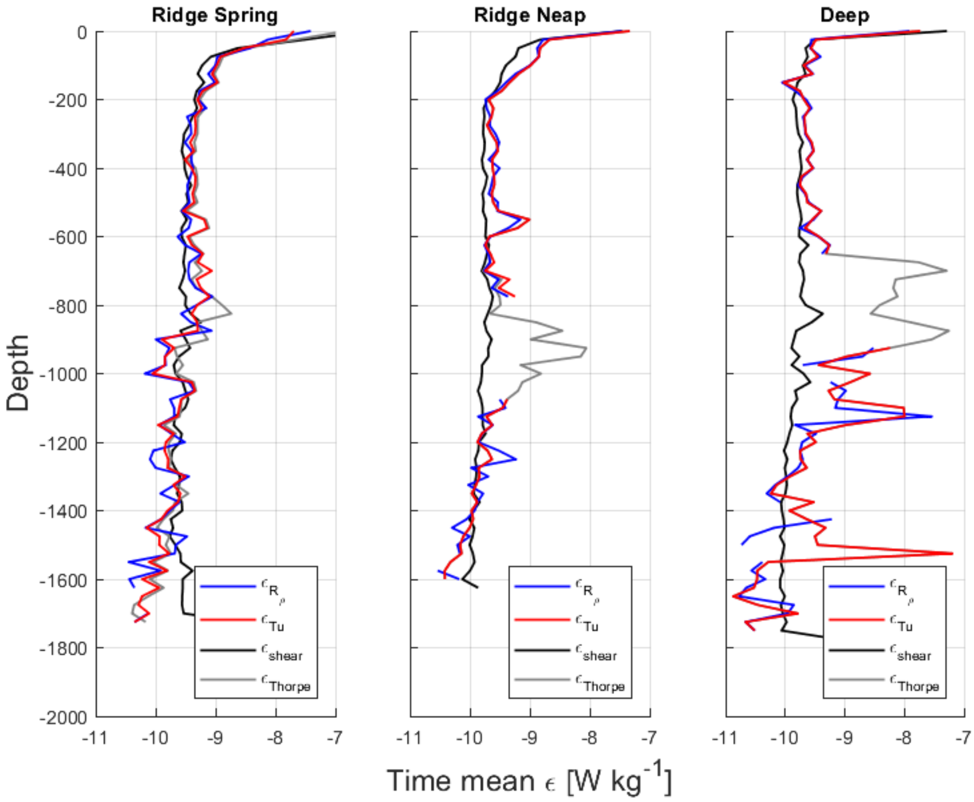

Figure 3.21: Time averaged TKE dissipation rates using Tu and R_ρ as filtering metrics together with manual data removal against unfiltered TKE dissipation estimates from Thorpe Scaling and shear, for each of the three datasets, RS, RN, D.

3.5.1 QUALITY CONTROL FINDINGS

MANUAL DATA REMOVAL

The concept of manual data removal is not novel, both in cleaning data before processing, as by Mater et al. (2015), or in the detection of certain oceanographic features once processing is complete, for example identifying thermohaline staircases by Schmitt et al. (1987). Even in the case of an automated system for cleaning data there is typically the ability for manual removal of any data points that an algorithm may miss (Queste, 2013). In the case of the work presented here, examining the T/S relationship prior to attempting to algorithmically remove data would have provided clear regions where our methodology was likely to fail before even being processed. The largest draw back to using temperature (either high resolution or otherwise) to estimate ε_{Thorpe} is the influence of salinity on the water column that is being studied (Mater et al., 2015).

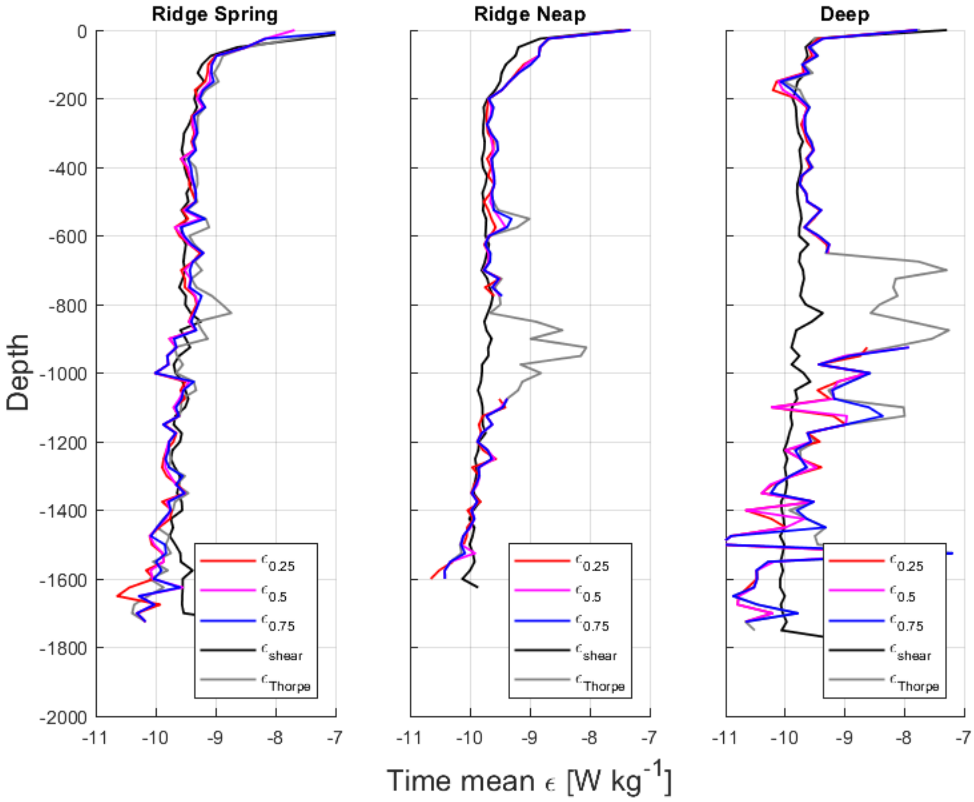

Figure 3.22: Time averaged TKE dissipation rates using variance ratio cut offs of 0.25, 0.5 and 0.75 as filtering metrics together with manual data removal against unfiltered TKE dissipation estimates from Thorpe Scaling and shear, for each of the three datasets, RS, RN, D.

However, the approach taken here was an attempt to algorithmically develop a simple post processing filtering method for dealing with regions of high ε_{Thorpe} that were compensated by salinity. This algorithmic product could aid the decision process of which areas of the water column are suitable for Thorpe scaling temperature for other studies. The largest benefit that this would give would be to apply the same region criteria to multiple datasets. An issue that was encountered when Mater et al. (2015) stated that they used manual data removal was that they indicated the regions for manual removal but supplied no information to the decision making process behind the removal.

3.5.2 ALGORITHMIC QUALITY CONTROL

The core of the work presented in this chapter was to investigate and develop (if possible) an algorithmic set of processes to remove data bins where the values of

ε_{Thorpe} within those bins were likely to be a poor reflection of reality. The studies mentioned earlier in the chapter (Gargett and Garner (2008); Mater et al. (2015); Ijichi and Hibiya (2018)) plus others including Hall et al. (2011) and Galbrath and Kelley (1995) focus on removing overturns or overturning regions that are false before estimating ε_{Thorpe}. Methods included excluding overturns based on R_ρ (Mater et al., 2015), run-length filtering (Galbrath and Kelley (1995); Howatt et al. (2021) [for removing overturning regions below the instrument noise floor, see Appendix A]) or visual inspection of T/S space at the point of an overturn (Gargett and Garner, 2008), a time consuming process on standard resolution CTD which would take considerably longer on high resolution data.

In Section 2.2.3 the methodology accounts for small overturning regions from noise (instrument or background) that would be removed by run-length filtering. Howatt et al. (2021) also removes noise with scales < 2 m, which if applied to high resolution data (applied to CTD data by Howatt et al. (2021)) would remove the benefit of applying Thorpe scaling to the high resolution data. Ijichi and Hibiya (2018) combines overturning regions less than 5 m in length within 1 m of other overturning regions into a single region, which does not reduce the minimum resolution of overturns used, but considers a high number of small overturns in close proximity to be a generated by a single event. In this thesis a modified version of this based on work shared by Carter (2020) is used (2 m rather than 5 m). The overturn by overturn automated removal used by Ijichi and Hibiya (2018) (excluding overturns where $-1/2 \leq R_\rho \leq 2$) worked poorly on this dataset, removing $\sim 90\%$ of overturns. This was especially interesting when the time means of each subset (Figures 3.21 and 3.22) of ε_{Thorpe} and ε_{shear} were compared which show broadly the same structure and values (also seen in profile by profile comparisons in this chapter), suggesting that the methods used by Ijichi and Hibiya (2018) were excluding a considerable amount of true overturns. Instead of attempting to remove individual overturns, focus was turned to removing bins that did not match a certain criteria. This provided two benefits to the methodology. The first that smaller overturning regions are not excluded, helping to reduce the potential overestimation of ε_{Thorpe} (Mater et al. (2015); Howatt et al. (2021); Sheehan et al. (2021)). The second was improved computational time due to a smaller number of regions needing to be examined per profile. Three difference methods were investigated to exclude bins, R_ρ, Tu and the

$r_{normalised}$ variance ratio. Of the three R_ρ performed the poorest, removing up to 40% of bins whilst providing minimum improvement to the fit between ε_{Thorpe} and ε_{shear}. Tu also proved to be of limited value by not removing enough bins (a maximum of 7%) to improve the fit between ε_{Thorpe} and ε_{shear}. The variance ratio was the developed as an alternative to R_ρ and Tu. Of the three threshold values investigated in depth in the variance method a value of 0.5 was the best compromise between the 3 subsets (RS, RN and D), fulfilling the aim of having a unified threshold value that could be used across all the subsets presented here, and any other data that the methods were applied to.

Based on the findings in this chapter the final set of quality control measures proposed for future datasets was to apply manual quality control based on the T/S regime of a given depth, removing potentially contaminated bins before Thorpe Scaling and using a value of $r_{normalised} = 0.5$ to exclude any bins that had potential salinity contamination. Values of ε_{Thorpe} using these quality control methods are compared with ε_{shear} based on the results of Vic et al. (2018) below.

3.5.3 COMPARISON OF FINAL ε_{Thorpe} WITH ε_{shear}

One of the main goals of the work in this chapter was to compare estimates of ε_{Thorpe} with published values of ε_{shear}. The ε_{shear} dataset in question was published by Vic et al. (2018). A section of research carried out by Vic et al. (2018) examined the differences between the spring and neap periods of the tidal cycle. Due to the marked differences shown in Vic et al. (2018) this was a focus of data comparison in this chapter. Values of ε_{Thorpe} estimated in this chapter are compared to the time means of ε_{shear} for both spring and neap periods of the tidal cycle. This was used to determine if ε_{Thorpe} compared well with ε_{shear} and also if ε_{Thorpe} could be used to distinguish between the two tidal periods. The final findings of this chapter are presented in Figure 3.23 and 3.24. The upper panels of Figure 3.23 are a reproduction of Figure 10 by Vic et al. (2018).

First we look at the ability of ε_{Thorpe} to provide a distinction between spring and neap tidal periods. In the upper 800 m of the water column the time mean of $\varepsilon_{Thorpe_{neap}}$ is less than that of $\varepsilon_{Thorpe_{spring}}$, with both time means sitting within a single standard deviation of the other; a trend that is also seen in ε_{shear}. Between

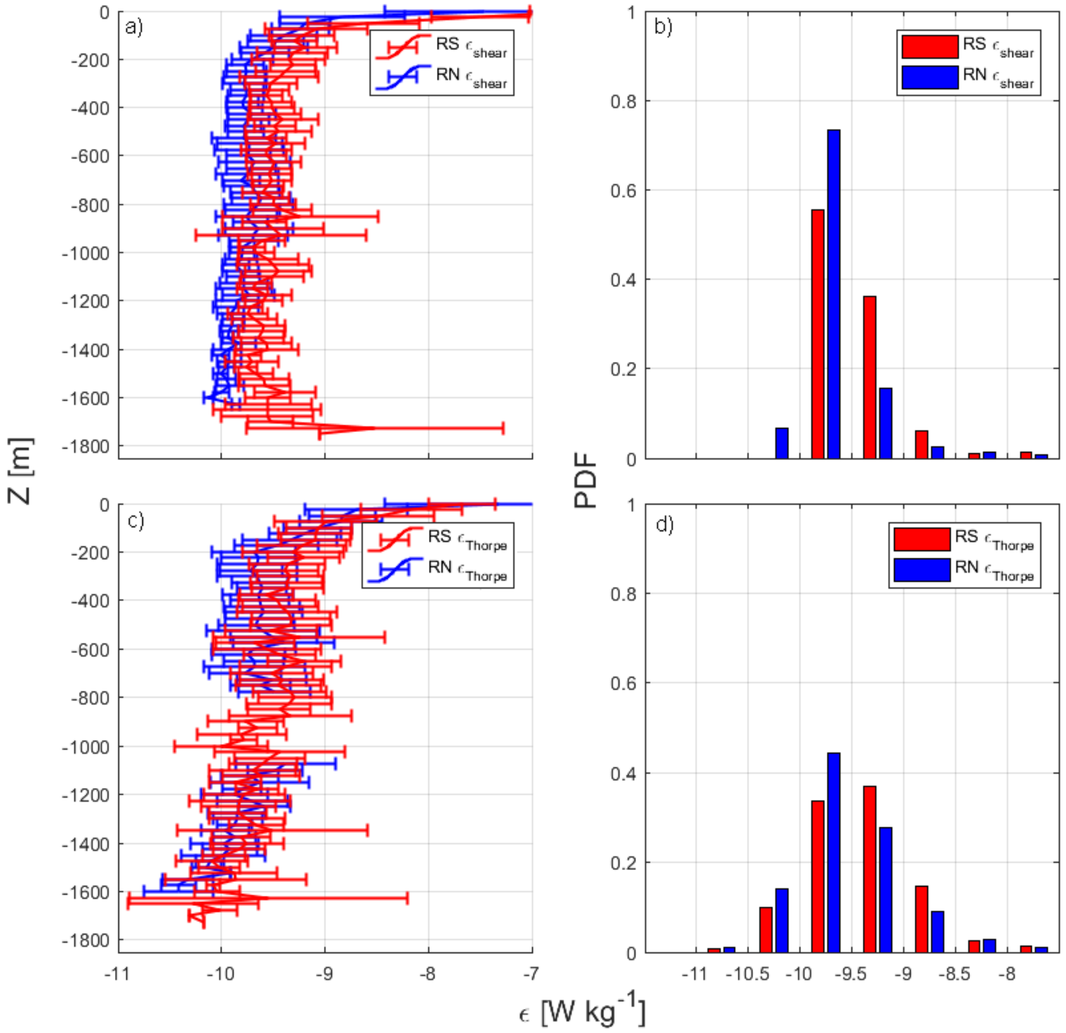

Figure 3.23: Ridge Spring and Ridge Neap datasets as both time mean and distribution of TKE dissipation estimates in 25 m bins as a probability density function (PDF). a) & b) represent a reproduction of Figure 10 from Vic et al. (2018) using ε_{shear}. c) & d) represent the same plot but created using ε_{Thorpe}. a) & c) show time mean ε with standard deviation. b) & d) show the PDF distribution of all bins

800 m and 1050 m it is not possible to determine the difference due to the lack of data from $\varepsilon_{Thorpe_{neap}}$. Below 1050 m the difference between $\varepsilon_{Thorpe_{neap}}$ and $\varepsilon_{Thorpe_{spring}}$ is more difficult to determine, although it is likely to be less than that seen in ε_{shear} where the difference between spring and neap increases with the standard deviations decreasing in size, especially below 1400 m. A noticeable difference between ε_{Thorpe} and ε_{shear} from both spring and neap at all depths is the larger standard deviation seen in ε_{Thorpe} values than in ε_{shear}. As overturns or overturning regions are more sporadic in nature values of ε_{Thorpe} will also have an increased range, dependent

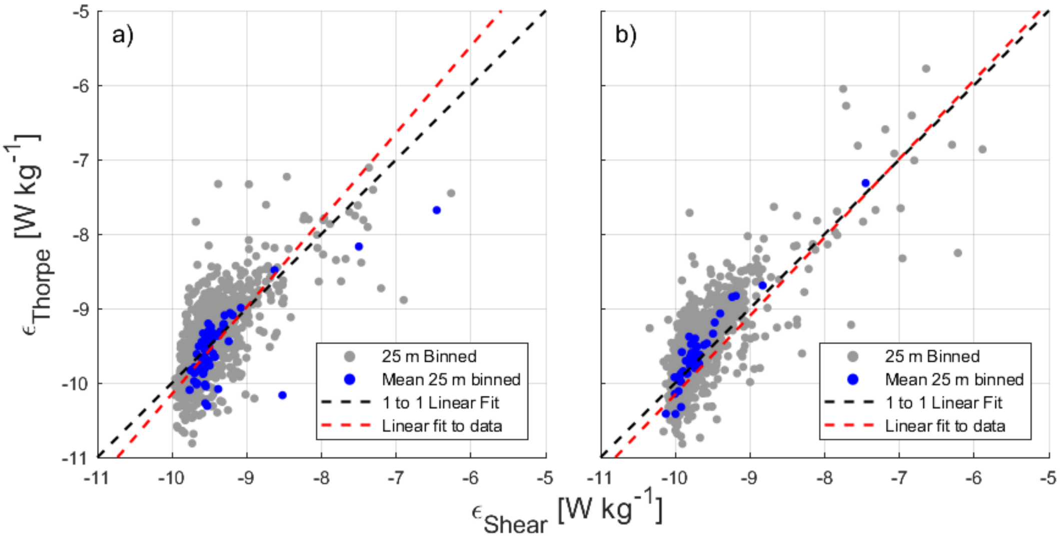

Figure 3.24: Values of ε_{shear} and ε_{Thorpe} compared with a 1 to 1 linear fit and linear regression. a) shows values for Ridge Spring. b) values from Ridge Neap

on the overturn size (Thorpe, 1977). This leads to 25 m bins of ε_{Thorpe} showing greater variability, which feeds through the to time mean standard deviations. Using the probability density function of the ε_{Thorpe} and ε_{shear} it can be seen that both share a similar structure. ε_{Thorpe} shows a more traditional bell shaped curve for both spring and neap extending from the lower end $(O)10^{-11}$ W kg^{-1} to $(O)10^{-8}$ W kg^{-1} with values more evenly spaced across this range than seen in the range of values of ε_{shear} that peak at $(O)10^{-10}$ W kg^{-1} and reduce in number drastically below that point. $\varepsilon_{shear_{spring}}$ shows no values of $(O)10^{-11}$ W kg^{-1}. When looking at the difference between spring and neap the difference of ε_{shear} between 1×10^{-10} W kg^{-1} to 5×10^{-10} W kg^{-1} is greater than the equivalent difference seen in ε_{Thorpe}. The difference between $\varepsilon_{shear_{neap}}$ and $\varepsilon_{shear_{spring}}$ is 0.18 in the -10 to -9.5 bracket and 0.2 in the -9.5 to -9 bracket ($\varepsilon_{shear_{neap}}$ being greater in the first and $\varepsilon_{shear_{spring}}$ the second). With ε_{Thorpe} the equivalent differences in the same brackets are both 0.06, three times less than that of ε_{shear}, however, they do show the same pattern with $\varepsilon_{Thorpe_{neap}}$ being greater in the first bracket and $\varepsilon_{Thorpe_{spring}}$ being greater in the second. From these results although the difference between spring and neap in the ε_{Thorpe} estimates is smaller it is concluded that is possible to determine the difference in the phase of the tidal cycle is possible using Thorpe scaled ε estimates.

Secondly, do the estimates of ε_{Thorpe} provide a good fit to those from ε_{shear}. At higher TKE dissipation rates ($(O)10^{-9}$ W kg^{-1} or higher), ε_{Thorpe} from both spring and neap show a greater number of bins than the equivalent range in ε_{shear}. The same is also seen in values of ε below $(O)10^{-10}$ W kg^{-1}. Where TKE dissipation rate estimates are of $(O)10^{-10}$ W kg^{-1}, ε_{shear} shows a higher concentration of bins in this range than ε_{Thorpe} does (up to 70% greater for $\varepsilon_{shear_{neap}}$ compared with $\varepsilon_{Thorpe_{neap}}$, the largest difference).

When looking at the time mean above 800 m it can be seen that both $\varepsilon_{Thorpe_{spring}}$ and $\varepsilon_{Thorpe_{neap}}$ are on average $1-2\times10^{-10}$ W kg^{-1} greater compared with the same tidal phases from ε_{shear}. In the upper 800 m both ε_{Thorpe} and ε_{shear} show a similar structure. A high mixing surface layer with values of ε up to and exceeding $(O)10^{-7}$ W kg^{-1} from both, dropping to $(O)10^{-10}$ W kg^{-1} below 100 m. Below 1050 m ε_{shear} stays fairly consistent, with $\varepsilon_{shear_{spring}}$ tending upwards towards $(O)10^{-9}$ W kg^{-1} from depths of 1400 m and deeper. This is in contrast to ε_{Thorpe} where below 1300 m values of ε decrease to values of $(O)10^{-11}$ W kg^{-1}, a region showing the greatest difference between the profiles of ε_{Thorpe} and ε_{shear}.

Figure 3.24 looks at the spread of results between $\varepsilon_{shear}$and ε_{Thorpe}. For the Ridge Spring dataset we see a linear regression showing slightly larger estimates of ε_{Thorpe}at high values and an underestimation of $\varepsilon_{Thorpe}((O)10^{-10}$ W kg$^{-1})$ when compared with $\varepsilon_{shear}((O)10^{-9}$ W kg$^{-1})$ at lower values. The underestimation here may be related to the noise floor of the shear probes. The same structure can be seen in the Ridge Neap dataset, although the overestimation at higher values here is lower than that seen in the Ridge spring dataset.

Even given these differences, with the broad structure of both the time mean and the PDF of values of ε_{Thorpe} being close to those of ε_{shear} it was decided that ε_{Thorpe} values were good enough to use the methodology presented in this and the previous chapter on further datasets without requiring supporting shear data, with the understanding that there may be some over or underestimation compared to if further work was carried out using only shear data.

3.5.4 SUMMARY OF AIMS

At the beginning of the chapter the following questions where proposed to be investigated:

- What considerations are required when developing a methodology for Thorpe

Scaling high resolution temperature data?

- When using a dataset with both high resolution shear and temperature, does Thorpe scaling high resolution temperature give comparable values of TKE dissipation rate estimates to those estimated with shear data?

In this summary answers to the questions are provided.

3.5.5 CONSIDERATIONS FOR THORPE SCALING HIGH RESOLUTION TEMPERATURE DATA

A number of different automated quality control methods were investigated to determine the most suitable to apply to the data used in this chapter (and future chapters) based on the view that Thorpe scaling temperature (of any resolution) can be a poor proxy for density due to the potential influence of salinity without any considerations taken into account. Of the three methods investigated the variance ratio method provided the most improvement of the data output for the least data lost to quality control.

The second investigation was into the need for manual quality control on the dataset. It was shown that manual quality control was required on this dataset, so that regions of the T/S profile that will cause issues with the Thorpe scale algorithms were identified. It was therefore determined that combined algorithmic and manual quality control will be used on further datasets used in this thesis.

3.5.6 ARE TKE DISSIPATION ESTIMATES FROM THORPE SCALING COMPARABLE WITH THOSE FROM SHEAR

The difference between ε_{Thorpe} and ε_{shear} was investigated, both to see if ε_{Thorpe} compared well with ε_{shear} and if ε_{Thorpe} was capable of identifying the difference in tidal cycles seen in ε_{shear}. Values of ε_{Thorpe} were higher overall when compared with ε_{shear} by up to $1-2\times10^{-10}$ W kg^{-1}. The exception to this was below 1400 m where ε_{Thorpe} showed lower values than those seen from ε_{shear}. When looking at the difference between values of ε between the spring and neap ε_{Thorpe} showed a similar pattern to that seen from ε_{shear} although the difference between the spring and neap was less in ε_{Thorpe} than in ε_{shear}. With the ability to see a difference across a tidal cycle and the broad pattern across the water column ε_{Thorpe} does a respectable job of replicating the values of ε_{shear}. However, it has the potential to overestimate ε compared to that estimated from shear data, a known issue with ε_{Thorpe} (Mater et al. (2015); Howatt et al. (2021); Sheehan et al. (2021)).

In the next chapter the methods presented in Chapter 2 and developed here are applied to a short Seaglider set to determine any glider specific issues that could arise and to investigate the ability of the Seaglider as a suitable platform for analysing values of ε_{Thorpe} from a non-vertical profiling platform.

4

MASSMO4: TESTING METHODS ON SEAGLIDER DATA

4.1 INTRODUCTION

In the previous chapter it was shown that the Thorpe Scale methodology gave good estimates of TKE dissipation when compared to estimates derived from shear probes mounted on the same VMP across a number of locations. The next step in developing this methodology is applying those algorithms to a glider fast thermistor dataset. In this chapter we set out to investigate the following questions:

- What glider specific issues might there be when using Thorpe Scaling for fast thermistor data?
- Can this methodology provide comparable estimates of TKE dissipation when compared to previous studies in the geographical region?

To accomplish these aims the developed methods will be applied to a dataset collected on the flank of the Wyville Thomson Ridge (WTR) in the Faroe Shetland Channel (FSC) as part of the 4th Marine Autonomous Systems in Support of Marine Observations (MASSMO4). This dataset was used due to its length, a large amount of supporting literature from the region and that the region itself is scientifically

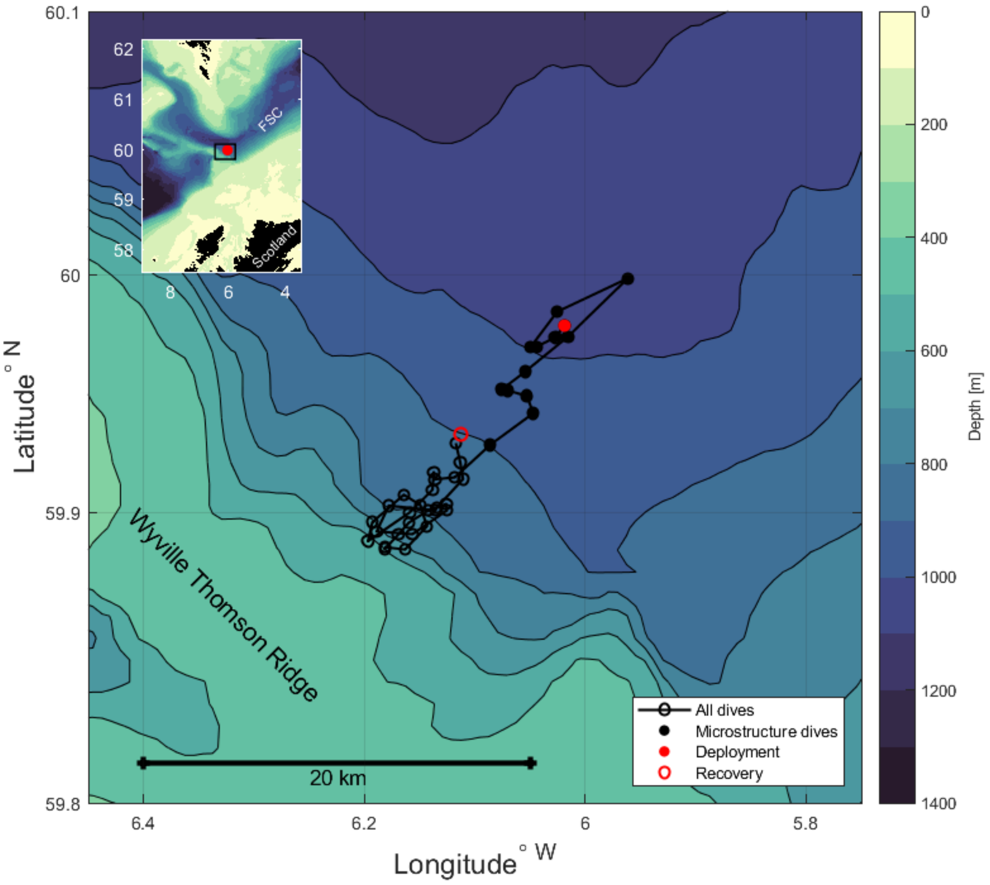

Figure 4.1: Locations of dive starts during the MASSMO4 deployment. Inset map shows the dive locations in relation to the wider area.

interesting. A description of the region and MASSMO4 will be presented, followed by some important mission specific data handling. The core findings are then presented with a discussion concluding the chapter and answering the questions above.

4.1.1 MASSMO4

In June 2017 Seaglider SG613 was deployed for 3 days as one of 11 autonomous marine assets part of an annual series of ocean going robotic trials co-ordinated by the National Oceanography Centre (NOC). This project brought together 16 different organisations representing research institutions, industry and the UK government (National Oceanography Centre, 2018). The aim of the trials was to showcase how large fleets of autonomous marine robots perform individually and how they work together to continue to explore the UK shelf seas from a biological, chemical and

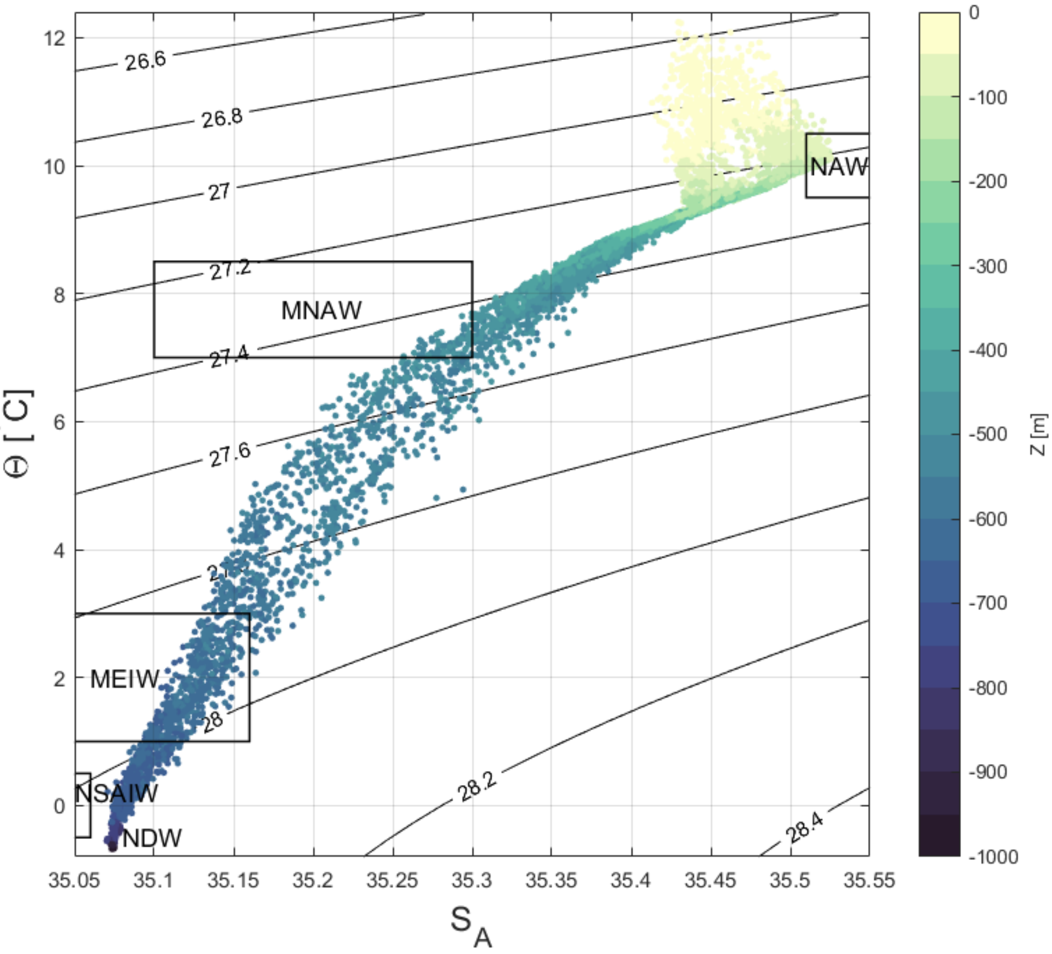

Figure 4.2: MASSMO4 T/S diagram with z plotted as the fill colour. Water mass regions highlighted in Table 4.1 represented by black boxes with associated abbreviations

physical angle. The data presented in this chapter was collected during SG613's deployment.

4.1.2 THE FAROE SHETLAND CHANNEL AND THE WYVILLE THOMSON RIDGE

The Faroe Shetland Channel (FSC) is situated to the northwest of the Shetland Isles (see inset, Figure 4.1). It is a bathymetric feature (1900 m at its deepest point) that separates the Shetland and Faroe Shelves (both ~200 m deep) and is one of three openings along the Scotland-Greenland Ridge (GSR) (Sherwin et al., 2006) allowing deep water formed in the Nordic Seas to pass to the North Atlantic (Hansen and Østerhus, 2000; Borenäs and Lundberg, 2004). The FSC has been a site of near

Full Name	Acronym	Θ range	S_A range
Modified North Atlantic Water	MNAW	$7.0 \rightarrow 8.5$°C	$35.10 \rightarrow 35.30$
North Atlantic Water	NAW	$9.5 \rightarrow 10.5$°C	$35.51 \rightarrow 35.61$
Modified East Icelandic Water	MEIW	$1.0 \rightarrow 3.0$°C	$34.86 \rightarrow 35.06$
Norwegian Sea Arctic Intermediate Water	NSAIW	$-0.5 \rightarrow 0.5$°C	$35.03 \rightarrow 35.06$
Norwegian Sea Deep Water	NSDW	< -0.5°C	35.07

Table 4.1: The main water masses found and exchanged across the Greenland-Scotland Ridge, associated conservative temperature, and absolute salinity. Based on Hansen and Østerhus (2000)

continuous study since 1893 (Turrell et al., 1999). At the southern end of the FSC is the Wyville Thomson Ridge (WTR), a sill with a depth of between 400 and 600 m (Sherwin et al., 2006) which partially blocks the southern end of the channel (Sherwin et al., 1999; Hall et al., 2011). Due to the role it plays in exchange of water between the North Atlantic and the Nordic Seas, any turbulent mixing in the FSC has the possibility of modifying $\Theta - S$ properties and potentially affecting large scale ocean circulation. A list of all water masses found in the region can be found in Table 4.1 and highlighted in T/S in Figure 4.2. A break down of the hydrographic properties of the study region (black box inset, Figure 4.1) are seen in Figure 4.3 which shows the time mean of all 38 glider dives.

THE FAROE SHETLAND CHANNEL

The FSC forms a deep trough (> 1500 m depth) that runs from the Nordic seas between the Scotland and Faroe shelves before turning north west once it has passed the Faroe Isles and joins the Faroe Bank Channel (FBC) that separates the Faroe plateau from the Faroe Bank (another section of the GSR with a depth of 850 m) (Sherwin et al., 2006). Water mass circulation in the FSC is complex (Gallego et al. (2018), Figure 4.4) with both shallow water masses travelling northwards to the Nordic Seas and deeper water masses originating in the Nordic Seas travelling southwards through the FSC and FBC (Sherwin et al., 1999). In the upper 500 m warm, saline water flows northward over the WTR and is dominated by North Atlantic Water (NAW). The remainder of the surface 500 m water is composed of cooler fresher Modified North Atlantic Water (MNAW) (Hansen and Østerhus, 2000). These water masses flow up the FSC on the Shetland side of the channel. Below 500 m (the depth of the main pycnocline) water masses are comprised of colder, less saline waters of

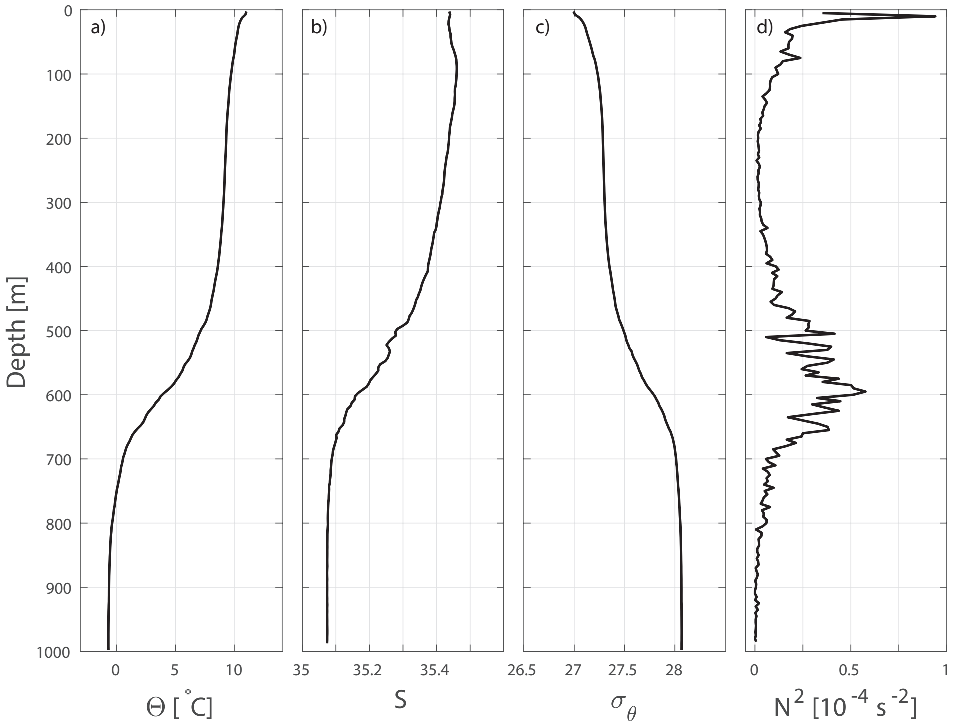

Figure 4.3: Time mean hydrographic data from MASSMO4 deployment a) conservative temperature b) absolute salinity c) potential density d) N^2.

the Nordic Seas. Modified East Icelandic Water (MEIW) originates east of Iceland and recirculates within the FSC joining the overflow through the FBC. The other intermediate water mass is the Norwegian Sea Arctic Intermediate Water (NSAIW) which, along with the deep water mass, the Norwegian Sea Deep Water (NSDW), enter the FSC from the Norwegian Sea and overflow through the FBC (Gallego et al., 2018). Occasionally the deeper water masses overspill the WTR into the Rockall Trough (Sherwin et al., 2008).

The FSC is a region of known high mesoscale variability (Sherwin et al., 1999) with surface meanders along the front between MNAW and NAW up to 80 km in length with velocities of up to 0.9 m s^{-1}, that mix the two water masses before they enter the Nordic Seas. These meanders can be observed in satellite data (SST and altimetry), drifter trajectories and measurements of water velocity, temperature and salinity (Gallego et al., 2018). At depth, mixing and interactions of water masses is dominated by internal wave interactions (internal tides) and enhanced by critical reflections of these internal tides off the sloping topography (Hall et al., 2011).

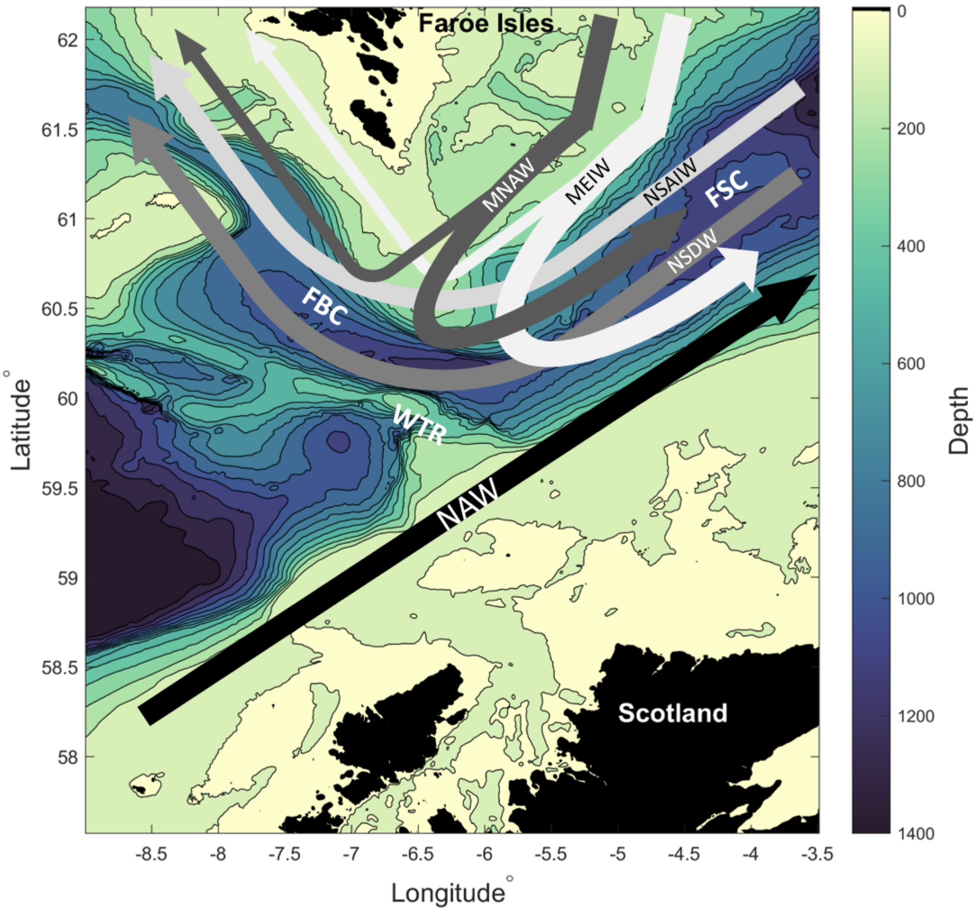

Figure 4.4: Diagram summarisig the circulation of the five main water masses within the FSC. Arrows indicate direction of mean transports. Water mass properties and names given in Table 4.1. Modified from Gallego et al. (2018).

THE WYVILLE THOMSON RIDGE

The location of the WTR at the southern most end of the FSC is considered to be a location of internal tide generation (Gallego et al., 2018; Hall et al., 2011; Sherwin, 1991). The location of the ridge obstructs the major axis of the North Atlantic barotropic tidal Kelvin wave travelling north (Gallego et al., 2018) resulting in vertical displacement of water on the Northern flank of the WTR, features that can be seen in panel b and c of Figure 4.5 from year day 153.5 onward. These displacements are generated with an M_2 tidal frequency and are centred around the deep pycnocline (~550 m). The existence of the large vertical displacements was first described by Knudsen (1911), from a continuous 67 hour period of observations. Later Sherwin (1991) and (Larsen et al., 2000) both observed the same feature. Larsen et al. (2000) observed a 37 m amplitude displacement in the main pycnocline associated with

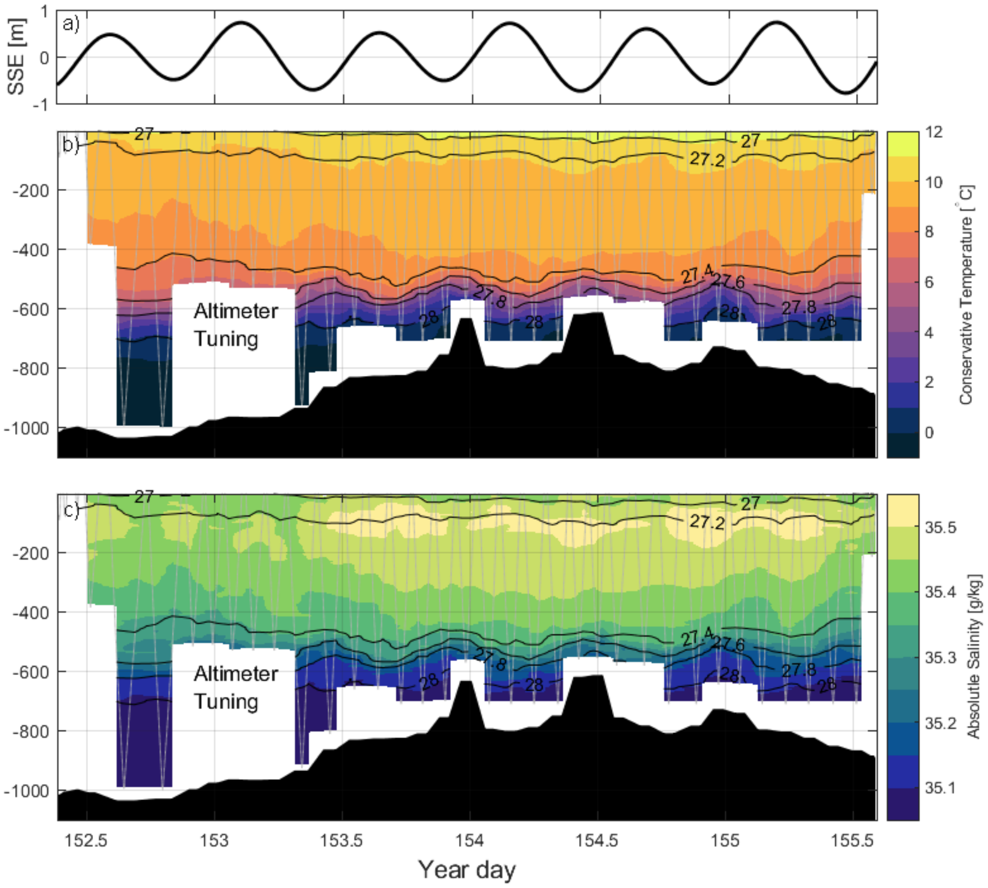

Figure 4.5: Hydrographic Data from MASSMO4 deployment. a) Sea Surface Elevation from the TOPEX European Shelf Sea model b) Conservative temperature (colour) overlaid potential density (black contours: 0.05 kgm^3 and overlaid binned glider data (grey dots) c) Absolute salinity(colour) overlaid potential density (black contours: 0.05 kgm^3 and overlaid binned glider data (grey dots).

the M_2 internal tide. Similar amplitudes of isopycnal displacement can be seen in Figure 4.5. Observations from microstructure profilers show patchy elevated mixing in the deep thermocline from breaking internal waves (Hosegood et al., 2005). A mixture of moored and profiling ADCP/CTD systems on the eastern flank of the FSC show semidiurnal internal tides and non-linear wave trains at the sea bed (Hall et al., 2011). It is unclear how far these internal waves propagate up the channel, especially as displacements to the water properties are mainly observed at the southern end of the FSC towards the WTR.

4.2 MASSMO4 DATA

4.2.1 MASSMO4 DATA COLLECTION

Seaglider SG613 was deployed from the *MRV Alliance* for 3 days from the 2 June 2017 to the 5 June 2017 North of the WTR. Deployment and recovery locations can be seen in Figure 4.1. During the deployment the Seaglider completed 78 profiles (39 complete dives). The first 25 of these profiles provided usable microstructure data (the focus of this chapter) with the other 53 profiles making up a 40 hour virtual mooring (Rudnick et al., 2004; Hall et al., 2019). The Seaglider was fitted with a standard Sea-Bird electronics conductivity-temperature (CT) sail and an RSI MicroPod system consisting of a single shear probe and a single FP07 fast thermistor (see Chapter 1 for further details on the glider set up). The Seaglider data was processed as described in Hall et al. (2019). The microstructure data was processed as described in Chapter 2. Mission specific quality control is discussed in the next section. For this chapter, profiles that are shorter than 100m are excluded from analysis as well as the upper 25 m of the water column; preventing surfaces biased by excess or highly variable values.

4.2.2 GLIDER VS. PROFILER

All the results in Chapter 3 came from a VMP-2000 (Vic et al., 2018), the standard method of taking measurements of temperature and shear to estimate turbulent mixing parameters. A distinct and important difference between a free fall profiler and a seaglider is the difference in the motion of the platform through the water column. A seaglider, although collecting most of the same raw variables, travels through the water along a slanted path, not a vertical one. The nature of the glider path used for measuring overturns was investigated by Thorpe (2012). A glider will travel through the water between 0.2 - 1 m s^{-1} with an angle (ϕ) of between 14° and 45° (Eriksen, 2009). The impact of glider flight on estimates of L_T must then be related to ϕ and the shape of the overturns (Thorpe, 2012). The work done by Thorpe (2012) shows that the error involved when calculating ε_{Thorpe} from the vertical scale of a Kelvin-Helmotz billow is at its greatest when the aspect ratio of the billow, $height_{billow}/length_{billow}$, is large and the gliders angle through the water,

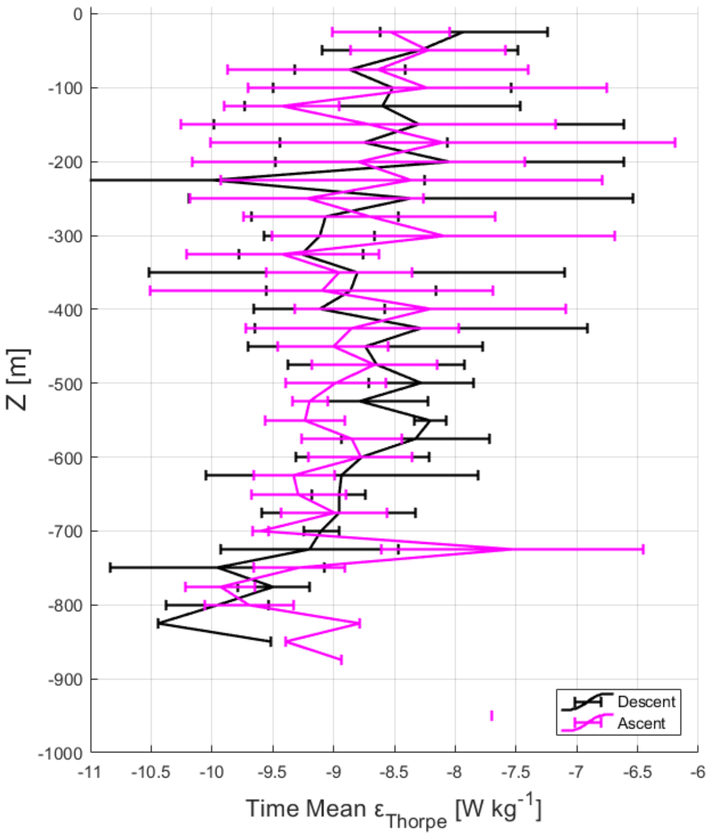

Figure 4.6: Time mean ε_{Thorpe} for up casts and down casts from glider data.

ϕ, is small. However, a glider is unlikely to underestimate ε_{Thorpe} by more than a factor of 2. Due to the range of potential estimates of ε_{Thorpe} and a standard level of uncertainty from estimating ε from shear probes Thorpe (2012) considers this potential underestimate insignificant. Glider path through the water is taken into account when determining minimum vertical resolution. Due to the length of time taken (typically 4 hours for a 1000 m dive) and the short distances between the start and end locations of dives $(O)1$ km, glider profiles are analysed as if they were vertical profiles after the initial quality control stages. It is worth noting that a free fall profiler may experience small fluctuations to its descent angle or its horizontal position in space due to internal wave motion. As long as the vertical velocity of the profiler through the water column is greater than these motions the profiler can still be considered to be travelling vertically through the water column (Thorpe, 2012) rather than on a slanted path.

A second important distinction between a glider dive and that of a vertical profiler is that a glider collects data during both down cast and up cast, compared to a profiler that collects data only in one direction (some profilers can be set to record whilst rising but still do not collect useful microstructure data in both directions). To check that direction does not cause a bias in estimates of ε_{Thrope} profiles of ε_{Thorpe} were divided into subsets, one for down casts and a second for up casts. A time mean and standard deviation of the subsets was calculated and then compared. The results of time mean can be seen in Figure 4.6. There are two instances where the standard deviations of the two estimates do not cross (bins 550 and 700 m) but across most of the water column estimates of ε_{Thorpe} from down casts or up casts fall within a single standard deviation of the other. Based on the comparison of down casts and up casts it was decided that they did not need to be treated independently with no obvious bias in either subset. Due to the way the glider was piloted during the MASSMO4 mission with regards to vertical speed and angle of flight the methods presented in Chapters 2 and 3 were considered acceptable to apply to the glider data. The only change made to the data processing of the raw microstructure data was to take into account the slower vertical speed of the glider when filtering the data to 100 Hz (see Chapter 2 for details).

4.2.3 MASSMO4 SPECIFIC QUALITY CONTROL

During the deployment, data acquisition issues arose because of a failure in the integration of the microstructure logger and the Seaglider. Due to this issue extra mission specific quality control was required. This issue manifests itself as unrealistically large variations in a given data stream. Microstructure and engineering data were compromised from profile 11, raw hydrodynamic data from profile 54. From profile 26 onwards the RSI toolbox used to convert raw microstructure data to readable formats could not extract any usable data. Missing glider data from profile 54 onwards was filled in using a simple linear interpolation. To remove the data spikes from the microstructure temperature data a partly manual and partly algorithmic method was used and is explained in detail below.

DE-SPIKING DATA

To minimise the need to manually inspect and remove each data spike a mask was developed to speed up the removal process. As the acquisition issue had impacted the engineering data that the Seaglider generates it was decided to analyse this in more depth and determine if commonalities could be identified. One data stream where the interference could be seen clearly was the battery draw. Large peaks in battery draw (in some cases much larger than physically possible, $\pm 20V$ on a 15 volt battery) existed. Battery draw was normalised around 0 to remove the affect of increased draw associated with glider surfacing or apogee manoeuvres. As well as surfacing and apogee the Seaglider performs other battery draining actions. These include running the motor to pitch and roll, also leading to increased battery draw.

To make sure that these periods of motion were kept but excessive draw was excluded a 21 point moving median of normalised battery draw was calculated. The moving median was then compared to the normalised draw. This comparison was used to determine a range of voltage draws that could be considered sensible. Threshold values of 0.18 volts and below -0.65 volts were used to create a mask where voltage draw could be considered excessive and removed. The spikes in the raw 512 Hz microstructure data are characterised by more than a single point. To remove all points associated with a given battery draw spike a window was created around the peak median value. A 600 point window masking 250 points before and 350 following the battery draw spike was used. This led to ~7.5 seconds of microstructure data being removed for each battery draw spike. Once this mask had been applied to the fast thermistor data each profile was manually checked to make sure that the temperature spikes had been correctly removed.

In most instances the battery draw mask was enough to correctly remove problematic data. However, there were a number of situations where the mask failed to remove a spike. This is especially true of the later profiles. These failures fall into two categories. The first, spikes which were not associated with battery draw. These spikes were removed manually. The second is where a spike was successfully removed but was very close to a second spike leaving up to two seconds worth of data points between spikes. It was decided that to prevent this data compromising any further calculations data between close spikes should also be removed. A breakdown of how much data was excluded (by the filter and manually) can be seen in Figure 4.7. Across all the profiles a total of ~ 2.7% of the data was removed, with up to ~ 6.5% of data being removed on the most affected profiles. Manual data removal only contributed ~ 0.18% of all data removed.

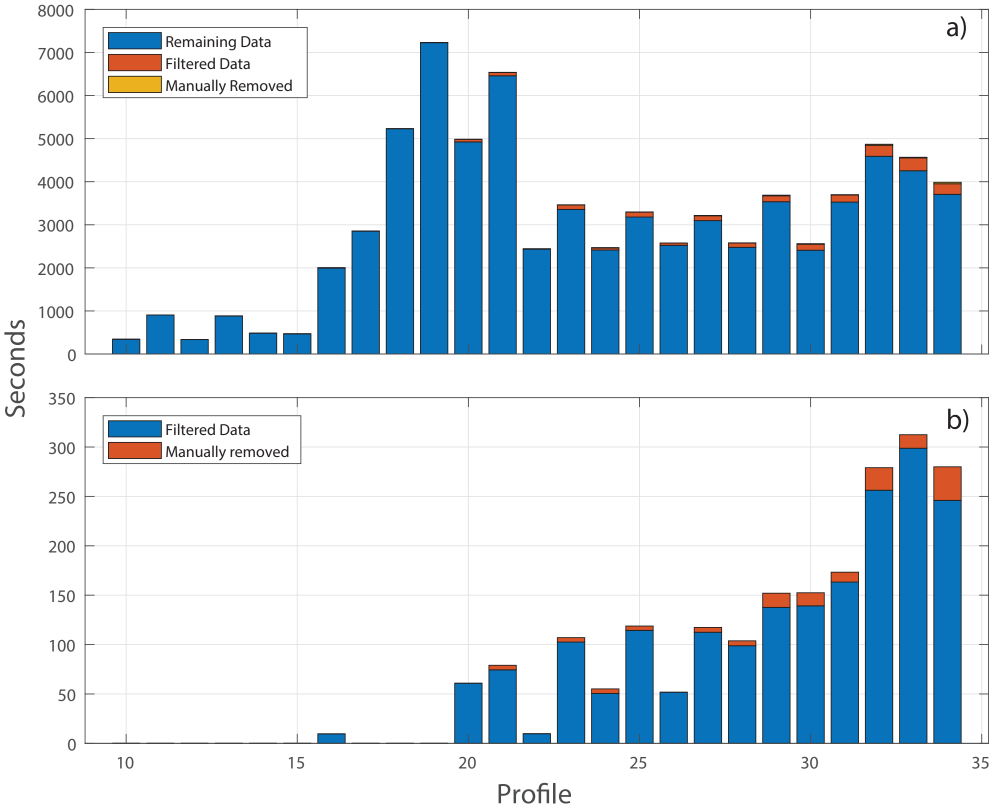

Figure 4.7: Figure showing breakdown of data removed by profile during the de-spiking processes (length given in seconds). a) Remaining data and all removed data. b) Breakdown of removed data.

4.3 RESULTS

In the following section a brief overview of the data will be presented, starting with a breakdown of the entire mission followed by sections looking at profiles organised by their distance from the WTR and their location within the M2 tidal cycle. Due to a lack of literature examining TKE dissipation rates on the flank of the WTR the results presented in this chapter will primarily be compared against Hosegood et al. (2005) and Hall et al. (2011) (using data collected in the FSC 230 km and 110 km up stream of the WTR respectively) and from Venables (2011) to the north west in the Wyville Bank Channel (95 km down stream from the WTR).

Figure 4.8 shows the individual profiles and associated time means of TKE dissipation rate estimates (ε_{Thorpe}) and vertical diapycnal eddy diffusivity (κ_{ρ}) from the MASSMO4 deployment. A profile by profile basis shows a large variability from

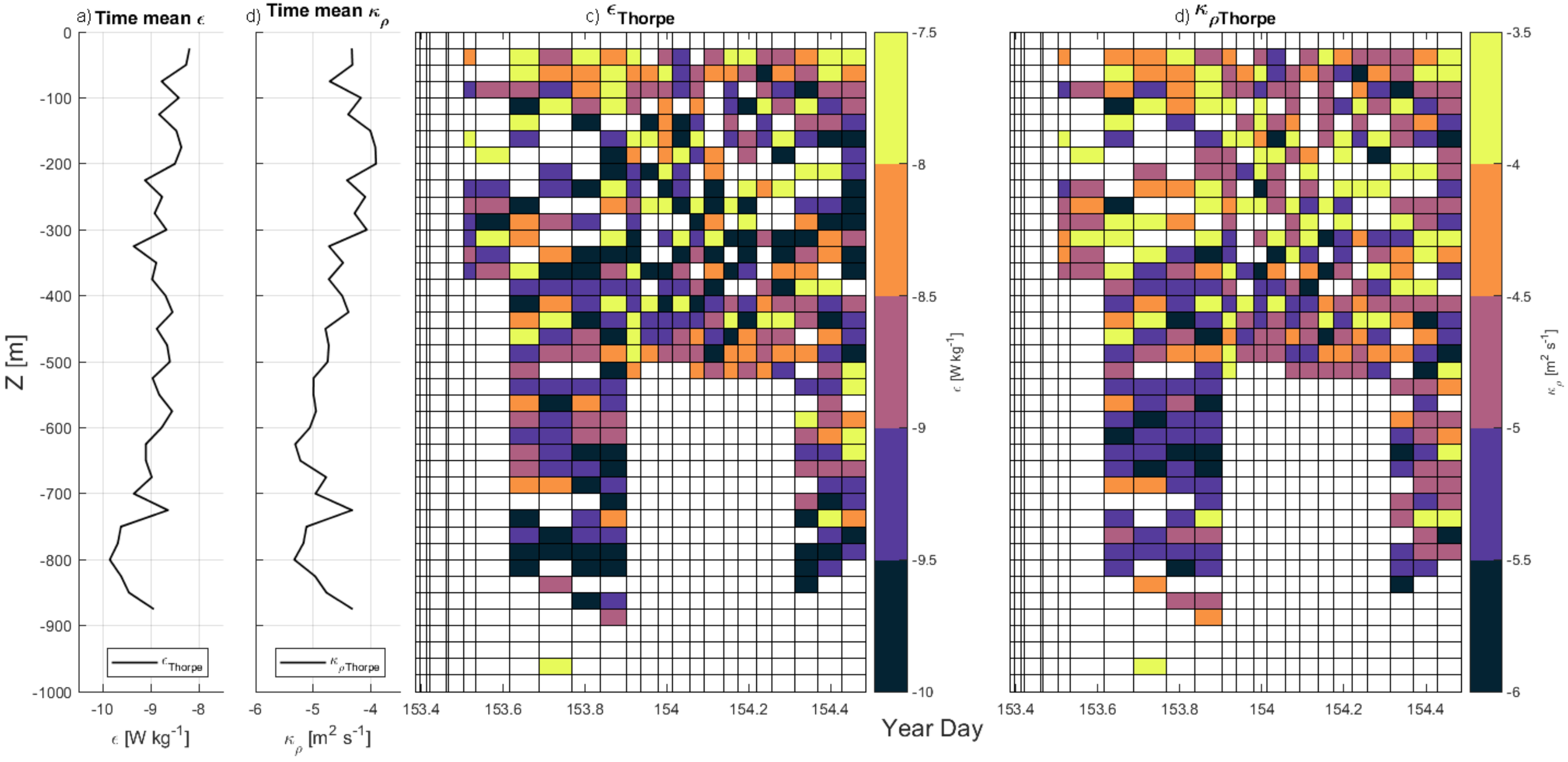

Figure 4.8: ε and κ_ρ estimated from Thorpe Length scales in 25 m bins. a) time mean ε_{Thorpe}. b) time mean $\kappa_{\rho Thorpe}$. c) ε_{Thorpe} for each profile against year day. d) $\kappa_{\rho Thorpe}$ for each profile against year day.

both estimates. ε_{Thorpe} range from > $(O)10^{-10}$ W kg^{-1} to < $(O)10^{-7.5}$ W kg^{-1}. Higher ε_{Thorpe} shows little consistency in location and can be found across all depths. Potential elevated regions exist in the upper 100 m of the water column and between 500 and 700 m compared to values immediately above and below these regions. This structure is clearest in the 3 profiles of greater than 500 m after year day 154.3. The elevated region of TKE dissipation rate estimates at depth is lower than that found near the surface. This is reflected by the time mean of ε_{Thorpe} seen in Figure 4.8 a. The time mean shows elevated mixing in the surface waters that decreases with depth. A subtle increase is seen in the time mean between 400 m and 600 m (the location of the deep pycnocline). The pattern is similar to that seen by Hall et al. (2011) although in our study the estimates are an order of magnitude lower. The higher values of ε_{Thorpe} seen between 400 m and 600 m may be attributed to patchy elevated mixing that is seen in the deep pycnocline (Hosegood et al., 2005).

The values of κ_ρ show elevated values in the surface with a peak at ~200 m which then steadily decreases at depths below the maxima. Values range from > $(O)10^{-6}$ m^{-2} s^{-1} to > $(O)10^{-4}$ m^{-2} s^{-1}. The final 3 profiles below 500 m (as with ε_{Thorpe}) show elevated values compared to the same depth in the first 4 profiles extending below 500 m. The large scale patterns seen in the time mean from κ_ρ show a good match for the work presented by Hall et al. (2011), but again are an order of magnitude lower. In this region we would expect to see a stronger signal from ε_{Thorpe} around the deep pycnocline, a pattern that was not immediately clear when the data is presented linearly with time, as in Figure 4.8.

To further investigate possible signals the data was visualised in two different ways. The first visualisation was the distance of a profile from the WTR. This would allow us to attempt to determine if moving a short distance away from a internal tidal generation location (Sherwin, 1991; Hall et al., 2011; Gallego et al., 2018) has an impact on ε_{Thorpe} and κ_ρ. The second visualisation was to order the profiles within the M_2 tidal cycle. This second visualisation was done to determine if the internal tide generation from the WTR was detectable in the data.

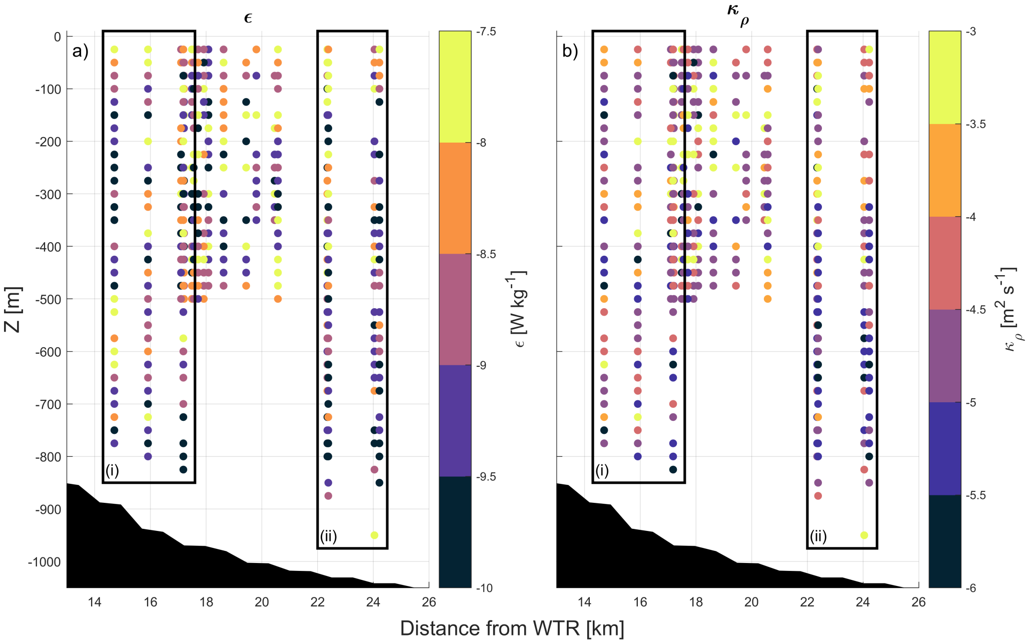

Figure 4.9: Profiles of a) ε_{Thorpe} and b) $\kappa_{\rho Thorpe}$ plotted as a function of distance from the WTR. Profiles greater than 600 m in boxes i) and ii) used to calculate on and off ridge averages respectively.

4.3.1 DISTANCE FROM THE WYVILLE THOMSON RIDGE

To investigate spatial patterns, TKE dissipation rate estimates and vertical diapycnal eddy diffusivities were plotted against distance from the WTR. The midpoint location of each profile was determined along with the distance from that location to a reference point on the flank of the WTR (59.85°N, 6.3°W). Each profile was then plotted in increasing distance from the WTR (see Figure 4.9). In Figure 4.9, two boxes i) and ii) are used to show two subsets of profiles greater than 500 m in depth, one over the ridge flank and the other 7 km further off the ridge. The time mean and standard deviation of ε_{Thorpe} and κ_ρ over these two subsets of profiles is shown in Figure 4.10.

TKE DISSIPATION ESTIMATES

In Figure 4.9 we observe elevated values of ε_{Thorpe} in the top 75 m over the ridge flank (Figure 4.9 a.i) and in the top 125 m off the ridge (Figure 4.9 a.ii). Between 150 m and 500 m there is patchy elevated ε_{Thorpe} but no clear structure within this depth range in either subset. Between 500 m and 650 m we see elevated ε_{Thorpe} in the ridge flank subset but no clear elevated ε_{Thorpe} at the same depth in the profiles off

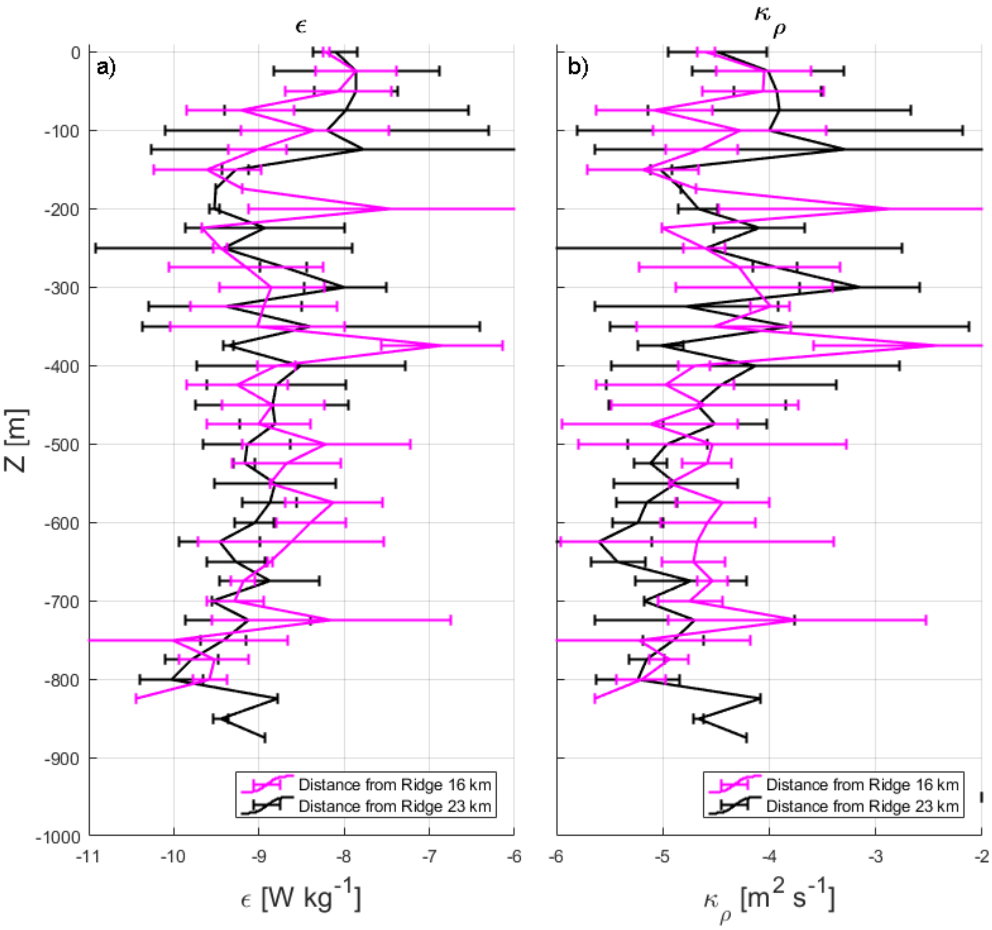

Figure 4.10: Location average of a) ε_{Thorpe} and b) $\kappa_{\rho Thorpe}$ calculated from profiles in Figure 4.9 i) and ii) - 16 and 23 km from WTR respectively. Horizontal bars indicate standard deviation.

the WTR. Below 650 m both the ridge flank and off the ridge show a similar range of variability within TKE dissipation rates. This pattern is visible, although less clear in Figure 4.10 a.

When taking individual profiles the two subsets show a marked variation with depth, however, this is not as visible in the time means, with both subsets often falling within a single standard deviation of each other. Between 500 and 650 m, where the largest difference between subsets exists there is also the most consistent variation in the time mean. Within this depth range bin averages exist where the standard deviations from each subset do not overlap (Figure 4.10 a). This suggests that at this depth there may be a distinct difference between the two subsets. However, due to the lack of profiles it is not possible to confirm whether this is the case.

VERTICAL DIAPYCNAL EDDY DIFFUSIVITY

In Figure 4.9 b we observe elevated κ_ρ in the upper 150 m of the water column in both subsets as well as between 200 and 300 m in the off ridge subset. Between 300 and 500 m both profile subsets show similar low values. Below 500 m the profiles on the ridge flank show elevated values compared to those off the ridge. The time mean values for both profile subsets (Figure 4.10 b) show a similar pattern to that seen in ε_{Thorpe} with the time means of both subsets being within a single standard deviation of the other for a majority of the water column. However, between 500 m and 700 m a majority of the time means are different by more than a single standard deviation. This is a more marked difference than the same depth region for ε_{Thorpe}.

From the small amount of usable microstructure data available to us from this mission there was a small visual distinction between the subset of profiles on the ridge flank compared to those off the ridge, specifically in the upper 200 m and between 500 and 700 m. The deeper of the two elevated regions of ε_{Thorpe} and κ_ρ suggest a process that is causing elevated mixing near the bed. This region is not directly above the seabed but at a minimum 200 m from the topography. This distinction between the flank and off ridge subsets is in part supported by the difference in time means at these depths (Figure 4.10). However, due to the lack of profiles it is difficult to provide a truly robust time mean (Smyth and Thorpe, 2012) leading to the difference between these two subsets being inconclusive.

4.3.2 PERIOD OF THE TIDAL PHASE

To investigate temporal patterns, TKE dissipation rate estimates and vertical diapycnal diffusivities were plotted against the phase of the local barotropic (surface tide) M_2 tidal cycle, which is the dominant tidal constituent in the FSC (Sherwin, 1991). The barotropic tide was generated by supplying the Tide Model Driver (TMD) tool box with the input provided from the TPXO08 European shelf model Egbert and Erofeeva (2002). Profiles of ε_{Thorpe} and κ_ρ were also compared to vertical isopycnal displacement and the baroclinic tide (internal tide). Two different depth averages were then calculated and are presented over an M_2 tidal cycle.

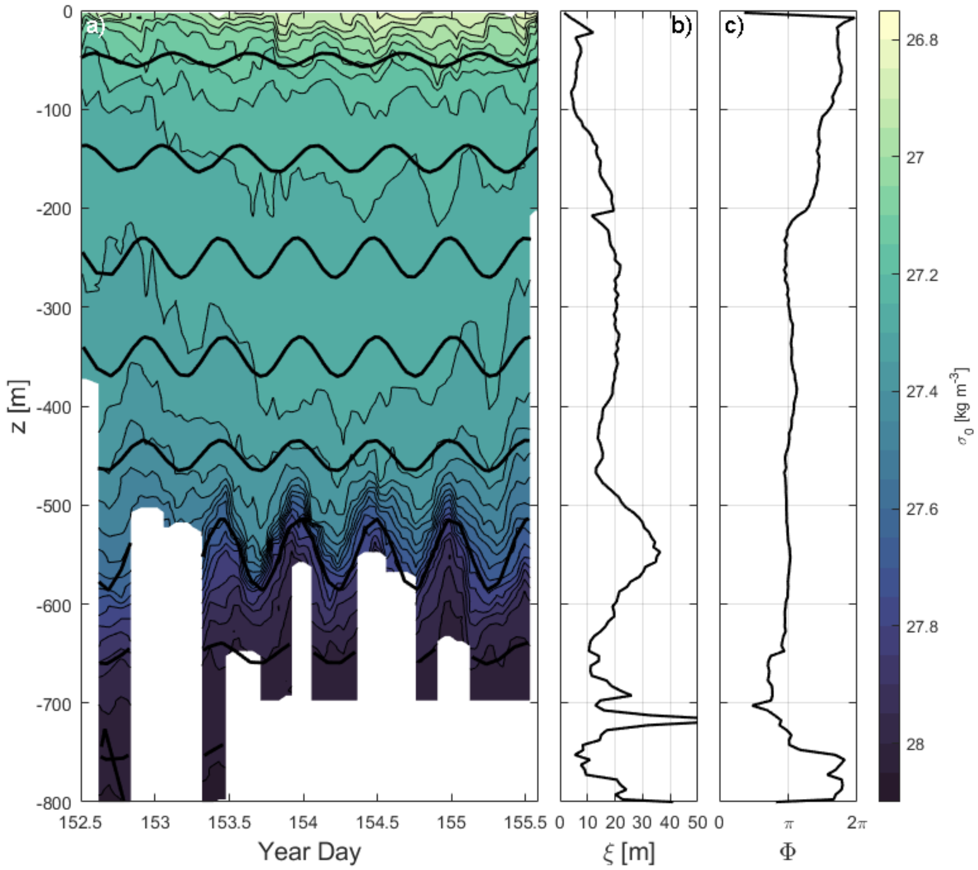

Figure 4.11: Isopycnal displacements and associated tidal phase. a) Potential density (colour) overlaid with the D_2 component of vertical isopycnal displacement at 100 m intervals. b) time mean isopycnal displacement. c) time mean D_2 tidal phase.

ISOPYCNAL DISPLACEMENT

To calculate vertical isopycnal displacement the method presented by Hall et al. (2019) was followed. For the entire mission the density anomaly, ρ', is calculated by subtracting the time mean density profile from potential density,

$$\rho'(z,t) = \rho(z,t) - \overline{\rho}(z) \tag{4.1}$$

where $\overline{\rho}(z)$ is time mean density and smoothed with a 50 m gaussian running mean to give a representative background density profile. Vertical isopycnal displacement is then calculated,

$$\xi(z,t) = \rho'(z,t)\left(\frac{\partial\overline{\rho}}{\partial z}\right)^{-1} \tag{4.2}$$

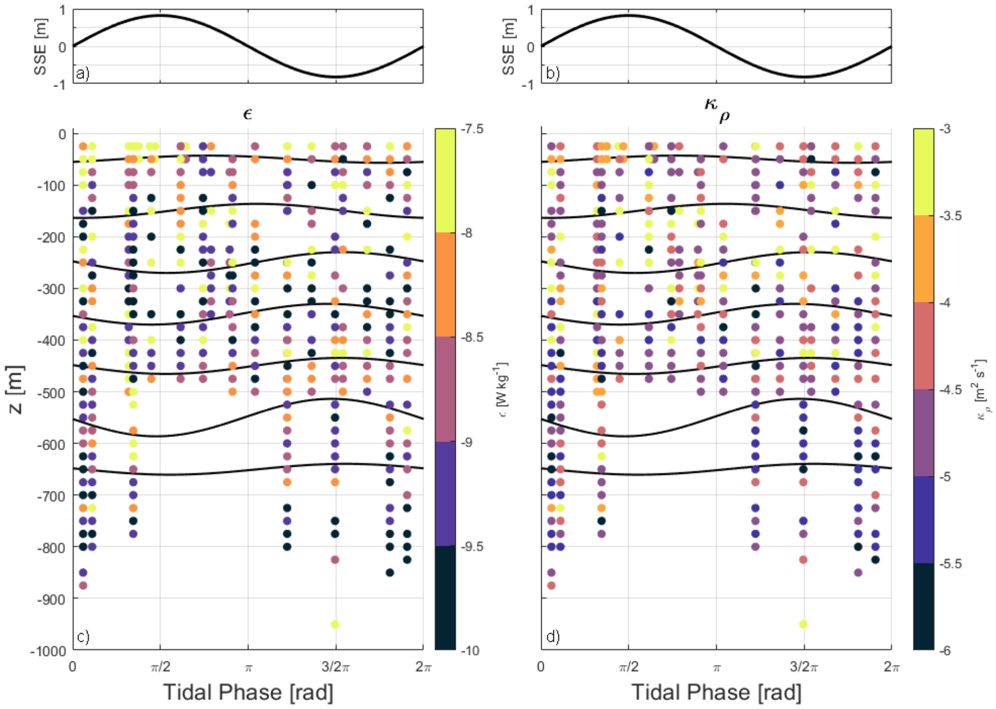

Figure 4.12: Profiles of ε_{Thorpe} and $\kappa_{\rho Thorpe}$ presented over an M$_2$ barotropic tidal cycle. a) and b) sea surface elevation from the TOPEX European Shelf Sea model. c) ε_{Thorpe}. d) κ_{ρ}. Vertical isopycnal displacement in 100 m increments across the M$_2$ baroclinic tidal phase in black.

where z is the amplitude and t the phase offset for each depth level (ξ). The M_2 tidal period harmonics are fitted to ξ on each $\Delta 5$ m depth level following Thomson and Emery (2014). The M$_2$ component of the tide is plotted every 100 m in Figure 4.11. The isopycnal displacement seen in these images conforms well with the contoured potential density variation seen. The amplitude and phase of each depth increment of ξ is used to calculate single M_2 phase curves between 50 and 650 m in increments of 100 m and plotted on Figure 4.12 along with profiles of ε_{Thorpe} and κ_{ρ} sorted based on the mid-depth year day within the M$_2$ tidal phase.

TKE DISSIPATION ESTIMATES

In Figure 4.12 c, ε_{Thorpe} is plotted as profiles against phase of the barotropic M_2 tidal cycle. Across all depths we see very little variation of ε_{Thorpe} that fits with either the phase of the barotropic or baroclinic tide. At the surface we can see a small amount of variation across the baroclinic tidal phase with slightly elevated ε_{Thorpe} with values between 5×10^{-9} W kg^{-1} and 5×10^{-8} W kg^{-1} around a phase of $\pi/2$ where SSE is at

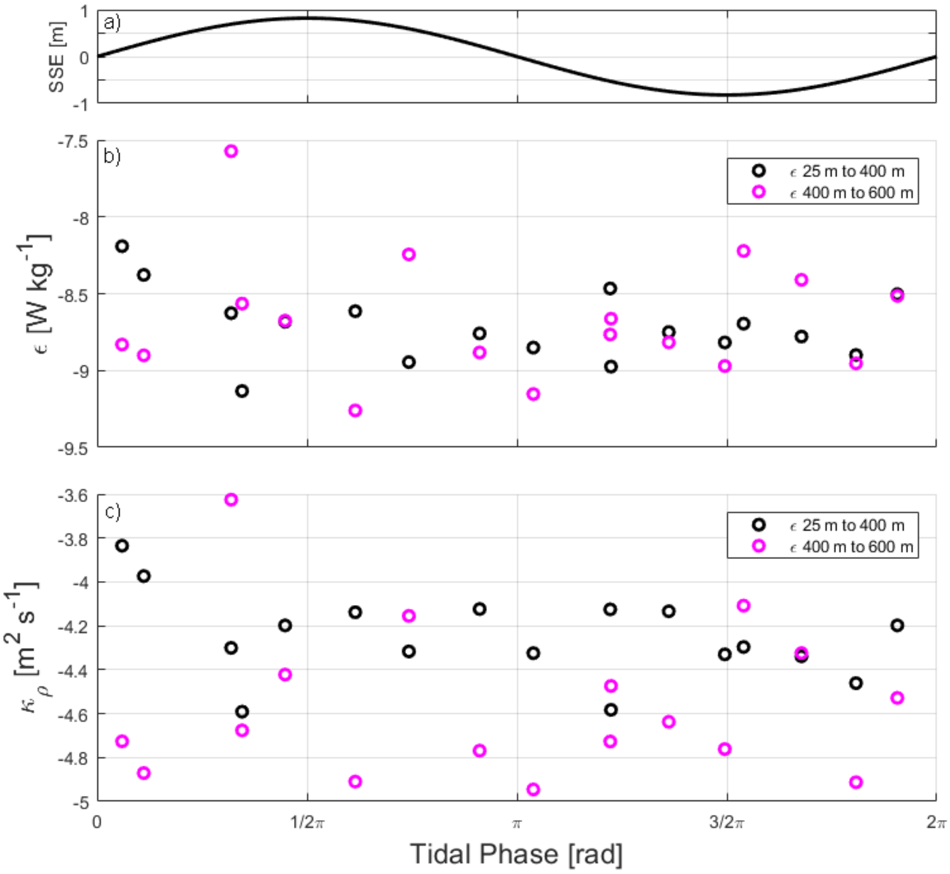

Figure 4.13: Depth mean of ε_{Thorpe} and $\kappa_{\rho Thorpe}$ between 25 m and 400 m and 400 m and 600 m presented over an M_2 tidal cycle. a) sea surface elevation from the TPXO European Shelf Sea model. b) ε_{Thorpe}. c) κ_{ρ}.

its highest compared to half a phase later ($3/2\pi$) where ε_{Thorpe} is 1×10^{-9} W kg^{-1} and 5×10^{-9} W kg^{-1}. Around the deep pycnocline we see very little evidence of elevated estimates of TKE dissipation matching with isopycnal displacement. Figure 4.13 b shows that even with a depth mean between 400 and 600 m (the depth of the deep pycnocline) there is no clear variation of ε_{Thorpe} in relation to either the barotropic or baroclinic M_2 phase. The upper 400 m of the water column were also depth averaged in Figure 4.13 b and also show no clear pattern.

DIAPYCNAL EDDY DIFFUSIVITY

In Figure 4.12 d κ_{ρ} is plotted as profiles against phase of the barotropic M_2 tidal cycle. Across all depths we see very little variation of κ_{ρ} that follows the structure of the barotropic or baroclinic tides. The small variation noticeable in the ε_{Thorpe} surface layer is not seen in the κ_ρ data. The lack of pattern can also be seen in Figure 4.13 c. Again there is no clear relationship between either depth averaged values compared with the structure of barotropic or baroclinic tides.

4.4 DISCUSSION

In the previous section of this chapter the key findings of the MASSMO4 deployment on the northern flank of the WTR were presented. In this section these findings will be further discussed, potential impacts of the findings and what may influence them will be discussed here as well the wider context.

4.4.1 VARIABILITY IN TKE DISSIPATION RATES

The first finding to be examined was the high range variability of the estimates of ε_{Thorpe} and κ_ρ that are seen in this study. A number of factors may influence this variability. In the FSC and along the eastern flank of the WTR it is known that there is a large amplitude oscillation of the deep pycnocline associated with the internal tides (Sherwin, 1991; Hall et al., 2011). To test the algorithms developed in Chapter 3 the dataset presented in this chapter was chosen as it was thought to have a high signal to noise ratio and was likely to reveal clear patterns. Estimates of ε_{Thorpe} from L_T are inherently patchy, before any averaging is done, as the length scale of L_T is related to a single overturning event (Thorpe, 1977). There is also the ability to observe false overturns that arise from instrument noise and motion (Gargett and Garner, 2008; Mater et al., 2015) or to miss overturns below the resolution limit of that instrument (Hall et al., 2011). In addition to the potential instrument related issues there is also the chance that the glider will pass through the overturn at any point in the overturning process (Thorpe, 2012) resulting in a smaller L_T and a lower estimate of ε_{Thorpe}.

Another important aspect of the variability is seen in the mission averaged ε_{Thorpe}. The number of profiles with usable high resolution data and profiles greater than 500 m deep are small in number. Smyth and Thorpe (2012) suggest that an average of over 100 profiles should be used to reduce horizontal intermittence in the time mean. This has not been possible with the dataset presented in this chapter

(19 profiles). Of the profiles presented 12 of 19 profiles are also shallower than 500 m (a period when the glider altimeter was being tuned). Which led to the region of greatest interest, the deep pycnocline, not being sampled. In Section 4.3.1 the distance from the ridge was investigated and showed some elevated mixing around the deep pycnocline. The time period during the altimeter tuning, although acting as a good break between the ridge flank and off the ridge profiles, is a period that would have been of great interest in identifying if the elevated values of ε_{Thorpe} that are seen between 500 and 650 m are indeed related to the deep pycnocline and proximity to the WTR.

Both Figure 4.5 and 4.11 show a clear pattern of an internal wave like structure between 500 and 700 m from year day 153.5 till the end of the mission. However, during the first four full profiles the oscillations associated with the internal tide are less defined. This supports the idea that the internal wave energy does not propagate perpendicular to the the WTR into the FSC (Hall et al., 2011), and is explored further below.

Another potential explanation for the lack of signal off the WTR could arise if the glider was advected vertically within any internal tide structure, although $d\mathrm{p}/dz$ data from the glider itself suggests that this is unlikely to be the case.

4.4.2 COMPARISON WITH PREVIOUS STUDIES

FAROE SHETLAND CHANNEL AND FAROE BANK CHANNEL REGION

As well as the spatial variations seen in ε_{Thorpe} and κ_ρ the range of these values should be considered. A number of other studies have estimated TKE dissipation rates over the WTR and in other regions of the FSC and FBC.

The estimates of ε_{Thorpe} and κ_ρ presented here are an order of magnitude lower than those presented by Hall et al. (2011). In the deep pycnocline (400 to 600 m) they showed ε_{Thorpe} of up to 5×10^{-7} W kg^{-1} averaged over 25 CTD casts. The results presented in Figure 4.10 at the same depth give ε_{Thorpe} estimates of 3×10^{-8} W kg^{-1} although show a high of up to 5×10^{-8} W kg^{-1} at 375 m. A difference in order of magnitude was also seen when comparing κ_ρ.

In Venables (2011) the author shows values of ε_{Thorpe} estimated from both shear data and Thorpe Length scales. Venables (2011) gives estimates of ε_{Thorpe} as high as 5×10^{-6} W kg^{-1} during periods where the pycnocline rises, which are two orders of magnitude higher than the largest values presented here. Outside the pycnocline, between 100 and 400 m and below 600 m Venables (2011) estimates a background TKE dissipation rate between 1×10^{-9} W kg^{-1} and 5×10^{-8} W kg^{-1}, values more consistent with those described here.

If individual bins are examined rather than time means there are some values in this work that match the values from Hall et al. (2011) and Venables (2011). For example, profile 25 shows increased dissipation rate estimates in the surface followed by a minima between 100 and 500 m of 1×10^{-10} W kg^{-1}, ε_{Thorpe} then increases to 5×10^{-8} W kg^{-1}, followed by a decrease back to values around 5×10^{-9} W kg^{-1} below 700 m. However, there are not enough profiles with this structure to impact the time averages. A longer time series from the glider would potentially reveal these patterns more clearly.

Work done further north in the FSC (235 km upstream of the WTR) by Hosegood et al. (2005) describes ε_{Thorpe} from both shear and Thorpe scales. Most of the values in their study are centred around 5×10^{-8} W kg^{-1}, more in line with the estimates described here with maxima in some instances reaching 5×10^{-6} W kg^{-1}.

DISSIPATION OF THE INTERNAL TIDE

The WTR is a known generator of the internal tide. Do the values of TKE dissipation estimated in this chapter match the theoretical generation and fit with internal tide energy fluxes in the Wyville Thomson Basin (WTB) from model outputs (Hall et al. (2011),Hall et al. (2019))? Internal tide energy flux into the WTB was calculated by Hall et al. (2019); using co-located glider and ADCP data and model outputs of fluxes from Hall et al. (2011). The bulk TKE dissipation estimate for the region is calculated as,

$$\varepsilon_{bulk} \simeq F_{net}/[\rho A(1+\Gamma)] \tag{4.3}$$

where F_{net} is the net energy flux into the region, A is the across slope cross-sectional area, ρ is a reference density of 1028 kg m^{-3} and Γ is the mixing efficiency taken as 0.2 (Oakey, 1982). Here we take F_{net} as 4.23 kW m^{-1} (Hall et al., 2019) and A as the depth F_{net} is calculated over (800 m) and 25 km in length (from the reference point on the flank of the ridge to the glider profile furthest from the reference point).

This gives a ε_{bulk} of 1.7×10^{-7} W kg^{-1}. This is up to 3.5 times greater than that found at the upper limits of TKE dissipation from our study in the pycnocline and up to 34 times greater than that of the time average across the pycnocline region.

One possible conclusion that these results point to is that the energy is not dissipated locally and is focused on the pycnocline. Taking into account the model outputs from Hall et al. (2011) it can be seen that the direction of energy from the WTR is not north up the FSC but radial in nature with a major portion being dissipated east along the flank of the WTR onto the Shetland shelf. We also show high TKE dissipation rate estimates near the surface further supporting the idea that the energy is not all dissipated locally. The difference in the values of dissipation seen close to the ridge and those seen further away also lend support to the idea of rapid radial dissipation of the energy generated at the WTR into the WTB.

A second possible conclusion is that the methods presented in Chapter 2 do a poor job of correctly estimating both ε_{Thorpe} and κ_ρ in this highly energetic region. This may be supported by results described here that on average ε_{Thorpe} was an order of magnitude lower than other studies in the FSC.

GLOBAL CONTEXT

The values of ε_{Thorpe} in this chapter, as well as being lower than other studies in the WTR region are at the lower end of estimates seen in other regions of high internal wave generation.

Compared to the work of Klymak et al. (2006) across the Hawaiian Ridge, the values of ε_{Thorpe} presented here fit within the ranges seen during the Hawaii Ocean Mixing Experiment (HOME); between 2×10^{-10} W kg^{-1} and 4×10^{-8} W kg^{-1}. However, higher values from HOME from regions off the Hawaiian Ridge with similar physical processes as seen in the pycnocline in the WTR are up to an order of magnitude higher than those in this study. The same can also be seen in κ_ρ which are an order of magnitude lower here than those presented by Klymak et al. (2006).

Values from the Luzon straight (Alford et al., 2011) are also at least an order of magnitude higher than those estimated here, but close to those found by Venables (2011) for the WBC.

Values of ε from Althaus et al. (2003) at the Mendocino Escarpment show a better fit to those estimated here. With results of up to $(O)1 \times 10^{-9}$ W kg^{-1} around the ridge itself, with values of up to 5×10^{-8} W kg^{-1} seen around the ridge crest. Although the intensity of turbulent dissipation in the study region was high, it only accounted for 1% of the energy flux from the internal tide, with the rest being radiated away as internal waves.

The estimates of ε_{Thorpe} and κ_ρ presented in this chapter do fit the structure and pattern seen in other studies within the WTR region. However, both ε_{Thorpe} and κ_ρ are underestimated compared with those studies. Similar underestimations are seen compared to most studies carried out on other active internal tide generating ridges.

IMPACTS

The WTR is an important submarine feature. It acts as a barrier between the deep temperate North Atlantic waters and the cold Nordic seas as well as being a region of high internal wave generation (Sherwin and Turrell, 2005). The high levels of mixing generated by the WTR is likely to have an impact on the water masses present in the FSC and the FBC (Table 4.1) leading to potential changes in Θ-S properties in turn impacting the flow of these water masses into the Northern Atlantic and around the Faroe Isles. Associated with this is that if there were any major changes to the flow around the FSC it has the potential to impact work done looking at potential oil spill pathways from deep oil rigs (Gallego et al., 2018).

4.5 SUMMARY

4.5.1 SUMMARY OF AIMS

At the beginning of the Chapter the following questions were posed:

- What glider specific issues might there be when using Thorpe Scaling for fast thermistor data?
- Can this methodology provide comparable estimates of TKE dissipation when compared to previous studies in the geographical region?

Here we look at both of those in context of the information discussed in this chapter.

4.5.2 GLIDER SPECIFIC CONSIDERATIONS

There are two major differences between a glider and a profiler. The first is the difference in path that the two different platforms take through the water. A glider will take a diagonal path through the water (ϕ between 14° and 45°) whereas a profiler travels vertically. The second is that a glider records data both on the up and down cast. In papers by Thorpe (2012) and Smyth and Thorpe (2012) work was carried out to look at the suitability of gliders for use in Thorpe scale methodology. Both studies found that when a glider is flown correctly (large ϕ) and the aspect ratio of an overturn ($\text{height}_{overturn}/\text{length}_{overturn}$) is small the standard error is less than estimating TKE dissipation from shear probes. Flying a glider directly along the direction of propagation of an internal wave field, as the glider was flown on MASSMO4, would therefore lead to larger levels of uncertainty and underestimation from the Thorpe scaled estimates of TKE dissipation. This has been shown in this investigation of the MASSMO4 data.

When looking at the difference between glider ascents and descents very little difference was observed, apart from around the deep pycnocline where some depth bins showed a greater than standard deviation of variation (Figure 4.6). Due to the limited nature of this it was decided that the ascents and descents were similar enough to be treated as one.

4.5.3 ESTIMATES OF ε_{Thorpe} COMPARED TO PREVIOUS STUDIES

The estimates of TKE calculated in this chapter were compared to a number of other studies including Hall et al. (2011),Hosegood et al. (2005) and Venables (2011) to determine how well the values compare to these studies. Peaks of ε_{Thorpe} in this study were $5 \times 10{-}8$ W kg^{-1} which in most cases are around 5 times lower than those from other studies from both Thorpe scaled and shear probe estimates. The background estimated rates of dissipation are up to 10 times smaller. It is clear that in this region ε_{Thorpe} from the glider temperature has underestimated TKE dissipation estimates compared with other studies. This is opposite to the over estimation of Thorpe scaled estimates of TKE dissipation rates in energetic regions suggested by Mater et al. (2015). The shape of the profiles however, show some promise around the ridge where we see a distinct difference between off and on the WTR flank, with increased dissipation estimates closer to the ridge. The time and spatial scale of the data prevents these differences from being examined further. Reasons for this underestimate of ε_{Thorpe} estimated in this study compared to other studies include the method of averaging (see Chapter 2), which is discussed further in the final chapter and the way that the glider was flown during the MASSMO4 deployment.

In this chapter it has been shown that high resolution temperature data from a Seaglider can be used to estimate TKE dissipation rates with a vertical structure comparable to previous studies, but with an underestimate of dissipation rates and vertical diffusivities. In the next chapter these methods will be applied to a much larger dataset collected as part of the the EUREC^{4}A project to the east of Barbados.

5

EUREC^{4}A: APPLICATION OF METHODS TO A FULL LENGTH GLIDER MISSION

5.1 INTRODUCTION

In the previous chapter we showed that it is possible to estimate TKE dissipation rates from high resolution temperature data collected by a Seaglider. Values found were comparable to previous studies. With a good understanding of how the methods developed in this thesis apply to data collected by a Seaglider, a longer dataset is examined and analysed. In this chapter we set out to investigate the following questions:

- Can the the methods developed in this thesis be successfully applied to a tropical open ocean dataset?
- How do TKE dissipation rate estimates from Thorpe scaling compare to other tropical open ocean studies?
- How do thermohaline staircases influence Thorpe scale estimates of TKE dissipation rates?

To accomplish these aims the method was applied to a dataset collected 200 km east of Barbados as part of the EUREC^{4}A (Elucidating the Role of Cloud-Circulation

Coupling in the Climate) field study campaign. The dataset was chosen for its different geographical location with interesting physical structure and an increased length, compared to that of MASSMO4. A description of the region and the EUREC^{4}A project is presented. This is followed by a brief overview of the data used in this chapter, the results for the application of the Thorpe scaling methodology to the data, a discussion and a summary.

5.1.1 EUREC^{4}A

The EUREC^{4}A field campaign took place between the 20 January 2020 and the 20 February 2020 to the east of the island of Barbados (Stevens et al., 2021). The original plan for the project can be found in Bony et al. (2017), a brief summary is provided below. The primary aims of the EUREC^{4}A campaign were to resolve contradictions that arise between process and climate models' depictions of trade wind cumuli clouds. The campaign was set up to quantify the physical properties of trade wind cumuli as a function within the large scale environment (Bony et al., 2017). The field campaign was also used as an opportunity to carry out complementary investigations, including studying ocean mesoscale eddies and air-sea interactions (Bony et al., 2017). The five weeks of the 2020 EUREC^{4}A field campaign involved 2500 sondes, 4 global-class research vessels, 4 research aircraft logging 400 hours, the Barbados Cloud observatory, a fleet of autonomous and tethered ocean platforms; and support from satellite remote sensing and weather/climate models (Stevens et al., 2021). As part of the autonomous complement of EUREC^{4}A, the University of East Anglia deployed three Seagliders with a variety of instruments, including SG620 carrying an RSI MicroPod system with a shear probe and FP07 fast thermistor.

5.1.2 EUREC^{4}A DATA

SG620 was deployed 200 km to the north east of Barbados (Figure 5.1 a, white square). The Seaglider was deployed on the 22 January 2020 (year day 22) and recovered on the 5 February 2020 (year day 36), completing 131 dives (262 microstructure profiles). After the initial dives used to trim the glider to the optimal flying parameters the Seaglider completed 121 dives to 780 m. There is a short period on year day 31 where a number of 200 m dives were conducted for compass calibration before reverting back

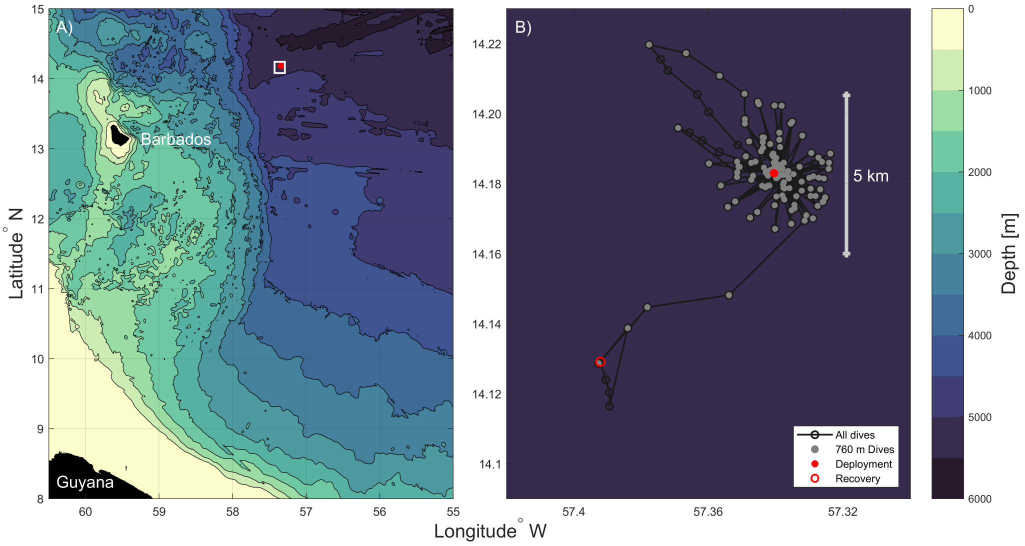

Figure 5.1: Location of EUREC^{4}A deployment. a) the broader region, the white box indicates the region from panel b. b) Dive start locations and recovery of the glider deployment.

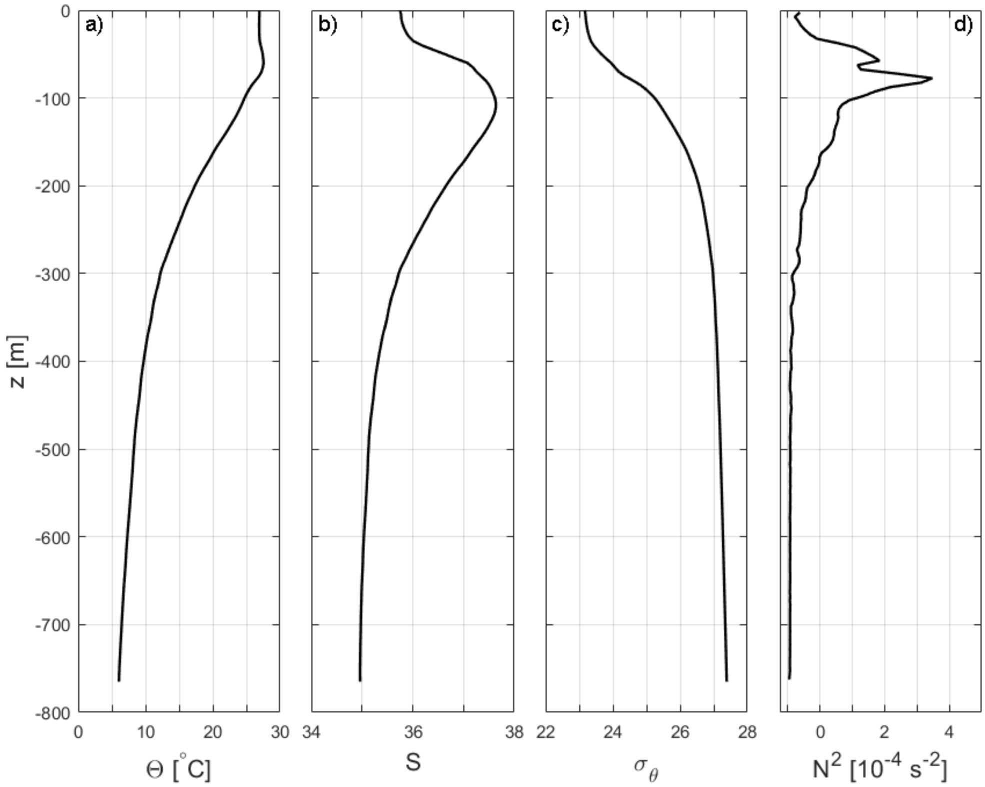

Figure 5.2: Time mean hydrographic data from the EUREC^{4}A deployment a) conservative temperature b) absolute salinity c) potential density d) N^2.

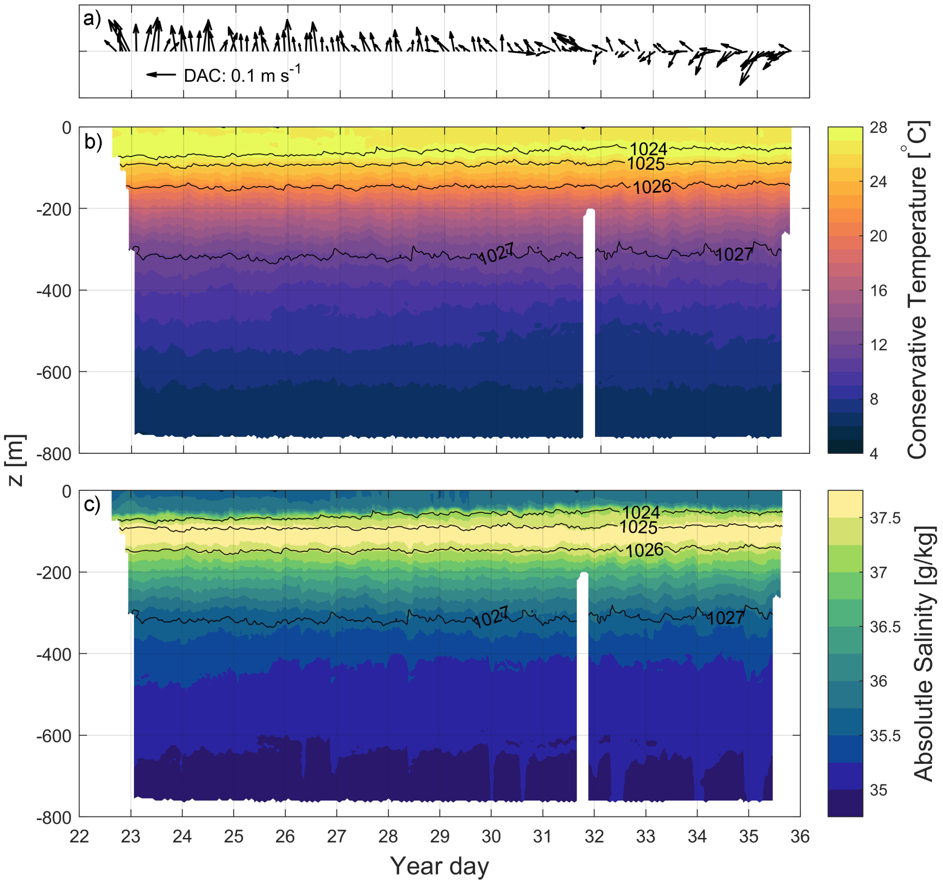

Figure 5.3: Hydrographic data from the EUREC^{4}A. a) dive averaged current (DAC) b) conservative temperature (colour) and overlaid potential density (black contours 1 kg m^{-3}) c) absolute salinity (colour) and overlaid density (black contours 1 kg m^{-3}).

to 780 m dives. The Seaglider was piloted in a virtual mooring mode in the same way as described in the MASSMO4 mission (Chapter 4).

HYDROGRAPHIC PROPERTIES

The time mean hydrographic properties from the Seaglider dives can be seen in Figure 5.2. Both the temperature and salinity are characterised by a surface mixed layer of 40 m in depth. The temperature maxima sits at 60 m with the salinity maxima at 100 m. The temperature maxima causes an issue with the Thorpe scale methodology (expanded later in Section 5.1.2.2). The maxima can also be seen in Figure 5.3 in both temperature and salinity. This shows clearly that these are persistent across the entire deployment (clearest in salinity). Below the maxima, temperature and salinity both decrease with depth. The T/S relationship (Figure 5.4),

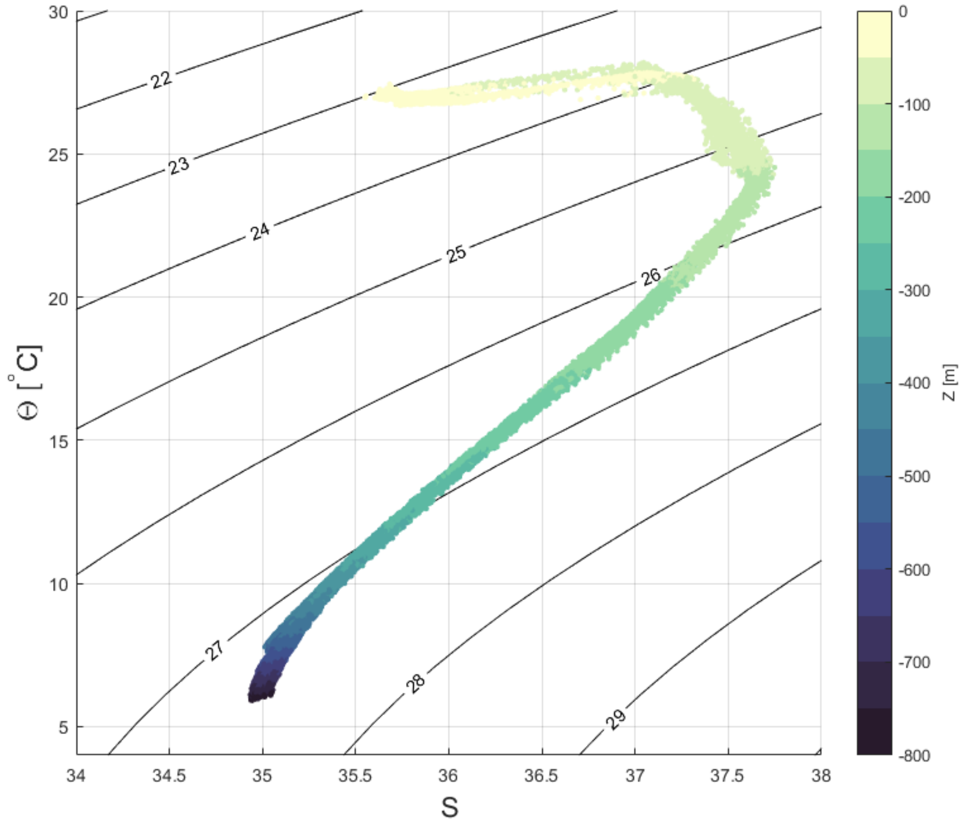

Figure 5.4: EUREC^{4}A T/S diagram with z plotted as fill colour.

shows large variations in salinity in the upper 100 m where there is only a small amount of temperature variability. The dive averaged current (DAC) is also shown in Figure 5.3. DAC is an estimate of the current velocity based on the difference between dead-reckoned glider displacements from glider speed (from the glider hydrodynamic model) and those calculated from surface GPS fixes at the beginning and end of dives (Eriksen et al., 2001). During this mission there was initially a northward DAC which weakens as day 31 is reached. At day 31 the direction of DAC swings between NW and SW with increasing magnitude towards year day 36 when the Seaglider was recovered.

MICROSTRUCTURE PROCESSING

Before processing the microstructure data any profile that was shallower than 100m was removed. This removes the earliest dives where the glider is being trimmed and flying in a way that does not collect high quality microstructure data. The microstructure data was then processed using the methods presented in Chapter 2.

Once the core processing was completed two mission specific quality control (QC) steps were applied to this dataset. The first of these was to remove the top 75 m (three 25 m bins) from each profile. Due to a subsurface maxima of temperature (centred around 60 m, Figure 5.2 a) the Thorpe Scale algorithms developed in this thesis treated the surface region as a single overturning region. This large single overturn (also centred around 60 m) led to estimates of TKE dissipation rates in excess of $(O)10^{-3}$ W kg^{-1}, values that are unrealistically large and were therefore removed by this QC step. Using Figure 5.4 it can be seen that in the upper 100 m the T/S profile is dominated by variation in salinity and not temperature. Any temperature overturns found in this region are likely to be compensated by salinity. This variability is similar to that seen in Chapter 3 where data was also removed through manual quality control.

The second of the mission specific QC steps was to apply an upper limit cut off to the TKE dissipation rate estimates across two periods of the deployment. The first of the regions occurs between year day 23 and 26.5 with a depth range of 350 m to 500 m. The second is between year day 29 and 34.25 with a depth range of 475 m to 550 m. Within these regions a number of large overturning structures were identified by the algorithms. These overturning regions gave high values of TKE dissipation rate estimates compared to the surrounding regions. These overturns were visually inspected and compared to low resolution salinity and density. The overturning regions seen in the high resolution temperature were present in the low resolution salinity but not in the density. The overturning regions were in excess of 20 metres in height and as such they would be resolvable in low resolution density. Had the overturning regions been present in low resolution density it would have been likely that these were true overturning regions. As they were not present in the low resolution density an upper cap of $\varepsilon \geq 1 \times 10^{-6}$ was applied to the two regions removing any bins contaminated by these large overturning structures. This cap was not applied to other regions of the dataset to prevent the suppression of true values of this magnitude.

The two mission specific quality control steps were applied to the 25 m binned estimates of TKE dissipation rate, before the calculations of vertical diffusivity or heat flux were made.

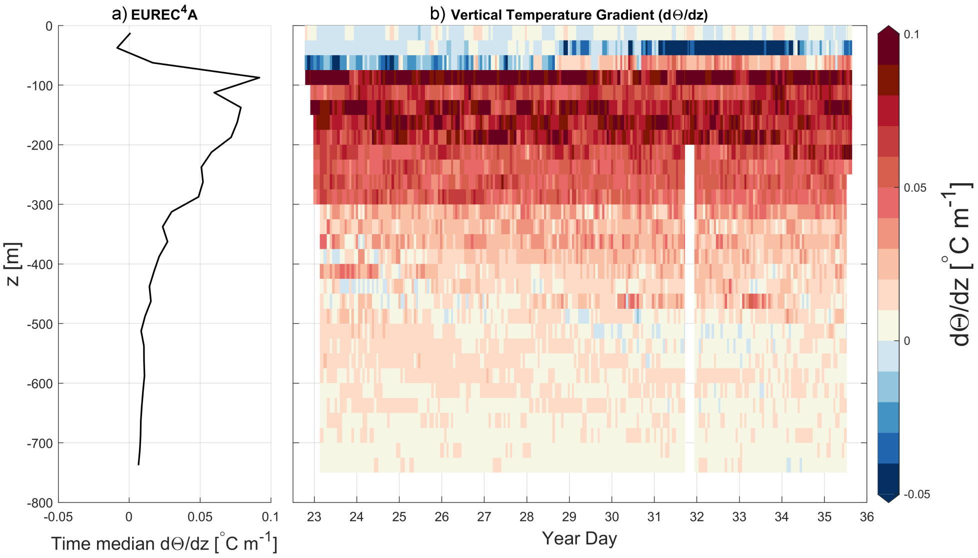

Figure 5.5: Vertical temperature gradient ($d\Theta/dz$) from CT sail temperature a) time median temperature gradient (Note: time average median used here for reasons explained in Section 2.4.2, Page 40) b) temperature gradient for each profile against year day.

CALCULATION OF HEAT FLUX

In addition to ε_{Thorpe} and κ_ρ vertical heat flux (Q) was calculated using κ_ρ and temperature from the CT sail using,

$$Q = \rho C_p \kappa_\rho \frac{\partial \Theta}{\partial z} \tag{5.1}$$

where ρ is the density of sea water, C_p is the ocean specific heat capacity, κ_ρ the vertical eddy diffusivity and $\frac{\partial \Theta}{\partial z}$ the vertical gradient of temperature with depth. A positive value of Q is an upward flux (Lique et al., 2014).

The heat flux calculation was carried out in each 25 m bin for each profile. Density is calculated from the Seaglider CT sail temperature and salinity binned to 25 m. Vertical temperature gradient was calculated across each 25 m by fitting a linear regression to 5 m binned temperature. This can be seen for the duration of the mission in Figure 5.5. A constant value of 3991 J kg^{-1} K^{-1} was used for C_p (McDougall et al., 2009). The vertical eddy diffusivities used in Equation 5.1 are shown in Figure 5.7. As limited data passes quality control between the surface and 75 m, a constant vertical eddy diffusivity of 3×10^{-6} m^{-2} s^{-1} is used for this depth range so that near-surface fluxes can be estimated. This constant value is the time-mean for

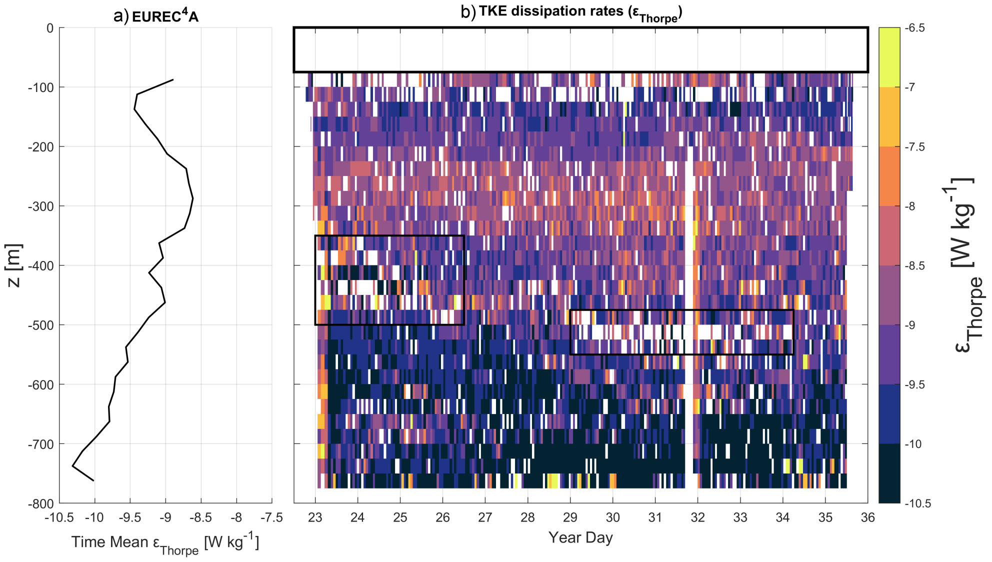

Figure 5.6: TKE dissipation rates estimated from Thorpe Length scales (ε_{Thorpe}). a) Time mean ε_{Thorpe}. b) ε_{Thorpe} for each profile against year day. Black boxes represent regions removed by visual quality control.

the 75 m to 100 m bin.

5.2 RESULTS

In the following section we will explore the structure of TKE dissipation rate estimates, vertical diffusivity, vertical heat flux calculated from vertical diffusivity and background vertical temperature gradient. These structures will then be placed into the broader context in Section 5.3.

5.2.1 TKE DISSIPATION RATE ESTIMATES AND VERTICAL DIFFUSIVITY

In Figure 5.6, 25 m binned TKE dissipation rate estimates from Thorpe scaling across the EUREC^{4}A deployment are shown. There are indications of a potentially elevated region of mixing in the surface based on the mean profile between 75 m and 100 m. A number of bins in this depth range reach values of 1×10^{-7} W kg^{-1}. However, due to a lack of data that passes quality control between 75 m and the surface this could not be explored further. A region of lower ε_{Thorpe} is seen between 100 m and 225 m (ε_{Thorpe} of $(O)10^{-10}$ W kg^{-1}). There is a band of elevated ε_{Thorpe} between 225 m and 350 m with values of up to 5×10^{-8} W kg^{-1}. TKE dissipation rate estimates decrease to

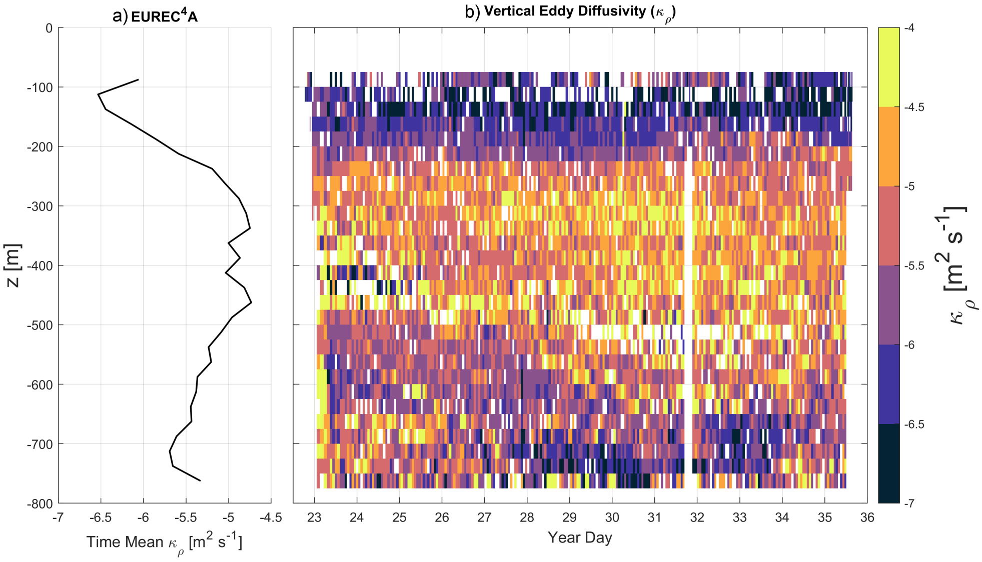

Figure 5.7: Vertical eddy diffusivity estimated from Thorpe Length scales (κ_ρ) a) Time mean κ_ρ. b) κ_ρ for each profile against year day.

$(O)10^{-9}$ W kg^{-1} between 350 m and 450 m on year days 23 to 29. This elevated band deepens to a maximum depth of 625 m around year day 32. ε_{Thorpe} then steadily decreases toward values of 5×10^{-11} at a depth of 775 m.

A similar structure to that of ε_{Thorpe} can be seen in κ_ρ, although the various regions pointed out for ε_{Thorpe} in Figure 5.6 are more pronounced for κ_ρ (Figure 5.7). At the surface, a number of bins with values of up to 5×10^{-5} m^{-2} s^{-1} are present in the 75 m to 100 m bin. Between 100 m and 225 m lower values of κ_ρ (down to $(O)10^{-7}$ m^{-2} s^{-1}), the lowest values of κ_ρ seen in the dataset. Below 225 m κ_ρ increases. The highest values of κ_ρ ($(O)10^{-4}$ m^{-2} s^{-1}) are between 300 m and 450 m. The region of elevated κ_ρ ends at 500 m between year day 23 and 28. The region of elevated κ_ρ then deepens to a maximum depth of 650 m by year day 31. After year day 31 there is a band of low κ_ρ below 650 m with values between 5×10^{-6} m^{-2} s^{-1} to 1×10^{-7} m^{-2} s^{-1}. On year day 23 to 28 there is also a band of higher κ_ρ below 650 m with values up to 5×10^{-5} m^{-2} s^{-1}.

5.2.2 VERTICAL HEAT FLUX

Figure 5.8 shows the distribution of Q for the whole mission. The dominant direction of the vertical heat flux below 75 m is downwards. There is a band of upward heat flux

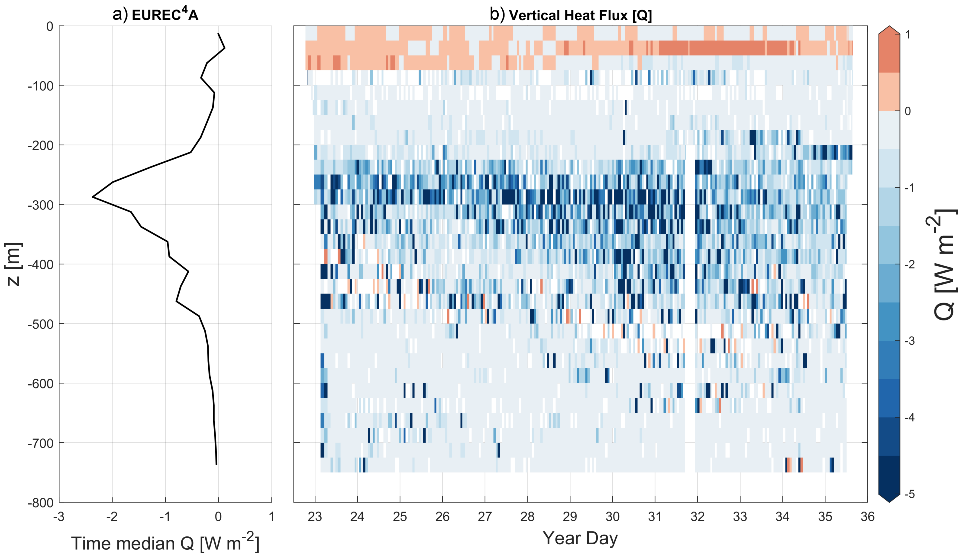

Figure 5.8: Vertical heat flux (Q) calculated from κ_ρ and vertical temperature gradient a) Time median Q flux (Note: time average median used here as for reasons explained in Section 2.4.2, Page 40) b) Q for each profile against year day.

between 0 m and 75 m with an elevated region occurring between year day 31 and 34, related to a strengthening of the subsurface temperature maximum and hence vertical temperature gradient during this time period (Figure 5.3 b). The heat flux in this depth range is completely controlled by the vertical temperature gradient due to having a constant value of κ_ρ applied. Between 75 m and 200 m we see a small downward flux of 0.5 W m^{-1} across the whole mission. Below 200 m down to a depth of 500 m there is a strengthening of the downward heat flux. This depth range also shows occasional regions of upwards heat flux; due to a negative vertical temperature gradient. Between 500 m and 775 m a region of low downwards heat flux (0.5 - 1 W m^{-1}) exists with occasional bins of greater downward flux. This is more defined in the region between 500 m and 650 m on year days 28 through 34, a pattern similar to that of ε_{Thorpe} and κ_ρ in the same regions (Figures 5.6 and 5.7).

Within the context of the other terms in the local heat budget the sensible heat flux (rate of heat gain/loss through the surface), is the smallest of heat sources ($(O)1 - 10$ W m^{-2}) in the study area, with the heat budget being dominated by incoming shortwave radiation ($(O)100$ W m^{-2}), and other terms still being an order of magnitude higher ($(O)10 - 100$ W m^{-2}). When compared to regional models and studies, the surface heat fluxes seen here are an order of magnitude lower at

$(O)0.1$ W m^{-2} compared with $(O)1$ W m^{-2} to $(O)10$ W m^{-2} from both observations and reanalysis (Stevens et al., 2021). When compared with ERA5 reanalysis products the same underestimates of the fluxes can be seen, although this work does capture the diurnal cycle seen in the ERA5 products. Further work from the EUREC^{4}A campaign is currently being carried out. Early work presented by Siddle et al. (2021) supports earlier studies showing that the work presented here is of at least an order of magnitude lower than expected, specifically at the air-sea interface.

It is important to reiterate that the near surface fluxes presented in this work did not use values of κ_ρ calculated from ε_{Thorpe} as was discussed earlier in Section 5.1.2.3. Not having these direct estimates of ε_{Thorpe} and κ_ρ leads to the benefits of studying the air-sea exchange with this dataset being limited.

5.3 DISCUSSION

In this section TKE dissipation rate estimates, vertical eddy diffusivity and vertical heat fluxes will be compared with other open ocean study regions and earlier studies off the Barbados coast. The role of thermohaline staircases in the estimation of ε_{Thorpe} is also examined.

In Abyssal recipes II: Energetics of tidal and wind mixing (Munk and Wunsch, 1998b), a value for open ocean diapycnal diffusivity, κ_ρ of 10^{-4} m^{-2} s^{-1} was given to maintain the abyssal stratification. The value was based on a uniform up-welling over the entire abyssal ocean. This value is unlikely to hold true over the entire open ocean (Garrett and St. Laurent, 2002) due to likely spatial variability of mixing rates. The values seen in this chapter are more in line with the values that are proposed by Garrett and St. Laurent (2002) where κ_ρ is $(O)10^{-4}$ m^{-2} s^{-1} at least 1000 m above rough topography. In our study region the depth is 5000 m or greater (Figure 5.1) with the Seaglider diving to a maximum depth of 780 m, putting the estimates in this chapter in a region outside of 1000 m of any topography. Other studies that present either ε or κ_ρ at least 1000 m above bottom topography were therefore considered suitable for comparison. Studies that match the above criteria include Vic et al. (2018) (North Atlantic), Mater et al. (2015) (South China Sea, Southern Atlantic Ocean and North Atlantic Ocean), Gregg and Sanford (1987) (North Atlantic Ocean) and Wunsch and

Ferrari (2004) (Indian, Atlantic and Pacific Oceans). We will start with the studies that present TKE dissipation rates.

Vic et al. (2018) used shear data from VMP-2000 profiles to estimate TKE dissipation rates. Locations of the VMP-2000 deployments come from stations both over the Mid Atlantic Ridge and away from the ridge to the west. All the stations fit our criteria for suitable comparison. Further detail on the project can be found in Chapter 3. We focus on ε_{shear} from Vic et al. (2018) in the top 1000 m as this depth range is comparable to our study range. Estimates of TKE dissipation rates of $\geq (O)10^{-9}$ W kg^{-1} are seen over the Mid Atlantic Ridge. Estimates away from the ridge are of $(O)10^{-10}$ W kg^{-1}. In our study region, above 200 m and below 500 m show ε_{Thorpe} that are comparable to estimates of ε away from the Mid Atlantic Ridge. Between 200 m and 500 m ε_{Thorpe} is comparable to ϵ from over the Mid Atlantic Ridge.

Mater et al. (2015) looked at three regions in their study. These were the Luzon straight from the Internal Waves in Straights Experiment (IWISE), the Southern Atlantic Ocean as part of the Brazil Basin Tracer Release Experiment (BBTRE) and the North Atlantic Tracer Release Experiment (NATRE), see Mater et al. (2015) and references therein for more details on the individual projects. Of the three regions in their study NATRE is the most representative of quiescent ocean interiors away from rough bottom topography, most similar to that seen in our study. 136 microstructure profiles from the NATRE study site are used in Mater et al. (2015). The NATRE site had no locally enhanced turbulent process due to interactions with topography therefore turbulent processes in this region are deemed to be representative of the ocean interior. The existence of thermohaline staircases is also discussed. Mater et al. (2015) point out that staircase structures can be easily interpreted as overturns (Schmitt, 1994), a point that is discussed later in this chapter. Thorpe scaling was used to estimate ε_{Thorpe}. Quality control by Mater et al. (2015) uses visual examination and exclusions of T/S space with considerable spread along constant lines of σ. Density for N^2required in Equation 2.7 came from a "pseudo" density ($\tilde{\sigma}$) using a profile of Θ with a constant arbitrary salinity. In the upper sections of the NATRE analysis (between 300 m and 600 m) values of $(O)10^{-8}$ W kg^{-1} are seen from ε_{Thorpe} and $(O)10^{-10}$ W kg^{-1} are seen in ε. In our study region we see regimes that fit with both of these numbers with the higher of these values seen between 200 m and 500 m and the lower values seen above 200 m and below 500 m.

The last study that looks specifically at ε is Gregg and Sanford (1987). The work in this study is based on the Caribbean-Sheets and Layers Transect (C-SALT) field program (Schmitt et al., 1987). The study area of C-SALT was the tropical North Atlantic to the east of Barbados, a region that encompasses the area of study in this chapter. Using a multi scale profiler (MSP) 17 profiles to a depth of ~700 m were collected in the centre of a staircase field. TKE dissipation rates were estimated from shear. The rate of dissipation averaged over a staircase from the MSP was 1.9×10^{-10} W kg^{-1}, the noise floor of the instrument, with values up to 4.3×10^{-10} W kg^{-1} seen across interface layers between mixed and stratified regions. The values of ε from the C-SALT study are between one and two orders of magnitude lower than those estimated from Thorpe scaling presented in this chapter.

Wunsch and Ferrari (2004) looks at values of κ_ρ rather than ε and focuses on deeper waters than are present in this chapter. They are still included here as a useful comparison for background values in quiescent open oceans. Table 1 in Wunsch and Ferrari (2004) lists values of κ_ρ for the Atlantic, Indian and Pacific oceans (both for deep [2000 m to 3800 m] and bottom [3800 m or deeper]) as well as bringing in 6 more specific study regions (Scotia Sea, Brazil Basin, Samoan Passage, Amirante Trench, Discovery Gap and the Romanche Fracture Zone). The Atlantic ocean values are taken from Ganachaud et al. (2000) where κ_ρ is based on a one dimensional global balance. For the deep Atlantic a value of $3 \pm 1.5 \times 10^{-4}$ m^{-2} s^{-1} is given, a value marginally smaller than those seen in the Pacific or Indian oceans ($4 \pm 1 \times 10^{-4}$ m^{-2} s^{-1} and $4 \pm 2 \times 10^{-4}$ m^{-2} s^{-1} respectively). The estimations in this thesis (Figure 5.7) are an order of magnitude or more smaller than the values from Ganachaud et al. (2000). A direct comparison here is more difficult as values of κ_ρ by Ganachaud et al. (2000) have been derived from basin wide and depth averages. A second value for the North Atlantic is also given elsewhere in the study, which is $(O)10^{-5}$ m^{-2} s^{-1} between 800 m and 2000 m, a value that is the same order of magnitude seen at the deepest sections of the estimates of κ_ρ presented above.

5.3.1 THERMOHALINE STAIRCASES

Thermohaline staircases are a sequence of mixed layers ranging from tens to hundreds of meters separated by steep gradient interfaces (Merryfield, 2000).

Staircases are found where temperature and salinity gradients both share the same sign in a manner that favours a double-diffusive regime (Schmitt, 1994). The vertical gradients of temperature and salinity in the background hydrography in this chapter (both decreasing downwards, Figure 5.2) suggest thermohaline staircases are possible below 100 m. We will now use two diagnostics to investigate this in more detail. The formation of thermohaline staircases is closely linked to the effects of thermal expansion and haline contraction. There are two methods of representing the effects of thermal expansion and haline contraction.

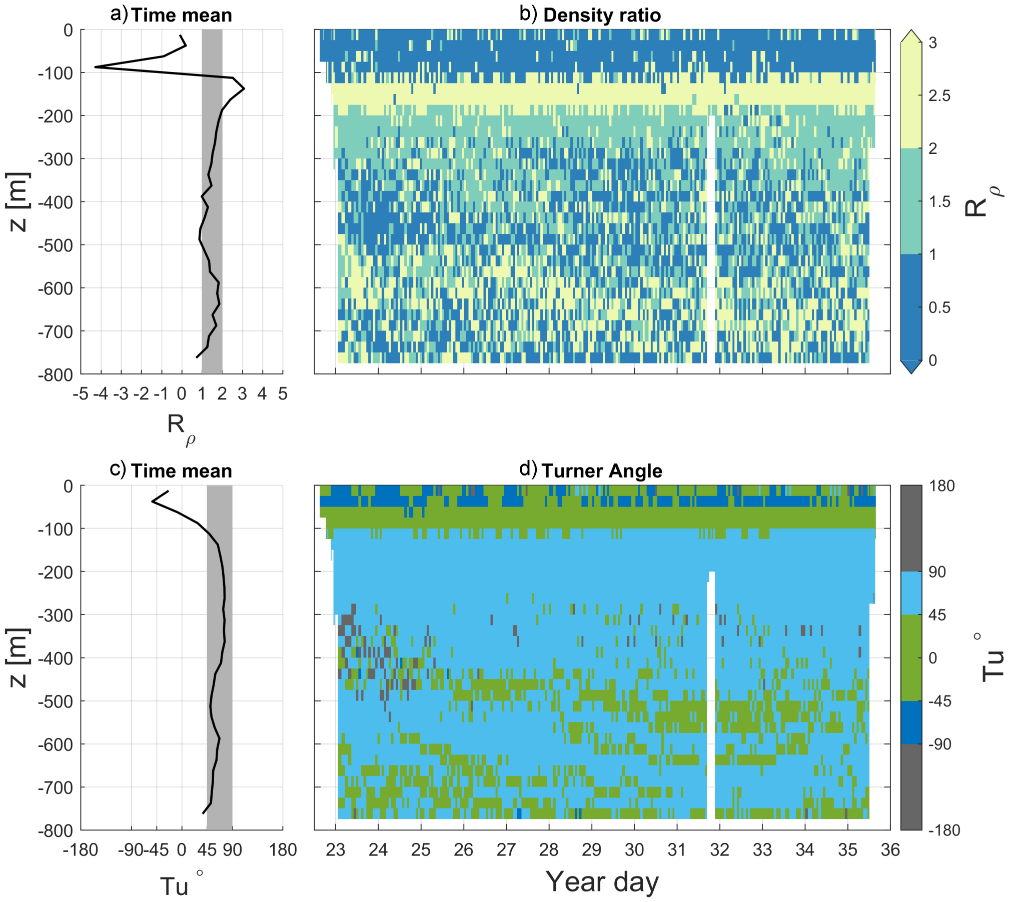

Figure 5.9: Density ratio and Turner angle. a) time mean density ratio, b) individual profile density ratio, c) time mean Turner angle d) individual profile Turner angle. All data is binned to 25 m. The grey highlighted region in a) and c) indicate water column properties that favour the formation of thermohaline staircases.

The first representation is the Turner angle (Tu, Equation 3.5). To form thermohaline staircases Tu must fall within the diffusion-convection ($-90° \leq Tu \leq -45°$) or salt fingering ($45° \leq Tu \leq 90°$) regimes, both of which are double-diffusive

(Rollo et al., 2021; George et al., 2020). The dominant of the two regimes in this study area is the salt fingering regime (seen in Figure 5.9). The second representation is the density ratio (R_ρ, Equation 3.2). The value of R_ρ must lie within a specific range for staircases to form. At the lower end R_ρ must be > 1. The upper limit is less well constrained with values ranging from $R_\rho = 1.6$ (Gregg and Sanford, 1987) and $R_\rho = 1.7$ (Schmitt et al., 1987) to $R_\rho = 2$ (Fer et al., 2010) or greater, with an upper limit of $R_\rho = 100$ suggested by Merryfield (2000).

Regions of the water column where thermohaline staircases could compromise estimates of TKE dissipation rate were investigated. A range of $1 \leq R_\rho \leq 2$ and $45^\circ \leq Tu \leq 90^\circ$ were used as the bounds for where thermohaline staircases are likely to be found in our dataset. Turner angles and density ratios for the EUREC^{4}A deployment can be found in Figure 5.9. Above 200 m R_ρ is outside our proposed range for thermohaline staircase formation (both $R_\rho < 1$ and $R_\rho > 2$). Between 200 m and 600 m R_ρ sits within our suggested range. Turner angles are consistently in the salt fingering regime from 100 m to 300 m and intermittently between 300 m and 500 m. Below 500 m horizontal bands of Tu in the salt fingering and statically stable regimes make up the rest of the water column. In the following section we will focus on the water column below 200 m with specific examination of the band of elevated ε_{Thorpe} between 200 m and 300 m.

5.3.2 THE IMPACT OF THERMOHALINE STAIRCASES ON THORPE SCALED ESTIMATES OF TKE DISSIPATION RATES

Mater et al. (2015) raise the issue of thermohaline staircases being mistaken for temperature overturns when there is no true overturn. As stated in Section 1.1.3, the Thorpe scale method relies on identifying the breaking of density overturns (such as a Kelvin-Helotz billow). This is a mechanical process that mixes waters converting APE to TKE. In comparison to this, the double diffusive regime required to generate thermohaline staircases (as seen in this area of study) does not require mechanical mixing (van der Boog et al., 2021). Here there is a destabilising salinity stratification within a statically stable density regime that cause these staircases. Re-stratification occurs by the release of potential energy from the unstable component (in this case salinity) leading to a counter-gradient buoyancy flux (Radko, 2013). These two

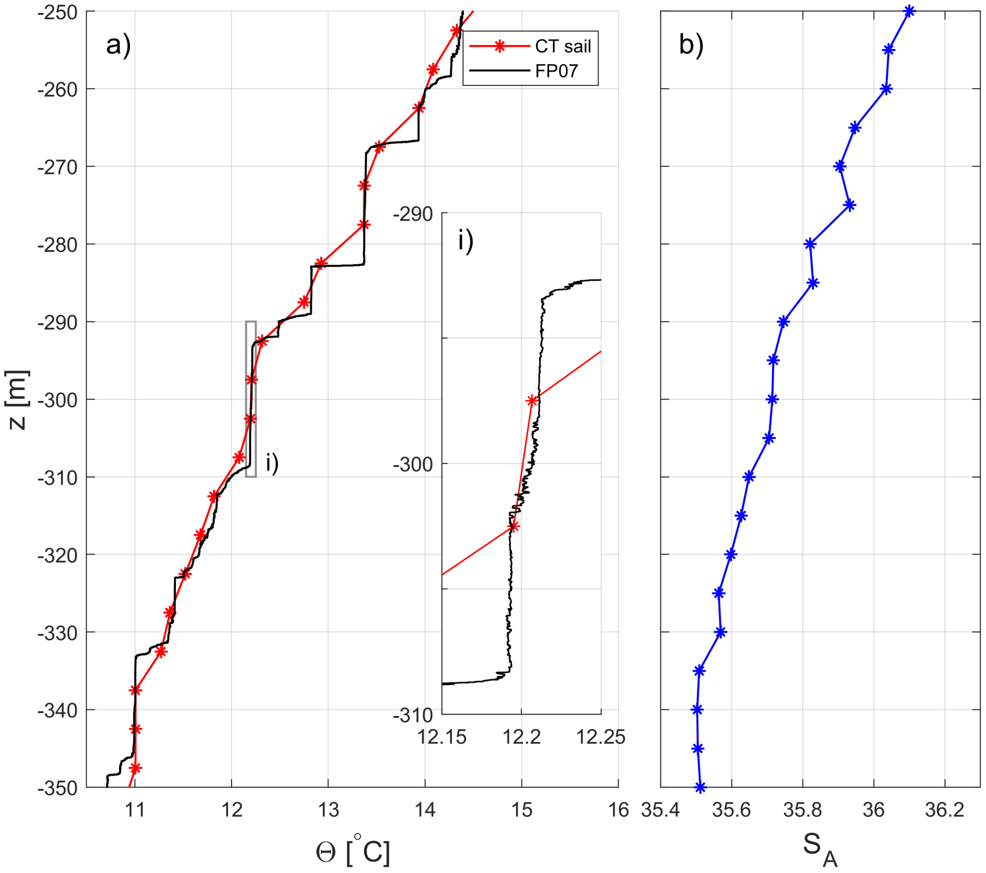

Figure 5.10: Conservative temperature (Θ) and absolute salinity (S_A). a) Θ from CT sail and FP07 thermistor. Area in grey rectangle (i) shown in greater detail in inset box i). b) S_A from CT sail

methods of releasing potential energy are in contrast with Thorpe scaling which requires some sort of mechanical component whereas double diffusion does not.

It is known that thermohaline staircases can be interpreted by Thorpe scaling algorithms as physical overturns, when in reality they are not. This will lead to potential positive bias in values of ε_{Thorpe}. Estimates of TKE dissipation rates will be higher when these false overturns are included in the vertical averaging process. The area of the EUREC^{4}A field deployment is a known area of thermohaline staircases from the C-SALT field campaign in the 1980s (Schmitt et al., 1987). Consideration must then be given to the fact that some realisations of ε_{Thorpe} may be overestimates due to contamination from thermohaline staircases compared to what might be expected for open ocean (Ganachaud and Wunsch, 2001).

Between 200 m and 300 m in Figure 5.6 we see a band of higher values of

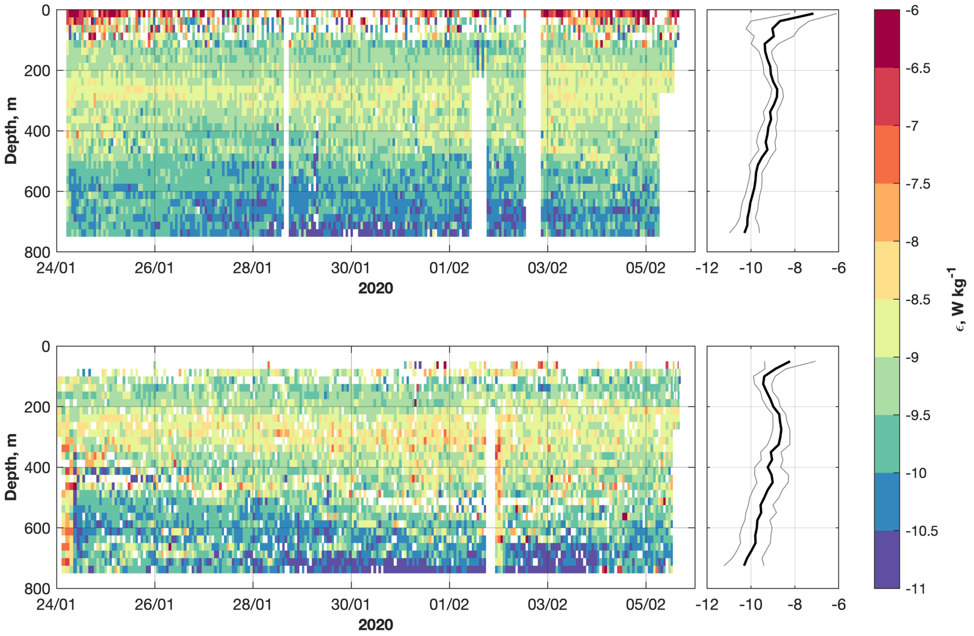

Figure 5.11: TKE dissipation rate estimates from Sheehan et al. (2021) (upper panel) and from Thorpe Scaling (lower panel, replicated from data in Figure 5.6) with associated time means and standard deviations. Image provided by Peter Sheehan Sheehan et al. (2021)

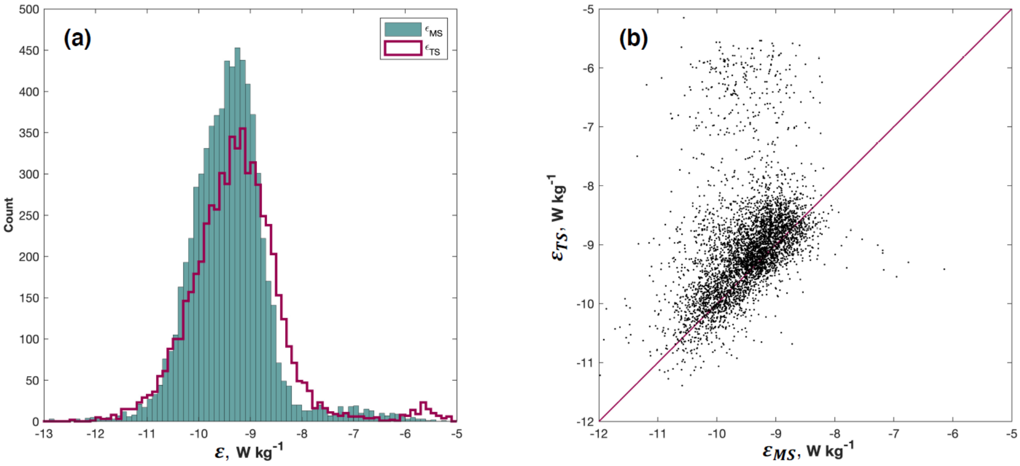

Figure 5.12: Comparison of 25 m binned ε_{Thorpe} and ϵ_{ms}. a) Histogram of number of bins and ϵ values. b) scatter plot of ϵ_{ms} against ε_{Thorpe}. Image provided by Peter Sheehan Sheehan et al. (2021)

ε_{Thorpe}, $(O)10^{-9}$ W kg^{-1}, a region that sits within favourable R_ρ and Tu regimes for thermohaline staircases. Visual inspection of a number of fast temperature profiles through these depths show the existence of staircase structures. An example of thermohaline staircases can be seen in Figure 5.10. The figure clearly shows the difference in resolution between the low resolution (CT sail) and high resolution temperature (FP07). The question then is do these staircases cause a positive bias in the ε_{Thorpe}? In Figure 5.11 the Thorpe scale methods from this chapter are compared to values of TKE dissipation rates (ε_{ms}) estimated from the same fast temperature data but using temperature variance. The temperature data was processed using a toolbox developed by Benjamin Scheifele and Jeffrey Carpenter (github.com/bscheife/turbulence_temperature), and described in full in Scheifele et al. (2018), and based on the theory presented by Peterson and Fer (2014). This method was also used recently by Howatt et al. (2021). Quality control was then provided by applying second order polynomials to the theoretical and observed spectra following Scott et al. (2021). Comparing ε_{ms} to ε_{Thorpe} (Figure 5.11) a good match is seen in regions of elevated TKE dissipation rates, although ε_{ms} shows a narrower horizontal band of elevated dissipation rates centred more closely around 300 m than ε_{Thorpe} which shows a greater depth range. ε_{ms} also shows less patchiness across the entire dataset compared with ε_{Thorpe}. Thorpe scaling identifies individual overturns (which are not equally spaced) that are then vertically averaged. In comparison Sheehan et al. (2021) integrates spectra over half-overlapping 32 second long segments before vertically averaging them. Below 300 m the two sets of estimates diverge with values ε_{Thorpe} staying elevated in some cases to as deep as 400 m with a second peak seen around 450 m. In the region below 300 m ε_{ms} shows lower values, suggesting that in this region there is a potential positive bias from the Thorpe scaled values compared to those from temperature variance. This suggests that the values of ε_{Thorpe} are comparable to those from other methods in the same region, with the potential to have a positive bias in these estimates in some areas of the water column. Figure 5.12 a, shows the spread of ε_{Thorpe} and ε_{ms}. Values of both share a peak at 6×10^{-10} W kg^{-1}, with ε_{Thorpe} showing more bins between 10^{-9} to 10^{-8} W kg^{-1} than ε_{ms} suggesting a potential overestimation of TKE dissipation rates in that range. In addition there is a region of ε_{Thorpe} peaking in $(O)10^{-6}$ W kg^{-1} not present in ε_{ms} also suggesting some overestimation at the upper limits. Figure 5.12 b, shows a scatter of the two methods for estimating ε against each other. Higher TKE dissipation rates can be seen than the equivalent bins in ε_{ms}.

The observed elevated values of TKE dissipation rates within staircase regimes are supported by Schmitt et al. (2005), where they show that salt fingering regions can enhance vertical diapycnal mixing by up to 5 times. They estimate TKE dissipation rates between 0.4 and 2.3×10^{-9} W kg^{-1} in thermohaline staircase regions. In the 200 m to 300 m section of the water column the values obtained in our study are in line with Schmitt et al. (2005), giving ε_{Thorpe} of $(O)10^{-9}$ W kg^{-1}. The greater spatial and temporal variability seen in ε_{Thorpe} compared to ε_{ms} which may be attributed to the Thorpe scale algorithms. In addition the work presented here still assumes that the dissipation rates seen here are driven by mechanical mixing, which may not be the case. Although the estimates of TKE dissipation rate are supported by alternative methods presented by Sheehan et al. (2021), a more in depth analysis of the interaction between the Thorpe Scale algorithms developed in this thesis and the regions of double-diffusion needs to be carried out to address potential false overturn identification.

5.4 SUMMARY

5.4.1 SUMMARY OF AIMS

At the beginning of the three questions were posed to be investigated,

- Can the the methods developed in this thesis be successfully applied to a tropical open ocean dataset?
- How do the values of TKE dissipation rate estimates from Thorpe scaling compare to other open ocean studies?
- How do thermohaline staircases influence Thorpe scale estimates of TKE dissipation rates?

in the following section a summary to these questions is provided.

5.4.2 APPLICATION TO OPEN OCEANS AND A LONGER DATASET

The application of the methods described in Chapter 2 to the EUREC^{4}A dataset was successful. The application was a simple process with no algorithmic issues occurring, even though the dataset was 10 times greater in length than any of the previous datasets seen in this chapter. This also provided enough profiles for a robust set of time mean values to be generated (Smyth and Thorpe, 2012). Mission specific quality control was applied as with previous datasets. Due to the hydrographic properties of the region and the improved functioning of the Seaglider, less mission specific quality control was required compared to the datasets presented in Chapters 3 and 4.

5.4.3 COMPARISON TO OTHER STUDIES

TKE dissipation rates and vertical eddy diffusivities were compared to other open ocean studies, including studies in the same geographic region. The comparison to the other studies show promising results from the Thorpe scaled estimates. There are no values seen here (after quality control) that are consistently higher ($> (O)10^{-8}$) or lower ($< (O)10^{-11}$) than other open ocean studies. We present TKE dissipation rates with lower values of $(O)10^{-11}$ up to higher values of $(O)10^{-8}$. A band of elevated ε_{Thorpe} between 200 m and 300 m is the region that shows the largest difference between the results presented here and estimates given by other studies. TKE dissipation estimates below 600 m fit well with background levels of ε from other open ocean studies. Vertical diapycnal eddy diffusivities compares better with other studies than TKE dissipation rates, including the background value set in (Munk and Wunsch, 1998a).

5.4.4 INFLUENCE OF THERMOHALINE STAIRCASES

Mater et al. (2015) showed that thermohaline staircases can have an impact on estimates of ε_{Thorpe} and may result in positive (overestimating) bias. The suggested overestimates due to contamination of TKE dissipation rate estimates from thermohaline staircases can be seen this chapter, especially below 300 m. When compared to temperature variance estimates of TKE dissipation rates from the same fast temperature data, some of the regions of elevated dissipation are not just a result of bias on Thorpe scaling thermohaline staircases. Further work is however, required to properly investigate the impact of staircase structures on this dataset and the magnitude of the bias.

This chapter has shown that the methods developed in this thesis can be applied to a longer open ocean dataset, provide estimates of ε_{Thorpe} and κ_ρ that are generally comparable to other studies and show that there may be a positive bias in the values of ε_{Thorpe} due to thermohaline staircases. Further work is required to examine the exact nature of this. In the following chapter the original questions set in Chapter 1 will be discussed, further work on the subject suggested and an overall summary to the thesis will be provided.

6

SYNTHESIS

In Chapter 1 we introduced the concept of ocean mixing, the key theory required for understanding the work presented in this thesis and the questions that we aimed to answer with our study. Chapter 2 lays out the final methodology that was developed as well as a number of considerations that went into the development (e.g. determining a value of N^2 for the estimation of ε_{Thorpe}) and discussion of other indirect methods. Chapter 3 expanded on the development of the methods in Chapter 2 and compares TKE dissipation rate estimates from Thorpe scaling to those from shear data. The work done in Chapter 4 tests the methods on autonomous ocean gliders rather than vertical microstructure profilers and determined what changes were required to make the methods function correctly to this new application. Regional and temporal investigation was completed around the Wyville Thomson Ridge. Then in Chapter 5 we showed that the methods developed in this thesis can be applied to other regional datasets and that we can get comparable TKE dissipation rates and vertical eddy diffusivities to other studies. We also identified that the methods may overestimate both ε_{Thorpe} and κ_ρ when compared to other studies, especially in regions where thermohaline staircases exist.

In the first three sections of this final chapter we will answer the questions posed in the first chapter of this thesis using our new findings alongside information from supplementary studies. The questions posed in Chapter 1 were,

1. How can the Thorpe Scale algorithm be applied to high resolution temperature datasets from microstructure systems? Considering that:
    (a) Only temperature is being used, where traditionally density is used for Thorpe Scaling and the physical issues that come from this
    (b) The resolution of data is an order of magnitude greater than the traditional CTD data this method is applied to.
2. What challenges arise from Thorpe Scaling high resolution temperature data from gliders? Considering that:
    (a) Gliders both do not move vertically through the water and don't measure their exact path through the water
    (b) A glider is a less stable platform for collecting microstructure data that a free fall profiler
3. Do values of turbulent kinetic energy dissipation and associated products from Thorpe Scaling high resolution temperature fit with estimates of the same products from other methods across different oceanic regions? Considering that:
    (a) Temperature based Thorpe Scaling is heavily dependant on the temperature and salinity, which is considerably varied across oceanic regions.
    (b) Thorpe Scaling may under- or over- estimate turbulent kinetic energy dissipation given the local conditions.

The final sections of this chapter will then focus on how our study compares with other studies, how would other methods have impacted this work and suggest further works that could be explored. We finish with a final summary of the entire thesis and relevant outcomes.

6.1 HOW CAN THE THORPE SCALE ALGORITHM BE APPLIED TO HIGH RESOLUTION TEMPERATURE DATASETS FROM MICROSTRUCTURE SYSTEMS

Firstly a question of "Is it conceptually possible to apply traditional Thorpe scaling algorithms to temperature profiles?" must be asked. At a theoretical level the difference is minimal. Before exploring Thorpe scaling temperature we revisit the development of the Thorpe scale method. The initial work of the Thorpe scale methodology was conducted by Thorpe (1977) in a Scottish loch (Loch Ness, a freshwater body), where current velocities, shear and temperature were measured. Temperature was used to infer density, and this density was used to develop the Thorpe scale method. In this instance temperature was the completely dominant variable on density, as there is no salt present in Loch Ness. This demonstrates that there is no difference between Thorpe scaling using temperature compared with density in a location where temperature is the dominant factor influencing density. In the ocean however, the answer to the question is more complex due to the presence of dissolved salts. This added complexity has not, however, prevented other studies from using temperature successfully as a proxy for density when Thorpe Scaling. These studies include Mater et al. (2015) and Ijichi and Hibiya (2018). These Studies showed that it is possible to get estimates of TKE dissipation rates from Thorpe scaling that compare well with studies showing estimates of TKE dissipation rates from shear data. The success of these studies is linked to robust quality control of the temperature data and determining regions of the water column to be excluded where salinity was a dominant control on density. More recently Howatt et al. (2021) and the work in this thesis have also shown that TKE dissipation estimates derived from Thorpe scaled glider data can also be comparable to those from shear data. This is also attributed to robust quality control and the exclusion of salinity dominated regions of the water column.

This shows that Thorpe scaling can be applied to temperature as a proxy for density. However, to apply the Thorpe scale method to temperature a number of factors need to be considered. These considerations can be split into two broad groups. The first is what are the differences between applying the method to temperature over density, discussed in Section 6.1.1. The second consideration is how the resolution, specifically high 512 Hz resolution, impacts the methods and is discussed in Section 6.1.2.

6.1.1 WHEN ONLY USING TEMPERATURE WHAT ARE THE PHYSICAL DIFFERENCES WITH DENSITY AND ISSUES THAT ARISE SURROUNDING THIS

To develop a methodology for Thorpe scaling temperature a number of studies were investigated to determine what current methods currently exist in the literature. During early steps of the methodological development there was a focus on general data quality control and preparation. Later steps focused more on temperature specific considerations.

Before delving deep into the methodologically developments it is worth re-stating why certain quality controls are required. As discussed in Section 1.1.3 Thorpe scaling relies on the existence of mechanical mixing in the form of over turning regions. This leads to two keys areas of investigation. Firstly, are the overturns seen in temperature space true overturns or are they compensated and are in fact statically stable. Secondly is the turbulent mixing in the region actually related to mechanical processes or other processes that can mix the oceans waters.

REMOVING FALSE OVERTURNS

Firstly we examine false overturns. When using Thorpe scaling (temperature or density) it is important to clean the datasets, to mitigate false overturns that could contaminate ε_{Thorpe} biasing the results both positively (large false overturns from salinity spikes) and negatively (small false overturns from instrument noise).

Early work by Galbrath and Kelley (1995) proposed the following steps for ensuring quality of the data used for Thorpe scaling (density or temperature).

1. Defining the resolution required to detect an overturn, to identify the smallest overturns detectable from the data, especially when taking into account sensor response time and the path of a CTD through the water column.

2. The run-length test, used to remove overturns considered spurious due to their length when compared to a noise threshold.

3. A water mass test, removing regions of the water column with lateral intrusions of salinity in T/S space using visual inspection of each overturn.

The run-length test (as described by Galbrath and Kelley (1995)) was also tested here (Appendix A) but was discarded as it performed poorly when applied to high resolution data. With the intention of comparing fine scale parametrization to Thorpe scaling Howatt et al. (2021) provided a different method for removing spurious overturns instead of using run-length tests (Galbrath and Kelley, 1995) or visual inspection (Gargett and Garner, 2008). Howatt et al. (2021) determined that an overturn was real where the density displacement was greater than twice that of the instrument noise (glider CTD). They also developed an overturning ratio to remove overturns that were non-symmetric. This recent study describes alternative quality control methods; however, they were not explored within this work as the data processing stages had already been completed.

All the considerations above are applicable to both density and temperature Thorpe scaling. But what cleaning is required that is specific to temperature alone? The most obvious difference between a profile of density and a profile of temperature is that if the density gradient is negative upwards then the water column is stable, so unlikely to vertically overturn (Talley et al., 2011). If we reorder density to be monotonically increasing with depth the water column is considered stable. The same cannot be said of temperature. Although across most of the world's oceans temperature is the driving force behind density (a majority of the world's oceans sit in a very narrow salinity band) it is not the driving factor everywhere. Regions such as those at high latitudes and those with high fresh water input (larger rivers or high rainfall) have important salinity inputs (Talley et al., 2011). The assumption in using temperature as a proxy for density when Thorpe scaling is that if temperature is reordered to be monotonically decreasing with depth the water column will be statically stable. Where temperature is the dominant control on density this is likely to be the case. However, the validity of this still needs to be addressed for a water column structure or study region. The first step is to remove any regions of the water column that are salinity dominated. Visual inspection of the water column in T/S space was used by Mater et al. (2015) to remove regions of the water column before any further processing was conducted. This method was also implemented on the data described in this thesis. This was done by visually inspecting T/S plots for a given deployment (seen in Chapters 3, 4 and 5). The deep dataset presented in Chapter 3 shows considerable interleaving in T/S space between 700 m and 900 m. This interleaving is due isopycnal rather than diapycnal energy transfer, a physical process that Thorpe scaling is not capable of processing. This example provides a clear example of where mixing in a region is not dominated by the mechanical process (such as the breaking of internal waves). The elevated estimates of TKE dissipation in this band highlight the issues that would arise if such regions would be left in calculating regional means. Especially if this product would then be fed into a model for example.

During processing, a second method of temperature specific quality control was investigated using the Turner angle (Tu) and the stability ratio (R_ρ) (IOC et al., 2010) to exclude data that was salinity compensated. Using R_ρ, Ijichi and Hibiya (2018) removed any overturns identified by their algorithms where $-0.5 \leq R_\rho \leq 2$. Although this method was investigated here (Chapter 3), it removed over 90% of overturns seen. By comparing our pre-masked ε_{Thorpe} with ε_{Shear} from Vic et al. (2018) it was clear that without the removal of any bins of ε_{Thorpe} the two matched reasonably well and that the masking process biased the results away from ε_{shear}. Instead, the method was examined in conjunction with Tu as a method of excluding 25 m bins. Tu proved to be a poor method removing less than 10% of bins and having no discernible impact on the time average. At the other extreme excluding bins where $-1/2 \leq R_\rho \leq 2$ removed up to 40% of bins but had a similar impact to using Tu with a minimal difference between the time means. A third method was then developed to remove bins based on the variation of salinity with the variation of temperature within a given bin. This method aimed to account for the isopycnal vs diapycnal influences on a given bin, removing those where the isopycnal processes had a greater impact than the diapycnal processes. To make this method usable in multiple regions the variation was normalised so that a single cut off value can be used as a mask limit irrespective of the location, allowing for datasets to be more easily compared. The final cut off value was set as 0.5 for this quality control step. Prior studies typically complete quality control at the overturning stage before calculating L_T and estimating ε_{Thorpe}. One of the benefits arising from applying extra quality control later in the process is that we are not removing the possibility of smaller overturns being included in our final results.

BUOYANCY FREQUENCY CONSIDERATIONS

An important difference between temperature and density when Thorpe scaling is ensuring a suitable value of N for estimation of ε_{Thorpe} (Equation 2.7) is provided. This values of N needs to represent the background stratification that an overturn is attempting to over come. When Thorpe scaling density N is calculated across the region of reordered density. This is not possible when using reordered temperature. A number of different methods for determining N have been presented (Mater et al., 2015; Ijichi and Hibiya, 2018).

The two methods that they put forward are the Bulk and Mean methods (See Chapters 2 and 3 for details). As well as these methods we also examined using a fixed N (based on the profile mean), as well as using the N from binned density from CT data (SBE3 on the VMP-2000 or glider CT sail). Although not developed further the fixed N method was a useful developmental metric. It was used to check that variation seen in ε_{Thorpe} could be attributed to variations in L_T and not variability in N^3. The other three variants were all examined in more detail. Of the three, the mean values proved the poorest fit (Chapter 3) giving overestimates of N when compared with all the other methods, where N from density was considered the ideal result. The Bulk method provided a good match for N but showed a number of erroneous regions with values up to two orders of magnitude greater than the N from density. As such the closest N from density to the depth of the overturn centre was used throughout the rest of the thesis.

A different potential process would be to attempt to use micro conductivity probes to provide a high-resolution density. Such probes have been attached to both profilers and gliders (Wolk et al., 2009; Sutherland et al., 2013; Fer et al., 2020). However, due to the shape of the probes (a two-pronged trident) if used for more than a couple of hours they typically get blocked with detritus the degrades the data, making them unsuitable for longer deployments.

6.1.2 WHAT CONSIDERATIONS ARE REQUIRED WHEN APPLYING THORPE SCALING TO HIGH RESOLUTION TEMPERATURE DATA

Once considerations are taken into account for Thorpe scaling temperature rather than density a few considerations are still needed to account for the resolution difference.

Before estimating ε_{Thorpe} from high resolution temperature, the temperature data needs to be processed in such a way to remove instrument related noise that could be picked up as overturns. The first step in doing this was to apply a 100 Hz low pass filter to the data. The 100 Hz threshold was picked based on work by Sommer et al. (2013). They showed that although the recording frequency of a FP07 fast thermistor was 512 Hz the response time of the instrument was lower and equates to consecutive samples at 100 Hz being independent of each other. The second step was to bin the data based on the along path speed of the platform, providing the smallest independent measure of temperature.

However this step alone still provides a large number of very small $O(0.1)$cm, which dominate vertical binning estimates, and in turn time means. Compared with using lower resolution temperature (or density) data the smallest overturns are limited by the resolution of the sensors, resulting in either smaller overturns being removed as noise or not being identified. This has the potential of biasing our results negatively, compared with the positive biases normally expected from Thorpe scaling estimates on low resolution data.

To mitigate some of the potential negative bias smaller overturns where combined into overturning regions as in Ijichi and Hibiya (2018). Ijichi and Hibiya (2018) used a minimum region size of 5 m, combining overturns smaller than this within 1 m of other overturns into a single region until greater than 5 m. We used a minimum of 2 m regions, combining overturns within 1 m of each other (Carter, 2020). The same range limits were placed on overturn length by Howatt et al. (2021). By reducing the minimum region range we aimed to balance resolution and noise. By applying this step, we were able to utilise the high resolution data to find small over turns but limited their potential impact on means by combining groups of these overturns into overturning regions.

During the algorithm development phase of the study run-length tests were also investigated as a potential method for the removal of these smaller overturns. When applied to low resolution 0.2 Hz CT sail data this worked well. However, due to the number of smaller overturns picked up from the fast thermistor the cut off value where the dataset crossed over the noise threshold (based on Galbrath and Kelley (1995)) was a run length of 2. This cut off removed very few overturns. Due to this the run-length method is a poor-quality control step method for dealing with high resolution output.

6.1.3 AVERAGING CONSIDERATIONS

One unexpected aspect that was encountered during the development of the methods presented here was the impact of averaging methods. The core issue is due to the difference between arithmetic and geometric means (both defined in Chapter 2). The arithmetic mean assumes a normal distribution, but the geometric mean assumes a log-normal distribution. ε_{Thorpe} has a log-normal distribution. When values span a number of orders of magnitude (typical of TKE dissipation estimates) the arithmetic mean is biased by larger values. To counter this effect it is suggested that a geometric mean is used (a variant on this was used throughout the thesis). This takes into consideration a potential range of magnitudes. Unfortunately few previous studies actually declare the method of averaging that is used. More recent studies including Howatt et al. (2021) and Sheehan et al. (2021) have declared the averaging methods used. In the case of Howatt et al. (2021) they use both arithmetic and geometric means of ε_{Thorpe} and the difference in these means is typically of an order of magnitude. A similar order of magnitude difference in means was seen when comparing published ε_{shear} from Vic et al. (2018) to ε_{Thorpe} and ε_{shear} in this thesis (Chapter 3), although the structure was equivalent. The difference from averaging TKE dissipation rate estimates using arithmetic and geometric means can cause difficulty when comparing different studies when the full method isn't provided.

Averaging vertically is also important with Thorpe scaling data (of any resolution). Due to ε_{Thorpe} being calculated for discreet overturns rather than fixed length time windows, comparing profile to profile is difficult unless the estimates are binned vertically in some manner. In this thesis it was decided that a bin depth of 25 m provided a good balance between vertical resolution and moise reduction. A range of different depth windows were investigated (1, 10, 20, 25 and 50 m). To do this binning, the mid point depth (the 'point' method) of each overturn was used. This prevented a single overturn affecting multiple bins. A comparison of this to 'pillar' binning can be found in Chapter 3, with the 'pillar' method giving overestimates of ε_{Thorpe} compared to those of the 'point' method.

The final aspect to the averaging is how many profiles or data points are required to create a robust average of ε_{Thorpe}. Smyth and Thorpe (2012) suggests that an order of 100 profiles are required to provide a robust estimate of ε_{Thorpe}. From the work conducted here, a larger number of profiles definitely provides an improved final estimate and reduces standard deviation. However, the work in Chapter 3 shows that closer to 25 profiles can provide a robust value time mean. Where the Ridge Spring and Neap data subsets both provide the closest comparison with the shear estimates is at depths where the greatest number of profiles are averaged together. Where less than 5 profiles are averaged, the standard deviations are largest. Increasing the number of profiles will usually give better mean values of ε_{Thorpe} (assuming the data is of good quality) and therefore, although large number of profiles (≥ 100) are unrealistic from vertical microstructure profilers, this is more readily achievable using gliders.

In this thesis we have investigated using the Thorpe scaling method to estimate TKE dissipation rates from high resolution temperature data. This involved understanding the differences between Thorpe scaling of density and temperature and the extra steps Thorpe scaling temperature data requires. We also investigated the extra considerations needed when applying methods to the high 512 Hz resolution temperature data over standard CTD resolution temperature data. Using a mixture of existing and newly developed methods we provide a robust platform agnostic methodology for applying Thorpe scaling to high resolution temperature data.

6.2 WHAT CHALLENGES ARISE FROM THORPE SCALING HIGH RESOLUTION TEMPERATURE DATA FROM GLIDERS

In the previous section we discussed the considerations required when Thorpe scaling temperature versus density. The second overarching question that we aimed to answer was what impact does the platform have on estimates of TKE dissipation from Thorpe scaling? Answering this takes into account platforms including CTDs mounted on rosettes deployed from ships, CTDs and FP07s from vertical microstructure profilers and CT sails and FP07s on gliders.

One major difference between the platforms is the angle of travel through the water column (discussed in more detail below). However, before investigating the motion of a platform (and hence the sensor) through the water column, it is important to be aware of the differences between how each platform determines its speed and direction through the water column. During the conversion of raw microstructure files to physical units, the ODAS MatLab library requires a speed through the water. A vertical microstructure profiler provides this from measured dP/dt (where P is pressure) (Lueck et al., 2018). But a MicroPod system mounted on a Seaglider does not directly measure pressure or speed (Creed et al., 2015; Lueck et al., 2018), so requires these data from the glider provided in the form of a hotel file during processing. Requiring a hotel file adds an extra step to the conversion stage but has no other impact on the outputs. This makes the data from a Seaglider more reliant on the glider flying well, highlighting the importance of a well tuned flight model (Frajka-Williams et al., 2011; Queste, 2013).

6.2.1 WHAT IS THE IMPACT ON ESTIMATES OF TURBULENT KINETIC ENERGY DISSIPATION RATES FROM THE DIFFERENCE IN ANGLE OF TRAVEL THROUGH THE WATER COLUMN

The passage through the water column is the key difference between a vertical profiler and a buoyancy driven glider. It is vital to understand the impact this difference has on Thorpe scaling a profile. To correctly process data for Thorpe scaling, change in pressure needs to be monotonic (Gargett and Garner, 2008). When using a CTD rosette on a tight cable (i.e. coupled to the motion of the ship), pressure inversions due to ship movement in swell need to be removed. This is to prevent spurious overturns that are related to the platforms path through the water. When using an untethered vertical profiler (such as a VMP-6000) this is unlikely to be an issue. When using a tethered profiler (such as a VMP-2000, used in Chapter 3) enough slack needs to be let out on the tether to de-couple ship motion and profiler motion (Lueck et al., 2002). A profiler that falls at a rate of ~0.5 m s^{-1} is travelling fast enough to be minimally influenced by wave induced horizontal and vertical motions and probes on these platforms will cross isopycnals as if they were frozen (Lueck et al., 2002; Thorpe, 2012). To aid in removing pressure inversions the ODAS Matlab library will isolate full profiles based on pressure continuously monotonically changing (Lueck et al., 2018).

In contrast to a vertical profiler, a buoyancy driven glider does not fall through the water vertically but typically between the angles (ϕ) of 14° and 45° to the horizontal (Eriksen, 2009). In addition to this a glider is more likely to feel the influence of the internal wave field (Smyth and Thorpe, 2012; Thorpe, 2012). The glider must be flown in such a way to minimise these influences. Ideally the glider needs to be flown with a large ϕ in a region where the vertical aspect ratio of a wave is large. Smyth and Thorpe (2012) suggests that flying a glider perpendicular to the direction of dominant internal wave propagation will also reduce bias as a result of the interaction of the gliders angle through the water and internal waves (in Chapter 4 the glider was flown parallel to the main flow). Knowing the main direction of the internal wave field in advance is not always possible but if possible should be taken into consideration when determining your deployment or the suitability of the Thorpe scale method. This is particularly the case when using temperature or density from a glider's CT sail due to the already limited ability to identify smaller overturns, leading to potentially even larger positive bias in ε_{Thorpe}. Although estimates of TKE dissipation rates from Thorpe scaling glider data can over or underestimate TKE dissipation rate by up to 2 orders of magnitude, this range is within the uncertainty present in estimates from shear probes (Thorpe, 2012). If the glider is holding a virtual mooring (Rudnick et al., 2004) (Chapter 5, Figure 4.1) the continued changing of glider direction will help reduce the positive bias as the glider will be unlikely to fly into wave fields for the whole deployment, if the deployment is long enough.

A second difference in the motion of a buoyancy driven glider compared to a vertical microstructure profiler is that a glider collects data on both the ascent and descent. A vertical profiler will only collect usable data in one direction. To confirm that there was no bias between the ascent and descent TKE dissipation rates were compared for both the MASSMO4 and EUREC^{4}A missions (Chapters 4 and 5). Neither of these deployments show a significant difference between ascents and descents and so all data was treated in the same manner. However, confirming that there is no difference between ascents and descents should be a step included in all deployments, in a similar manner to checking the outputs from platforms that mount a pair of shear probes or FP07s to confirm they are giving similar results.

6.2.2 WHAT CONSIDERATIONS NEED TO BE TAKEN INTO ACCOUNT TO MINIMISE THE IMPACT OF A GLIDER NOT KNOWING ITS EXACT SPEED AND HOW DOES THIS APPLY TO OTHER AUV PLATFORMS

In this thesis the methods developed were applied to two different platforms capable of recording high resolution data; a Seaglider with MicroPods and a VMP-2000. These, however, are not the only high resolution capable platforms available. Two widely used gliders with this capability are the Slocum and SeaExplorer with MicroRider packages (Wolk et al., 2009; Rockland Scientific, 2021). Differences between the MicroPod and MicroRider packages lead to minor differences when using the ODAS MatLab Library to convert raw microstructure files to physical data. The main difference is a MicroRider doesn't require a hotel file as the MicroRider measures pitch, roll and pressure so the ODAS MatLab library can estimate speed from it. However, it is advised that a hotel file is used as the glider's speed is likely to be a better estimate than the one from the MicroRider (Lueck et al., 2018). The reason that an accurate estimate of the gliders speed is needed is so that two fold. The first is having an understanding of the vertical speed through the water. As discussed in the previous section it is vital to have the glider flying as steep and as fast as possible to minimise the impact of the internal wave field. The second is so that an accurate depth can be applied to each temperature point. This is important in the data cleaning processes, especially in the removal of spurious overturns relating to sensor noise.

In addition to measuring pitch, roll and pressure, a MicroRider also provides two FP07 fast thermistors giving the user a direct comparison between independent probes to determine how well they are functioning. Comparison of these two data streams would provide a potential method for confirming the existence of overturns. Mounted close together the two FP07s could provide easy cross comparison. Combining the two streams would also allow for an average L_T to be determined. This could also be done on a vertical profiler with two or more FP07s.

However all the gliders mentioned here encounter the same issue that they are a broadly less stable platform than a microstructure capable vertical profiler. This partly stems from the fact that a glider will modify its course during guidance and control intervals during both descent and ascent. To minimise excess roll and pitch variation in the glider flight the number of times a glider conducts such changes can be limited (Wolk et al., 2009; Evans et al., 2018) preventing the glider performing such manoeuvres after apogee. This theoretically increases the stability of the glider, however puts the glider in a position to be more greatly affected by ocean currents and the internal wave field than might otherwise be the case.

MICROSCALE MEASUREMENTS FROM OTHER AUV PLATFORMS

There are other platforms that have also had high resolution logging sensors attached. Some of these include the Hydroid Remus Autonomous Underwater Vehicle (AUV), SeaSoar towed vehicle (Rockland Scientific, 2021), Autosub Long Range AUV (Furlong et al., 2012; Rockland Scientific, 2021), and even military submarines (Lueck et al., 2002). The question is then, is the methodology presented in this thesis applicable to any of these platforms? TKE dissipation rates from shear have successfully been collected aboard AUVs (McPhail et al., 2019; Frajka-Williams et al., 2022). However, due to vibrational issues with propelled AUVs dissipation rates of lower than 1×10^{-9} W kg^{-1} may be difficult to detect. As Thorpe scaling identifies vertical overturns (Thorpe, 1977) a horizontal AUV track is unlikely to identify overturns due to density displacement. An AUV that is profiling in a saw tooth pattern in the same manner as a glider (Rudnick, 2016) would still be an applicable platform. As long as the pressure record was monotonic the vibrational impact on shear estimates of TKE dissipation rate estimates is unlikely to be seen in temperature estimates of TKE dissipation rates from Thorpe scaling.

6.3 DO VALUES OF TURBULENT KINETIC ENERGY DISSIPATION AND ASSOCIATED PRODUCTS FROM THORPE SCALING HIGH RESOLUTION TEMPERATURE FIT WITH ESTIMATES OF THE SAME PRODUCTS FROM OTHER METHODS ACROSS DIFFERENT OCEANIC REGIONS

Previous studies have shown that the Thorpe scale methodology can be applied successfully in many ocean regions. These include; Loch Ness (Thorpe, 1977), the Ross Sea and the coast of New Zealand (Gargett and Garner, 2008), the Faroe Shetland Channel (Hall et al., 2011), the Luzon Straight, Southern Atlantic Ocean and the Brazil Basin (Mater et al., 2015), Western and central North Pacific and Southern Ocean (Ijichi and Hibiya, 2018), the Samoan Passage (Carter, 2020) and the Roseway Basin Canada (Howatt et al., 2021). In this thesis Thorpe scale methodology was successfully applied to 3 high resolution temperature datasets from different regions. Open ocean Mid Atlantic over the Mid Atlantic Ridge (Chapter 3). A highly energetic region close to bottom topography in the Faroe Shetland Channel (Chapter 4). Finally open ocean in the tropical North Atlantic away from deep ocean topography (Chapter 5). Across all these study regions, a large and varied set of oceanic regimes are covered.

6.3.1 HOW DO THORPE SCALE ESTIMATES OF TURBULENT KINETIC ENERGY DISSIPATION RATES COMPARE BETWEEN OUR AND OTHER STUDIES

In the opening chapter of this thesis the relevance of dissipation and diffusivity in the ocean was discussed. As part of this discussion typical ranges of dissipation and diffusivity found across the oceans were presented. Here a summary of the values estimated from the methods in this thesis are again compared with other relavent studies and global values presented in Chapter 1.

RIDGEMIX, CHAPTER 3

In Chapter 3 we compared estimates of turbulent kinetic energy dissipation from Thorpe scaling to those from shear data collected by a vertical microstructure profiler deployed over the Mid-Atlantic Ridge (Vic et al., 2018). We show comparable estimates of dissipation ($(O)10^{-11}$ to $(O)10^{-9}$ W kg^{-1}) across both ε_{Thorpe} and ε_{shear}. TKE dissipation rates from Thorpe scaling show a greater spread of standard deviations when the time means are compared. Estimates of ε_{Thorpe} can be seen that are lower than those from ε_{shear}, especially at depth ($(O)10^{-11}$ W kg^{-1} compared with $(O)10^{-10}$ W kg^{-1}), suggesting that Thorpe scaling here can provide estimates that are lower than the noise floor of the VMP-2000. A clear distinction between spring and neap tidal periods is also seen, with a peak at 7×10^{-10} W kg^{-1} for spring and 1×10^{-10} W kg^{-1} for neaps. These values of TKE dissipation estimates also fit with open ocean values presented in Chapter 1, although they are at the lower end. This similarity, however, isn't surprising as this study site was open ocean away from the bottom boundary, with no obvious conditions that would lead to any form of enhanced mixing. Values of diffusivity were not examined in Chapter 3.

MASSMO4, CHAPTER 4

In Chapter 4 we used a short glider deployment on the flank of the WTR. We show that it is possible to provide estimates of dissipation from Thorpe scaling high resolution temperature from a glider that are comparable to other studies. Although the values of TKE dissipation estimates do fit within the broad global range, the values estimated in this thesis are low compared with both other studies in the region (up to an order of magnitude lower at $(O)10^{-9}$ W kg^{-1}) and with the location of the measurements, given the proximity to rough bottom topography and a point of internal tide generation. In contrast to TKE dissipation estimates, calculated values of diffusivity fit well within both the global spread of such values and show elevated values where expected. Higher values can be seen in the surface layers, a region heavily influenced by wind and wave mixing. Higher values (up to $(O)10^{-4}$ m^{2} s^{-1}) can also be seen at depth and closer to the WTR, both regions close to rough bottom topography.

In addition to presenting values of TKE dissipation estimates and diffusivity, other studies in the same region (Hall et al., 2011; Venables, 2011) suggest a strong signal would be seen around the deep pycnocline due to internal wave activity, an element this study could not replicate. The lack of signal was investigated by visualising the data both as distance from the WTR and across the M_2 tidal cycle. A small signal is seen through the visualisation of the distance from the ridge was visualised, with depths between 500 m and 700 m in profiles closest to the ridge showing ε_{Thorpe} half an order of magnitude higher ($(O)10^{-8}$ W kg^{-1}) than at the same depth further from the ridge. No clear pattern emerges when the data is visualised over the tidal cycle. Both of these are unexpected results given the location given the location to an internal tide generator in the form the WTR.

EUREC^{4}A, CHAPTER 5

In Chapter 5 we used a glider dataset from the sub-tropical North Atlantic. Here we show ε_{Thorpe} and κ_ρ with mean values of $(O)10^{-10}$ W kg^{-1} and $(O)10^{-5}$ m^{-2} s^{-1} respectively. These values are both ε_{Thorpe} and
$kappa_\rho$ are representative of background ocean presented in Chapter 1 and other studies (Munk and Wunsch, 1998a). This is unsurprising given the open ocean location away from any boundary features or mechanical turbulence formation locations. However, a different physical feature present in this region of the world's ocean compared to the other datasets used in this thesis is the presence of thermohaline staircases. The impact of thermohaline staircases on the ε_{Thorpe} from Thorpe scaling was also investigated. Thermohaline staircases have the potential to increase ε_{Thorpe} (Schmitt et al., 2005). We show that in a specific regime this method may provide an overestimate of dissipation rates, with values of $(O)10^{-8}$ W kg^{-1} in regions with thermohaline staircases, compared with $(O)10^{-10}$ W kg^{-1} for regions at depth where staircases are not present.

6.3.2 HOW DO THE DATA AND RESULTS PRESENTED IN THIS THESIS FIT WITHIN THE WIDER OCEAN

We have discussed each of the datasets presented in this thesis in detail between the previous section and the relevant chapters. The results of each have been discussed and compared with other studies either in a similar region or similar regions in other areas of the ocean. The scope of this work, however, did not focus on the fact that each study site is not an isolated region but connected to the wider ocean and has the ability to impact it.

We shall start with the most interconnected region, the results from MASSMO4. The data from this project was collected on the northern flank of the Wyville-Thomson Ridge (WTR) situated at the southernmost end of the Faroe-Shetland Channel (FSC), in a region where 6 different oceanic water masses are present (Gallego et al., 2018). As mentioned in Chapter 1 the role of ocean mixing is to redistribute heat in the oceans, transferring this heat to higher latitudes where it is lost and then the colder waters return at depth setting up a meridional overturn circulation (de Lavergne et al., 2022). Along with the Faroe Bank Channel (FBC), the FSC provides one of two main routes (the other being the Denmark straight) by which cold waters formed in the Nordic seas flows over the Greenland-Scotland ridge and into the North Atlantic at depth (Hansen and Østerhus, 2000; Hall et al., 2011). In addition to being a path for cold dense return water, warm fresh Atlantic water flows northwards over the WTR setting up a point of internal tide generation, which in turn leads to breaking internal waves. These physical processes can lead to changes in the T-S relationship within the water masses present in the channel. These changes have the potential to change the local circulation, which has the ability to change the global circulation. The understanding of the processes of mixing in this part of world aid in the broader understanding of global ocean circulation.

The other regions studied in this thesis are in the open ocean away from boundaries. Both, however, have different regimes and the cases for studying them are different.

The first of these was the data looked at from the RidgeMix dataset. Mixing arising from internal tide generation is not a new scientific phenomenon (Vic et al., 2018). The RidgeMix project set out to quantify the mixing generated due to the Mid-Atlantic Ridge (MAR) and the impact that this mixing has on biogeochemical processes in the North Atlantic Subtropical Gyre (Sharples, 2016; Vic et al., 2018; Spingys et al., 2021). Although the work in this thesis did not touch upon vertical diffusivities or involved nutrient fluxes, the reason for picking it as a study area is still relevant to the original RidgeMix project. A test dataset was required to compare the Thorpe scale method to a published dataset. Vic et al. (2018) had both a published dataset and also an investigation showing a clear difference between dissipation rates at spring and neap tides over the MAR.

From a testing point of view, and directly relevant to this thesis the benefit of using this data was was twofold. The first, does the Thorpe scale method match estimates of shear (considered a ‘gold’ standard for estimating ocean mixing) from the same platform. The second, is the Thorpe scale method capable of discerning the differences between spring and neap diffusivities. From a physical point it is diapycnal mixing, diapycnal advection and isopycnal stirring that are major drivers in providing enough nutrients to the base of the euphotic zone for phytoplankton growth (Spingys et al., 2021), although only diapycnal mixing is studied in this thesis. Understanding the changes that the tidal cycle may then play on this required nutrient flux is vital to the understanding of phytoplankton growth within the North Atlantic Subtropical Gyre, an oligotrophic region of the ocean that is already limited in nutrients and growth. With the expected strengthening of stratification due to climate change in the next 80 years, leading to a fall of between 4% and 11% in primary productivity (Bindoff et al., 2019) this diapycnal mixing will play an important role in keeping the euphotic zone supplied with nutrients.

The final dataset in this thesis came from the EUREC^{4}A project, with details of how it fit within the project discussed more in depth in Chapter 5. Although open ocean, as with RidgeMix, the focus here was firstly on air-sea interaction and the impact it has on trade cloud formation (Stevens et al., 2021) and as an important driver on weather and climate variability (Siddle et al., 2021). Originally the aim was to examine the vertical fluxes of temperature, with a look at air-sea fluxes and how they compare with other measurements from the region and climate models. Due to both time constraints and technical issues, close examination of the air-sea interaction was not possible.

The dataset did, however, bring to the fore a process for ocean mixing that had not been present in the prior two study regions. This process was thermohaline staircases, formed via double diffusive processes, which can enhance diapycnal mixing in the open ocean, in some cases by up to five times the background values (van der Boog et al., 2021; Rollo et al., 2021). The global impact of this enhanced mixing is, however, somewhat limited providing local increases but playing a small role in the broader ocean energy budget. It is suggested by van der Boog et al. (2021) that the double diffusive fluxes from thermohaline staircases only provide 7.5 GW to the energy budget which is small when compared with the 2 TW required to maintain global stratification. If these structures are then more important at a local scale than at the global scale their continued study is still important. One of the key findings of the work presented in this thesis is that the Thorpe scale method does highlight elevated mixing from thermohaline staircases. This is a surprise as Thorpe scaling relies on the presence of mechanical mixing to occur, not double diffusive mixing. Again due to time constraints it was not possible to investigate this interaction any further, but it highlights the fact that the Thorpe scale method is not universally applicable, especially when using temperature as a density proxy.

6.4 WHAT BENEFITS ARE THERE TO USING THE THORPE SCALE METHOD COMPARED WITH OTHER INDIRECT METHODS OF ESTIMATING DISSIPATION

6.4.1 FINESCALE PARAMETRISATIONS

In Section 2.5 the concept of finescale parametrisation was introduced and two different methods for doing so were introduced. Although a small amount of discussion was had around the differences between those methods and Thorpe scaling a short discussion is presented here on how each would have been used if calculated alongside the Thorpe Scaling in each chapter.

FINESCALE PARAMETERISATION AND THE DATA IN THIS THESIS

Of the finescale methods, the large-eddy method (LEM) would be a poor fit for using on a VMP as there is a lack of either instrumentation to provide a direct measure of velocity, such as in Gargett (1999), or an idealised velocity model to compare against, such as in Evans et al. (2018). As the LEM has been shown to work well on glider data previously (Evans et al., 2018) the work in Chapters 4 and 5 would have been excellent candidates to further test this method. In contrast to the LEM, shear/strain parametrisation would have been applicable to all of the datasets. Although a shear value is required for R_ω, the shear/strain ratio, a fixed value can be used for shear, however this has the potential to introduce bias (Frants et al., 2013; Waterman et al., 2013). This would be most relevant again in Chapters 4 and 5 due to technical issues encountered with the shear datasets from these two missions. Although it is possible to apply finescale parametrisation to VMP data, it is of less use if the VMP is functioning correctly as you already have the ability to estimate dissipation rates directly using the shear data. However, as used in this thesis, VMPs are a useful test bed for developing finescale and other indirect methods, providing a ‘gold’ standard dataset to compare against.

THORPE SCALING, FINESCALE PARAMETRISATION AND SHEAR DATA

For any study where the study of dissipation and diffusion is the primary aim it is recommended that a vertical profiler equipped with microstructure instrumentation is used or a tracer release experiment is conducted (Frajka-Williams et al., 2022). Although costly and potentially limited spatially and temporally these will provide the most robust results available currently.

The Thorpe scale method and finescale parameterisations are useful in situations where a greater temporal or spatial coverage is required or the ability to use vertical profilers or conduct a tracer release experiment is not possible. Thorpe scaling, and the two finescale methods focused on in this thesis have benefits and weaknesses.

Firstly, the LEM. This is excellent for applying to long glider datasets giving the ability to provide a long temporal dataset for analysis, vital for understanding seasonal changes (Evans et al., 2018). The LEM, however, requires a second velocity profile to be compared against as well as a background value for dissipation. This makes the method less independent of other methods but useful within an observational campaign.

Secondly the shear/strain parameterisation is very useful if using ADCP or LADCPs, as long as the correct processing is done to clean the data (Polzin et al., 2002; Damerell et al., 2012). This method gives good values for background dissipation, however, due to the ranges that the processing is conducted over, typically $O(100)$m, the resolution of the method is relatively coarse which could cause issues depending on what phenomenon is being studied.

Finally, Thorpe scaling. This method is independent of other measurements and directly associates physical overturns with a value for mixing. It is important to clean the data used for this method (either in temperature or density space) to remove spurious overturns that can be attributed to instrument noise rather than physical processes. If just using temperature other factors need to be considered including where is temperature a relevant proxy for density and what is used as a value of N^2 for the estimation of dissipation.

All three methods have a major drawback in that they assume some sort of mechanical process is driving the turbulent release of energy that is inferred from them. In the case of the LEM it is eddies, shear/strain paramerisation assumes the breaking of the internal tide locally (which has been shown to not always be true (Waterman et al., 2013)) and Thorpe scaling assumes all overturns detected are suggestive of unstable water masses (if done in temperature space). These methods don’t take into account other ways that energy can be transferred such as along isopycnals or through double diffusive processes. As each of these methods provides a different solution to the same problem it needs to be decided on a case by case basis which of them is the most appropriate for a dataset. In addition the following must also be considered; what physical questions need answering, what resolution the results are required in and what instrumentation is available to collect the data? The answer to each of these will have an impact on picking the most appropriate method.

6.4.2 WHAT CONSIDERATIONS ARE REQUIRED WHEN PICKING A DATASET TO APPLY THE THORPE SCALE METHODOLOGY TO

The predominant factor in determining the suitability of the Thorpe scale method for an oceanic region is that temperature is the dominant influence on density. If applying the method to existing data the T/S regime of a study site should be examined before processing. If a new study is being planned and T/S data exists, examining this prior to conducting the study will aid in determining if Thorpe scaling is suitable. Where large amounts of temperature and salinity interleaving occur (such as in RidgeMix) isopycnal energy transfer is likely to be playing a role, and these regions of the water column should be removed from any processing. This is due to the Thorpe scale method only looking at diapycnal energy transfer. At a smaller scale there may be overturns that are compensated by salinity even if broadly the water column is not. To remove these regions a T/S variance ratio (Section 3.4) can be used to exclude bins where values are contaminated by smaller salinity intrusions.

In addition to controls on density, understanding the physical processes that generate mixing will aid in planning deployments of buoyancy driven gliders. As discussed in Section 6.2.1 flying a glider into, rather than perpendicular to, the dominant direction of internal wave propagation (E.g. during the MASSMO4 deployment, Chapter 4) has the potential to increase bias seen in ε_{Thorpe} from gliders (Smyth and Thorpe, 2012). Regions with highly energetic regimes may therefore be a poor fit for Thorpe scaling glider data, unless flown in a manner to minimise potential bias from turbulent features. A method that could minimise the influence of internal waves would be to deploy a glider in a virtual mooring set up. Deploying in such a manner will provide profiles distributed around a single point that when averaged together should remove potential bias (positive and negative).

The resolution of the data available should play a role in determining the suitability of the Thorpe scaling method. If using lower resolution CT data, minimum identifiable overturn lengths will be large and as such will provide a large positive bias on the final values of ε_{Thorpe}. Similarly if the correct care is not taken with high resolution temperature data it is possible to identify noise as potential overturns and provide a negative bias to the final values of ε_{Thorpe}.

The number of profiles used in a study is also an important factor. A lower number of profiles present in the study will result in seeing a greater variability in ε_{Thorpe}. Smyth and Thorpe (2012) recommends the minimum number of profiles to be $(O)100$. Results presented in Chapter 3 show that when too few profiles are averaged together the time mean is dominated by the dominant ε_{Thorpe}, regardless of its bias, and therefore under or overestimates in the time mean will occur. This work suggests, however, that 25 profiles is sufficient to provide a robust time mean.

A final, and important consideration that links in part to the temperature variance budget, is what are the major factors controlling turbulent mixing in a given area. As shown in Chapter 3 there are regions of the water column where diapycnal mixing is not the driving force on temperature variance, and that isopycnal processes are more important. In Chapter 5 it is discussed that thermohaline staircases are formed through double diffusive process, a non-mechanical mixing processes, rather than mechanical mixing processes that the Thorpe scale method relies upon. Both of these regions then are inappropriate locations for Thorpe scaling as a primary method of determining TKE dissipation estimates.

If the factors noted above can be taken into consideration then the Thorpe scale methodology can be made applicable across all ocean regions that fit within the criteria. A brief investigation of T/S profiles (Talley et al., 2011) for the major ocean basins (Atlantic, Pacific, Indian and Southern) was conducted to determine some broad regions where the method would potentially be suitable. The regions were selected through the presence of temperature dominated density in the T/S profile. In the Atlantic Ocean water masses where the temperature range is between 5°C and 23°C should be suitable. In the Pacific Ocean a smaller range of 7°C and 17°C is the most obvious. The Indian Ocean range is 5°C and 15°C. In the Southern Ocean temperatures below 2°C and above 4°C are likely to be suitable. In each of these basins the actual range suitable is also dependent on the water mass, for example winter water in the Southern Ocean will never be suitable. Outside of the ranges presented, region by region examination is required. This examination did not look into the main mixing drivers in these areas and would also need a region by region examination.

6.5 POTENTIAL FURTHER WORKS

The methodology and results laid out in this thesis deliver a robust method for providing TKE dissipation rate estimates using Thorpe scaling high resolution temperature on two different platforms. There are, however, areas that could be investigated to potentially improve both the method and the results it generates.

The first of these would be to apply the method to a dataset where a buoyancy driven glider was deployed alongside a vertical microstructure profiler. This would give access to estimates of TKE dissipation rates from shear, temperature variance, and Thorpe scaling high resolution temperature for both platforms. The results could then be compared across the platforms, with the aim of determining any over or underestimates of TKE dissipation rates. Although a single dataset is not indicative of the entire ocean, a study of this type would provide further proof that the different methods can provide comparable results. It also allows for further investigation into regions where the different methods are not comparable. Determining the reasons behind these differences could then be fed back into quality control steps.

The second area of study that could prove beneficial would be to refine how regions of the water column for exclusion are determined. A number of the additional studies used in this thesis, including Mater et al. (2015), Ijichi and Hibiya (2018) and Howatt et al. (2021), all use different methods of determining regions of the water column to be excluded making cross comparison more difficult. Providing an algorithmic method for interrogating the T/S relationship that was region agnostic would allow future studies to use a standardised method for excluding data. An algorithmic approach would be repeatable and less reliant on visual inspection of data (which reduces the repeatability). The variance ratio in Chapter 3 provides a semi-algorithmic method that would be a solid foundation for further development. This method could be expanded through incorporation of additional parameters to expand the applicability of the algorithm. If a universal method was developed it could be applied to T/S data from existing datasets, or the World Ocean Atlas, to determine regions of the worlds oceans where temperature based Thorpe scaling is applicable.

In addition to the current quality control methods, investigating those presented by Howatt et al. (2021) would be of great interest. The methods used in that study were applied to the CT sail data on a Slocum OMG. During the development of the methodology for Thorpe scaling in this thesis it was found that the resolution of the data had an influence on the performance of the quality control steps (such as the run-length test). The inclusion of additional quality control steps that can increase the reliability and robustness of our methods would be welcome.

To add some further robustness to some of the values presented in Chapters 4 and 5 applying other finescale parametrisations to the glider data would provide a useful comparison. The LEM would expand the scope of the work presented in Chapter 4 as a longer time series could be created instead of relying on the 25 usable micro structure profiles. The LEM would also greatly expand the data available around the work presented in Chapter 5 as there were two other gliders in close proximity to the one with the microstructure package. This would considerably lengthen the time series from that dataset.

The scripts developed here for processing high 512 Hz resolution data are provided alongside this thesis as a tool box on Github to anyone to use. The final piece of work based on the methodology developed here that would benefit the ocean mixing community greatly would be adapting and testing the methods here for use on low resolution data.

Even if glider missions were only capable of providing a single representative estimate of background mixing in a given region this would aid our understanding of the impacts of mixing including water mass transformation and biochemical fluxes (Thorpe, 2007), especially in the ocean interior. The added benefit of using low resolution data would be the ability to process in density space rather than temperature, reducing some of the considerations presented in this chapter. This idea of Thorpe scaling general CT data from platforms is not a new one and was proposed by Gargett and Garner (2008) but hasn't become a standard of the mixing community.

6.6 FINAL SUMMARY

In this thesis we set out to expand on existing methods for investigating turbulent mixing processed using high resolution temperature sensors on autonomous ocean gliders. In this work we have developed methods of TKE dissipation that are complementary to the existing methods but are applicable on a wider range of platforms. In addition to the platform agnostic nature of the methods, they also incorporate algorithms for the majority of the data exclusion. Algorithmic quality control is a key step that improves the reproducibility of ocean research. To do this we took the core Thorpe scaling algorithm and expanded on it by developing a platform agnostic methodology that provided robust estimates of TKE dissipation rates. Thorpe scaling as a method for estimating TKE dissipation rates has its own caveats. But, these do not prevent it being a low computational cost, rapid and robust way of providing estimates of TKE dissipation rates if the correct considerations are taken into account. Over the course of the work that is presented in this thesis these considerations where explored and developed into the methodology presented in Chapter 2.

During the process of this development we first applied the methods to a vertical microstructure profiler and compared our results of ε_{Thorpe} with those from the shear probes on the platform. The comparison was excellent with ε_{Thorpe} and ε_{shear} providing comparable results and a distinct difference between spring and neap tides seen. When we had confirmed that the methods yielded comparable results to shear they were then applied to a short Seaglider dataset to determine any other steps required to apply the method to a buoyancy driven glider platform. Once additional steps required to make the methods work for a glider were determined, they were then applied to a longer open ocean dataset. The results from our algorithms and methodology compare well with background ocean mixing estimates provided by other studies as well as dissipation rates from temperature variance on the same temperature data that was Thorpe scaled.

The algorithms developed in the thesis are available for any party to use and develop at https://github.com/PLeadbitter/Temperature_Thorpe_Scale.

BIBLIOGRAPHY

Abernathey, R., Gnanadesikan, A., Pradal, M. A., and Sundermeyer, M. A. *Isopycnal mixing*. Number 2016. Elsevier Inc., 2021. ISBN 9780128215128. doi: 10.1016/B978-0-12-821512-8.00016-5. URL https://doi.org/10.1016/B978-0-12-821512-8.00016-5.

Alford, M. H., Pickering, A., Rainville, L., Mackinnon, J. A., Pinkel, R., Sun, O., Musgrave, R., Beitzel, T., Nash, J. D., Simmons, H., Klymak, J. M., Fu, K.-H., and Lu, C.-W. Energy flux and dissipation in luzon strait: Two tales of two ridges. *Journal of Physical Oceanography*, 41(11):2211–2222, 2011. ISSN 0022-3670. doi: 10.1175/JPO-D-11-073.1.

ALSEAMAR-ALCEN. SEAEXPLORER X2 Multi-mission underwater glider. Technical report, 2019. URL https://www.alseamar-alcen.com/sites/alseamar-alcen.com/files/pdf/products/alseamar-sea_explorer_x2-18x30_web.pdf.

Althaus, A. M., Kunze, E., and Sanford, T. B. Internal tide radiation from Mendocino escarpment. *Journal of Physical Oceanography*, 33(7):1510–1527, 2003. ISSN 00223670. doi: 10.1175/1520-0485(2003)033<1510:ITRFME>2.0.CO;2.

Barry, M. E., Ivey, G. N., Winters, K. B., and Imberger, J. Measurements of diapycnal diffusivities in stratified fluids. *Journal of*, 442:267–291, 2001.

Batchelor, G. *An Introduction to Fluid Dynamics*. Cambridge University Press, 1973.

Batchelor, G. K. Small-scale variation of convected quantities like temperature in turbulent fluid: Part 1. General discussion and the case of small conductivity. *Journal of Fluid Mechanics*, 5(1):113–133, 1959. ISSN 14697645. doi: 10.1017/S0022112059000106.

Beaird, N., Fer, I., Rhines, P., and Eriksen, C. Dissipation of turbulent kinetic energy inferred from seagliders: An application to the eastern Nordic Seas overflows.

Journal of Physical Oceanography, 42(12):2268–2282, 2012. ISSN 00223670. doi: 10.1175/JPO-D-12-094.1.

Bindoff, N. L., Cheung, W. W., Kairo, J. G., Arístegui, J., Guinder, V. A., Hallberg, R., Hilmi, N. J. M., Jiao, N., Karim, M. S., Levin, L., O'Donoghue, S., Purca Cuicapusa, S. R., Rinkevich, B., Suga, T., Tagliabue, A., and Williamson, P. Changing Ocean, Marine Ecosystems, and Dependent Communities. *IPCC special report on the ocean and cryosphere in a changing climate*, pages 477–587, 2019.

Bony, S., Stevens, B., Ament, F., Bigorre, S., Chazette, P., Crewell, S., Delanoë, J., Emanuel, K., Farrell, D., Flamant, C., Gross, S., Hirsch, L., Karstensen, J., Mayer, B., Nuijens, L., Ruppert, J. H., Sandu, I., Siebesma, P., Speich, S., Szczap, F., Totems, J., Vogel, R., Wendisch, M., and Wirth, M. *EUREC4A: A Field Campaign to Elucidate the Couplings Between Clouds, Convection and Circulation*, volume 38. 2017. ISBN 1071201794. doi: 10.1007/s10712-017-9428-0.

Borenäs, K. and Lundberg, P. The Faroe-Bank Channel deep-water overflow. *Deep-Sea Research Part II: Topical Studies in Oceanography*, 51(4-5):335–350, 2004. ISSN 09670645. doi: 10.1016/j.dsr2.2003.05.002.

Boyd, T., Inall, M., Dumont, E., and Griffiths, C. AUV observations of mixing in the tidal outflow from a Scottish sea loch. *2010 IEEE/OES Autonomous Underwater Vehicles, AUV 2010*, 2010. ISSN 1522-3167. doi: 10.1109/AUV.2010.5779670.

Brearley, J. A. Personal Correspondence, 2018.

Carter, G. S. Personal Correspondence, 2020.

Crawford, W. R. A compariosn of Length Scales and Decay Times of Turbulence in Stably Stratified Flows. *Journal of Physical Oceanography*, 16:1847–1854, 1986.

Creed, E., Ross, W., Lueck, R., Stern, P., Douglas, W., Wolk, F., and Hall, R. Integration of a RSI microstructure sensing package into a Seaglider. *Oceans 2015, MTS/IEEE Washington*, pages 1–6, 2015.

Cunningham, S. a., Kanzow, T., Rayner, D., Baringer, M. O., Johns, W. E., Marotzke, J., Longworth, H. R., Grant, E. M., Hirschi, J. J., Beal, L. M., Meinen, C. S., and Bryden,

H. L. Temporal Variability of the Atlantic Meridional Overturning Circulation at 26.5 degrees norht. 317(August):935–938, 2007.

Damerell, G., Sheehan, P., Hall, R., Matthews, A., and Heywood, K. Dissipation in the Bay of Bengal from a Seaglider. In *EGU General Assembly*, 2021.

Damerell, G. M., Heywood, K. J., Stevens, D. P., and Naveira Garabato, A. C. Temporal Variability of Diapycnal Mixing in Shag Rocks Passage. *Journal of Physical Oceanography*, 42(2000):370–385, 2012. doi: 10.1175/2011JPO4573.1.

Davis, R., Eriksen, C., and Jones, C. Autonomous buoyancy-driven underwater gliders. ... *Applications of Autonomous Underwater ...*, pages 1–11, 2002. doi: doi: 10.1201/9780203522301.ch3. URL http://www.ifremer.fr/lpo/gliders/donnees_tt/references/techno/4Gliders.pdf.

de Bruyn Kops, S. M. Classical scaling and intermittency in strongly stratified Boussinesq turbulence. *Journal of Fluid Mechanics*, 775:436–463, 2015. doi: 10.1017/jfm.2015.274.

de Lavergne, C., Groeskamp, S., Zika, J., and Johnson, H. L. The role of mixing in the large-scale ocean circulation. In *Ocean Mixing*, pages 35–63. Elsevier Inc., 2022. ISBN 9780128215128. doi: 10.1016/b978-0-12-821512-8.00010-4. URL https://doi.org/10.1016/B978-0-12-821512-8.00010-4.

Dillon, T. M. Vertical overturns: A comparison of Thorpe and Ozmidov length scales. *Journal of Geophysical Research*, 87(C12):9601, 1982. ISSN 0148-0227. doi: 10.1029/jc087ic12p09601.

Egbert, G. D. and Erofeeva, S. Y. Efficient inverse modeling of barotropic ocean tides. *Journal of Atmospheric and Oceanic Technology*, 19(2):183–204, 2002. ISSN 07390572. doi: 10.1175/1520-0426(2002)019<0183:EIMOBO>2.0.CO;2.

Eriksen, C. C. Gliders. In Cochram, J. K., Bokuniewicz, H. J., and Yager, P. L., editors, *Encyclopedia of Ocean Sciences (Third Edition)*, pages 102–108. Academic Press, 3rd edition, 2009. ISBN 9780128130810. doi: 10.1016/B978-0-12-813081-0.00728-X.

Eriksen, C. C., Osse, T. J., Light, T., Wen, R. D., Lehmann, T. W., Sabin, P. L., Ballard, J. W., and Chiodi, A. M. Long Range Autonomous Underwater Vehicle for Oceanographic Research. *IEEE Journal of Oceanic Engineering*, 26(4):424–436, 2001. ISSN 03649059. doi: 10.1109/48.972073.

Evans, D. G., Lucas, N. S., Hemsley, V., Frajka-Williams, E., Naveira Garabato, A. C., Martin, A., Painter, S. C., Inall, M. E., and Palmer, M. R. Annual Cycle of Turbulent Dissipation Estimated from Seagliders. *Geophysical Research Letters*, 45 (19):10,560–10,569, 2018. ISSN 19448007. doi: 10.1029/2018GL079966.

Fer, I., Nandi, P., Holbrook, W. S., Schmitt, R. W., and Páramo, P. Seismic imaging of a thermohaline staircase in the western tropical North Atlantic. *Ocean Science*, 6(3): 621–631, 2010. ISSN 18120784. doi: 10.5194/os-6-621-2010.

Fer, I., Peterson, A. K., and Ullgren, J. E. Microstructure measurements from an underwater glider in the turbulent Faroe Bank Channel overflow. *Journal of Atmospheric and Oceanic Technology*, 31(5):1128–1150, 2014. ISSN 15200426. doi: 10.1175/JTECH-D-13-00221.1.

Fer, I., Nilsen, F., Falck, E., Bosse, A., Koenig, Z., and Peterson, A. Ocean Mixing Process Study 2018. Technical Report 1, 2020.

Ferrari, R. and Polzin, K. L. Finescale structure of the T-S relation in the eastern North Atlantic. *Journal of Physical Oceanography*, 35(8):1437–1454, 2005. ISSN 00223670. doi: 10.1175/JPO2763.1.

Ferron, B., Mercier, H., Speer, K., Gargett, A., and Polzin, K. Mixing in the Romanche Fracture Zone. *Journal of Physical Oceanography*, 28(10):1929–1945, 1998. ISSN 00223670. doi: 10.1175/1520-0485(1998)028<1929:MITRFZ>2.0.CO;2.

Frajka-Williams, E., Eriksen, C. C., Rhines, P. B., and Harcourt, R. R. Determining vertical water velocities from Seaglider. *Journal of Atmospheric and Oceanic Technology*, 28(12):1641–1656, 2011. ISSN 07390572. doi: 10.1175/2011JTECHO830.1.

Frajka-Williams, E., Brearley, J. A., Nash, J. D., and Whalen, C. B. *New technological frontiers in ocean mixing*. Elsevier Inc., 2022. ISBN 9780128215128. doi: 10.1016/b978-0-12-821512-8.00021-9. URL https://doi.org/10.1016/B978-0-12-821512-8.00021-9.

Frants, M., Damerell, G. M., Gille, S. T., Heywood, K. J., MacKinnon, J., and Sprintall, J. An assessment of density-based finescale methods for estimating diapycnal diffusivity in the southern Ocean. *Journal of Atmospheric and Oceanic Technology*, 30(11):2647–2661, 2013. ISSN 07390572. doi: 10.1175/JTECH-D-12-00241.1.

Furlong, M. E., Paxton, D., Stevenson, P., Pebody, M., McPhail, S. D., and Perrett, J. Autosub Long Range: A long range deep diving AUV for ocean monitoring. *2012 IEEE/OES Autonomous Underwater Vehicles, AUV 2012*, 2012. doi: 10.1109/AUV.2012.6380737.

Galbrath, P. S. and Kelley, D. E. Identifying Overturns in CTD Profiles. *Journal of Atmospheric and Oceanic Technology*, 13:688–702, 1995.

Gallego, A., O'Hara Murray, R., Berx, B., Turrell, W. R., Beegle-Krause, C. J., Inall, M., Sherwin, T., Siddorn, J., Wakelin, S., Vlasenko, V., Hole, L. R., Dagestad, K. F., Rees, J., Short, L., Rønningen, P., Main, C. E., Legrand, S., Gutierrez, T., Witte, U., and Mulanaphy, N. Current status of deepwater oil spill modelling in the Faroe-Shetland Channel, Northeast Atlantic, and future challenges. *Marine Pollution Bulletin*, 127(April 2017):484–504, 2018. ISSN 18793363. doi: 10.1016/j.marpolbul.2017.12.002. URL https://doi.org/10.1016/j.marpolbul.2017.12.002.

Ganachaud, A. and Wunsch, C. Erratum: Improved estimates of global ocean circulation, heat transport and mixing from hydrographic data. *Nature*, 408(6825):453–458, 2001. ISSN 00280836. doi: 10.1038/35065660.

Ganachaud, A., Wunsch, C., Marotzke, J., and Toole, J. Meridional overturning and large-scale circulation of the Indian Ocean. 105(Cll):26117–26134, 2000.

Garabato, A. C., Polzin, K. L., Ferrari, R., Zika, J. D., and Forryan, A. A microscale view of mixing and overturning across the Antarctic Circumpolar Current. *Journal of Physical Oceanography*, 46(1):233–254, 2016. ISSN 15200485. doi: 10.1175/JPO-D-15-0025.1.

Gargett, A. Velcro Measurement of Turbulence Kinetic Energy Dissipation Rate ϵ. *American Meteorological Society*, pages 1973–1993, 1999.

Gargett, A. and Garner, T. Determining Thorpe scales from ship-lowered CTD density profiles. *Journal of Atmospheric and Oceanic Technology*, 25(9):1657–1670, 2008. ISSN 07390572. doi: 10.1175/2008JTECHO541.1.

Garrett, C. and Munk, W. Space-Time of Internal Waves: A Progress Report. *Journal of Geophysical Research*, 80(3):291–297, 1975.

Garrett, C. and St. Laurent, L. Aspects of deep ocean mixing. *Journal of Oceanography*, 58(1):11–24, 2002. ISSN 09168370. doi: 10.1023/A:1015816515476.

George, J. V., Vinayachandran, P. N., and Nayak, A. A. Enhanced Double-Diffusive Salt Flux from the High-Salinity Core of Arabian Sea Origin Waters to the Bay of Bengal. *Journal of Physical Oceanography*, 51(2):505–518, 2020. ISSN 0022-3670. doi: 10.1175/jpo-d-20-0192.1.

Giddings, J. Personal Correspondence, 2019.

Gould, W. J. From Swallow floats to Argo - The development of neutrally buoyant floats. *Deep-Sea Research Part II: Topical Studies in Oceanography*, 52(3-4):529–543, 2005. ISSN 09670645. doi: 10.1016/j.dsr2.2004.12.005.

Gregg, M. C. and Horne, J. K. Turbulence , Acoustic Backscatter , and Pelagic Nekton in Monterey Bay. *Journal of Physical Oceanography*, 39:1097–1114, 2009. doi: 10.1175/2008JPO4033.1.

Gregg, M. C. and Sanford, T. B. Shear and turbulence in thermohaline staircases. *Deep Sea Research*, 34(10):1689–1696, 1987.

Gregg, M. C., D'Asaro, T. J. S., and Larsson, N. Observations of Persistent Mixing and Near Interial Waves*. *Journal of Physical Oceanography*, 16:856–885, 1986.

Gregg, M. C., D'Asaro, E. A., Riley, J. J., and Kunze, E. Mixing efficiency in the ocean. *Annual Review of Marine Science*, 10(September 2017):443–473, 2018. ISSN 19410611. doi: 10.1146/annurev-marine-121916-063643.

Hall, R., Berx, B., and Damerell, G. Internal tide energy flux over a ridge measured by a co-located ocean glider and moored ADCP. *Ocean Science*, pages 1–21, 2019. ISSN 1812-0822. doi: 10.5194/os-2019-15.

Hall, R. A., Huthnance, J. M., and Williams, R. G. Internal tides, nonlinear internal wave trains, and mixing in the Faroe-Shetland Channel. *Journal of Geophysical Research: Oceans*, 116(3):1–15, 2011. ISSN 21699291. doi: 10.1029/2010JC006213.

Hansen, B. and Østerhus, S. North Atlantic-Nordic Seas exchanges. *Progress in Oceanography*, 45(2):109–208, 2000. ISSN 00796611. doi: 10.1016/S0079-6611(99)00052-X.

Hieronymus, M., Nycander, J., Nilsson, J., Döös, K., and Hallberg, R. Oceanic overturning and heat transport: The role of background diffusivity. *Journal of Climate*, 32(3):701–716, 2019. ISSN 08948755. doi: 10.1175/JCLI-D-18-0438.1.

Holmes, A., Illowsky, B., Dean, S., and Hadley, K. *Introductory Business Statistics*. LibreTexts Project, 2017. URL https://libretexts.org.

Hosegood, P., van Haren, H., and Veth, C. Mixing within the interior of the Faeroe-Shetland Channel. *Journal of Marine Research*, 63:529–561, 2005. ISSN 00222402. doi: 10.1357/0022240054307902.

Howatt, T., Waterman, S., and Ross, T. On using the finescale parameterization and Thorpe scales to estimate turbulence from glider data. *Journal of Atmospheric and Oceanic Technology*, pages 1187–1204, 2021. ISSN 0739-0572. doi: 10.1175/jtech-d-20-0144.1.

Ijichi, T. and Hibiya, T. Observed variations in turbulent mixing efficiency in the deep ocean. *Journal of Physical Oceanography*, 48(8):1815–1830, 2018. ISSN 15200485. doi: 10.1175/JPO-D-17-0275.1.

IOC, SCOR, and IAPSO. *The international thermodynamic equation of seawater - 2010: Calculation and use of thermodynamic properties*. UNESCO, intergover edition, 2010.

Jackson, L. C., Kahana, R., Graham, T., Ringer, M. A., Woollings, T., Mecking, J. V., and Wood, R. A. Global and European climate impacts of a slowdown of the AMOC in a high resolution GCM. *Climate Dynamics*, 45(11-12):3299–3316, 2015. ISSN 14320894. doi: 10.1007/s00382-015-2540-2. URL http://dx.doi.org/10.1007/s00382-015-2540-2.

Jackson, P. R. and Rehmann, C. R. Laboratory Measurements of Differential Diffusion in a Diffusively Stable , Turbulent Flow. *Journal of Physical Oceanography*, 33:1592–1603, 2003.

Johnston, T. M., Rudnick, D. L., Carter, G. S., Todd, R. E., and Cole, S. T. Internal tidal beams and mixing near Monterey Bay. *Journal of Geophysical Research: Oceans*, 116(3):1–20, 2011. ISSN 21699291. doi: 10.1029/2010JC006592.

Kageyama, M., Paul, A., Roche, D. M., and Van Meerbeeck, C. J. Modelling glacial climatic millennial-scale variability related to changes in the Atlantic meridional overturning circulation: A review. *Quaternary Science Reviews*, 29(21-22):2931–2956, 2010. ISSN 02773791. doi: 10.1016/j.quascirev.2010.05.029. URL http://dx.doi.org/10.1016/j.quascirev.2010.05.029.

Klein, P., Treguier, A.-m., and Hua, B. L. Three-dimensional stirring of thermohaline fronts. *Journal of Marine Research*, 56:589–612, 1998.

Klymak, J. M., Moum, J. N., Nash, J. D., Kunze, E., Girton, J. B., Carter, G. S., Lee, C. M., Sanford, T. B., and Gregg, M. C. An estimate of tidal energy lost to turbulence at the Hawaiian Ridge. *Journal of Physical Oceanography*, 36(6):1148–1164, 2006. ISSN 00223670. doi: 10.1175/JPO2885.1.

Knauss, J. A. *Introduction to Physical Oceanogrpahy*. Waveland Press Inc, 2nd edition, 2005.

Knudsen, M. *Danish hydrographical investigations at the Faroe Islands in the spring of 1910*. Reitzel, 1911.

Kunze, E. Yes , We Have No Abyssal Mixing. In *Near-Boundary Processes and Their Parameterizations: Proc.'Aha Huliko'a Hawaiian Winter Workshop*, number 1, pages 85–93, 2003.

Lambourne, R. and Tinker, M., editors. *Basic Mathematics for the Physical Sciences*. Wiley, 5th edition, 2000.

Larsen, K. M. H., Hansen, B., Kristiansen, R., and Østerhus, S. Internal tides in the waters surrounding the Faroe Plateau. *ICES CM*, 50:09–13, 2000. URL http://www.hav.fo/PDF/Ritgerdir/ELDRI/Internal_tides_grein.pdf.

Laurent, L. S. and Schmitt, R. W. The contribution of salt fingers to vertical mixing in the North Atlantic Tracer Release Experiment. *Journal of Physical Oceanography*, 29(7):1404–1424, 1999a. ISSN 00223670. doi: 10.1175/1520-0485(1999)029<1404:tcosft>2.0.co;2.

Laurent, L. S. and Schmitt, R. W. The contribution of salt fingers to vertical mixing in the North Atlantic Tracer Release Experiment. *Journal of Physical Oceanography*, 29(7):1404–1424, 1999b. ISSN 00223670. doi: 10.1175/1520-0485(1999)029<1404:tcosft>2.0.co;2.

Leadbitter, P., Hall, R., and Brearly, A. A methodology for Thorpe scaling 512 Hz fast thermistor data from buoyancy-driven gliders to estimate turbulent kinetic energy dissipation rate in the ocean. *OCEANS 2019 MTS/IEEE SEATTLE*, pages 0–5, 2019.

Ledwell, J. R., Duda, T. F., Sundermeyer, M. A., and Seim, H. E. Mixing in a coastal environment : 1 . A view from dye dispersion. *Journal of Geophysical Research*, 109:1–20, 2004. doi: 10.1029/2003JC002194.

Ledwell, J. R., St. Laurent, L. C., Girton, J. B., and Toole, J. M. Diapycnal Mixing in the Antarctic Circumpolar Current. *Journal of Physical Oceanography*, 41:241–246, 2011. doi: 10.1175/2010JPO4557.1.

Lee, R. S., Pritchard, T. R., Ajani, P. A., and Black, K. P. The influence of the East Australian Current eddy field on phytoplankton dynamics in the coastal zone. *Journal of Coastal Research*, (SPEC. ISSUE 50):576–584, 2007. ISSN 07490208.

Legg, S., Briegleb, B., Chang, Y., Chassignet, E. P., Danabasoglu, G., Ezer, T., Gordon, A. L., Griffies, S., Hallberg, R., Jackson, L., Large, W., Özgökmen, T. M., Peters, H., Price, J., Riemenschneider, U., Wu, W., Xu, X., and Yang, J. Improving Oceanic Overflow Representation in Climate Models. *Bulletin of the American Meteorological Society*, 90(5):657–670, 2009. ISSN 00030007. doi: 10.1175/2008BAMS2667.I. URL 10.1175/2008BAM2667.1%5Cnhttp://search.ebscohost.com/login.aspx?direct=true&db=a9h&AN=42732807&site=ehost-live.

Lique, C., Guthrie, J. D., Steele, M., Proshutinsky, A., Morison, J. H., and Krishfield, R. Diffusive vertical heat flux in the Canada Basin of the Arctic Ocean inferred from moored instruments. *Journal of Geophysical Research: Oceans*, 119(1):496–508, 2014. ISSN 21699291. doi: 10.1002/2013JC009346.

Lueck, R., Murowinski, E., and McMillan, J. A Guide to data processing (RSI Technical Note 039). Technical report, 2018.

Lueck, R. G., Wolk, F., and Yamazaki, H. Oceanic velocity microstucture measurements in the 20th century. *Journal of Oceanography*, 58:153–174, 2002.

Luyten, J. R., Pedlosky, J., and Stommel, H. The Ventilated Thermocline. *Journal of Physical Oceanography*, 13:292, 1982.

Mashayek, A., Caulfield, C. P., and Peltier, W. R. Time-dependent , non-monotonic mixing in stratified turbulent shear flows : implications for oceanographic estimates of buoyancy flux. *Journal of Fluid Mechanics*, 736:570–593, 2013. doi: 10.1017/jfm.2013.551.

Mater, B. D., Venayagamoorthy, S. K., St. Laurent, L., and Moum, J. N. Biases in Thorpe-Scale Estimates of Turbulence Dissipation. Part I: Assessments from Large-Scale Overturns in Oceanographic Data. *Journal of Physical Oceanography*, 45(10): 2497–2521, 2015. ISSN 0022-3670. doi: 10.1175/jpo-d-14-0128.1.

McDougall, D., Millero, F.J., J., and Jackett, D. R. An algorithm for estimating Absolute Salinity in the global ocean. *Ocean Science Discussions*, 6:215–242, 2009. ISSN 1812-0822. doi: 10.5194/osd-6-215-2009.

McDougall, T. J., Thorpe, S., and Gibson, C. H. Small-scale turbulence and mixing in the ocean: A glossary. In Nihoul, J. and Jamart, B., editors, *Small-scale Turbulence and Mixing in the Ocean*, pages 3–9. Elsevier, 1988.

McPhail, S., Templeton, R., Pebody, M., Roper, D., and Morrison, R. Autosub long range AUV missions under the filchner and ronne ice shelves in the weddell sea, antarctica - An engineering perspective. *OCEANS 2019 - Marseille, OCEANS Marseille 2019*, 2019-June, 2019. doi: 10.1109/OCEANSE.2019.8867206.

Melet, A., Hallberg, R., Legg, S., and Polzin, K. Sensitivity of the ocean state to the vertical distribution of internal-tide-driven mixing. *Journal of Physical Oceanography*, 43(3):602–615, 2013. ISSN 00223670. doi: 10.1175/JPO-D-12-055.1.

Melet, A. V., Hallberg, R., and Marshall, D. P. The role of ocean mixing in the climate system. In *Ocean Mixing*, number Chapter 3, pages 5–34. Elsevier Inc., 2022. ISBN 9780128215128. doi: 10.1016/b978-0-12-821512-8.00009-8. URL https://doi.org/10.1016/B978-0-12-821512-8.00009-8.

Merckelbach, L., Berger, A., Krahmann, G., Dengler, M., and Carpenter, J. R. A dynamic flight model for Slocum gliders and implications for turbulence microstructure measurements. *Journal of Atmospheric and Oceanic Technology*, 36(2):281–296, 2019. ISSN 15200426. doi: 10.1175/JTECH-D-18-0168.1.

Meredith, M. and Naveira Garabato, A., editors. *Ocean Mixing: Drivers, Mechanisms and Impacts*. Elsevier, 2021. URL https://doi.org/10.1016/C2019-0-03674-6.

Merryfield, W. J. Origin of thermohaline staircases. *Journal of Physical Oceanography*, 30(5):1046–1068, 2000. ISSN 00223670. doi: 10.1175/1520-0485(2000)030<1046:OOTS>2.0.CO;2.

Molodtsov, S., Anis, A., Amon, R. M., and Perez-Brunius, P. Turbulent Mixing in a Loop Current Eddy From Glider-Based Microstructure Observations. *Geophysical Research Letters*, 47(14):1–9, 2020. ISSN 19448007. doi: 10.1029/2020GL088033.

Mourn, J. N. Energy-containing scales of turbulence in the ocean thermocline. *Journal of Geophysical Research: Oceans*, 101(C6):14095–14109, 1996. ISSN 01480227. doi: 10.1029/96jc00507.

Munk, W. and Wunsch, C. Abyssal recipes II: Energetics of tidal and wind mixing. *Deep-Sea Research Part I: Oceanographic Research Papers*, 45(12):1977–2010, 1998a. ISSN 09670637. doi: 10.1016/S0967-0637(98)00070-3.

Munk, W. and Wunsch, C. Abyssal recipes II: Energetics of tidal and wind mixing. *Deep-Sea Research Part I: Oceanographic Research Papers*, 45(12):1977–2010, 1998b. ISSN 09670637. doi: 10.1016/S0967-0637(98)00070-3.

Munk, W. H. Abyssal recipes. *Deep-Sea Research and Oceanographic Abstracts*, 13(4):707–730, 1966. ISSN 00117471. doi: 10.1016/0011-7471(66)90602-4.

Nasmyth, P. W. Turbulence and microstructure in the upper ocean. *Mem. Soc. Roy. Sci. Liege*, 4:47–56, 1973.

National Oceanography Centre. MASSMO, 2018. URL http://projects.noc.ac.uk/massmo/.

Naveira Garabato, A. and Meredith, M. Ocean mixing: oceanography at a watershed. In *Ocean Mixing*, pages 1–4. Elsevier Inc., 2022. ISBN 9780128215128. doi: 10.1016/b978-0-12-821512-8.00008-6. URL https://doi.org/10.1016/B978-0-12-821512-8.00008-6.

Oakey, N. S. Determination of the Rate of Dissipation of Turbulent Energy from Simultaneous Temperature and Velocity Shear Microstructure Measurements, 1982. ISSN 0022-3670.

Osborn, T. R. Estimates of the Local Rate of Vertical Diffusion from Dissipation Measurements, 1980. ISSN 0022-3670. URL http://journals.ametsoc.org/doi/abs/10.1175/1520-0485%281980%29010%3C0083%3AEOTLRO%3E2.0.CO%3B2.

Ozmidov, R. V. On the turbulent exchange in a stably stratified ocean. Izv. Acad. Sci. USSR. *Atmos. Oceanic Phys.*, 1:861–871, 1965.

Palmer, M. R., Inall, M. E., and Sharples, J. The physical oceanography of Jones Bank: A mixing hotspot in the Celtic Sea. *Progress in Oceanography*, 117:9–24, 2013. ISSN 00796611. doi: 10.1016/j.pocean.2013.06.009. URL http://dx.doi.org/10.1016/j.pocean.2013.06.009.

Palmer, M. R., Stephenson, G. R., Inall, M. E., Balfour, C., Düsterhus, A., and Green, J. A. Turbulence and mixing by internal waves in the Celtic Sea determined from ocean glider microstructure measurements. *Journal of Marine Systems*, 144:57–69, 2015. ISSN 09247963. doi: 10.1016/j.jmarsys.2014.11.005. URL http://dx.doi.org/10.1016/j.jmarsys.2014.11.005.

Park, J. J. K., Laurent, L. S., and Owens, B. Test Deployment of Long-endurance Microstructure Sensors on a Spray Glider, 2012. URL http://www.whoi.edu/page.do?pid=107997&tid=3622&cid=142190.

Peterson, A. K. and Fer, I. Dissipation measurements using temperature microstructure from an underwater glider. *Methods in Oceanography*, 10:44–69, 2014. ISSN 22111220. doi: 10.1016/j.mio.2014.05.002. URL http://dx.doi.org/10.1016/j.mio.2014.05.002.

Polzin, K., Naveira Garabato, A. C., Huussen, T. N., Sloyan, B. M., and Waterman, S. N. Finescale parameterizations of turbulent dissipation. *Journal of Geophysical Research : Oceans*, pages 1383–1419, 2014. doi: 10.1002/2013JC008979.Received.

Polzin, K. L., Toole, J. M., and Schmitt, R. W. Finescale parameterizations of turbulent dissipation, 1994. ISSN 21699291.

Polzin, K. L., Kunze, E., Hummon, J. M., and Firing, E. The Finescale Response of Lowered ADCP Velocity Profiles. *Journal of Atmospheric and Oceanic Technology*, 19:205–224, 2002.

Pujiana, K., Moum, J. N., Smyth, W. D., and Warner, S. J. Distinguishing ichthyogenic turbulence from geophysical turbulence. *Journal of Geophysical Research : Oceans*, pages 3792–3804, 2015. doi: 10.1002/2014JC010659.Received.

Queste, B. Y. *Hydrographic observations of oxygen and related physical variables in the North Sea and western Ross Sea Polynya*. PhD thesis, University of East Anglia, 2013. URL https://ueaeprints.uea.ac.uk/id/eprint/48678/1/BYQ_Thesis_printcopy.pdf.

Radko, T. *Double-diffusive convection*. Cambridge University Press, 2013.

Rainville, L., Gobat, J. I., Lee, C. M., and Shilling, G. B. Multi-month dissipation estimates using microstructure from autonomous underwater gliders. *Oceanography*, 30(2):49–50, 2017.

Rockland Scientific. MicroRider, 2021. URL https://rocklandscientific.com/products/modular-systems/microrider/.

Roemmich, D., Riser, S., Davis, R., and Desaubies, Y. Autonomous Profiling Floats: Workhorse for Broad-scale Ocean Observations. *Marine Technology Society Journal*, 38(1):21–29, 2004. ISSN 00253324. doi: 10.4031/002533204787522802.

Roemmich, D., Johnson, G., Riser, S., Davis, R., Gilson, J., Owens, W., Garzoli, S., Schmid, C., and Ignaszewski, M. Observing the Global Ocean Argo Program. *Oceanography*, 22(2):34–43, 2009. doi: 10.5670/oceanog.2009.36.COPYRIGHT.

Rollo, C., Heywood, K. J., and Hall, R. A. Glider Observations of Thermohaline Staircases in the Tropical North Atlantic Using an Automated Classifier. 2021.

Ruddick, B. A practical indicator of the stability of the water column to double-diffusive activity. *Deep Sea Research*, 30(10):1105–1107, 1983.

Rudnick, D. L. Ocean Research Enabled by Underwater Gliders. *Annual Review of Marine Science*, 8(1):519–541, 2016. ISSN 1941-1405. doi: 10.1146/annurev-marine-122414-033913.

Rudnick, D. L., Davis, R. E., Eriksen, C. C., Fratantoni, D. M., and Perry, M. J. Underwater Gliders for Ocean Research. *Marine Technology Society Journal*, 38(2):73–84, 2004. ISSN 00253324. doi: 10.4031/002533204787522703. URL http://openurl.ingenta.com/content/xref?genre=article&issn=0025-3324&volume=38&issue=2&spage=73.

Salehipour, H., Caulfield, C. P., and Peltier, W. R. Turbulent mixing due to the Holmboe wave instability at high Reynolds number. *Journal of Fluid Mechanics*, 803:591–621, 2016. doi: 10.1017/jfm.2016.488.

Scheifele, B., Waterman, S., Merckelbach, L., and Carpenter, J. R. Measuring the Dissipation Rate of Turbulent Kinetic Energy in Strongly Stratified, Low-Energy Environments: A Case Study From the Arctic Ocean. *Journal of Geophysical Research: Oceans*, 123(8):5459–5480, 2018. ISSN 21699291. doi: 10.1029/2017JC013731.

Schmitt, R. W. Double diffusion in oceanography. *Annual Review of Fluid Mechanics*, 26(1):255–285, 1994. ISSN 00664189. doi: 10.1146/annurev.fl.26.010194.001351.

Schmitt, R. W., Perkins, H., Boyd, J. D., and Stalcup, M. C. C-SALT: An investigation of the thermohaline staircase in the western tropical North Atlantic. *Deep Sea Research Part A, Oceanographic Research Papers*, 34(10):1655–1665, 1987. ISSN 01980149. doi: 10.1016/0198-0149(87)90014-8.

Schmitt, R. W., Ledwell, J. R., Montgomery, E. T., Polzin, K. L., and Toole, J. M. Ocean science: Enhanced diapycnal mixing by salt fingers in the thermocline of the tropical atlantic. *Science*, 308(5722):685–688, 2005. ISSN 00368075. doi: 10.1126/science.1108678.

Schofield, O., Kohut, J., Aragon, D., Creed, L., Graver, J., Haldeman, C., Kerfoot, J., Roarty, H., Jones, C., Webb, D., and Glenn, S. Slocum Gliders: Robust and Ready. *Journal of Field Robotics*, 23(24):473–485, 2007. doi: 10.1002/rob.20200.

Schultze, L. K. P., Merckelbach, L., and Carpenter, J. R. Turbulence and Mixing in a Shallow Shelf Sea From Underwater Gliders. *Journal of Geophysical Research : Oceans*, 122:9092–9109, 2017. ISSN 00280836. doi: 10.1038/175238c0.

Scott, R. M., Brearley, J. A., Naveira Garabato, A. C., Venables, H. J., and Meredith, M. P. Rates and Mechanisms of Turbulent Mixing in a Coastal Embayment of the West Antarctic Peninsula. *Journal of Geophysical Research: Oceans*, 126(5), 2021. ISSN 21699291. doi: 10.1029/2020JC016861.

Seim, H. E. and Gregg, M. C. Detailed observations of a naturally occurring shear instability. *Journal of Geophysical Research*, 99(C5), 1994. ISSN 01480227. doi: 10.1029/94jc00168.

Sharples, J. RRS James Clark Ross 25th Mat - 10th July 2016: RidgeMix NERC Responsive Mode Project. University of Liverpool JR15-007 Cruise Rep. Technical report, 2016. URL https://www.bodc.ac.uk/resources/inventories/cruise_inventory/reports/jr15007.pdf.

Sheehan, P., Damerell, G. M., Leadbitter, P., Heywood, K. J., and Hall, R. A. Turbulent kinetic energy dissipation rate and attendant fluxes in the western tropical Atlantic estimated from ocean glider observations. 2021.

Sherman, J., Davis, R. E., Owens, W. B., and Valdes, J. The autonomous underwater glider" Spray". *Oceanic Engineering, IEEE Journal of*, 26(4):437–446, 2001. URL http://ieeexplore.ieee.org/xpls/abs_all.jsp?arnumber=972076%5Cnhttp://ieeexplore.ieee.org/xpl/login.jsp?tp=&arnumber=972076&url=http%3A%2F%2Fieeexplore.ieee.org%2Fxpls%2Fabs_all.jsp%3Farnumber%3D972076.

Sherwin, T. J. Evidence of a deep internal tide in the Faerie-Shetland Channel. In Parker, B. B., editor, *Tidal Hydrodynamics*, pages 469–488. John Wiley, 1st edition, 1991.

Sherwin, T. J. and Turrell, W. R. Mixing and advection of a cold water cascade over the Wyville Thomson Ridge. *Deep-Sea Research Part I: Oceanographic Research Papers*, 52(8):1392–1413, 2005. ISSN 09670637. doi: 10.1016/j.dsr.2005.03.002.

Sherwin, T. J., Turrell, W. R., Jeans, D. R. G., and Dye, S. Eddies and a mesoscale deflection of the slope current in the Faroe-Shetland Channel. *Deep-Sea Research Part I: Oceanographic Research Papers*, 46(3):415–438, 1999. ISSN 09670637. doi: 10.1016/S0967-0637(98)00077-6.

Sherwin, T. J., Williams, M. O., Turrell, W. R., Hughes, S. L., and Miller, P. I. A description and analysis of mesoscale variability in the Färoe-Shetland Channel. *Journal of Geophysical Research: Oceans*, 111(3):1–17, 2006. ISSN 21699291. doi: 10.1029/2005JC002867.

Sherwin, T. J., Griffiths, C. R., Inall, M. E., and Turrell, W. R. Quantifying the overflow across the Wyville Thomson Ridge into the Rockall Trough. *Deep-Sea Research Part I: Oceanographic Research Papers*, 55(4):396–404, 2008. ISSN 09670637. doi: 10.1016/j.dsr.2007.12.006.

Siddle, E., Heywood, K. J., Webber, B. G., and Bromley, P. First measurements of ocean and atmosphere in the Tropical North Atlantic using Caravela, a novel uncrewed surface vessel. *Royal Meterological Society*, 76(6):200–204, 2021. ISSN 14778696. doi: 10.1002/wea.4004.

Simpson, J. H., Crawford, W. R., Rippeth, T. P., Campbell, A. R., and Cheok, J. V. S. The Vertical Structure of Turbulent Dissipation in Shelf Seas, 1996. ISSN 0022-3670. URL http://journals.ametsoc.org/doi/abs/10.1175/1520-0485%281996%29026%3C1579%3ATVSOTD%3E2.0.CO%3B2.

Smyth, W. D. and Moum, J. N. Encyclopedia of Ocean Sciences (Third Edition). Number September 2018, chapter 3D Turbule, pages 486–496. Academic Press, Oxford, third edit edition, 2019. ISBN 9780124095489. doi: 10.1016/B978-0-12-409548-9.09728-1.

Smyth, W. D. and Thorpe, S. A. Glider measurements of overturning in a Kelvin-Helmholtz billow train. *Journal of Marine Research*, 70(1):119–140, 2012. ISSN

00222402. doi: 10.1357/002224012800502381. URL http://openurl.ingenta.com/content/xref?genre=article&issn=0022-2402&volume=70&issue=1&spage=119.

Smyth, W. D., Moum, J. N., and Caldwell, D. R. The Efficiency of Mixing in Turbulent Patches: Inferences from Direct Simulations and Microstructure Observations. *Journal of Physical Oceanography*, 31(8):1969–1992, 2002. ISSN 0022-3670. doi: 10.1175/1520-0485(2001)031<1969:teomit>2.0.co;2.

Sommer, T., Carpenter, J. R., Schmid, M., Lueck, R. G., and Wüest, A. Revisiting microstructure sensor responses with implications for double-diffusive fluxes. *Journal of Atmospheric and Oceanic Technology*, 30(8):1907–1923, 2013. ISSN 07390572. doi: 10.1175/JTECH-D-12-00272.1.

Spingys, C. P., Williams, R. G., Tuerena, R. E., Garabato, A. N., Vic, C., Forryan, A., and Sharples, J. Observations of Nutrient Supply by Mesoscale Eddy Stirring and Small-Scale Turbulence in the Oligotrophic North Atlantic Global Biogeochemical Cycles. pages 1–20, 2021. doi: 10.1029/2021GB007200.

St. Laurent, L. and Merrifield, S. Measurements of near-surface turbulence and mixing from autonomous ocean gliders. *Oceanography*, 30(2):116–125, 2017.

St. Laurent, L. C., Simmons, H. L., and Jayne, S. R. Estimating tidally driven mixing in the deep ocean. *Geophysical Research Letters*, 29(23):19–22, 2002. ISSN 19448007. doi: 10.1029/2002GL015633.

Steinhart, J. S. and Hart, S. R. Calibration curves for thermistors. *Deep-Sea Research and Oceanographic Abstracts*, 15(4):497–503, 1968. ISSN 00117471. doi: 10.1016/0011-7471(68)90057-0.

Stevens, B., Bony, S., Farrell, D., Ament, F., Blyth, A., Fairall, C., Karstensen, J., Quinn, P., Speich, S., Aemisegger, F., Albright, A., Bodenschatz, E., Chewitt-Lucas, R., Delanoë, J., Ewald, F., Forde, M., George, G., Hausold, A., Hagen, M., Hirsch, L., Jansen, F., Kinne, S., Klocke, D., Kölling, T., Konow, H., Mohr, W., Naumann, A., Nuijens, L., Pincus, R., Reverdin, G., Roberts, G., Schnitt, S., Sullivan, P., Touzé-Peiffer, L., Vial, J., Vogel, R., Acquistapace, C., Alexander, N., Alves, L., Arixi, S., Asmath, H., Bagheri, G., Bailey, A., Baranowski, D., Baron, A., Barrau, S., Barrett, P., Behrendt, A., Bellenger, H., Bendinger, A., Beucher, F., Bigorre, S., Blossey, P., Bock, O., Bosser, P., Bourras, D., Bouruet-Aubertot, P., Bower, K., Branger, H., Brennek, M., Brewer, A., Brügmann, B., Buehler, S., Burke, E., Burton, R., Böing, S., Calmer, R., Carton, X., Cato, G., Charles, J., Chazette, P., Chen, Y., Choularton, T., Chuang, P., Clarke, S., Coe, H., Cornet, C., Coutris, P., Couvreux, F., Crewell, S., Cronin, T., Cui, Z., Cuypers, Y., Daley, A., Damerell, G., Dauhut, T., Denby, L., Deneke, H., Douet, V., Drushka, K., Dütsch, M., Ehrlich, A., Emanuel, K., Emmanouilidis, A., Etienne-Leblanc, S., Faure, G., Feingold, G., Ferrero, L., Fildier, B., Fix, A., Flamant, C., Flatau, P., Foltz, G., Gadian, A., Galewsky, J., Gallagher, M., Gallimore, P., Gaston, C., Gentemann, C., Geyskens, N., Giez, A., Gourbeyre, C., Gross, S., Grosz, R., Gutleben, M., Güttler, J., Hall, K., Harris, G., Helfer, K., Henze, D., Herbert, C., Heywood, K., Holanda, B., Ibanez-Landeta, A., Intrieri, J., Iyer, S., Jacob, M., Julien, F., Kalesse, H., Kazil, J., Kellman, A., Kirchner, U., Klingebiel, M., Kremper, L., Kretzschmar, J., Krüger, O., Kurz, A., Körner, M., Lachlan-Cope, T., Laing, A., Landschützer, P., Lang, T., Lange, D., Lange, I., Laplace, C., Laxenaire, R., Leandro, M., Lefevre, N., Lenschow, D., Li, Q., Lloyd, G., Los, S., Losi, N., Lothon, M., Lovell, O., Luneau, C., Makuch, P., Malinowski, S., Manta, G., Marinou, E., Marsden, N., Matthieu, L., Maury, N., Mayer, B., Mayers-Als, M., Mazel, C., Mcgeary, W., Mcwilliams, J., Mech, M., Mehlmann, M., Meroni, A., Mieslinger, T., Minikin, A., Muller, C., Musat, I., Möller, G., Napoli, A., Neuberger, A., Noone, D., Nordsiek, F., Nowak, J., Olivier, L., Oswald, L., Parker, D., Peck, C., Person, R., Plueddemann, A., Pologne, L., Posyniak, M., Prange, M., Pöhlker, M., Pöhlker, C., Pörtge, V., Pöschl, U., Radtke, J., Ramage, K., Reimann, J., Renault, L., Reus, K., Reyes, A., Ribbe, J., Ringel, M., Ritschel, M., Rocha, C., Rochetin, N., Rollo, C., Röttenbacher, J., Saffin, L., Sandiford, S., Sandu, I., Schemann, V., Schirmacher, I., Schlenczek, O., Schmidt, J., Schröder, M., Schulz, H., Schwarzenboeck, A., Schäfer, M., Sealy, A., Serikov, I., Shohan, S., Siddle, E., Siebesma, A., Späth, F., Stephan, C., Stolla, M., Szkółka, W., Tarot, S., Tetoni, E., Thompson, E., Thomson, J., Tomassini, L., Totems, J., Villiger, L., Walther, A., Webber, B., Wendisch, M., Whitehall, S., Wiltshire, A., Wing, A., Wirth, M., Wiskandt, J., Wolf, K., Worbes, L., Wright, E., Wulfmeyer, V., Young, S., Zhang, D., Zhang, C., Ziemen, F., Zinner, T., Zuidema, P., and Zöger, M. Eurec 4 a. *Earth System Science Data Discussions*, pages 1–78, 2021.

Stommel, H. The Slocum Mission. *Oceanography*, 2(1):22–25, 1989. ISSN 10428275. doi: 10.5670/oceanog.1989.26.

Strang, E. J. and Fernando, H. J. S. Entrainment and mixing in stratified shear flows. *Journal of Fluid Mechanics*, 428:349–386, 2001.

Sutherland, G., Ward, B., and Christensen, K. H. Wave-turbulence scaling in the ocean mixed layer. *Ocean Science*, 9(4):597–608, 2013. ISSN 18120784. doi: 10.5194/os-9-597-2013.

Talley, L. D., Pickard, G. L., Emery, W. J., and Swift, J. H. *Descriptive physical oceanography: an introduction*. Academic Press, 2011.

Tanaka, M., Genin, A., Endo, Y., Ivey, G. N., and Yamazaki, H. The potential role of turbulence in modulating the migration of demersal zooplankton The potential role of turbulence in modulating the migration of demersal zooplankton. *Limnology and Oceanography*, (March):1–10, 2021. doi: 10.1002/lno.11646.

Thomson, R. E. and Emery, W. J. *Data analysis methods in physical oceanography*. Elsevier, 3rd edition, 2014.

Thorpe, S. Turbulence and mixing in a Scottish Loch. *Philosophical Transactions of the Royal Society of London*, 286:125 – 181, 1977.

Thorpe, S. *An Introduction to Ocean Turbulence*. Cambridge University Press, 2007. ISBN 9780521676809. doi: 10.1029/2008EO520011. URL http://doi.wiley.com/10.1029/2008EO520011.

Thorpe, S. A. Measuring overturns with gliders. *Journal of Marine Research*, 70(1): 93–117, 2012. ISSN 00222402. doi: 10.1357/002224012800502417.

Turrell, W. R., Slesser, G., Adams, R. D., Payne, R., and Gillibrand, P. A. Decadal variability in the composition of Faroe Shetland Channel bottom water. *Deep-Sea Research Part I: Oceanographic Research Papers*, 46(1):1–25, 1999. ISSN 09670637. doi: 10.1016/S0967-0637(98)00067-3.

van der Boog, C. G., Dijkstra, H. A., Pietrzak, J. D., and Katsman, C. A. Double-diffusive mixing makes a small contribution to the global ocean circulation. *Communications Earth & Environment*, 2(1):1–9, 2021. ISSN 2662-4435. doi: 10.1038/s43247-021-00113-x. URL http://dx.doi.org/10.1038/s43247-021-00113-x.

Venables, E. J. *Shear-Induced Vertical Mixing in the Wyville Thomson Basin: A Study of its Driving Mechanisms, Strength and Influence.* PhD thesis, University of Aberdeen, 2011.

Vic, C., Garabato, A. C., Green, J. A., Spingys, C., Forryan, A., Zhao, Z., and Sharples, J. The lifecycle of semidiurnal internal tides over the Northern Mid-Atlantic Ridge. *Journal of Physical Oceanography*, 48(1):61–80, 2018. ISSN 15200485. doi: 10.1175/JPO-D-17-0121.1.

Waterman, S. N., Naveira Garabato, A. C., and Polzin, K. L. Internal Waves and Turbulence in the Antarctic Circumpolar Current. *Journal of Physical Oceanography*, 43(2):259–282, 2013. doi: 10.1175/JPO-D-11-0194.1.

Webb, D. C., Simonetti, P. J., and Jones, C. P. SLOCUM: An underwater glider propelled by environmental energy. *IEEE Journal of Oceanic Engineering*, 26(4):447–452, 2001. ISSN 03649059. doi: 10.1109/48.972077.

Wijesekera, H. W., Dillon, T. M., and Padman, L. Some statistical and dynamical properties of turbulence in the oceanic pycnocline. *Journal of Geophysical Research*, 98(C12):665–679, 1993. ISSN 01480227. doi: 10.1029/93jc02352.

Wolk, F., Yamazaki, H., Seuront, L., and Lueck, R. G. A new free-fall profiler for measuring biophysical microstructure. *Journal of Atmospheric and Oceanic Technology*, 19(5):780–793, 2002. ISSN 07390572. doi: 10.1175/1520-0426(2002)019<0780:ANFFPF>2.0.CO;2.

Wolk, F., Lueck, R. G., Canada, B. C. V. Z., and Laurent, L. S. Turbulence Measurements from a Glider. *OCEANS 2009, MTS/IEEE Biloxi - Marine Technology for Our Future: Global and Local Challenges*, pages 1 – 6, 2009.

Woods Hole Oceanographic Insitution. Know your Ocean. URL https://www.whoi.edu/know-your-ocean/.

Wunsch, C. and Ferrari, R. Vertical mixing, energy, and the general circulation of the oceans. *Annual Review of Fluid Mechanics*, 36(1):281–314, 2004. ISSN 00664189. doi: 10.1146/annurev.fluid.36.050802.122121.

Appendix

A - RUN-LENGTH TEST

RUN-LENGTH FILTER

Figure A.1 shows a close to idealised Z shaped overturning region, many overturning regions picked out through the Thorpe scale method are not so clear. It is then important to determine which overturning regions are due to actual turbulent motions and which result from instrument noise. Galbrath and Kelley (1995) proposed using run-lengths as a method of determining a lower threshold for turbulently formed overturns

If random noise is added to a stratified temperature profile inversions may arise that will picked out as an overturning event. Using the 'run-length' of these overturning events it can be determined if they are true turbulent events or related to instrument noise. A time series of Thorpe fluctuations are examined sequentially and adjacent values of the same sign are grouped into 'runs'. Each run is assigned a run-length value, i.e. the number of sequential Thorpe fluctuations with the same sign. For example, a time series +1 +2 +1 -1 -2 -3 -2 will have two runs with lengths of 3 and 4 respectively. The root mean square is then taken of the runs in an overturning region giving a run-length for a given overturning region. For the previous example that is a value of 3.5. The run-length probability density function (PDF) of an uncorrelated series of negative and positive values is,

$$P(n) = 2^{-n} \tag{1}$$

where $P(n)$ is the probability of a run-length n (e.g. as (Gregg et al., 1986)). Therefore if a density inversion is caused by random noise then the associated PDF should be as Equation 1. Overturns not caused by random noise are likely to have

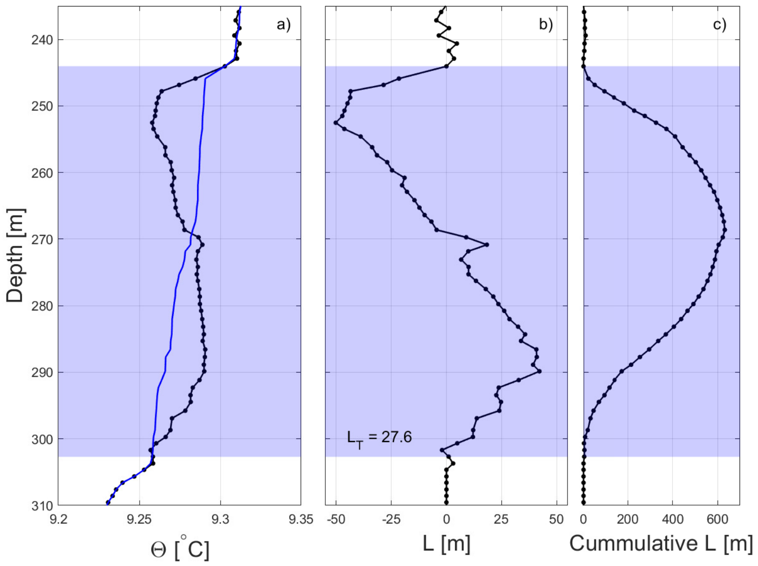

Figure A.1: Figure showing a) Measured (black) and reordered (blue) conservative temperatures profiles. b) Associated Thorpe displacements c) Cumulative Thorpe displacements. Shaded blue areas mark the vertical extent of the complete overturn.

long positive runs followed by long negative runs, so if a real overturn is present in the time series then the associated PDF will be larger than Equation 1. For a run-length test, the rms run-length of Thorpe fluctuation is calculated over a region defined as an overturn. If this value is longer than a threshold value then the overturn is considered real. The threshold value is different for each dataset. The threshold run-length is defined as the first crossover of the observed PDF and double the noise PDF (Galbrath and Kelley, 1995). An example of the threshold value can be seen in Figure A.2. All Overturns with a run-length below the threshold level are removed.

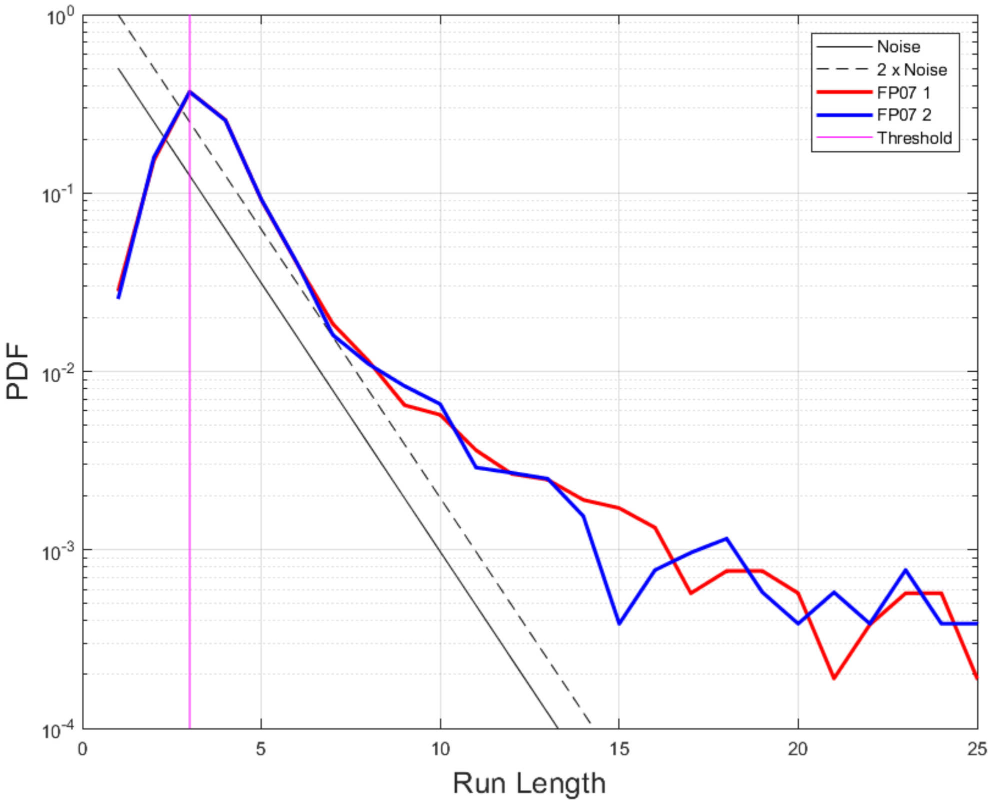

Figure A.2: Example of calculating the run-length threshold using FP07 fast thermistor data from RidgeMix, Chapter 3. Here both FP07 fast thermistors cross the double noise limit between a run-length of 2 and 3, giving a run-length threshold of 3 as indicated by the magenta line.

B - PROBE COMPARISON

A VMP carries 2 shear and 2 FP07 probes. In Chapter 3 only data from a single shear probe and FP07 are presented. The figures in this appendix form the basis for that decision. A time mean for both probe 1 and 2 of shear and FP07 was calculated and then plotted against each other and a linear gradient of that relationship calculated. Across all three datasets the temperature from the FP07 shows a correlation that is very close to 1. (Figures B.1-B.3) The shear probes show a correlation that is slightly less than 1, with values between 0.92 and 0.97 (Figures B.4-B.6). This was considered close enough to 1 to indicate there were no major biases towards either probe.

FP07 Probes

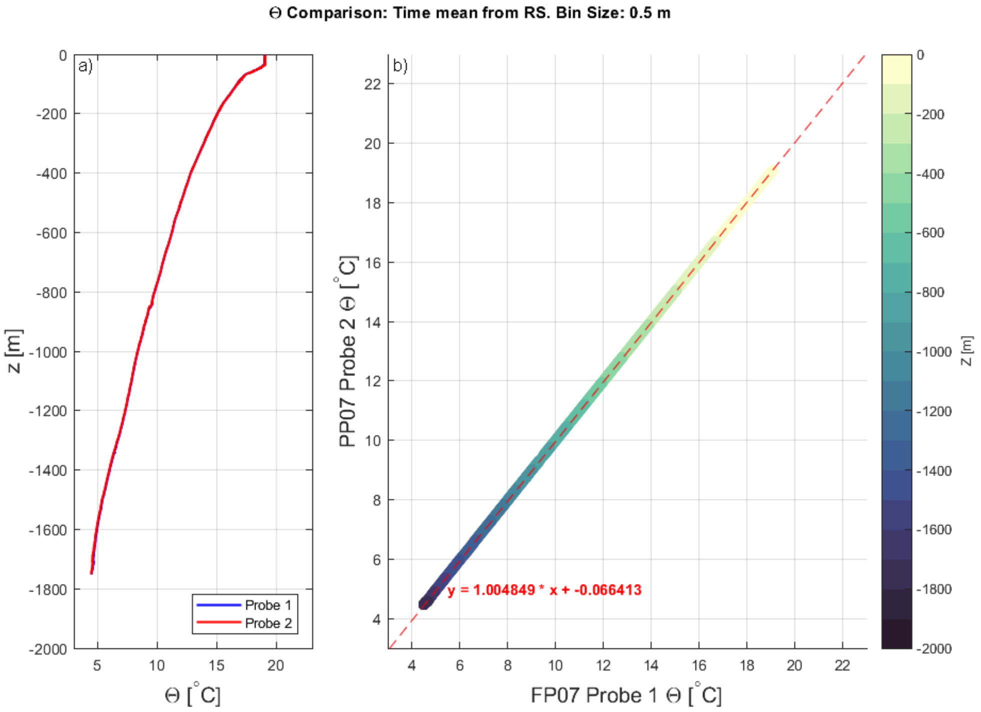

Figure B.1: Temperature analysis from the two FP07 probes on the VMP-2000 from the Ridge Spring data set. a) time mean of both against depth. b) the two probes plotted against each other with a linear fit applied

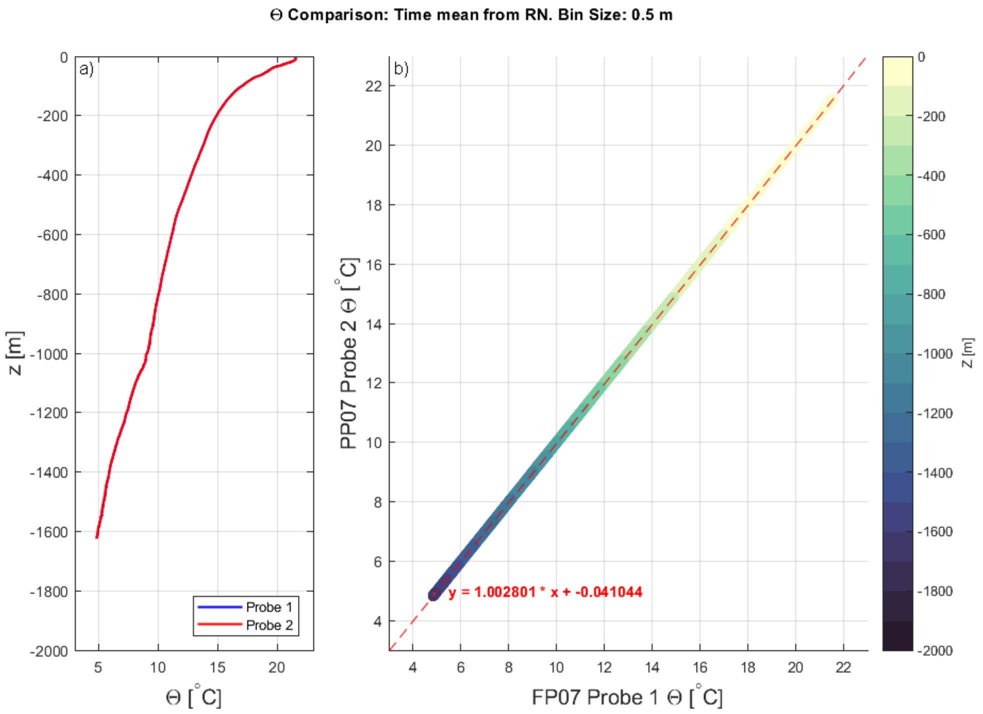

Figure B.2: Temperature analysis from the two FP07 probes on the VMP-2000 from the Ridge Neap data set. a) time mean of both against depth. b) the two probes plotted against each other with a linear fit applied

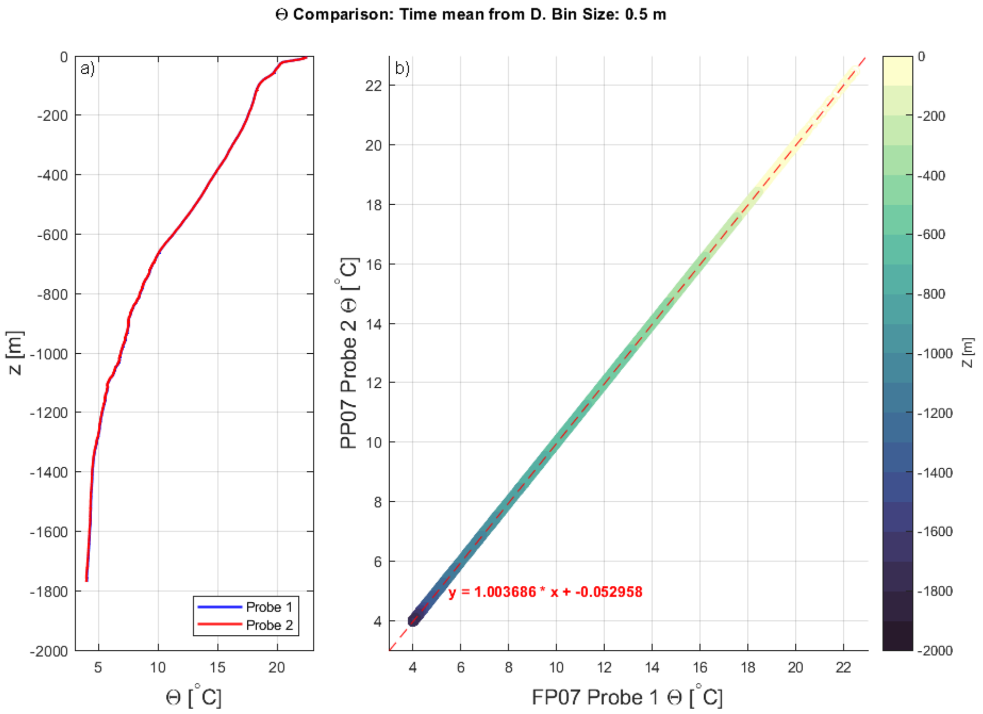

Figure B.3: Temperature analysis from the two FP07 probes on the VMP-2000 from the Deep data set. a) time mean of both against depth. b) the two probes plotted against each other with a linear fit applied

SHEAR PROBES

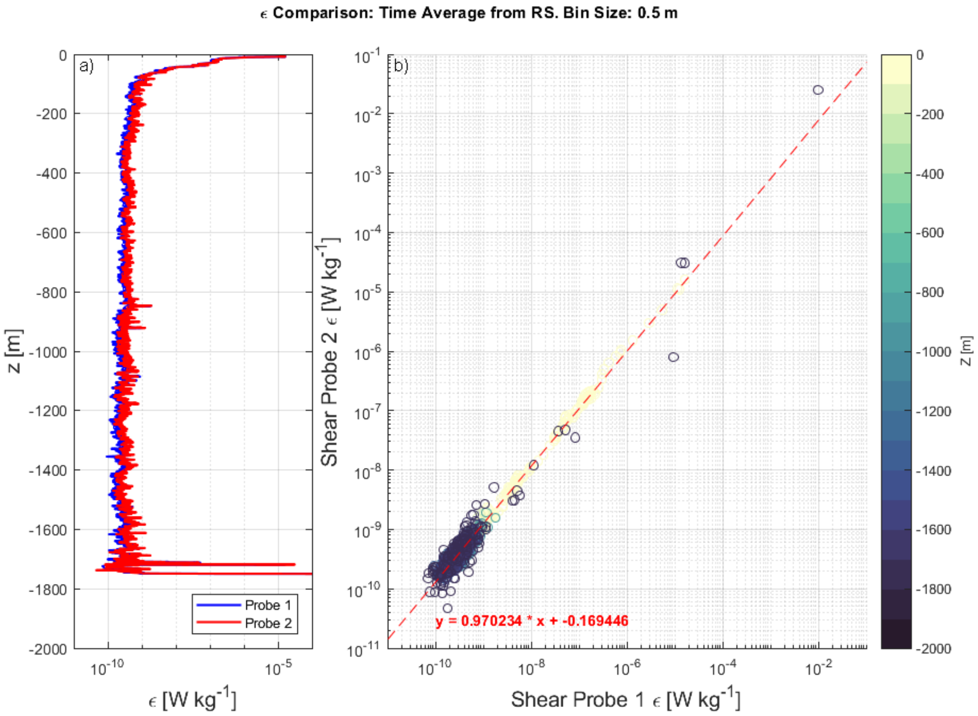

Figure B.4: TKE dissipation estimates from the two shear probes on the VMP2000 from the Ridge Spring data set. a) time mean of both against depth. b) the two probes plotted against each other with a linear fit applied

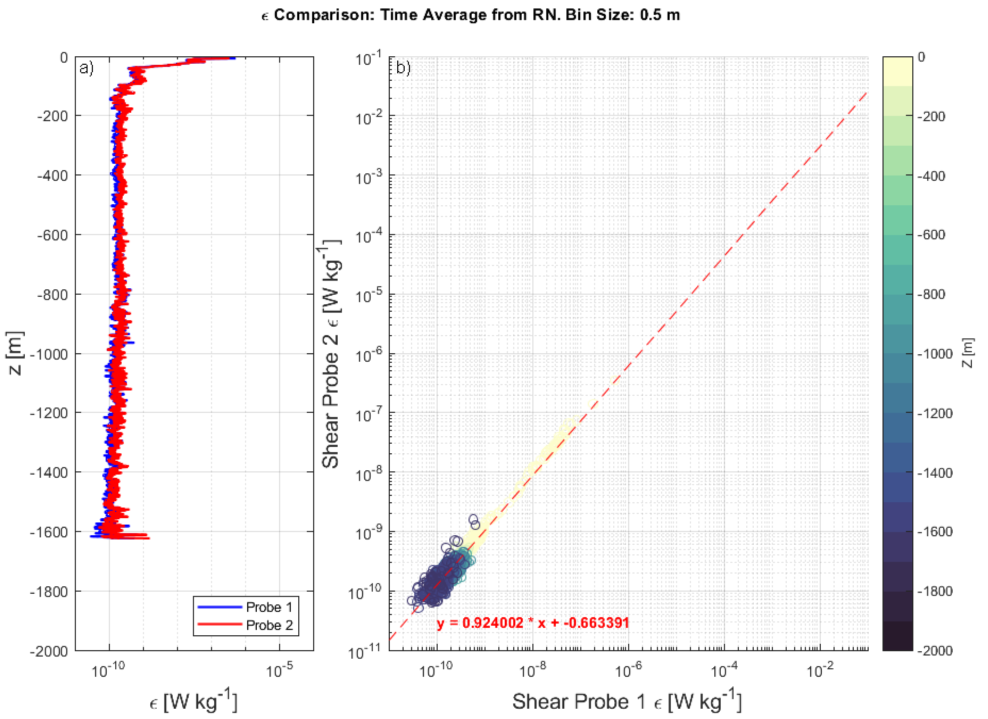

Figure B.5: TKE dissipation estimates from the two shear probes on the VMP2000 from the Ridge Neap data set. a) time mean of both against depth. b) the two probes plotted against each other with a linear fit applied

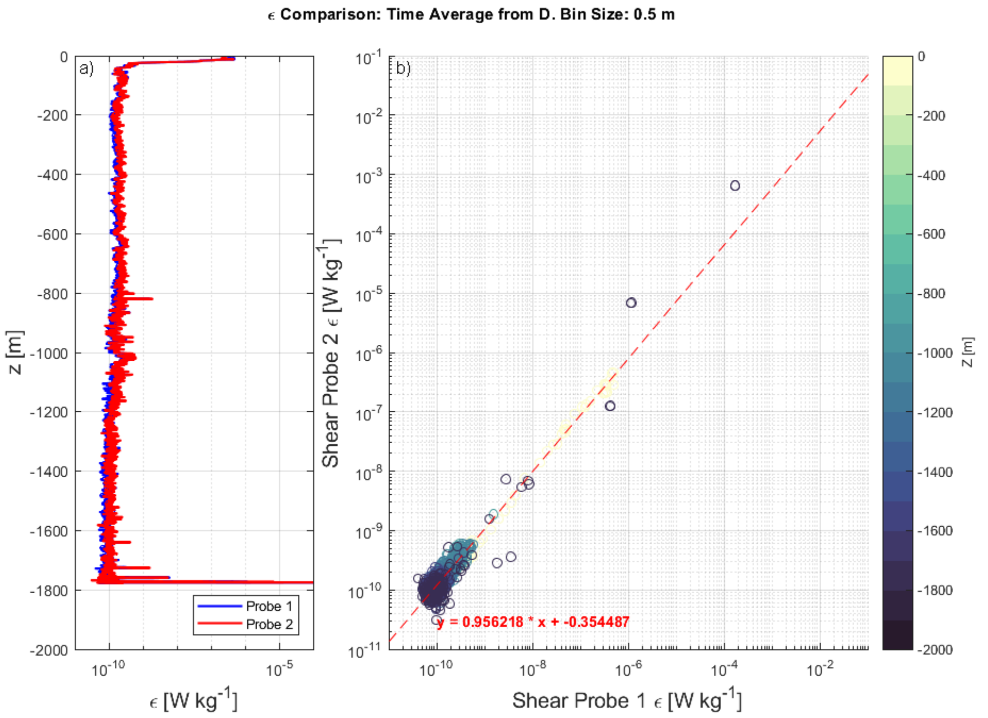

Figure B.6: TKE dissipation estimates from the two shear probes on the VMP2000 from the Deep data set. a) time mean of both against depth. b) the two probes plotted against each other with a linear fit applied